A Novel Synthetic Biology Method to Study the Cooperative Behavior of Kinesin Motors in Cells

by

Stephen R. Norris

A dissertation submitted in partial fulfillment
of the requirements for the degree of
Doctor of Philosophy
(Biophysics)
in The University of Michigan
2014

Doctoral Committee:

Professor Kristen J. Verhey, Chair
Assistant Professor Dawen Cai
Assistant Professor Allen P. Liu
Professor David S. Sept
Assistant Professor Sivaraj Sivaramakrishnan

2014

Acknowledgments

"No man is an island…" – John Donne. None of this would have been possible without the amazing and nurturing research community here at Michigan. First, I need to thank my research advisor, Professor Kristen Verhey. I struggle to properly articulate how supportive she has been for my research and growth, but she is a truly wonderful scientist and mentor. I will always strive to emulate her approach to research and advising in the future. I would also like to sincerely thank my thesis committee, Sivaraj Sivaramakrishnan, David Sept, Dawen Cai, and Allen Liu. Your patience, ideas, and feedback have been invaluable.

The Verhey lab has been an incredible place during my time here at Michigan. I thank everyone in the lab and am lucky to count them as friends. Lynne Blasius, in particular, is a walking encyclopedia of lab protocols, and she goes above and beyond in helping others. Lynne, I'm sorry for all the questions. Viru Soppina trained me during my lab rotation and is an exceptionally gifted researcher and microscopist. He has taught me a number of great techniques over the years. Aslan Dizaji implemented an automated particle-tracking technique for single molecules that led to great insights in this project. Martin Engelke has always found time to discuss the latest techniques and occasionally grab a quick lunch. I would also like to thank other current and former lab members: Daisuke Takao, Yang Yue, John Dishinger, Lynn Kee, Jay Pieczynski, and many others who have come and gone. Thank you all for being so supportive, helpful, and fun.

I have had the pleasure of working directly with a number of rotation students in the lab, including Aslan Dizaji, Kristin Schimert, Marcos Núñez, Torey Arnold, and Caroline Becker. Each of you are poised for great things and I sincerely thank you for your patience and hard work during your time in the lab.

A number of collaborators, including my committee members and their lab members, have made this work possible. I specifically want to thank Rizal Hariadi in the Sivaramakrishnan lab for valuable discussions. Additional collaborators include Corey Williams in the laboratory of Jeffrey Martens, Neha Kaul in the laboratory of Edgar Meyhöfer, and external collaborators Erkan Tuzel and Jennifer Ross. I would also like to thank Sam Straight at the Center for Live Cell Imaging (CLCI) for help with FRET experiments, and Sethu Pitchiaya and Tristan Tabouillot at the Single Molecule Analysis in Real Time (SMART) Center for help with TIRF imaging. A special thank you to Billy Tsai, Diane Fingar, Mara Duncan, and their labs for feedback at weekly lab meetings.

Thank you to Biophysics, especially Sara Grosky, for all of your help and support. A special thank you to biophysics graduate students Josh Jasensky and Tony Mustoe for being with me through the whole process and providing friendship, sanity, and moral support. Thanks to the Cell and Developmental Biology faculty and staff for providing a "home away from home" here at UM.

I also wish to thank my undergraduate advisor, Professor Richard Superfine, and Jeremy Cribb, who trained me in the lab. A special thank you to Professor Jens-Christian Meiners and Joshua Milstein who supervised my lab rotation in my first semester at UM.

To all of the friends I've made in Ann Arbor, thank you for everything. I will miss this town dearly, but our friendships are just beginning. A special thank you to the BeerLab ™ group for proposing additional experiments in the field of microbiology.

To Leila, thank you for being a constant source of inspiration, love, comfort, and humility. As a side note, hopefully I attributed that Donne quote correctly, but I'm guessing it's probably out of context anyway.

Finally, thank you so much to my family for all of your love and support. I am truly blessed to be surrounded by such a nurturing, caring, smart, and weird-but-in-a-good-way family. A heartfelt thanks to all of you: my parents, Rick and Jan; my sister, Madison; my grandparents, and everyone else. There are too many of you to list here, but I guess that's just how we roll.

Table of Contents

List of Figures

List of Tables

Abstract

Collective motor dynamics drives important cellular processes ranging from muscle contraction to spindle organization to vesicle trafficking (Chapter 1). Although the biomechanical and biochemical properties of individual motors have been widely studied, how motors coordinate their motility when attached to the same cargo is largely unknown.

In this dissertation, I present a synthetic biology technique (Chapter 2) to generate multi-motor assemblies whose biological properties can be examined *in vitro* and in living cells. To do this, we assembled a "toolbox" of protein components consisting of scaffolds and linkers. We characterized scaffold proteins of different lengths that allow for specific separation distances between the components. We then characterized four different linker systems that enable constitutive or regulated attachment of individual motors to scaffolds. We then showed, through FRET and subcellular localization experiments, that this toolbox could be used to generate defined assemblies in living cells.

Next, I present a characterization of fluorescent tags for use in single-molecule experiments (Chapter 3), and show that certain tags lead to aberrant kinesin-1 run lengths due to oligomerization. This study will provide a valuable reference for the field in choosing proper fluorescent tags for single-molecule experiments.

I then present a series of experiments where we use this system to investigate the behavior

of two motors attached to a scaffold (Chapter 4). We find that two kinesin motors in complex act independently (do not help or hinder each other) and can alternate their activities. For complexes containing a slow kinesin-1 and fast kinesin-3 motor, the slow motor dominates motility *in vitro* but the fast motor can dominate on certain subpopulations of microtubules in cells. Both motors showed dynamic interactions with the complex, suggesting that motor-cargo linkages are sensitive to forces applied by the motors. We conclude that kinesin motors in complex act independently in a manner regulated by the microtubule track.

Overall, the approach presented in this dissertation is applicable to other biological questions such as the generation of complex signaling networks as well as the assembly of artificial biological systems for engineering applications (Chapter 5).

Chapter 1 Introduction: motor proteins and cooperation in intracellular transport

1.1 Introduction

Eukaryotic cells are extraordinarily organized. Each cell – far from the jumbled sack of organelles and compartments it appears to be in a high school student's biology textbook – resembles a meticulously planned city, complete with roads, subways, and landmarks. In order for this organization to be achieved, the cell cannot simply rely on random diffusion of its constituent parts within its plasma membrane borders. The cell must somehow direct traffic – generate directed movement in a timely fashion – for each component to arrive at a specific destination at a desired time. Over millennia, the cell has evolved to contain a highly regulated system of transport with the purpose of providing this infrastructure. The cytoskeleton, a complex network of microtubules and actin filaments, serves as the train tracks and roads; processive molecular motors, enzymes which convert ATP to mechanical work, serve as trains and cars; organelles and subcellular cargoes serve as the landmarks and important features in the city. Understanding how this intracellular trafficking functions is a central question for cell biologists and is key to advancing treatments for neurodegeneration, cancer, and wound healing, as well as countless other medical applications.

1.2 Molecular motors: discovery and fundamentals

Molecular motors are enzymes that catalyze the hydrolysis of ATP, converting the released energy into mechanical work inside the cell (Schliwa, 2003). Three families of molecular motors are known to walk along cytoskeletal tracks (Fig. 1.1): kinesin, which walks toward the cell periphery to plus-ends of microtubules (Hirokawa et al., 2009); cytoplasmic dynein, which walks toward the interior of the cell to minus-ends of microtubules (Roberts et al., 2013); and processive myosin, which walks along polarized actin filaments in either direction (Sweeney and Houdusse, 2010). Together, these molecular motors and cytoskeletal tracks create a versatile and effective toolbox for intracellular transport (Vale, 2003).

1.2.1 Myosin: a large superfamily of actin-based motors with diverse functions

Of these three motors, the discovery of myosin occurred first and provided our first key insights into models of cytoskeletal motility throughout the 20th century. Conventional myosin was discovered in 1859 by F.W. Kuhne when he observed clotting of frog skeletal muscle plasma, naming the protein component of this clot "myosin." An enormous breakthrough observation came nearly a century later by Albert Szent-Gyorgyi, when he showed that myosin fibers isolated from rabbit muscle contracted in the presence of ATP (Szent-Gyorgyi, 1941-1942). This observation indicated an enzymatic activity inherent to muscle and led to a flurry of biochemical and biophysical studies, culminating in two landmark theoretical models for muscle contraction (Huxley and Niedergerke, 1954; Huxley and Hanson, 1954). The model proposed by H.E. Huxley eventually led to the swinging cross-bridge hypothesis of muscle contraction, which was immensely influential in describing cell motility and remains heavily cited (Huxley, 1969). In

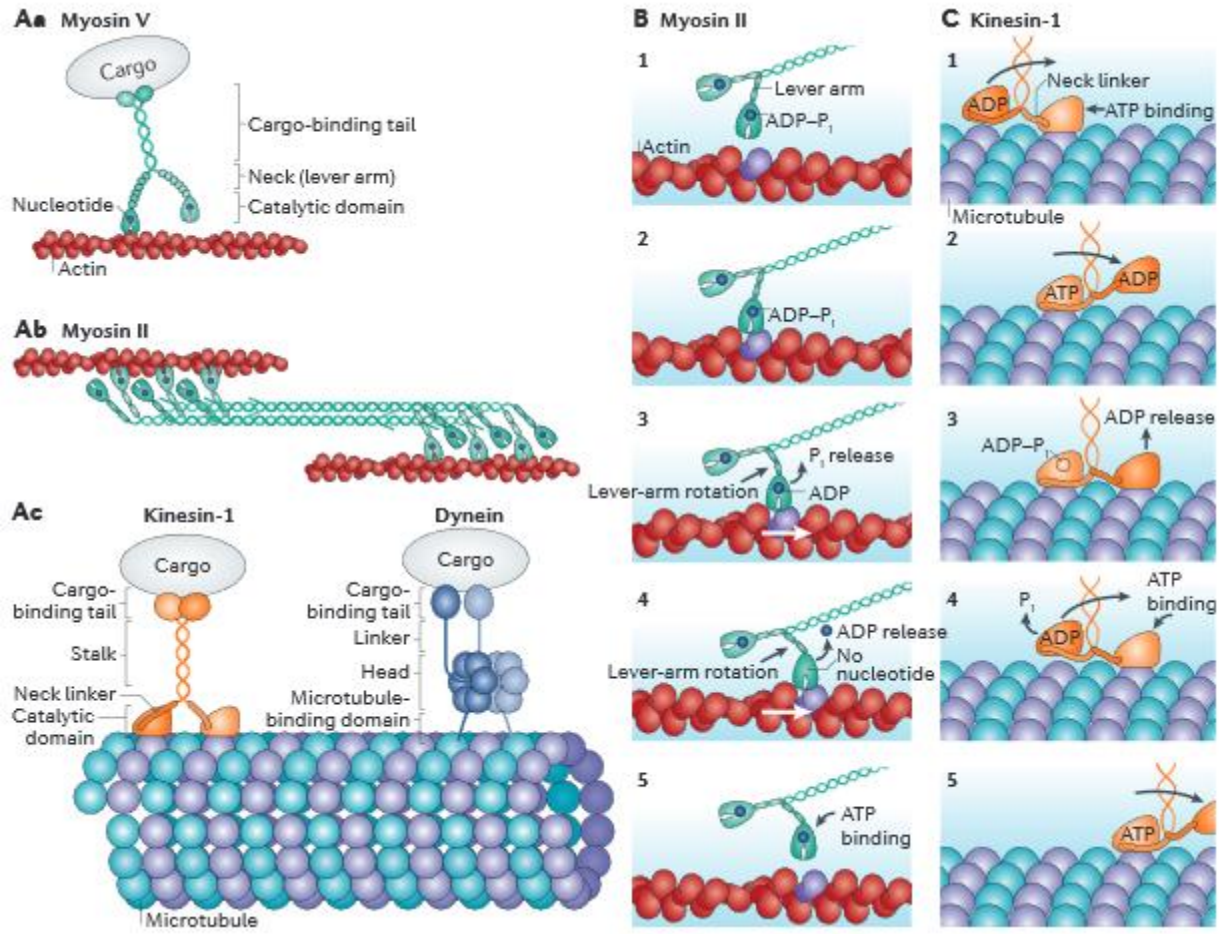

Figure 1.1. Cytoskeletal motor structures and functions.

(Aa) Myosin V works as a dimer to 'processively' transport intracellular cargo along actin filaments. Its functional segments are labeled. **(Ab)** 'Non-processive' dimeric myosin II has similar functional domains to myosin V but assembles in a different manner. Several proteins associate through their tail domains into bipolar filaments that can exert tension between actin filaments. **(Ac)** Kinesins and dyneins move along microtubules. Kinesin-1 and cytoplasmic dynein (shown in the figure) are processive and move intracellular cargo. Kinesins have a similar domain structure to myosins (functional segments are labeled). Dynein also acts as a dimer, but it is structurally different from other cytoskeletal motors. **(B)** Structural changes of a myosin II head during its power stroke. The respective nucleotide state is indicated. The motor head starts in an unbound state (step 1), then binds to actin with the products of ATP hydrolysis, ADP and inorganic phosphate (Pi), bound to the catalytic site (step 2). The release of Pi is coupled to a first lever-arm rotation, which causes actin to move (step 3; actin movement is indicated by the white arrow). Release of the ADP causes a second, smaller rotation of the lever arm and additional actin movement (step 4). ATP binding induces detachment of the motor (step 5). **(C)** Structural changes of a dimeric Kinesin-1 during a processive step, with nucleotide states indicated. ATP binding to the bound head (step 1) causes neck-linker docking, which directs the unbound head forward to the next binding site along the microtubule (step 2).

Binding at this site causes ADP release (step 3). ATP hydrolysis followed by Pi release causes the now trailing head to detach (step 4). ATP binding to the leading head again causes neck-linker docking, and the cycle repeats (step 5).

Figure used, with permission, from Veigel, C., and Schmidt, C.F. (2011). Moving into the cell: single-molecule studies of molecular motors in complex environments. Nature reviews Molecular cell biology 12, 163-176. (Veigel and Schmidt, 2011).

---

contrast to the processive motors primarily discussed in this work, the conventional myosin responsible for this muscle contraction (Myosin II) is a non-processive monomeric motor that utilizes its low duty ratio to work in large groups to move actin cooperatively (Fig. 1.1Ab) (Huxley, 1969).

The discovery and characterization of processive, dimeric myosin occurred many decades later, when Myosin V dimers were shown to move processively toward the barbed (+) end of actin filaments and the periphery of the cell (Fig. 1.1Aa) (Mehta et al., 1999), and Myosin VI dimers were shown to move processively toward the pointed (-) end of actin filaments and the interior of the cell (Wells et al., 1999). Although each myosin motor uses the same basic cross-bridge cycle, the seventeen different myosin family members have vastly different key properties: duty ratio, thermodynamic coupling of actin, nucleotide binding to myosin, and the degree of strain-sensitivity (Bloemink and Geeves, 2011). Variations between myosin family members arise mostly from divergent tail domains and allow the myosin superfamily to accomplish versatile tasks in the cell ranging from muscle contraction to long-range transport (Oliver et al., 1999).

1.2.2 Dynein: a very large, microtubule-based, minus-end directed motor

The discovery of dynein (Gibbons and Rowe, 1965) in the early 1960's is reminiscent of the discovery of myosin; in both cases, a large structure important for biological movement (flagella in the case of dynein, muscle filaments in the case of myosin) was studied, and a protein component was isolated and shown to generate this movement via ATP hydrolysis. Dynein is a very large (typically ~1.5 MDa) protein complex comprised of multiple subunits that hydrolyze ATP to move in the minus-end direction of microtubules (Fig. 1.1Ac) (Vallee et al., 2004). Because of the complexity and large size of dynein, detailed studies of dynein have historically lagged behind that of kinesin and a partial crystal structure of dynein was only recently obtained (Carter et al., 2011; Kon et al., 2012).

In contrast to myosin and kinesin, which have a similar core mechanism, share a G-protein related fold, and seem to have descended from a common ancestor, dynein belongs to the AAA+ superfamily (ATPases associated with diverse activities), a class of proteins that typically function as hexameric rings (Vale and Milligan, 2000). Dynein heavy chain (DHC, typically ~500 kDa) consists of a central six AAA+ modules as well as multiple appendages that enable motor function, including a microtubule-binding domain, linker, stalk, neck, and divergent tail (Roberts et al., 2013). Processive cytoplasmic dynein also contains a dimerization domain which is necessary for processive motion, suggesting a two-headed mechanism (Reck-Peterson et al., 2006; Shima et al., 2006). Unlike kinesin and processive myosin, dynein appears not to walk in a hand-over-hand manner and is able to take steps of multiple sizes, a unique adaptation which has been proposed to aid in more efficient transport for groups of dynein motors (Rai et al., 2013). Dynein's divergent tail domain can bind a variety of cargoes, adaptors, intermediate and light chains which allow diverse function in the cell (Vallee et al., 2004).

Dynein can be broken down into two classes: axonemal dyneins, which are responsible for the movement of cilia and flagella (Porter and Sale, 2000), and cytoplasmic dyneins, which are responsible for processive motion and cargo transport in the minus-end direction of microtubules throughout the cell (Karki and Holzbaur, 1999). In contrast to kinesin and myosin, which encompass a variety of motors active in intracellular transport, only two cytoplasmic dyneins have been identified: cytoplasmic dynein 1 ("cytoplasmic dynein"), which is responsible for the vast majority of processive minus-end directed MT transport, and cytoplasmic dynein 2 ("IFT dynein"), which is responsible for processive minus-end transport in flagella and cilia known as intraflagellar transport or IFT (Roberts et al., 2013). Because only one cytoplasmic dynein is responsible for such a wide variety of intracellular transport, dynein is thought to be regulated by an array of multifunctional adaptors, including dynactin, lissencephaly 1 (LIS1), nuclear distribution protein E (NUDE) and NUDE-like, Bicaudal D, Rod-ZW10-Zwilch, and Spindly (Kardon and Vale, 2009).

1.2.3 Kinesin: a large superfamily of microtubule-based, plus-end directed motors

Kinesin was first discovered in the context of axonal transport in the mid-1980's, decades after the discoveries of myosin and dynein (Hirokawa et al., 2009). The polarized system of the axon was crucial for kinesin's discovery. A retrograde transporter was already known in dynein, but an anterograde transporter had yet to be properly identified although candidate molecules had been visualized by cryo-electron microscopy (Hirokawa, 1982; Miller and Lasek, 1985). Vale et al. (1985) first identified and purified kinesin from the axoplasm of a squid giant axon. This was done by co-sedimenting a fraction with microtubules in the presence of a non-hydrolyzable ATP

analog, then confirming that this fraction was responsible for inducing ATP-dependent movement in a manner independent from myosin and dynein (Vale et al., 1985a).

Similar to the many classes of myosin, the kinesin superfamily contains fifteen kinesin families according to phylogenic analysis and 45 different mammalian genes (with more potential isoforms possible through alternative mRNA splicing), most of which have a relatively conserved motor domain and a divergent tail domain allowing specific cargo binding (Fig. 1.2) (Hirokawa and Noda, 2008). Conventional kinesin, also known as kinesin-1 or KIF5, consists of two ~120 kDa kinesin heavy chains (KHC) and occasionally two ~60 kDa kinesin light chains (KLC). In general, most processive kinesin motors dimerize through a C-terminal coiled coil "stalk," possess an N-terminal motor "head," and achieve processive motion toward the plus-end of microtubule tracks in 8-nm steps through a coordinated hand-over-hand action of the motor heads (Figs. 1.1Ac, 1.1C) (Vale, 2003; Yildiz et al., 2004). Numerous nonconventional kinesins have evolved to have their motor domain at the C-terminus or an intermediate location and result in minus-end directed motion or microtubule depolymerization, respectively (Ovechkina and Wordeman, 2003). Additionally, kinesin-5 family members form homotetramers that crosslink and slide microtubules, a function critical for bipolar mitotic spindles in eukaryotes (Cross and McAinsh, 2014). Similar to dynein, adaptor and scaffold molecules provide additional versatility for linking motors to specific cargoes in the cell (Akhmanova and Hammer, 2010; Kamal and Goldstein, 2002). Together, the kinesin superfamily has evolved to achieve a stunning variety of tasks inside the cell (Fig. 1.2) and some additional work remains to characterize the more elusive kinesin family members.

Kinesin's smaller size and relative structural simplicity compared to dynein make it comparatively easier to purify and thus an ideal candidate for *in vitro* experiments

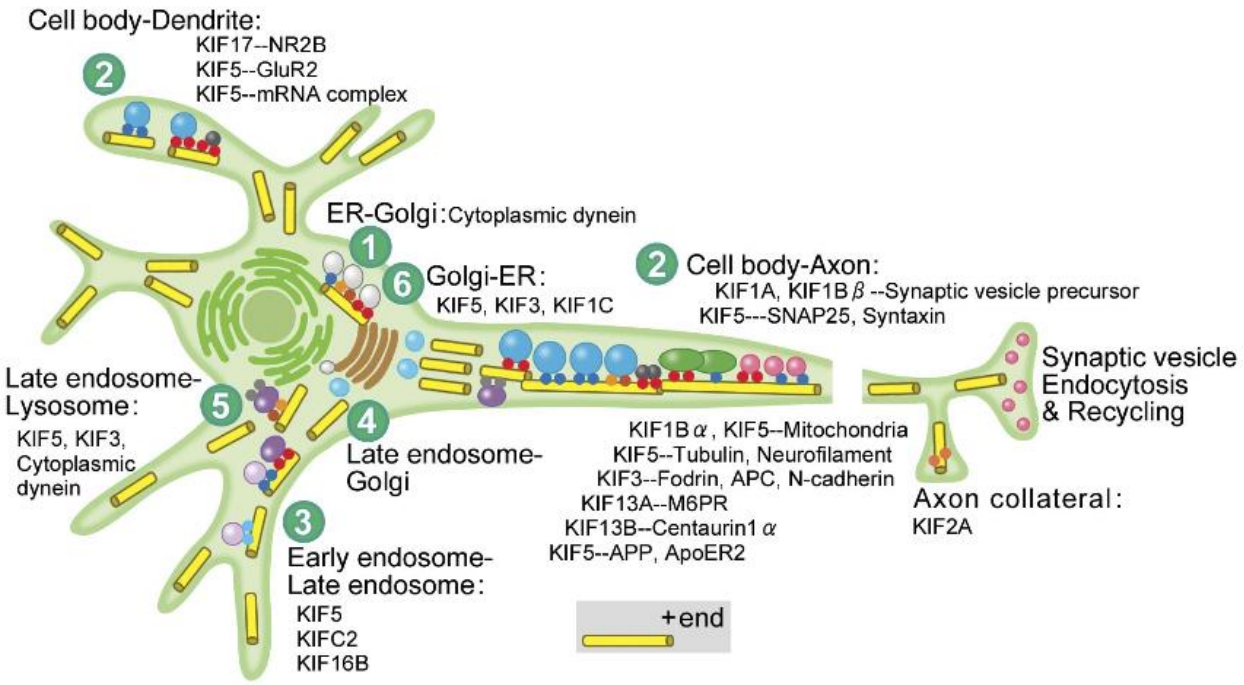

Figure 1.2. Intracellular transport by molecular motors in neuronal cells.

Various kinesin superfamily members and cytoplasmic dynein are essential for intracellular cargo transport from (1) ER to Golgi, (2) Cell body to Axon or Dendrite (unique to neurons), (3) Early endosome to Late endosome, (4) Late endosome to Golgi, (5) Late endosome to Lysosome, (6) Golgi to ER. The implicated motors are labeled on the figure.

Figure used, with permission, from Hirokawa, N., and Noda, Y. (2008). Intracellular transport and kinesin superfamily proteins, KIFs: structure, function, and dynamics. Physiological reviews 88, 1089-1118. (Hirokawa and Noda, 2008).

(Peterman et al., 2004). The concurrent development of TIRF microscopy and optical tweezers in the 1980's allowed for single fluorescent motors to be visualized and manipulated with great precision (Ashkin et al., 1986; Axelrod, 1981). This ushered in a relative golden age of single-molecule biophysics in which the biochemical and biophysical mechanisms of individual kinesin motors were studied and elucidated in great detail (Svoboda and Block, 1994a; Vale and Fletterick, 1997). Though some debate remains on finer points, the current overall consensus is that the

biomechanical cycle of an individual kinesin motors is quite well understood (Fig. 1.1C) (Jeppesen and Hoerber, 2012).

1.3 Multiple motor transport: history and experimental approaches

Although the properties of individual motors are relatively well understood, we currently lack a clear understanding of how multiple motors might cooperate for more efficient intracellular transport. Electron microscopy studies dating to the 1980s show clear evidence for the presence of multiple motors on a cargo, perhaps even dozens in the case of larger cargoes (Fig. 1.3) (Ashkin et al., 1990; Hirokawa, 1982; Hirokawa et al., 1989; Miller and Lasek, 1985). The benefits of having multiple motors on a cargo are relatively intuitive *a priori*. Cargoes driven by multiple motors are expected to show enhanced processivity due to redundant microtubule binding, and multiple motors are expected to generate additional forces required to pull bulky cargoes through the crowded, viscoelastic cytosol.

Through the various studies described in this section, three canonical rules have been established for how multiple kinesin motors coordinate on a given cargo: 1) multiple kinesins do not lead to faster cargo transport under zero load, 2) multiple kinesins typically lead to enhanced cargo run length over that of a single motor, and 3) multiple kinesins are able to generate additive force under load. Additionally, we have learned that multiple dynein or myosin motors cooperate more effectively than multiple kinesins, and that opposite-polarity motors such as kinesin and dynein present on the same cargo are crucial for efficient transport. This section will describe and weigh the evidence for each claim and discuss additional questions that still need to be considered in the field.

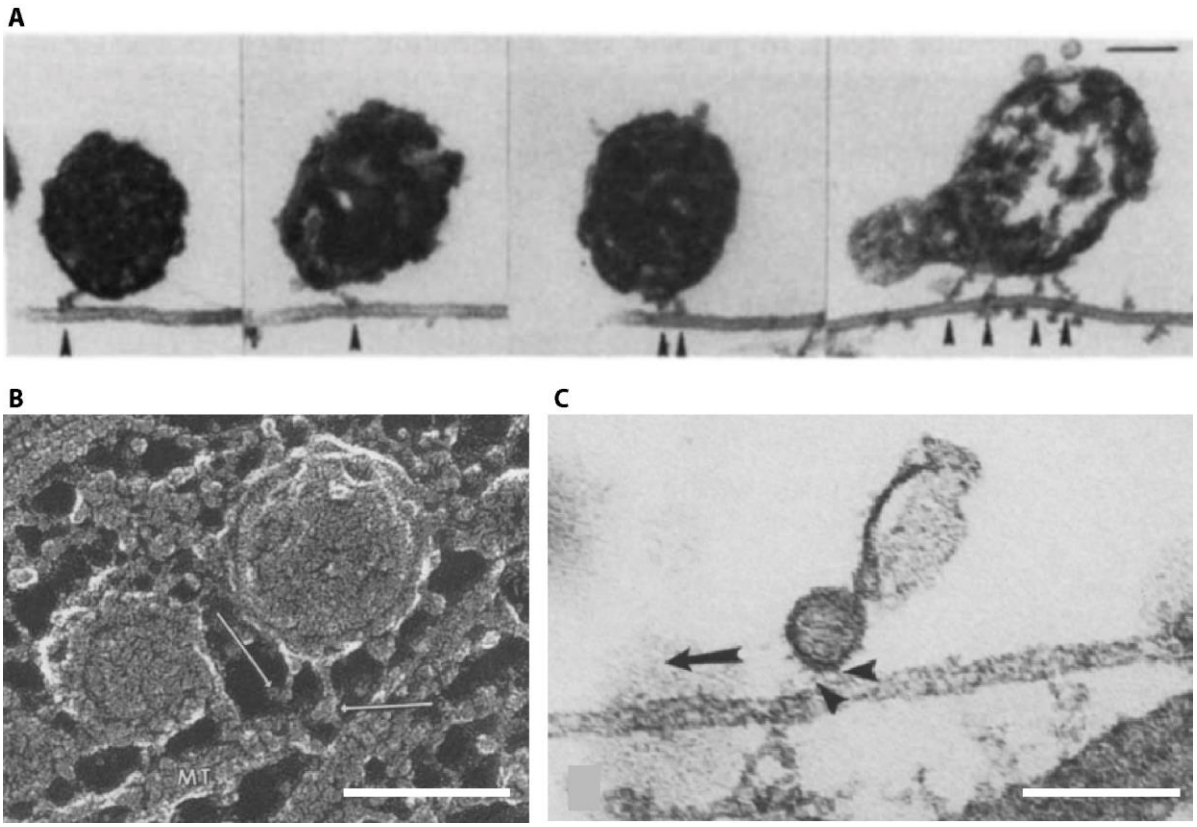

Figure 1.3. Electron microscopy provides evidence of multiple-motor based intracellular transport.

(A) Examples of mitochondria from *Reticulomyxa* with 1, 2, and 4 crossbridges to a microtubule, as seen by electron microscopy (EM). Crossbridges are likely molecular motors and are indicated by arrowheads. *Reticulomyxa* networks were spread on coverslips, lysed, fixed in glutaraldehyde, and processed for electron microscopy (Ashkin et al., 1990). Scale bar, 100 nm. **(B)** Structures with the morphology of kinesin appear to cross-link membrane-bound organelles to microtubules in the neurite. A rat spinal cord was processed for quick-freeze, deep-etch EM, and neurite regions were examined. Many crossbridges were observed that contained globular bulges reminiscent of kinesin motors where they seemed to contact microtubules (arrows). (Hirokawa et al., 1989) Scale bar, 100 nm. **(C)** Electron microscopy of squid giant axoplasm where cold blocks were selectively applied to proximal or distal segments of the axoplasm. Arrows represent the probable direction of movement, which is anterograde in this orientation. Note that vesicles are attached to microtubules by apparent crossbridges (arrowheads) (Miller and Lasek, 1985). Scale bar, 250 nm.

(A) Used, with permission, from Ashkin, A., Schutze, K., Dziedzic, J.M., Euteneuer, U., and Schliwa, M. (1990). Force generation of organelle transport measured in vivo by an infrared laser trap. Nature 348, 346-348. (Ashkin et al., 1990).

(B) Used, with permission, from Hirokawa, N., Pfister, K.K., Yorifuji, H., Wagner, M.C., Brady, S.T., and Bloom, G.S. (1989). Submolecular domains of bovine brain kinesin identified by electron microscopy and monoclonal antibody decoration. Cell 56, 867-878. (Hirokawa et al., 1989).

(C) Used, with permission, from Miller, R.H., and Lasek, R.J. (1985). Cross-bridges mediate anterograde and retrograde vesicle transport along microtubules in squid axoplasm. The Journal of cell biology 101, 2181-2193. (Miller and Lasek, 1985).

1.3.1 Gliding assays

Historically, researchers have reconstituted motor-cargo interactions *in vitro* in one of two geometries: gliding assays and motor-cargo assays (Fig. 1.4a). Much early work on microtubule-based transport was performed using gliding assays, in which purified motors are adsorbed onto a glass cover slip with the motor head domains extending into solution and free to bind microtubules (Fig. 1.4a, left) (Scholey, 1996). When microtubules contact the motors, the motors effectively walk along the microtubule track, but the motors themselves show no displacement because of their firm attachment to the glass cover slip. As a result, the microtubules "glide" along the surface. This behavior was first observed in squid axoplasm preparations and was initially puzzling (Allen et al., 1985) until the role of motors and cargoes in axonal transport was more clearly understood.

A number of technical factors make gliding assays appealing for multiple motor studies. Typically, motor-microtubule interactions are persistent on the scale of one second. In gliding assays, however, the bulky microtubule does not diffuse away and can reengage with another surface-bound motor (or multiple surface-bound motors at a time), resulting in remarkably persistent and steady motion which is easy to analyze (Scholey, 1996). Data acquisition and analysis is also aided by the fact that very little out-of-focus Brownian diffusion exists due to microtubules nearly always gliding along the surface. Gliding assays also minimize surface effects by minimizing large surface-surface interactions; for instance, in motor-cargo assays, the relatively

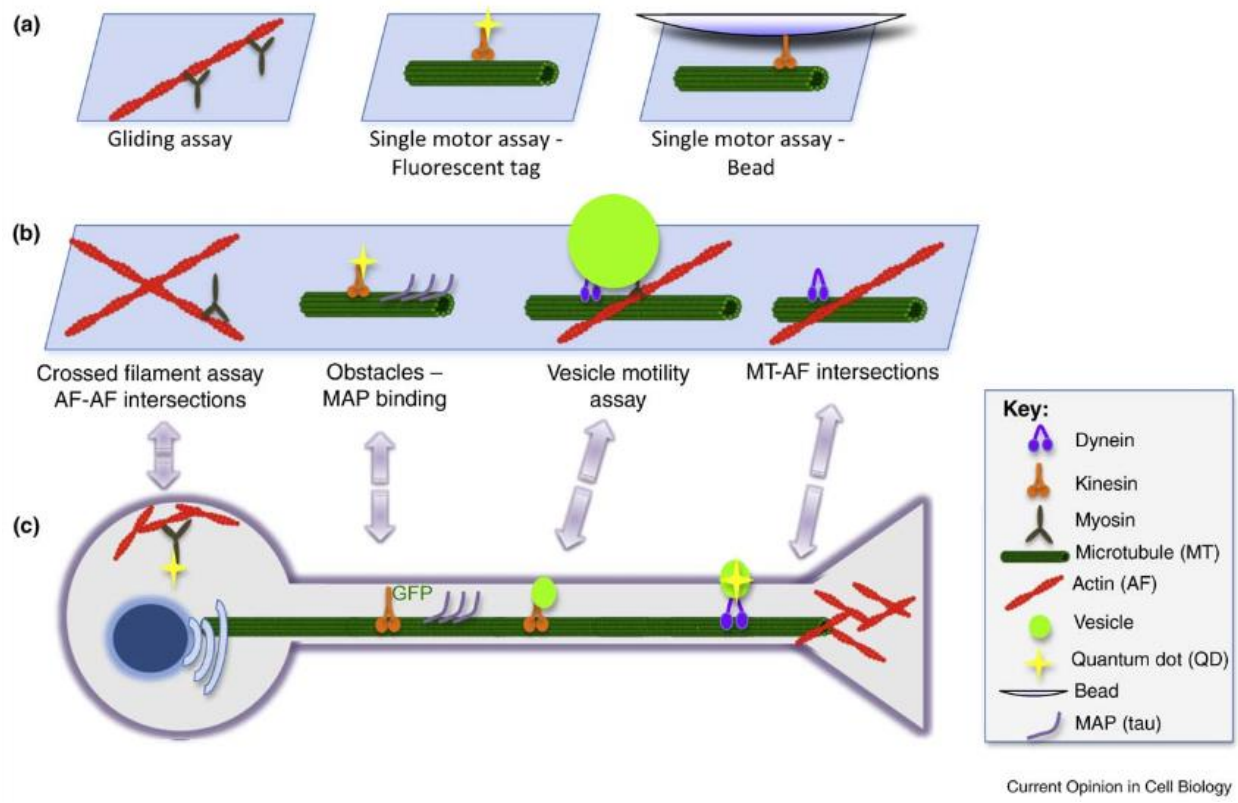

Figure 1.4. Modeling intracellular motility with in vitro assays.

(a) In gliding assays for all three types of motors (myosins, kinesins, and dynein) the motors are attached to a glass slide and movement of actin filaments or microtubules across the surface is observed. In single motor assays, actin filaments or microtubules are attached to a glass slide and the movement of the motor is observed directly via a fluorescent tag such as GFP, organic fluorophores, or a quantum dot. In motor assays with beads, motors are immobilized on a large (typically 1-2 μm) bead approximating a cellular cargo, and the movement of the bead is observed. Motor number is controlled by varying the concentration of motors and beads. **(b)** These *in vitro* assays can be further varied to more closely approximate the complex environment of the cell, such as track crossing or obstacles on the track such as microtubule associated proteins (MAPs). **(c)** Motility measurements inside cells can be obtained by directly observing endogenous cellular vesicles, expressing GFP-labeled motors, or studying exogenous cargoes such as quantum dots that have been introduced inside the cell.

Figure used, with permission, from Holzbaur, E.L., and Goldman, Y.E. (2010). Coordination of molecular motors: from in vitro assays to intracellular dynamics. Current opinion in cell biology 22, 4-13. (Holzbaur and Goldman, 2010).

large plastic beads can interact with the glass surface and inhibit motility (Schnitzer and Block, 1997). Overall, gliding assays provide a valuable method for investigating the bulk behavior of motors with minimal complications.

1.3.2 Motor-cargo assays

Perhaps the most conceptually straightforward method for reconstituting intracellular traffic *in vitro* is to adsorb purified motor proteins onto a latex or polystyrene bead that simulates a cellular cargo (Fig. 1.4a, right) (Mallik et al., 2005; Vale et al., 1985b; Vershinin et al., 2007; Xu et al., 2012). This method provides a number of advantages: 1) it closely resembles the geometry of the cellular motor-cargo interaction, 2) it allows for detailed force manipulation via optical trapping of the dielectric cargo (Svoboda and Block, 1994a), and 3) it allows for motor assembly on a variety of synthetic cargoes including the aforementioned plastic beads, highly photostable quantum dots (QDs) (Conway et al., 2012; Seitz and Surrey, 2006) or gold nanoparticles (AuNPs) for dark-field microscopy (Nan et al., 2008). Drawbacks to this type of assay include: 1) potential surface-surface interactions between the large bead and glass surface, and 2) the exact number of motors on a bead must be estimated from the relative concentration of protein and beads.

1.3.3 Optical trap assays

Arguably the largest advantage of the motor-cargo geometry is the potential use of an optical trap, or optical tweezers (Svoboda and Block, 1994a). In an optical tweezers setup, a laser beam (typically of infrared wavelength) is tightly focused on a dielectric particle such as a plastic bead. This tightly focused beam generates a very strong electric field gradient where, if the

refractive index of the dielectric particle is sufficiently different from its surroundings, the particle is attracted to the center of the beam (Ashkin et al., 1986; Moffitt et al., 2008). When the particle is displaced from the center of the beam, it experiences a restoring force, typically on the scale of pN, that scales linearly with displacement and thus can be accurately described by Hooke's Law. The trap stiffness (or spring constant in the Hooke's Law analogy) is a calibrated constant that depends on the incident laser power.

Molecular motors researchers can use optical tweezers in two ways. First, the trap can be turned on and motors allowed to displace the bead from the center of the trap (Svoboda and Block, 1994b). This allows the typical stall force of a motor to be calculated by measuring the displacement, and thus force, at which the motor is no longer able to displace the bead. The value of this stall force for a single kinesin motor is ~6 pN for kinesin-1 (Svoboda and Block, 1994b) and ~1 pN for mammalian cytoplasmic dynein (Mallik et al., 2004), although this reported value can vary slightly. Detachment force, the average force at which the motor detaches from the track, can also be estimated using this method. This value is typically comparable to the stall force of an individual motor but the stochastic nature of motor detachment makes it difficult to estimate whether a motor is more likely to stall or detach (Jamison et al., 2010). As a second method, one can also maintain a constant force on the particle of interest by maintaining a constant distance via a feedback loop known as a "force clamp" (Jamison et al., 2012; Visscher et al., 1999). This approach permits studies under a controlled external load and has provided additional insights into the mechanochemical cycle of motors such as the load-rate dependence of individual chemical transitions within the motors ATPase cycle (Visscher et al., 1999).

1.4 Collective motor behavior: what do we know?

The previous section introduced the concept of molecular motors working together to generate enhanced run lengths and forces, and introduced basic experimental approaches to study this behavior. This section summarizes the field's current knowledge of multiple-motor based transport based on these experiments.

1.4.1 How many motors are on cellular cargoes?

Estimating the exact number of motors on a given cargo is notoriously difficult due to variable cargo size, composition, and technical issues in live cells (Barlan et al., 2013). Additionally, one must distinguish between the number of motors *present* on a cargo versus the number of motors *actively engaged* in transport. Because multiple motors combine to generate additional force under load, one can estimate the number of engaged motors on a cargo by applying a force via optical tweezers and correlating the observed generated force to motor number. Using this method, Shubeita et al. (2008) determined that the vast majority of lipid droplets in *Drosophila* embryos are driven by just one or two engaged kinesin-1 motors (Shubeita et al., 2008). Soppina et al. (2009) used force measurements to determine that endosomes in *Dictyostelium* typically contain multiple (4-8) engaged dynein motors competing against one engaged kinesin motor (Soppina et al., 2009). Hendricks et al. (2010) purified neuronal transport vesicles from mice and used a combination of optical trap experiments, photobleaching, and quantitative western blotting to estimate that one to five dynein and one to four kinesin motors (kinesin-1 and kinesin-2) are present on the vesicles (Hendricks et al., 2010). Sims et al. (2009) used an optical trap on lipid droplets in human A549 cells to determine that, although the majority of motile lipid droplets are

driven by a single kinesin or dynein, a number of the lipid droplets are driven by a two or three motors (Sims and Xie, 2009). Another study has used quantitative fluorescence intensities to determine that early endosomes in *Ustilago maydis* typically contain four to five kinesin-3 motors and one dynein (Schuster et al., 2011).

The number of actin-associated motors on most intracellular cargoes is still unclear, although this number seems to be much higher than microtubule-associated motors. In melanosomes, the number of myosin-V motors is highly regulated and estimated to be between 65 and 90 (Gross et al., 2002), whereas in axonal transport vesicles this number is estimated to between 6 and 120 (Tabb et al., 1998).

Taken together, most canonical 1-2 μm cargoes in cells are driven on microtubules by a relatively low number (typically 1-7) of microtubule-based motors, and are driven on actin filaments by a higher number (typicaly several dozen) of myosin motors (Holzbaur and Goldman, 2010).

1.4.2 Multiple motors of the same type: effects on run length, velocity, and force

This section summarizes the field's knowledge of an important question: how do multiple copies of molecular motors *of the same type* cooperate for more efficient transport? This is investigated both *in vitro* and in living cells, and effects on velocity, run length, and force are considered.

1.4.2.1 The effect of multiple motors on transport velocity is load-dependent *in vitro*

In vitro gliding assays provide the first canonical rule in the case of kinesin motors: multiple kinesins do not result in faster cargo transport under zero load. When the surface density of full length purified kinesin was varied by multiple orders of magnitude, for instance, the mean velocity of the gliding microtubule remained unchanged (Howard et al., 1989). In motor-cargo assays under zero load, the velocity of kinesin-driven cargoes also appears to be independent of motor number *in vitro* (Beeg et al., 2008; Block et al., 1990; Coy et al., 1999; Seitz and Surrey, 2006; Vershinin et al., 2007) . In contrast, gliding assays performed with non-processive muscle myosin result in gliding velocities ten times faster than KHC (kinesin heavy chain) even though ATPase rate of a single myosin motor is roughly half that of KHC (Higuchi and Goldman, 1991; Yanagida et al., 1985). Because of muscle myosin's extremely low duty ratio (proportion of ATPase cycle bound to the track) relative to kinesin, it has been proposed that low-duty ratio motors are better able to coordinate for faster velocities than high-duty ratio processive motors (Howard, 1997). When gliding assays were driven by many dynein motors, a very slight increase in velocity was observed (Reck-Peterson et al., 2006). In motor-cargo assays, multiple dyneins also led to a small increase in transport speed for constant-velocity segments (Mallik et al., 2005).

In contrast to gliding assays with full-length KHC, another set of experiments showed that when the surface density of purified, truncated, constitutively active KHC was increased to high levels, the velocity of the gliding microtubule actually decreased substantially, demonstrating what the authors called negative interference (Bieling et al., 2008). KHC(aa 1-401), a minimal dimeric construct including only the motor domain, neck linker, and coiled coil neck, showed a much lower velocity at high motor concentration than KHC(aa 1-612), which contains an extended neck and a flexible swivel and hinge. In the context of the previous full-length results, the authors suggested

that multiple kinesins require a loose mechanical coupling to avoid this so-called negative interference (Bieling et al., 2008). Evidence for this negative interference is also seen in the motor-cargo geometry where kinesin-driven quantum dot cargoes show a decrease in velocity under very crowded kinesin concentrations (Conway et al., 2012).

Another type of gliding assay shows evidence for poor cooperation between multiple kinesin motors. Leduc et al. (2007) used fluorescently labeled KHC(aa 1-430)-GFP and multi-color fluorescence microscopy to perform gliding assays at low concentrations where the location of the fluorescently labeled motor was known on the surface (Leduc et al., 2007). To provide higher-resolution spatial imaging, microtubules were also labeled with a quantum dot. Similar to previous studies (Howard et al., 1989), when microtubules were moved by a single motor, they were found to swivel around a single pivot point, indicating a torque generation by the motor and providing a simple qualitative readout of single-motor motion. In the case of microtubule gliding by two motors, 4 nm center-of-mass displacements of the quantum dot were detected rather than 8 nm displacements, suggesting that the two kinesin motors step separately.

When *in vitro* gliding assays were performed in a high-viscosity medium, the presence of multiple kinesin motors led to an increase in velocity, suggesting that multiple kinesins can cooperate in response to load (Hunt et al., 1994). When a large 2-μm bead was attached to the microtubule during gliding assays in a viscoelastic medium, gliding velocity was found to increase with microtubule length, which indicates an increase in motor number (Gagliano, 2010). These results indicate that multiple kinesin motors may be crucial to transporting cargo at physiological speeds in the crowded cytosol. It is important to note that a load force due to a viscous medium requires the movement of a relatively large object such as the microtubule itself or a large cargo inside cells. This effective load force is governed by the size and velocity of the object and is

described by Stokes' Law (Holzwarth et al., 2002). Individual kinesin motors with no associated cargo are unaffected by higher viscosity media because they are driven by thermal motion and are too small to feel these effects. Additionally, estimating the viscosity of cytosol and recreating the complex rheological environment of the cell *in vitro* is notoriously difficult, which can complicate these interpretations significantly (Peterson, 2008).

1.4.2.2 The effect of multiple motors on transport velocity in cells is difficult to interpret

Although *in vitro* experiments contribute essential biophysical information, they provide only rough approximations of the true cellular environment due to their limited geometries and use of purified components. In order for multiple motor transport to be fully understood, these experiments must be performed on endogenous tracks with all cytosolic components present (Veigel and Schmidt, 2011). Individual kinesin motors behave remarkably similar in living cells and *in vitro*, as shown by a number of studies. For instance, Courty et al. (2006) internalized quantum dots bound to a single kinesin motor into HeLa cells via pinocytosis and investigated the motile properties of the cargo, finding no difference between motility in cells and *in vitro* (Courty et al., 2006). In another study, Cai et al. (2007) expressed constitutively active kinesin-1 in COS7 cells and compared the single-molecule motility properties in living cells to those of cell lysates *in vitro* (Cai et al., 2007). The authors found extremely similar velocity and run length distributions in both cases. Although individual motors seem to behave similarly in cells and *in vitro*, our understanding of the impact of cellular environment for multiple motor transport is still unclear.

The observation that cargo velocity depends on motor number in viscous environments (section 1.4.2.1) has been used to interpret the effects of multiple motors in living cells.

Endogenous vesicles in PC12 neurites, for instance, have been observed to move with discrete constant-velocity segments which the authors interpreted as a readout of the number of active motors (Hill et al., 2004). In another study, GFP-labeled peroxisomes in Drosophila S2 cells were shown to move at up to ten times the *in vitro* speed of kinesin-1 or dynein with discrete peaks in their velocity distribution, which the authors initially attributed to the cooperative action of multiple motors (Kural et al., 2005). The authors also found an average pairwise step size of 8 nm, in contrast to the *in vitro* gliding assay results described above (Leduc et al., 2007). The extremely fast velocity observations in this study were later revisited and reinterpreted as contributions due to the movement of the microtubule track itself (Kulic et al., 2008). Additionally, multimodal velocities have been observed in Xenopus melanophores (Levi et al., 2006). Another study varied the amount of kinesin-1 on APP vesicles in Drosophila axons via genetic manipulation and found that both velocity and run length depended on the amount of KHC present (Reis et al., 2012). When kinesin-conjugated quantum dots were internalized into human breast cancer cells via lipid transfection, maximum velocities up to twice the *in vitro* velocity were observed with frequent starts and stops (Yoo et al., 2008).

In contrast to these observed increases in velocity, numerous studies have shown no effect on velocity in live cells when the number of kinesin motors is varied. By altering the expression level of KHC in *Drosophila* embryos, Shubeita et al. were able to study the effect of motor number on lipid droplet transport (Shubeita et al., 2008). Although the authors found clear evidence for simultaneous engagement of multiple motors via optical trapping assays, they surprisingly found a slight decrease in transport velocity when motor copy number is increased. A recent study varied the density of kinesin and myosin motors on peroxisomes in COS7 cells via doxycycline-inducible expression of engineered motors and cargo-binding proteins (Efremov et al., 2014). When kinesin-

1 density was varied, the authors found insignificant effects on transport velocity, but found a significant increase in velocity when myosin-V density was increased. When considering all of these experiments together, the effect of multiple motors on cellular cargo velocities is still unclear, and may depend on either the specific cargo or the local rheological environment of the cell.

1.4.2.3 Multiple processive motors lead to an increase in transport run length *in vitro*

In vitro motor-cargo assays provide a foundational result in our understanding of multiple motor transport: as more motors are present on a given cargo, the overall cargo run length, also known as processivity, is increased. The reason for this processivity increase is conceptually simple. The detachment of a single kinesin motor from a microtubule is a stochastic event which happens after an average of ~120 8-nm steps, leading to an average run length on the scale of 1 μm when one motor is present (section 1.2.3). When two kinesin motors are present, the two motors on the bead must *simultaneously* detach in order for the bead to stop its processive run, which is far less likely. This phenomenon has been described in great detail theoretically via both mean-field theory and stochastic modeling (Klumpp and Lipowsky, 2005; Kunwar et al., 2008). The effect on run length has been predicted to increase roughly from ~1 μm to ~3.5 μm when increasing from one to two motors, with an exponential increase in run length expected as the number increases further.

The evidence for an increase in run length is overwhelming in *in vitro* motor-cargo assays. An early study varying the amount of purified kinesin motors on a 200-nm latex bead found that beads with multiple kinesins were more likely to bind to a microtubule surface, traveled for much longer distances, and were more resistant to force-dependent unbinding than beads with a single

kinesin (Block et al., 1990). A later study using 500-nm carboxylated beads shows an increase in run length from 1.5 μm in the case of a single motor to > 8 μm in the case of two motors (Vershinin et al., 2007). Interestingly, this increase in run length is not seen when microtubules are decorated with the longest isoform of human tau, a microtubule-associated protein known to decrease the on-rate of kinesin. A recent study using an antibody-based method to two motors to a bead found a similar result: at saturating ATP, the run length of a single-motor bead was 1.7 μm, and the run length of two-motor beads was 3.0 μm (Xu et al., 2012). Notably, the authors found a much larger increase in run length from one to two motors at limiting ATP. Presumably this is because each motor spends more time in the relatively strongly-bound ATP-waiting state. Another study that transiently recruited additional kinesin motors to quantum-dot cargoes found a run length increase from 1.8 μm under single-motor conditions to 6.2 μm when multiple motors were present (Conway et al., 2012). Other additional studies have also seen a substantial increase in run length for multiple kinesin motors (Beeg et al., 2008; Block et al., 1990; Coy et al., 1999; Seitz and Surrey, 2006). The presence of multiple dynein motors has also been shown to greatly increase cargo run length relative to a single motor (Mallik et al., 2005). Together, *in vitro* motor-cargo experiments provide vast evidence for the role of multiple motors in increasing cargo transport distance.

1.4.2.4 Experiments in living cells show no evidence for enhanced run length for multiple motors

Interestingly, no direct evidence has been shown that suggests multiple motors can cooperate for longer, more processive runs in living cells. Quantifying cargo run length in cells (Fig. 1.4c) is particularly difficult for a number of reasons. In the *in vitro* geometry, the cargo simply diffuses away from its active track on the surface, whereas in live cells, a cargo might

diffuse away from its active track only to either immediately encounter another track directly above it or to reencounter the same track due to the three-dimensional spatial constraints of the cell. Additionally, an *in vitro* cargo is typically only examined on one individual track on a two-dimensional surface, whereas in live cells, a large cargo may encounter and engage many tracks simultaneously, including both actin filaments and microtubules, in a three-dimensional space (Holzbaur and Goldman, 2010). For these reasons, the run length inside cells is typically defined in terms of the length of constant-velocity, processive segments.

Most studies indicate no obvious change in run length for constant-velocity segments in live cells when the number of motors is varied. In both *Drosophila* lipid droplets and COS7 peroxisomes, no run length dependence on motor number is observed (Efremov et al., 2014; Shubeita et al., 2008). Another study saw no obvious run length enhancement in the case of higher motor number on *Drosophila* APP vesicles, but did see a lower pause frequency with increased cargo velocities, suggesting at least some dependence on motor copy number (Reis et al., 2012). This weak correlation in live cells between run length and motor number may simply be attributable to the technical difficulty of such an observation, but cargo rigidity may have some effect as well. *In vitro* motor-cargo studies showing a strong correlation between run length and motor number use inflexible, rigid cargo such as polystyrene beads, whereas real cellular cargoes are typically coated in a fluid, lipid bilayer. This dependence on cargo stiffness is being actively studied and the work in this dissertation supports the hypothesis that more rigid cargoes allow greater motor cooperation.

1.4.2.5 Multiple processive motors lead to additive force generation under load

The use of optical tweezers *in vitro* leads to another rule of multiple motor transport: when multiple motors are present on a cargo, motors can cooperate to generate additive force under load. Typically, the stall forces of multiple-motor cargoes show multi-modal distributions where each additional peak is a quantized multiple of the single-motor stall force. This has been shown for kinesin motors, where the stall forces for a single-motor cargo show a single peak distribution at 4.8 pN and the stall forces for a two-motor cargo show a bimodal distribution with peaks at 4.7 and 9.0 pN (Vershinin et al., 2007). A similar result has been shown for dynein, where cargoes driven by multiple motors show multimodal stall force distributions with distinct peaks at 0.9, 2.1, and 3.2 pN (Mallik et al., 2005). A later study showed that, in stark contrast to kinesin, multiple dynein motors cooperate very efficiently to generate large loads, presumably because of dynein's unique ability to walk with a variable step size (Rai et al., 2013). Together, these phenomena allow the number of motors present on the cargo can be estimated (section 1.4.1).

1.4.3 Different motors on the same cargo

In contrast to the previous sections were multiple copies of the same motor were discussed, this section summarizes the field's knowledge of how *different* motors either work together or oppose each other on the same cargo. This includes opposite-polarity motors such as kinesin and dynein, as well as microtubule-based and actin-based motors.

1.4.3.1 Motors of the same polarity but different velocities lead to intermediate transport speeds

In gliding assays, fast and slow motors can be mixed in different proportions (Bieling et al., 2010; Larson et al., 2009; Pan et al., 2006). This allows an *in vitro* reconstitution of systems where fast and slow motors are thought to work together, such as intraflagellar transport (Pan et al., 2006) or meiotic chromatin (Bieling et al., 2010). In all cases, when fast and slow motors were mixed together, the microtubule gliding velocity was an intermediate value between the velocities of the individual motors, although the dependence of this velocity on fast and slow motor proportion varied from study to study (Bieling et al., 2010; Larson et al., 2009; Pan et al., 2006). The intermediate velocities observed in these gliding assays provide a valuable prediction for the case of intracellular transport although it is important to note that this type of assay is an ensemble readout of many more motors than are present on most cellular cargoes (section 1.4.1).

1.4.3.2 Opposite-polarity motors: tug-of-war or coordinated switching?

Although much *in vitro* and live cell work studies the coordination of multiple copies of identical motors, endogenous cellular cargoes must be driven by a combination of plus-end directed motors and minus-end directed motors in order for cells to achieve sufficiently high levels of spatial organization (Barlan et al., 2013). When considering opposite-polarity motors present on the same cargo, a central question emerges: how does the cargo determine which motor is primarily active and thus which direction to move along the microtubule? Two proposed models provide potential explanations for this. The first possibility is a "coordinated switching" model, in which the cell can implement some higher-order regulatory mechanism to specifically control which motor is actively engaged with the microtubule, either by controlling motor-cargo or motor-

track attachment for a specific motor. This model was initially favored due to its theoretically high efficiency, but this was difficult to prove in early experiments in living cells (Jolly and Gelfand, 2011; Kunwar et al., 2011) . The second possibility, a "tug-of-war" model, proposes that multiple motors are simultaneously engaged with the microtubule and hydrolyzing ATP in a direct mechanical competition. Under this scenario, the stronger of the two competing forces would eventually dominate and lead to unidirectional motion. Because motor forces are additive (section 1.4.2), the cell could regulate the direction of motility by transiently recruiting more or less motors of a specific type. Although this model initially seems energy-inefficient and perhaps counterintuitive, numerous lines of evidence suggest this as a possibility (Hendricks et al., 2010; Muller et al., 2008; Soppina et al., 2009). Other lines of evidence suggest that opposite-polarity motors actually enhance each other's motility properties. *Drosophila* S2 cells expressing motility-deficient kinesin mutants were unable to trigger dynein-driven peroxisome motility, suggesting that this competing mechanical force is necessary for efficient bidirectional transport (Ally et al., 2009). Another recent study suggests that dynein is present and active even on plus-end directed motile events in living cells, providing further evidence for a tug-of-war model (Blehm et al., 2013). It now seems likely that cargo-bound adaptor complexes such as JIP1 or Milton/Miro (Akhmanova and Hammer, 2010) likely provide higher-order control to regulate bidirectional transport mechanically *via* a tug-of-war mechanism.

1.4.3.3 Microtubule-based and actin-based motors on the same cargo change transport properties

For additional spatiotemporal organization, the cell utilizes two types of tracks for transport: microtubules and actin filaments. Typically, microtubules are used for long-distance

transport and actin filaments are used for shorter range transport to the final cargo destination, a process which has been studied in great detail in melanosomes (Kural et al., 2007). Although many groups are currently investigating the behavior of groups of microtubule-based motors (see above), how these motors interact with actin-based myosin motors on cargoes remains poorly understood.

A handful of studies have speculated that kinesin and myosin are intimately related and must work together for proper cellular function. Ali et al. (2008) studied this cooperation *in vitro* by adsorbing both full length kinesin-1 and myosin V (which walks processively along actin filaments and diffuses on microtubules due to a positive charge in its head domain) to quantum dots (Ali et al., 2008). The authors found that myosin V enhanced the run length of kinesin-1 on microtubules roughly two-fold, presumably due the electrostatic interaction between myosin and microtubules creating a tether-like behavior. Additionally, the processive run length of myosin V on actin filaments also increased in the presence of kinesin. This hypothesis was validated in yeast, when the overexpression of kinesin family member Smy1p rescued transport defects of a mutant class V myosin Myo2p (Hodges et al., 2009). In contrast to this, another study has shown that myosin V can oppose kinesin-driven transport when a large number of myosin V motors are recruited to peroxisomes (Kapitein et al., 2013). The cooperation between microtubule-based motors and myosin at actin/microtubule track intersections is also being actively studied (Fig. 1.4b). An *in vitro* study found that number of microtubule- or actin-based motors decides which track the cargo chooses, similar to the proposed tug-of-war mechanism described above (Schroeder et al., 2010). Taken together, it seems although they walk on different tracks, microtubule- and actin-based motors work together to enhance specificity of cargo transport in cells.

1.5 Synthetic biology approaches allow precise studies of motor complexes in vitro

One clear drawback to the *in vitro* approaches described above is the difficulty of knowing how motors assemble on a given cargo. The number of motors on a bead, for instance, must either be estimated from the concentration of purified motors relative to beads or inferred from optical trapping experiments (Vershinin et al., 2007). One key approach taken by synthetic biologists is to use biological components to self-assemble objects with known structure and function. Clearly, synthetic biology approaches to assemble and study multiple-motor complexes with defined features would be hugely beneficial to our understanding of motor coordination and function.

1.5.1 Using synthetic biology to assemble structures: history and development

DNA-based nanotechnology has been used for over thirty years as the basis of structure assembly *in vitro* dating to Seeman et al. in 1983 (Seeman and Kallenbach, 1983; Torring et al., 2011). Our extensive knowledge of both the mechanical properties of DNA and its base-pairing properties make DNA an ideal molecule for *de novo* design of biological objects. Most early DNA-based nanostructures were designed and created via the base-pairing characteristics of oligonucleotides. An enormous leap forward for the field occurred in 2006 when Rothmund established the strategy behind DNA origami, a new technique which allows relatively massive and complex structures to be designed and constructed *in vitro* (Rothemund, 2006). In the DNA origami approach, a very long single strand of DNA is folded into shape via base-pair interactions with complementary oligonucleotide "staples" which fold the hold the structure in place. The DNA origami field is currently booming due to the overwhelming amount of *de novo* complexity now at the research community's fingertips.

In contrast to DNA-based synthetic biology techniques, protein-based synthetic biology techniques provide much less control over specific folding properties. Although some basic protein-based assembly strategies have been characterized with a focus on building block components (Grunberg and Serrano, 2010), this technology has remained largely underdeveloped due to the highly increased complexity of such systems. One notable exception is the implementation of engineered protein scaffolds to study MAP kinase pathway signaling dynamics in yeast (Bashor et al., 2008). This and similar work from the Lib lab suggests significant potential for using synthetic protein biology to understand cellular processes at the level of multiple proteins.

The first synthetic biology study to investigate multiple motor assembly was performed by Diehl et al. (Diehl et al., 2006). In this study, purified monomers of kinesin-1 were connected via alternating rigid and flexible peptide components to form linear chains consisting of one, two, or three kinesin-1 monomers. When the motility properties of these assemblies were investigated via gliding assays, trimeric and dimeric assemblies were found to move microtubules faster than their monomeric counterparts, suggesting that kinesin monomers can be engineered to cooperate more efficiently. This foundational study provided the groundwork for subsequent multiple motor studies, including much of the work presented in this dissertation.

1.5.2 Using DNA-based multi-kinesin assemblies to study motor coordination

A major breakthrough in our approach to multiple motor transport occurred in 2009 when Rogers et al. assembled two dimeric kinesin-1 motors on a 50 nm dsDNA scaffold connected via coiled-coil peptides (Rogers et al., 2009), leading to a flurry of studies from the Diehl lab. When these assemblies were tagged with a quantum dot and investigated in motility assays, the authors

found that two-motor assemblies moved only slightly longer than single kinesin-1 motors, a distance much shorter than the theoretical predicted two-motor run length (Klumpp and Lipowsky, 2005). Furthermore, in an analysis similar to previous studies (Leduc et al., 2007), an investigation of pairwise distance distributions of two-motor assemblies showed a large population of fractional stepping rather than the 8-nm periodicity observed for single motors, suggesting that the two motors primarily move independently. Together, the authors concluded that two kinesin-1 motors negatively interfere with each other's motility.

A follow-up study from the Diehl lab investigated the effect of static external loads on these two-motor complexes and showed that although two kinesin-1 motors are capable of generating additional force, they typically only utilize the action of one motor (Jamison et al., 2010). Another follow-up study used an optical force clamp to show that two-motor complexes can cooperate for increased run lengths and forces under external loads greater than the stall force of a single motor, but the overall effect of multiple motors remains net negative cooperative (Jamison et al., 2012). This system was also described in great detail from a theoretical perspective in two complementary studies (Driver et al., 2011; Driver et al., 2010), concluding that although both motors have access to the microtubule, only one motor is typically able to engage for motility due to the energetic costs of assembly deformation. In contrast to kinesin, this same system has been used in recent years to assemble complexes of two myosin V motors, which *do* show significantly enhanced run length properties relative to a single motor, although the velocity decreases slightly (Lu et al., 2012). When the entire body of work from the Diehl lab is considered, it appears that two kinesin motors do not efficiently cooperate for enhanced transport, a conclusion which is largely supported by the work in this dissertation.

1.5.3 Using alternative multi-motor assembly techniques to study motor coordination

Recently, two other groups have used independently developed DNA-based motor assemblies to expand on the work of the Diehl group (Derr et al., 2012; Furuta et al., 2013). Derr et al. used a DNA origami-based method to attach up to seven kinesin-1 motors, cytoplasmic dynein motors, or mixed kinesin/dynein assemblies. Complexes of two kinesin motors showed only a slight increase in run length compared to a single motor, but larger numbers showed higher run lengths approaching 8 μm for seven kinesin motors. Interestingly, this run length depends on copy number in a sub-linear fashion which is far less than the exponential dependence predicted by early theoretical models (Klumpp and Lipowsky, 2005) and is conceptually consistent with the negative interference proposed by the Diehl lab. Dynein's run length increased more dramatically with higher copy number, suggesting more efficient coupling than kinesin as proposed recently (Rai et al., 2013). Derr et al. also provided validation for the tug-of-war model proposed previously (Soppina et al., 2009) by showing that stalled tug-of-war events of mixed motor assembly can be resumed after photocleaving-induced disassembly.

Furuta et al. used SNAP and HALO tags to covalently assemble up to four kinesin motors on dsDNA scaffolds of various length. In this study, the run length of kinesin-1 was shown to be roughly linearly dependent on copy number, which is the strongest cooperative run length behavior of all the synthetic biology-based multiple motor studies to date. The authors also studied assemblies of the nonprocessive minus end-directed kinesin-14 motor Ncd and mixed kinesin-1/Ncd assemblies. Interestingly, Ncd showed a strong run length dependence on copy number and began to move processively when the copy number was two or more. The authors also used optical trapping experiments to show that the force generated by groups of Ncd is additive while the force

for multiple kinesin-1 motors depends only weakly on motor number, confirming a previous study (Jamison et al., 2010).

When considered as a whole, DNA-based synthetic biology approaches provide an extremely valuable technique to study multiple motor-based transport. These approaches have greatly expanded our knowledge of cell-based motility events by allowing researchers to consider assembly of multiple purified proteins with great precision and resolution. These approaches have generally concluded that multiple kinesin-1 motors do not cooperate for more efficient motility whereas multiple cytoplasmic dynein, processive myosin, and nonprocessive kinesin work efficiently together. The great precision afforded by DNA-based assembly comes at a cost, however. Each component must be purified and studied *in vitro*, and DNA origami-based methods are currently not available in the cell. In order to carefully study multiple motor transport inside the cell, a new, protein-based system must be developed, which is the subject of this dissertation.

1.6 References

Akhmanova, A., and Hammer, J.A., 3rd (2010). Linking molecular motors to membrane cargo. Current opinion in cell biology *22*, 479-487. doi: 10.1016/j.ceb.2010.04.008

Ali, M.Y., Lu, H., Bookwalter, C.S., Warshaw, D.M., and Trybus, K.M. (2008). Myosin V and Kinesin act as tethers to enhance each others' processivity. Proceedings of the National Academy of Sciences of the United States of America *105*, 4691-4696. doi: 10.1073/pnas.0711531105

Allen, R.D., Weiss, D.G., Hayden, J.H., Brown, D.T., Fujiwake, H., and Simpson, M. (1985). Gliding movement of and bidirectional transport along single native microtubules from

squid axoplasm: evidence for an active role of microtubules in cytoplasmic transport. The Journal of cell biology *100*, 1736-1752

Ally, S., Larson, A.G., Barlan, K., Rice, S.E., and Gelfand, V.I. (2009). Opposite-polarity motors activate one another to trigger cargo transport in live cells. The Journal of cell biology *187*, 1071-1082. doi: 10.1083/jcb.200908075

Ashkin, A., Dziedzic, J.M., Bjorkholm, J.E., and Chu, S. (1986). Observation of a single-beam gradient force optical trap for dielectric particles. Optics letters *11*, 288

Ashkin, A., Schutze, K., Dziedzic, J.M., Euteneuer, U., and Schliwa, M. (1990). Force generation of organelle transport measured in vivo by an infrared laser trap. Nature *348*, 346-348. doi: 10.1038/348346a0

Axelrod, D. (1981). Cell-substrate contacts illuminated by total internal reflection fluorescence. The Journal of cell biology *89*, 141-145

Barlan, K., Rossow, M.J., and Gelfand, V.I. (2013). The journey of the organelle: teamwork and regulation in intracellular transport. Current opinion in cell biology *25*, 483-488. doi: 10.1016/j.ceb.2013.02.018

Bashor, C.J., Helman, N.C., Yan, S., and Lim, W.A. (2008). Using engineered scaffold interactions to reshape MAP kinase pathway signaling dynamics. Science *319*, 1539-1543. doi: 10.1126/science.1151153

Beeg, J., Klumpp, S., Dimova, R., Gracia, R.S., Unger, E., and Lipowsky, R. (2008). Transport of beads by several kinesin motors. Biophysical journal *94*, 532-541. doi: 10.1529/biophysj.106.097881

Bieling, P., Kronja, I., and Surrey, T. (2010). Microtubule motility on reconstituted meiotic chromatin. Current biology : CB *20*, 763-769. doi: 10.1016/j.cub.2010.02.067

Bieling, P., Telley, I.A., Piehler, J., and Surrey, T. (2008). Processive kinesins require loose mechanical coupling for efficient collective motility. EMBO reports *9*, 1121-1127. doi: 10.1038/embor.2008.169

Blehm, B.H., Schroer, T.A., Trybus, K.M., Chemla, Y.R., and Selvin, P.R. (2013). In vivo optical trapping indicates kinesin's stall force is reduced by dynein during intracellular transport. Proceedings of the National Academy of Sciences of the United States of America *110*, 3381-3386. doi: 10.1073/pnas.1219961110

Block, S.M., Goldstein, L.S., and Schnapp, B.J. (1990). Bead movement by single kinesin molecules studied with optical tweezers. Nature *348*, 348-352. doi: 10.1038/348348a0

Bloemink, M.J., and Geeves, M.A. (2011). Shaking the myosin family tree: biochemical kinetics defines four types of myosin motor. Seminars in cell & developmental biology *22*, 961-967. doi: 10.1016/j.semcdb.2011.09.015

Cai, D., Verhey, K.J., and Meyhofer, E. (2007). Tracking single Kinesin molecules in the cytoplasm of mammalian cells. Biophysical journal *92*, 4137-4144. doi: 10.1529/biophysj.106.100206

Carter, A.P., Cho, C., Jin, L., and Vale, R.D. (2011). Crystal structure of the dynein motor domain. Science *331*, 1159-1165. doi: 10.1126/science.1202393

Conway, L., Wood, D., Tuzel, E., and Ross, J.L. (2012). Motor transport of self-assembled cargos in crowded environments. Proceedings of the National Academy of Sciences of the United States of America *109*, 20814-20819. doi: 10.1073/pnas.1209304109

Courty, S., Luccardini, C., Bellaiche, Y., Cappello, G., and Dahan, M. (2006). Tracking individual kinesin motors in living cells using single quantum-dot imaging. Nano letters *6*, 1491-1495. doi: 10.1021/nl060921t

Coy, D.L., Wagenbach, M., and Howard, J. (1999). Kinesin takes one 8-nm step for each ATP that it hydrolyzes. The Journal of biological chemistry *274*, 3667-3671

Cross, R.A., and McAinsh, A. (2014). Prime movers: the mechanochemistry of mitotic kinesins. Nature reviews Molecular cell biology *15*, 257-271. doi: 10.1038/nrm3768

Derr, N.D., Goodman, B.S., Jungmann, R., Leschziner, A.E., Shih, W.M., and Reck-Peterson, S.L. (2012). Tug-of-war in motor protein ensembles revealed with a programmable DNA origami scaffold. Science *338*, 662-665. doi: 10.1126/science.1226734

Diehl, M.R., Zhang, K., Lee, H.J., and Tirrell, D.A. (2006). Engineering cooperativity in biomotor-protein assemblies. Science *311*, 1468-1471. doi: 10.1126/science.1122125

Driver, J.W., Jamison, D.K., Uppulury, K., Rogers, A.R., Kolomeisky, A.B., and Diehl, M.R. (2011). Productive cooperation among processive motors depends inversely on their mechanochemical efficiency. Biophysical journal *101*, 386-395. doi: 10.1016/j.bpj.2011.05.067

Driver, J.W., Rogers, A.R., Jamison, D.K., Das, R.K., Kolomeisky, A.B., and Diehl, M.R. (2010). Coupling between motor proteins determines dynamic behaviors of motor protein

assemblies. Physical chemistry chemical physics : PCCP *12*, 10398-10405. doi: 10.1039/c0cp00117a

Efremov, A.K., Radhakrishnan, A., Tsao, D.S., Bookwalter, C.S., Trybus, K.M., and Diehl, M.R. (2014). Delineating cooperative responses of processive motors in living cells. Proceedings of the National Academy of Sciences of the United States of America *111*, E334-343. doi: 10.1073/pnas.1313569111

Furuta, K., Furuta, A., Toyoshima, Y.Y., Amino, M., Oiwa, K., and Kojima, H. (2013). Measuring collective transport by defined numbers of processive and nonprocessive kinesin motors. Proceedings of the National Academy of Sciences of the United States of America *110*, 501-506. doi: 10.1073/pnas.1201390110

Gagliano, J., Walb, M., Blaker, B., Macosko, J.C., and Holzwarth, G. (2010). Kinesin velocity increases with the number of motors pulling against viscoelastic drag. European Biophysics Journal *39*

Gibbons, I.R., and Rowe, A.J. (1965). Dynein: A Protein with Adenosine Triphosphatase Activity from Cilia. Science *149*, 424-426. doi: 10.1126/science.149.3682.424

Gross, S.P., Tuma, M.C., Deacon, S.W., Serpinskaya, A.S., Reilein, A.R., and Gelfand, V.I. (2002). Interactions and regulation of molecular motors in Xenopus melanophores. The Journal of cell biology *156*, 855-865. doi: 10.1083/jcb.200105055

Grunberg, R., and Serrano, L. (2010). Strategies for protein synthetic biology. Nucleic acids research *38*, 2663-2675. doi: 10.1093/nar/gkq139

Hendricks, A.G., Perlson, E., Ross, J.L., Schroeder, H.W., 3rd, Tokito, M., and Holzbaur, E.L. (2010). Motor coordination via a tug-of-war mechanism drives bidirectional vesicle transport. Current biology : CB *20*, 697-702. doi: 10.1016/j.cub.2010.02.058

Higuchi, H., and Goldman, Y.E. (1991). Sliding distance between actin and myosin filaments per ATP molecule hydrolysed in skinned muscle fibres. Nature *352*, 352-354. doi: 10.1038/352352a0

Hill, D.B., Plaza, M.J., Bonin, K., and Holzwarth, G. (2004). Fast vesicle transport in PC12 neurites: velocities and forces. European biophysics journal : EBJ *33*, 623-632. doi: 10.1007/s00249-004-0403-6

Hirokawa, N. (1982). Cross-linker system between neurofilaments, microtubules, and membranous organelles in frog axons revealed by the quick-freeze, deep-etching method. The Journal of cell biology *94*, 129-142

Hirokawa, N., and Noda, Y. (2008). Intracellular transport and kinesin superfamily proteins, KIFs: structure, function, and dynamics. Physiological reviews *88*, 1089-1118. doi: 10.1152/physrev.00023.2007

Hirokawa, N., Noda, Y., Tanaka, Y., and Niwa, S. (2009). Kinesin superfamily motor proteins and intracellular transport. Nature reviews Molecular cell biology *10*, 682-696. doi: 10.1038/nrm2774

Hirokawa, N., Pfister, K.K., Yorifuji, H., Wagner, M.C., Brady, S.T., and Bloom, G.S. (1989). Submolecular domains of bovine brain kinesin identified by electron microscopy and monoclonal antibody decoration. Cell *56*, 867-878

Hodges, A.R., Bookwalter, C.S., Krementsova, E.B., and Trybus, K.M. (2009). A nonprocessive class V myosin drives cargo processively when a kinesin- related protein is a passenger. Current biology : CB *19*, 2121-2125. doi: 10.1016/j.cub.2009.10.069

Holzbaur, E.L., and Goldman, Y.E. (2010). Coordination of molecular motors: from in vitro assays to intracellular dynamics. Current opinion in cell biology *22*, 4-13. doi: 10.1016/j.ceb.2009.12.014

Holzwarth, G., Bonin, K., and Hill, D.B. (2002). Forces required of kinesin during processive transport through cytoplasm. Biophysical journal *82*, 1784-1790. doi: 10.1016/S0006-3495(02)75529-X

Howard, J. (1997). Molecular motors: structural adaptations to cellular functions. Nature *389*, 561-567. doi: 10.1038/39247

Howard, J., Hudspeth, A.J., and Vale, R.D. (1989). Movement of microtubules by single kinesin molecules. Nature *342*, 154-158. doi: 10.1038/342154a0

Hunt, A.J., Gittes, F., and Howard, J. (1994). The force exerted by a single kinesin molecule against a viscous load. Biophysical journal *67*, 766-781. doi: 10.1016/S0006-3495(94)80537-5

Huxley, A.F., and Niedergerke, R. (1954). Structural changes in muscle during contraction; interference microscopy of living muscle fibres. Nature *173*, 971-973

Huxley, H., and Hanson, J. (1954). Changes in the cross-striations of muscle during contraction and stretch and their structural interpretation. Nature *173*, 973-976

Huxley, H.E. (1969). The mechanism of muscular contraction. Science *164*, 1356-1365

Jamison, D.K., Driver, J.W., and Diehl, M.R. (2012). Cooperative responses of multiple kinesins to variable and constant loads. The Journal of biological chemistry *287*, 3357-3365. doi: 10.1074/jbc.M111.296582

Jamison, D.K., Driver, J.W., Rogers, A.R., Constantinou, P.E., and Diehl, M.R. (2010). Two kinesins transport cargo primarily via the action of one motor: implications for intracellular transport. Biophysical journal *99*, 2967-2977. doi: 10.1016/j.bpj.2010.08.025

Jeppesen, G.M., and Hoerber, J.K. (2012). The mechanical properties of kinesin-1: a holistic approach. Biochemical Society transactions *40*, 438-443. doi: 10.1042/BST20110768

Jolly, A.L., and Gelfand, V.I. (2011). Bidirectional intracellular transport: utility and mechanism. Biochemical Society transactions *39*, 1126-1130. doi: 10.1042/BST0391126

Kamal, A., and Goldstein, L.S. (2002). Principles of cargo attachment to cytoplasmic motor proteins. Current opinion in cell biology *14*, 63-68

Kapitein, L.C., van Bergeijk, P., Lipka, J., Keijzer, N., Wulf, P.S., Katrukha, E.A., Akhmanova, A., and Hoogenraad, C.C. (2013). Myosin-V opposes microtubule-based cargo transport and drives directional motility on cortical actin. Current biology : CB *23*, 828-834. doi: 10.1016/j.cub.2013.03.068

Kardon, J.R., and Vale, R.D. (2009). Regulators of the cytoplasmic dynein motor. Nature reviews Molecular cell biology *10*, 854-865. doi: 10.1038/nrm2804

Karki, S., and Holzbaur, E.L. (1999). Cytoplasmic dynein and dynactin in cell division and intracellular transport. Current opinion in cell biology *11*, 45-53

Klumpp, S., and Lipowsky, R. (2005). Cooperative cargo transport by several molecular motors. Proceedings of the National Academy of Sciences of the United States of America *102*, 17284-17289. doi: 10.1073/pnas.0507363102

Kon, T., Oyama, T., Shimo-Kon, R., Imamula, K., Shima, T., Sutoh, K., and Kurisu, G. (2012). The 2.8 A crystal structure of the dynein motor domain. Nature *484*, 345-350. doi: 10.1038/nature10955

Kulic, I.M., Brown, A.E., Kim, H., Kural, C., Blehm, B., Selvin, P.R., Nelson, P.C., and Gelfand, V.I. (2008). The role of microtubule movement in bidirectional organelle

transport. Proceedings of the National Academy of Sciences of the United States of America *105*, 10011-10016. doi: 10.1073/pnas.0800031105

Kunwar, A., Tripathy, S.K., Xu, J., Mattson, M.K., Anand, P., Sigua, R., Vershinin, M., McKenney, R.J., Yu, C.C., Mogilner, A., *et al.* (2011). Mechanical stochastic tug-of-war models cannot explain bidirectional lipid-droplet transport. Proceedings of the National Academy of Sciences of the United States of America *108*, 18960-18965. doi: 10.1073/pnas.1107841108

Kunwar, A., Vershinin, M., Xu, J., and Gross, S.P. (2008). Stepping, strain gating, and an unexpected force-velocity curve for multiple-motor-based transport. Current biology : CB *18*, 1173-1183. doi: 10.1016/j.cub.2008.07.027

Kural, C., Kim, H., Syed, S., Goshima, G., Gelfand, V.I., and Selvin, P.R. (2005). Kinesin and dynein move a peroxisome in vivo: a tug-of-war or coordinated movement? Science *308*, 1469-1472. doi: 10.1126/science.1108408

Kural, C., Serpinskaya, A.S., Chou, Y.H., Goldman, R.D., Gelfand, V.I., and Selvin, P.R. (2007). Tracking melanosomes inside a cell to study molecular motors and their interaction. Proceedings of the National Academy of Sciences of the United States of America *104*, 5378-5382. doi: 10.1073/pnas.0700145104

Larson, A.G., Landahl, E.C., and Rice, S.E. (2009). Mechanism of cooperative behaviour in systems of slow and fast molecular motors. Physical chemistry chemical physics : PCCP *11*, 4890-4898. doi: 10.1039/b900968j

Leduc, C., Ruhnow, F., Howard, J., and Diez, S. (2007). Detection of fractional steps in cargo movement by the collective operation of kinesin-1 motors. Proceedings of the National Academy of Sciences of the United States of America *104*, 10847-10852. doi: 10.1073/pnas.0701864104

Levi, V., Serpinskaya, A.S., Gratton, E., and Gelfand, V. (2006). Organelle transport along microtubules in Xenopus melanophores: evidence for cooperation between multiple motors. Biophysical journal *90*, 318-327. doi: 10.1529/biophysj.105.067843

Lu, H., Efremov, A.K., Bookwalter, C.S., Krementsova, E.B., Driver, J.W., Trybus, K.M., and Diehl, M.R. (2012). Collective dynamics of elastically coupled myosin V motors. The Journal of biological chemistry *287*, 27753-27761. doi: 10.1074/jbc.M112.371393

Mallik, R., Carter, B.C., Lex, S.A., King, S.J., and Gross, S.P. (2004). Cytoplasmic dynein functions as a gear in response to load. Nature *427*, 649-652. doi: 10.1038/nature02293

Mallik, R., Petrov, D., Lex, S.A., King, S.J., and Gross, S.P. (2005). Building complexity: an in vitro study of cytoplasmic dynein with in vivo implications. Current biology : CB *15*, 2075-2085. doi: 10.1016/j.cub.2005.10.039

Mehta, A.D., Rock, R.S., Rief, M., Spudich, J.A., Mooseker, M.S., and Cheney, R.E. (1999). Myosin-V is a processive actin-based motor. Nature *400*, 590-593. doi: 10.1038/23072

Miller, R.H., and Lasek, R.J. (1985). Cross-bridges mediate anterograde and retrograde vesicle transport along microtubules in squid axoplasm. The Journal of cell biology *101*, 2181-2193

Moffitt, J.R., Chemla, Y.R., Smith, S.B., and Bustamante, C. (2008). Recent advances in optical tweezers. Annual review of biochemistry *77*, 205-228. doi: 10.1146/annurev.biochem.77.043007.090225

Muller, M.J., Klumpp, S., and Lipowsky, R. (2008). Tug-of-war as a cooperative mechanism for bidirectional cargo transport by molecular motors. Proceedings of the National Academy of Sciences of the United States of America *105*, 4609-4614. doi: 10.1073/pnas.0706825105

Nan, X., Sims, P.A., and Xie, X.S. (2008). Organelle tracking in a living cell with microsecond time resolution and nanometer spatial precision. Chemphyschem : a European journal of chemical physics and physical chemistry *9*, 707-712. doi: 10.1002/cphc.200700839

Oliver, T.N., Berg, J.S., and Cheney, R.E. (1999). Tails of unconventional myosins. Cellular and molecular life sciences : CMLS *56*, 243-257

Ovechkina, Y., and Wordeman, L. (2003). Unconventional motoring: an overview of the Kin C and Kin I kinesins. Traffic *4*, 367-375

Pan, X., Ou, G., Civelekoglu-Scholey, G., Blacque, O.E., Endres, N.F., Tao, L., Mogilner, A., Leroux, M.R., Vale, R.D., and Scholey, J.M. (2006). Mechanism of transport of IFT particles in C. elegans cilia by the concerted action of kinesin-II and OSM-3 motors. The Journal of cell biology *174*, 1035-1045. doi: 10.1083/jcb.200606003

Peterman, E.J., Sosa, H., and Moerner, W.E. (2004). Single-molecule fluorescence spectroscopy and microscopy of biomolecular motors. Annual review of physical chemistry *55*, 79-96. doi: 10.1146/annurev.physchem.55.091602.094340

Peterson, D.R., and Bronzino, J.D. (2008). Biomechanics: Principles and Applications (Boca Raton, FL: CRC Press).

Porter, M.E., and Sale, W.S. (2000). The 9 + 2 axoneme anchors multiple inner arm dyneins and a network of kinases and phosphatases that control motility. The Journal of cell biology *151*, F37-42

Rai, A.K., Rai, A., Ramaiya, A.J., Jha, R., and Mallik, R. (2013). Molecular adaptations allow dynein to generate large collective forces inside cells. Cell *152*, 172-182. doi: 10.1016/j.cell.2012.11.044

Reck-Peterson, S.L., Yildiz, A., Carter, A.P., Gennerich, A., Zhang, N., and Vale, R.D. (2006). Single-molecule analysis of dynein processivity and stepping behavior. Cell *126*, 335-348. doi: 10.1016/j.cell.2006.05.046

Reis, G.F., Yang, G., Szpankowski, L., Weaver, C., Shah, S.B., Robinson, J.T., Hays, T.S., Danuser, G., and Goldstein, L.S. (2012). Molecular motor function in axonal transport in vivo probed by genetic and computational analysis in Drosophila. Molecular biology of the cell *23*, 1700-1714. doi: 10.1091/mbc.E11-11-0938

Roberts, A.J., Kon, T., Knight, P.J., Sutoh, K., and Burgess, S.A. (2013). Functions and mechanics of dynein motor proteins. Nature reviews Molecular cell biology *14*, 713-726. doi: 10.1038/nrm3667

Rogers, A.R., Driver, J.W., Constantinou, P.E., Kenneth Jamison, D., and Diehl, M.R. (2009). Negative interference dominates collective transport of kinesin motors in the absence of load. Physical chemistry chemical physics : PCCP *11*, 4882-4889. doi: 10.1039/b900964g

Rothemund, P.W. (2006). Folding DNA to create nanoscale shapes and patterns. Nature *440*, 297-302. doi: 10.1038/nature04586

Schliwa, M. (2003). Molecular Motors (Weinheim, Germany: Wiley-VCH Verlag GmbH & Co.).

Schnitzer, M.J., and Block, S.M. (1997). Kinesin hydrolyses one ATP per 8-nm step. Nature *388*, 386-390. doi: 10.1038/41111

Scholey, J.M. (1996). Motility assays for motor proteins, Vol 39 (New York: Academic Press).

Schroeder, H.W., 3rd, Mitchell, C., Shuman, H., Holzbaur, E.L., and Goldman, Y.E. (2010). Motor number controls cargo switching at actin-microtubule intersections in vitro. Current biology : CB *20*, 687-696. doi: 10.1016/j.cub.2010.03.024

Schuster, M., Lipowsky, R., Assmann, M.A., Lenz, P., and Steinberg, G. (2011). Transient binding of dynein controls bidirectional long-range motility of early endosomes. Proceedings of the National Academy of Sciences of the United States of America *108*, 3618-3623. doi: 10.1073/pnas.1015839108

Seeman, N.C., and Kallenbach, N.R. (1983). Design of immobile nucleic acid junctions. Biophysical journal *44*, 201-209. doi: 10.1016/S0006-3495(83)84292-1

Seitz, A., and Surrey, T. (2006). Processive movement of single kinesins on crowded microtubules visualized using quantum dots. The EMBO journal *25*, 267-277. doi: 10.1038/sj.emboj.7600937

Shima, T., Imamula, K., Kon, T., Ohkura, R., and Sutoh, K. (2006). Head-head coordination is required for the processive motion of cytoplasmic dynein, an AAA+ molecular motor. Journal of structural biology *156*, 182-189. doi: 10.1016/j.jsb.2006.03.014

Shubeita, G.T., Tran, S.L., Xu, J., Vershinin, M., Cermelli, S., Cotton, S.L., Welte, M.A., and Gross, S.P. (2008). Consequences of motor copy number on the intracellular transport of kinesin-1-driven lipid droplets. Cell *135*, 1098-1107. doi: 10.1016/j.cell.2008.10.021

Sims, P.A., and Xie, X.S. (2009). Probing dynein and kinesin stepping with mechanical manipulation in a living cell. Chemphyschem : a European journal of chemical physics and physical chemistry *10*, 1511-1516. doi: 10.1002/cphc.200900113

Soppina, V., Rai, A.K., Ramaiya, A.J., Barak, P., and Mallik, R. (2009). Tug-of-war between dissimilar teams of microtubule motors regulates transport and fission of endosomes. Proceedings of the National Academy of Sciences of the United States of America *106*, 19381-19386. doi: 10.1073/pnas.0906524106

Svoboda, K., and Block, S.M. (1994a). Biological applications of optical forces. Annual review of biophysics and biomolecular structure *23*, 247-285. doi: 10.1146/annurev.bb.23.060194.001335

Svoboda, K., and Block, S.M. (1994b). Force and velocity measured for single kinesin molecules. Cell *77*, 773-784

Sweeney, H.L., and Houdusse, A. (2010). Structural and functional insights into the Myosin motor mechanism. Annual review of biophysics *39*, 539-557. doi: 10.1146/annurev.biophys.050708.133751

Szent-Gyorgyi, A. (1941-1942). The contraction of myosin threads. Stud Inst Med Chem Univ Szeged *1*, 17-26

Tabb, J.S., Molyneaux, B.J., Cohen, D.L., Kuznetsov, S.A., and Langford, G.M. (1998). Transport of ER vesicles on actin filaments in neurons by myosin V. Journal of cell science *111 (Pt 21)*, 3221-3234

Torring, T., Voigt, N.V., Nangreave, J., Yan, H., and Gothelf, K.V. (2011). DNA origami: a quantum leap for self-assembly of complex structures. Chemical Society reviews *40*, 5636-5646. doi: 10.1039/c1cs15057j

Vale, R.D. (2003). The molecular motor toolbox for intracellular transport. Cell *112*, 467-480

Vale, R.D., and Fletterick, R.J. (1997). The design plan of kinesin motors. Annual review of cell and developmental biology *13*, 745-777. doi: 10.1146/annurev.cellbio.13.1.745

Vale, R.D., and Milligan, R.A. (2000). The way things move: looking under the hood of molecular motor proteins. Science *288*, 88-95

Vale, R.D., Reese, T.S., and Sheetz, M.P. (1985a). Identification of a novel force-generating protein, kinesin, involved in microtubule-based motility. Cell *42*, 39-50

Vale, R.D., Schnapp, B.J., Reese, T.S., and Sheetz, M.P. (1985b). Organelle, bead, and microtubule translocations promoted by soluble factors from the squid giant axon. Cell *40*, 559-569

Vallee, R.B., Williams, J.C., Varma, D., and Barnhart, L.E. (2004). Dynein: An ancient motor protein involved in multiple modes of transport. Journal of neurobiology *58*, 189-200. doi: 10.1002/neu.10314

Veigel, C., and Schmidt, C.F. (2011). Moving into the cell: single-molecule studies of molecular motors in complex environments. Nature reviews Molecular cell biology *12*, 163-176. doi: 10.1038/nrm3062

Vershinin, M., Carter, B.C., Razafsky, D.S., King, S.J., and Gross, S.P. (2007). Multiple-motor based transport and its regulation by Tau. Proceedings of the National Academy of Sciences of the United States of America *104*, 87-92. doi: 10.1073/pnas.0607919104

Visscher, K., Schnitzer, M.J., and Block, S.M. (1999). Single kinesin molecules studied with a molecular force clamp. Nature *400*, 184-189. doi: 10.1038/22146

Wells, A.L., Lin, A.W., Chen, L.Q., Safer, D., Cain, S.M., Hasson, T., Carragher, B.O., Milligan, R.A., and Sweeney, H.L. (1999). Myosin VI is an actin-based motor that moves backwards. Nature *401*, 505-508. doi: 10.1038/46835

Xu, J., Shu, Z., King, S.J., and Gross, S.P. (2012). Tuning multiple motor travel via single motor velocity. Traffic *13*, 1198-1205. doi: 10.1111/j.1600-0854.2012.01385.x

Yanagida, T., Arata, T., and Oosawa, F. (1985). Sliding distance of actin filament induced by a myosin crossbridge during one ATP hydrolysis cycle. Nature *316*, 366-369

Yildiz, A., Tomishige, M., Vale, R.D., and Selvin, P.R. (2004). Kinesin walks hand-over-hand. Science *303*, 676-678. doi: 10.1126/science.1093753

Yoo, J., Kambara, T., Gonda, K., and Higuchi, H. (2008). Intracellular imaging of targeted proteins labeled with quantum dots. Experimental cell research *314*, 3563-3569. doi: 10.1016/j.yexcr.2008.09.014

Chapter 2 Creating defined assemblies of multiple proteins in cells

Portions of this chapter have been adapted from the following publication:

Norris, S.R., Soppina, V., Dizaji, A.S., Schimert, K.I., Sept, D., Cai, D., Sivaramakrishnan, S., and Verhey, K.J. (2014). A method for multi-protein assembly in cells reveals independent action of kinesins in complex. *Journal of Cell Biology*, Accepted.

Author contributions:

S.R.N., V.S., D.C., and K.J.V. designed research. S.R.N., V.S., A.S.D., and K.S. performed research. A.S.D., D.S., and S.S. contributed new reagents or analytic tools. S.R.N. and A.S.D. analyzed data. S.R.N. and K.J.V. wrote the paper with input from all authors.

2.1 Introduction

Teams of processive molecular motors are critical for intracellular transport and organization, yet coordination between motors remains poorly understood (Chapter 1). A growing body of work has attempted to characterize how teams of kinesin, dynein, or myosin motors can work together for efficient transport, but these studies are limited (Barlan et al., 2013). For instance, experiments using multiple-motor assembly on beads (Mallik et al., 2005; Vale et al., 1985; Vershinin et al., 2007; Xu et al., 2012) or DNA-based scaffolds (Derr et al., 2012; Furuta et al., 2013; Rogers et al., 2009) are limited to *in vitro* applications, whereas determining the number

of motors on a cargo in cell-based experiments is extremely difficult (Efremov et al., 2014; Hill et al., 2004; Kural et al., 2005; Levi et al., 2006; Shubeita et al., 2008). Thus, studying multiple-motor coordination in a cellular environment with a high level of detail has previously been unattainable. To address these issues, we developed a system for linking protein components with defined spacing and composition in cells. This system is widely applicable to the study of multi-protein assemblies in cells and enables the study of multi-motor transport in a manner that a) more closely mimics the physiological state of motor-cargo linkages and b) reveals the influence of cellular architecture on motility events.

In order to develop this system, we first needed to characterize a "toolbox" of protein-based components that would be used to create these assemblies. In this chapter, I first describe the detailed characterization of each of these toolbox components: scaffolds, which provide a rigid protein component of defined spacing; linkers, which drive protein-protein assembly between motors and scaffolds; and a biotin tag, which allows these components to be attached to streptavidin-labeled beads or surfaces for further *in vitro* experiments. After characterization of these components, I use a FRET-based approach and a subcellular recruitment study to verify that these tools can be used to assemble multi-protein complexes inside living cells in a tunable fashion. Finally, I present a preliminary experiment where two identical kinesin-1 motors are recruited to opposite ends of a scaffold using the same linker, resulting in a modest increase in run length. Taken together, the work in presented in this chapter presents compelling evidence that multiple motor complexes can be assembled inside cells using a tunable, protein-based system.

2.2 Materials and Methods

Plasmids. Constitutively active versions of the kinesin-1 motor rat KIF5C (aa 1-560) and the kinesin-3 motor rat KIF1A (aa 1-393 with the leucine zipper dimerizing segment of GCN4) have been described (Cai et al., 2009; Cai et al., 2007; Soppina et al., 2014). DNA fragments encoding SAH domains of various lengths were generated by PCR cloning of the relevant sequences: 5 nm helix from *H. sapiens* translation initiation factor IF-2; 10 nm helix from *S. scrofa* Myosin VI medial tail; 20 nm helix from *S. cerevisiae* mannosyltransferase MNN4; and 30 nm helix from *T. vaginalis* Kelch-motif family protein (Sivaramakrishnan et al., 2008; Sivaramakrishnan et al., 2009). The 60 nm helix is a tandem repeat of 30 nm helices separated by four tandem Gly-Ser-Gly (GSG) sequences. Multiple GSG repeats were also included between all scaffold and linker components to ensure flexibility and rotational freedom of each component. IA/IQ fusions were generated by insertion of oligonucleotides encoding the peptides. Plasmids encoding FKBP and FRB were obtained from Ariad Pharmaceuticals (Cambridge, MA) and are now available from Clontech (Mountain View, CA) as DmrA and DmrC, respectively. Plasmids encoding mNeonGreen were obtained from Allele Biotechnology (San Diego, CA). EF Hand and tandem mCherry sequences were synthesized (DNA 2.0, Menlo Park, CA). Plasmids encoding split superfolder GFP components were a gift from F. Pinaud (University of Southern California). The above components were subcloned behind the cytomegalovirus promoter in the EGFP-N1 vector (Clontech, Mountain View, CA); this vector also contains a SV40 origin for replication in mammalian cells and a kanamycin resistance cassette for amplification in *E. coli*. All plasmids were verified by DNA sequencing.

Cell culture, transfection, western blotting, and immunofluorescence. COS cells were cultured, transfected and lysed as described (Cai et al., 2007; Soppina et al., 2014). For

immunoprecipitation, lysates were incubated with antibodies for 3 h at 4˚C, Protein A agarose beads were added for an additional 30 min at 4˚C, and the immunoprecipitates were analyzed by blotting with a monoclonal antibody to bovine brain kinesin-1 or KHC (Mouse MAb1614, Millipore, Billerica, MA) or a polyclonal antibody raised in rabbits against a GFP peptide (antigen sequence CFKEDGNILGHKLE). For immunoprecipitation experiments using DmrA/C linkers, 20 ng/mL rapamycin (Millipore, Billerica, MA) was added 1 h prior to lysis and maintained throughout lysis and immunoprecipitation. For immunofluorescence, monoclonal antibodies to total β-tubulin (Mouse E7, Developmental Studies Hybridoma Bank, Iowa City, IA) and acetylated α-tubulin (Mouse 6-11B-1, #T7451, Sigma-Aldrich, St. Louis, MO) were used. In biotinylation experiments, the following antibodies were used: GFP (polyclonal, see above, used to recognize mCitrine), KHC (monoclonal, see above), and HA (12CA5 hybridoma ascites). Biotinylated proteins were detected by incubating 5 μg/mL Avidin D Horseradish Peroxidase (Av-HRP, Vector Laboratories #A-2004 Burlingame, CA) in 5% BSA. BSA was used to block the membrane because of the presence of endogenous biotinylated proteins in milk.

FRET stoichiometry. Fluorescence images of live COS7 cells were collected at 37˚C in Leibowitz L-15 without phenol red (Life Technologies, Carlsbad, CA) using an Olympus IX70 inverted microscope with a 40X objective (LCPlan Fl, NA = 0.6, 1.5X tube lens) and an X-Cite 120 metal halide light source (EXFO; Mississauga, ON, Canada). For DmrA/C FRET experiments, A/C heterodimerizer (Clontech, Mountain View, CA), equivalent to Rapalog-1 AP21967 (Ariad Pharmaceuticals, Cambridge, MA) was added at 500 nM for 60 minutes unless otherwise noted. Fluorescence excitation and emission wavelengths were selected using a DAPI/FITC/Tx Red filter set (Chroma Technology, Rockingham, VT) and a Lambda 10-3 filter wheel controller (Sutter Instruments, Novato, CA) equipped with a shutter for epifluorescence

illumination control. Images were recorded with a CoolSnap HQ2 14-bit CCD camera (Photometrics, Tuscon, AZ). Image acquisition was performed using MetaMorph (Molecular Devices, Sunnyvale, CA) and FRET values were calculated using the MATLAB-based (The MathWorks, Natick, MA) program FRET calculator (available online: http://sitemaker.umich.edu/4dimagingcenter/fret_calculator). FRET microscopy and analysis was carried out using equations described in (Hoppe et al., 2002) as follows. Each collected image was corrected for uneven illumination shading by collecting flat-field shade images from a fluorescent cover glass and normalizing by these values. Images were then corrected for pixel bias offset by collecting images with the excitation light blocked and normalizing by these values. In order for the FRET stoichiometry equations to be used, the FRET microscope was then calibrated to obtain the parameters α, β, γ, and ξ, which describe the baseline fluorescence contributions from each fluorophore in each channel for the imaging filter set (see Hoppe et al., 2012). These parameters were calculated from COS7 cells expressing mCherry alone (α), superfolder GFP alone (sfGFP) (β), or a mCherry-sfGFP molecule linked by 12 aa (γ and ξ). sfGFP was used in calibrations to allow proper comparison to the split superfolder GFP used in protein assembly. For the baseline FRET efficiency parameter used in calculations of γ and ξ, we use the previously reported value in (Khmelinskii et al., 2012), where FRET efficiency for the sfGFP-mCherry pair was determined by fluorescence correlation spectroscopy (FCS) measurements using recombinant proteins. For each cell, the background-subtracted, bias/shade-corrected average values of the donor (sfGFP ex/em), acceptor (mCherry ex/em), and FRET (sfGFP ex, mCherry em) images were used in all calculations. Mean values of the apparent FRET efficiency relative to acceptor (E_A) and donor (E_D) fluorescence and for the molar ratio of acceptor to donor (R) were then calculated using FRET stoichiometry equations (Hoppe et al., 2002) for each cell:

$$E_A = \gamma\left[\frac{I_F - \beta I_D}{\alpha I_A} - 1\right]$$

$$E_D = \left[1 - \frac{I_D}{(I_F - \alpha I_A - \beta I_D)(\xi/\gamma) + I_D}\right]$$

$$R = \left(\frac{\xi}{\gamma^2}\right)\frac{\alpha I_A}{(I_F - \alpha I_A - \beta I_D)(\xi/\gamma) + I_D},$$

where I_F, I_D, and I_A are the fluorescence intensities in the FRET, donor, and acceptor channels, respectively. Reported values are averages of all pixels inside the cell, where phase images were used to draw an outline of the cell periphery. Only cells with molar ratio (Rm) < 2.5 were considered. A two-tailed *t*-test was used to compare steady-state E_D values from $N \geq 31$ cells from three independent experiments for each data point.

Characterization of linkers by single molecule motility assays. Non-fluorescent kin1 motors and GFP-labeled scaffolds in lysates containing 2 mM ATP were diluted in P12 buffer (12 mM PIPES/KOH, 1 mM EGTA, and 2 mM $MgCl_2$, pH 6.8). 5 μL of each lysate was added to flow chambers containing taxol-stabilized MTs (Cytoskeleton, Denver, CO) and 45 μL of oxygen scavenger buffer (1 mM DTT, 1 mM MgCl2, 2 mM ATP, 10 mM glucose, 0.1 mg/mL glucose oxidase, 0.08 mg/mL catalase, 10 mg/mL BSA, and 10 μM taxol in P12). Linker screening assays were carried out at the Single Molecule Analysis in Real Time (SMART) Center at the University of Michigan (Ann Arbor, MI). Images were acquired at room temperature using an Olympus IX-81 microscope with a 60X 1.49 NA oil immersion TIRF objective with 4X tube lens (Olympus, Center Valley, PA) equipped with five fiber-coupled lasers (405nm, 488nm, 532nm, 561nm, 640nm) and independently focused via Cell^TIRF module (Olympus). Individual mCitrine-labeled motors or GFP-labeled scaffolds were excited at 488nm with 100 ms exposure and images

were collected via an EMCCD detector (iXon 897, 512x512, 16μM array, Andor, Belfast, UK). For linker screening assays, the SpotTracker plugin for ImageJ (Sage et al., 2005), available online at http://bigwww.epfl.ch/sage/soft/spottracker/, was modified to batch-process motility data (Cai et al., 2009) and used to calculate the speed and run length.

Cumulative distribution functions (CDFs). CDFs of velocities and run lengths were generated via MATLAB and mean values were obtained as described (Thorn et al., 2000). CDFs were used for statistical analysis because they are continuous and do not introduce any subjective binning. To obtain mean run length values, run length distributions were first reorganized into a CDF with the built-in MATLAB function ecdf, then the lsqcurvefit function was used to generate a least squares fit of the experimental CDF to the hypothetical distribution from x_0 to infinity, where x_0 is the minimum run length 0.3 μm (run length values less than 0.3 μm were deleted from the run length CDF):

$$CDF(x) = 1 - e^{(x_0 - x)/t},$$

where the decay constant *t* is the only fitted parameter. The mean run length for the distribution is then defined by adding the minimum run length x_0 to the decay constant. Errors were estimated by the bootstrap technique (Thorn et al., 2000) by using the MATLAB function bootfunc for resampling. Each distribution was resampled 200x and refit to the above CDF equation. The standard deviation of the bootstrap distribution for the resampled data sets was taken as the error for each fitted quantity.

Mean velocity values were obtained in an identical way only no minimum velocity was defined. Velocity CDFs were fit to the hypothetical CDF for a normal distribution using a nonlinear least squares fit with free parameters μ (mean) and σ (standard deviation):

$$CDF(x) = \frac{1}{2}\left[1 + erf\left(\frac{x-\mu}{\sqrt{2\sigma^2}}\right)\right]$$

$$PDF(x) = \frac{\phi}{\sigma_1\sqrt{2\pi}} Exp\left[\frac{-(x-\mu_1)^2}{2\sigma_1^{\,2}}\right] + \frac{1-\phi}{\sigma_2\sqrt{2\pi}} Exp\left[\frac{-(x-\mu_2)^2}{2\sigma_2^{\,2}}\right]$$

Creation of COS7 cell line stably overexpressing HA-BirA. To create a COS7 cell line stably overexpressing HA-BirA, HA-BirA was cloned into the pQCXIP retroviral vector (Clontech, Mountain View, CA), a bicistronic expression vector designed to express a target gene along with a puromycin selection marker (Julius et al., 2000). HEK293T cells were transfected with 1 μg of the pQCXIP/HA-BirA vector along with 1 μg each of the packaging vectors pVSV and pGAG/POL. HEK293T cell culture supernatants containing retrovirus were filtered through 0.45 μm pore filters (Fisher Scientific, Chicago, IL) and used to transduce COS7 cells in the presence of 2 μg/mL polybrene (Sigma, St. Louis, MO). Transduced COS7 cells were then selected and pooled in 2.5 μg/mL puromycin.

Motility assays with biotin-motors attached to beads or quantum dots. To non-specifically conjugate neutravidin to beads, 3 μL of fluorescent polystyrene beads (1 μm diameter, Fluoresbrite YG #18860, Polysciences, Warrington, PA) were incubated with 40 μL neutravidin (1.25 mg/mL, #A2666, Life Technologies, Carlsbad, CA) for four hours at room temperature, then centrifuged at 14,000 rpm and resuspended 10 x in wash buffer (50 mM Tris, pH 8.0, 0.5 mg/mL BSA, resuspended to 20 μL). To test for neutravidin conjugation, washed beads were added to a flow chamber coated with BSA-biotin (Sigma, A8549), washed, and quantified at the surface. To conjugate biotinylated motors to beads, 1 μL of washed neutravidin beads were added to 25 μL of

COS7 lysate expressing both HA-BirA and KHC(1-560)-AviTag and incubated on ice for 30 minutes. To conjugate biotinylated motors to quantum dots, 0.25 μL of quantum dots (QDot 525 streptavidin conjugate, #Q10141MP, Life Technologies, Carlsbad, CA) was added to 25 μL of COS7 lysate expressing both HA-BirA and KHC(1-560)-AviTag and incubated on ice for 15 minutes.

Flow chambers were prepared identical to above, only cover slips were first plasma cleaned for 5 minutes at 100 mTor (DV-502, Denton, Moorestown, NJ) to minimize bead-surface interactions and casein was used to block the surface rather than BSA. Motor-conjugated beads were diluted in BRB80 buffer (80 mM PIPES/KOH, 1 mM EGTA, and 2 mM $MgCl_2$, pH 6.8). 5 μL of the motor-bead mix was added to flow chambers containing taxol-stabilized, rhodamine-labeled MTs (Cytoskeleton, Denver, CO) and 45 μL of oxygen scavenger buffer (1 mM DTT, 1 mM MgCl2, 2 mM ATP, 10 mM glucose, 0.1 mg/mL glucose oxidase, 0.08 mg/mL catalase, 6 mg/mL casein, and 10 μM taxol in P12). For experiments using 1 μm beads, images were acquired on an inverted epifluorescence microscope (TE2000-E, Nikon) with 500 ms exposures. For experiments using quantum dots, images were acquired identically to single-molecule experiments.

2.3 Results

2.3.1 Scaffolds and linkers for self-assembly of defined complexes in mammalian cells

To assemble protein complexes of defined number and spacing in mammalian cells, we developed a biosynthetic system using proteins with well-characterized structural and assembly

properties. The basis of our system is a scaffold protein (Fig. 2.1A). For this, we chose polypeptides that form a single alpha helix (SAH) stabilized by ionic interactions between the side chains of alternating glutamate (E) and arginine (R) or lysine (K) residues (thus also called ER/K helices) (Fig. 2.1C) (Baboolal et al., 2009; Knight et al., 2005; Sivaramakrishnan et al., 2008). SAH domains of various lengths are found across phylogenetic kingdoms (Sivaramakrishnan et al., 2008) and we selected helices of 5, 10, 20, and 30 nm (see Materials and Methods). We tested the solubility of each helix by expressing scaffold constructs in COS7 cells and analyzing by SDS-PAGE and western blot (Fig. 2.1D). We confirmed that each SAH was soluble (detectable by SDS-PAGE) and that increasing the size of the scaffold's SAH increased the apparent molecular weight in SDS-PAGE. To ensure scaffold solubility for all subsequent constructs, we also added a globular SNAP tag to the N-terminus of each construct (Fig. 2.1A). This tag also allows fluorescent labeling of the scaffold via SNAP ligands (NEB) when necessary.

To attach proteins to the scaffold, we selected linker proteins that self-associate (Fig. 2.1B). We first tested α-helical protein segments that form coiled-coil structures of defined orientation and oligomeric state. Since our overall goal was to recruit dimeric kinesin motors to a monomeric scaffold, we focused on sequences shown to form trimeric coiled-coils (Fig. 2.2). Trimeric coiled-coils would lead to ideal binding stoichiometry, as every component of the linker would be incorporated in a complex and no "loose ends" would be available for longer chain formation (see Discussion, Fig. 2.14). Other coiled-coil structures would likely be more useful in other applications; for instance, heterodimeric coils would be ideal for assembly between two monomers, or heterotetrameric coils would be ideal for assembly between two dimers. We tested

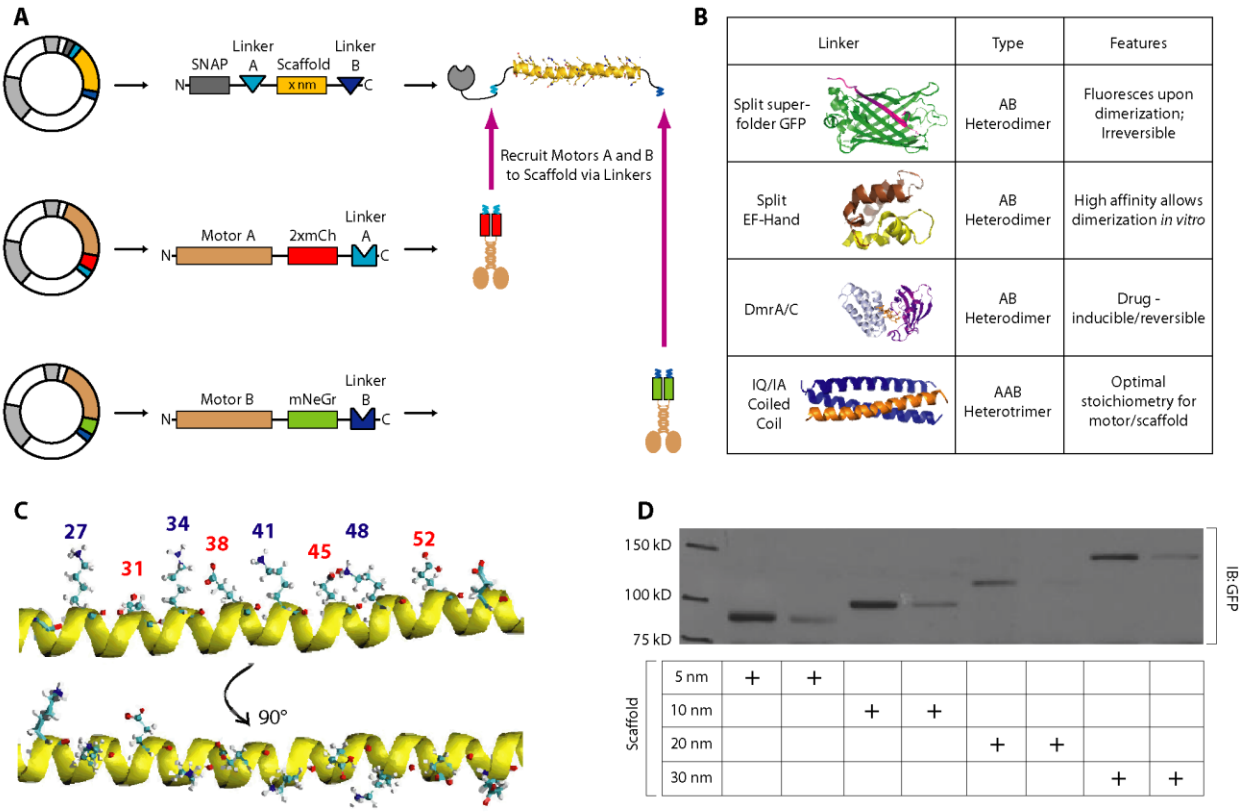

Figure 2.1. A protein-based system for assembly of defined multi-protein complexes.

(A) Plasmids for expression of scaffold (top) and motor components (middle and bottom) are co-transfected into mammalian cells and the protein components are allowed to self-assemble. The scaffold (yellow) is a single alpha-helix (SAH) with linkers (blue) attached at each end. **(B)** Summary of the four linker components and their features. **(C)** Orthogonal views of residues 24-55 of the SAH domain of mannosyltransferase. Charge interactions between amino acid side chains stabilize the SAH domain, where blue indicates a lysine (K) residue and red indicates a glutamatic acid residue (E). Because of these E-K or occasionally E-R interactions, this component is also called the ER/K helix. Figure adapted from (Sivaramakrishnan et al., 2008). **(D)** Scaffolds containing SAH domains of the indicated length (denoted by +) were expressed in COS7 cells and verified by western blot. Proteins in cell lysates run on SDS-PAGE and detected by immunoblotting (IB) with an antibody to GFP, which detects mCit-labeled scaffold (IB: GFP). Scaffold: AviTag-3xmCitrine-IQ-x nm SAH-IQ.

---

the following coiled-coil sequences for scaffold assembly: a homotrimeric variant of the leucine zipper from *S. cerevisiae* GCN4 (Holton and Alber, 2004), the homotrimeric coiled-coil domain of mammalian coronin 1 (Kammerer et al., 2005), and de-novo designed coiled-coils of

A

Schematic	Linker	Type	Notes	Reference
	IQ/IA	Antiparallel heterotrimeric coiled-coil (AAB-type)	Worked well in motility and Co-IP screen (Fig. 2, S1)	Kiyokawa et al., 2004
	GCN4 Trimer	Antiparallel homotrimeric coiled-coil; mutant version (N16A) of leucine zipper of yeast transcriptional activator GCN4 (AAA-type)	Very limited motility in screen	Holton and Alber, 2004
	ccCor1	Homotrimeric coiled-coil domain of mammalian actin-associated protein coronin 1 (parallel, AAA-type)	Worked well in screen; Abandoned due to complications from homotrimeric form and interactions with actin	Kammerer et al., 2005
	p4	Antiparallel coiled-coil designed de novo; forms homotrimer (AAA-type)	No motility in screen	Burkhard et al., 2002
	EK Coil	Heterodimeric coiled-coil designed de novo (AB-type)	Very limited motility in screen	Litowski and Hodges, 2002

Figure 2.2. Characterization of potential coiled-coil linkers.

(A) A number of potential coiled-coil linkers were screened via single-molecule motility assays (see Fig. 2.4) to determine their suitability for assembling kin1 motors and SAH scaffolds. The heterotrimeric IA/IQ sequences were most efficient at recruiting kin1 motors to monomeric SAH scaffolds.

Virupakshi Soppina in the Verhey lab cloned most of the constructs conducted experiments in Figure 2.2.

---

homotrimeric (Burkhard et al., 2002), homodimeric (Litowski and Hodges, 2002), or heterotrimeric (IA/IQ, (Kiyokawa et al., 2004) form (Fig. 2.2). The use of a particular coiled-coil sequence is likely to be context-specific and in our geometry, the heterotrimeric IA/IQ coiled-coil sequence worked best (Fig. 2.3F, Fig. 2.4D) and the other sequences were not pursued further.

We also tested several protein-protein linkers that confer unique advantages to studying macromolecular assembly. We tested a split superfolder GFP (hereafter referred to as split GFP) molecule which provides a green fluorescent signal upon assembly and an essentially irreversible linkage (Pinaud and Dahan, 2011). We tested the split EF Hand domain from calbindin (Lindman et al., 2009) which assembles with a high affinity (K_D ~ 1 nM) that can be increased (K_D ~ 1 pM) in the presence of calcium (Lindman et al., 2009). In our system, the tight association of the split

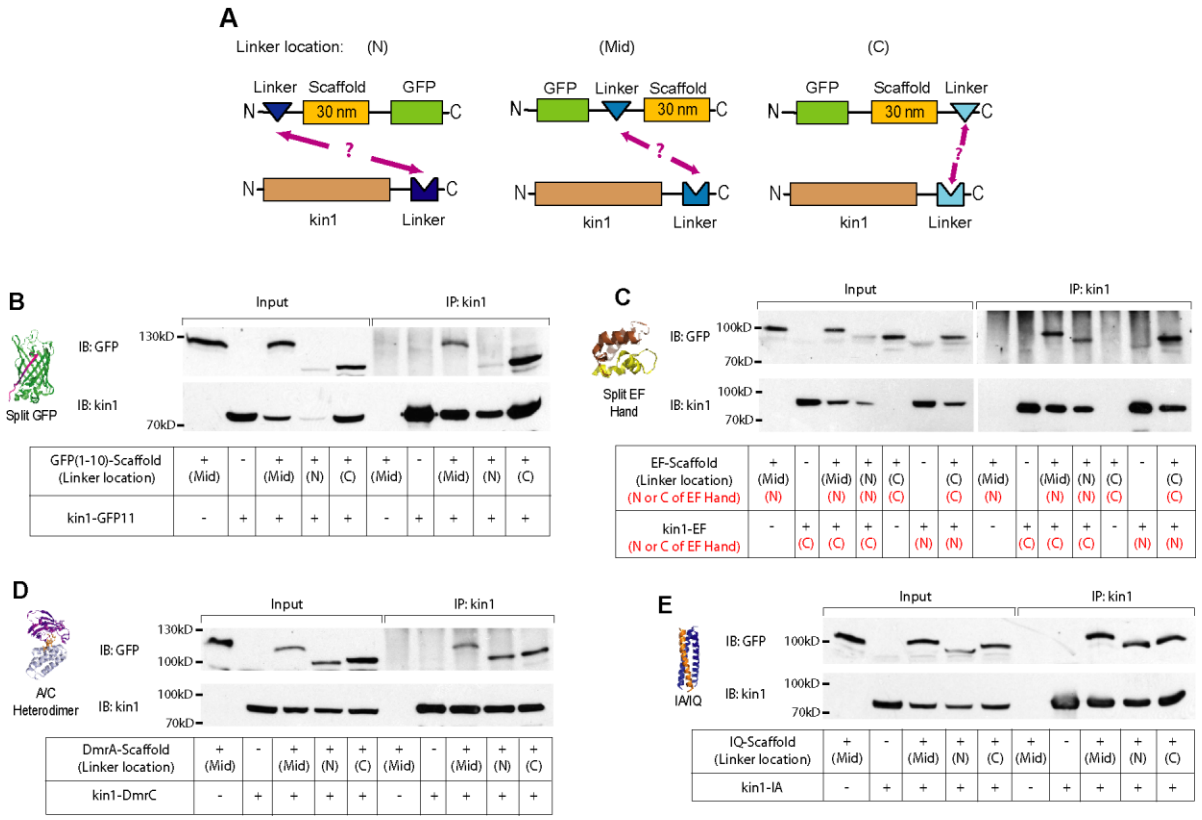

Figure 2.3. Characterization of linker components by co-immunoprecipitation.

(A) The ability of each linker to connect a non-fluorescent kin1 motor to a GFP-labeled SAH scaffold was tested for linkers positioned at the N terminus (N), middle (Mid) or C terminus (C) of the scaffold. **(B-E)** Co-immunoprecipitation assays. Motor-linker and linker-scaffold-GFP components were co-expressed in COS7 cells, immunoprecipitated (IP) from cell lysates with a monoclonal antibody to kin1 (IP:kin1 lanes), and the presence of scaffold was detected by immunoblotting (IB) for the GFP tag (IB:GFP). Input = 1/4 of lysate compared to IP lanes. +/- indicates presence of plasmid in transfection. The position of the linker with respect to the scaffold is indicated in black text as N-terminus (N), middle (Mid) or C-terminus (C). For the split GFP linker **(B)**, the first 10 strands of the barrel [GFP(1-10)] were attached to the scaffold and the last strand (GFP11) was attached to kin1. For the split EF Hand linker **(C)**, the red text indicates whether the N-terminal half (N) or C-terminal half (C) of the EF Hand domain was attached to the scaffold or motor components. The opposite configurations showed no assembly.

EF Hand enables interactions of proteins mixed *in vitro*. We also tested the drug-inducible dimerization of DmrA (FKBP) and DmrC (FRB domain) upon addition of A/C Heterodimerizer

(Rapalog-1, AP21967) that has been used to induce dimerization of proteins in cells (DeRose et al., 2013).

To characterize these linkers, we tested their ability to recruit a kinesin-1 motor to a scaffold using two assays, co-immunoprecipitation (Fig. 2.3) and single-molecule motility assays (Fig. 2.4). Each linker was tested at three different locations with respect to the scaffold: at the N-terminus (N), in the middle (Mid), and at the C-terminus (C) (Fig. 2.3A). For these experiments, we used the 30 nm SAH as a scaffold and a truncated, constitutively active version of the kinesin-1 motor, KIF5C(1-560), hereafter referred to as kin1, as the motor.

Co-immunoprecipitation and SDS-PAGE analysis enabled us to verify protein expression and solubility as well as the interaction between kin1 and the scaffold. By examining the input lanes containing whole cell lysates expressing the indicated constructs (Fig. 2.3B-E, left lanes), we observed that all motor-linker and scaffold-linker constructs expressed well, with the exception of the scaffold with the GFP(1-10) linker located at the N-terminus (Fig. 2.3B, lane 4, IB:GFP). Expression of this construct also led to decreased expression of the co-transfected kin1-GFP11 construct (Fig. 2.3B, lane 4, IB:kin1). We speculate that proteins containing an N-terminal fusion of the GFP(1-10) linker are highly unstable and lead to cell stress, and we thus avoided using this linker as an N-terminal fusion in subsequent assays.

To examine bulk biochemical interactions between the motor and scaffold, we immunoprecipitated the kin1 motor via an antibody to kinesin-1 and probed for a scaffold signal via an antibody to GFP (Fig. 2.3B-E, IP:kin1 lanes). We verified that each linker drives motor-scaffold interactions with every linker arrangement (N, Mid, C) with the exception of the split EF-hand linker, which is sensitive to orientation. When the N-terminal portion of the EF-Hand linker was placed at the C-terminus of the scaffold, we observed no interaction with the C-terminal

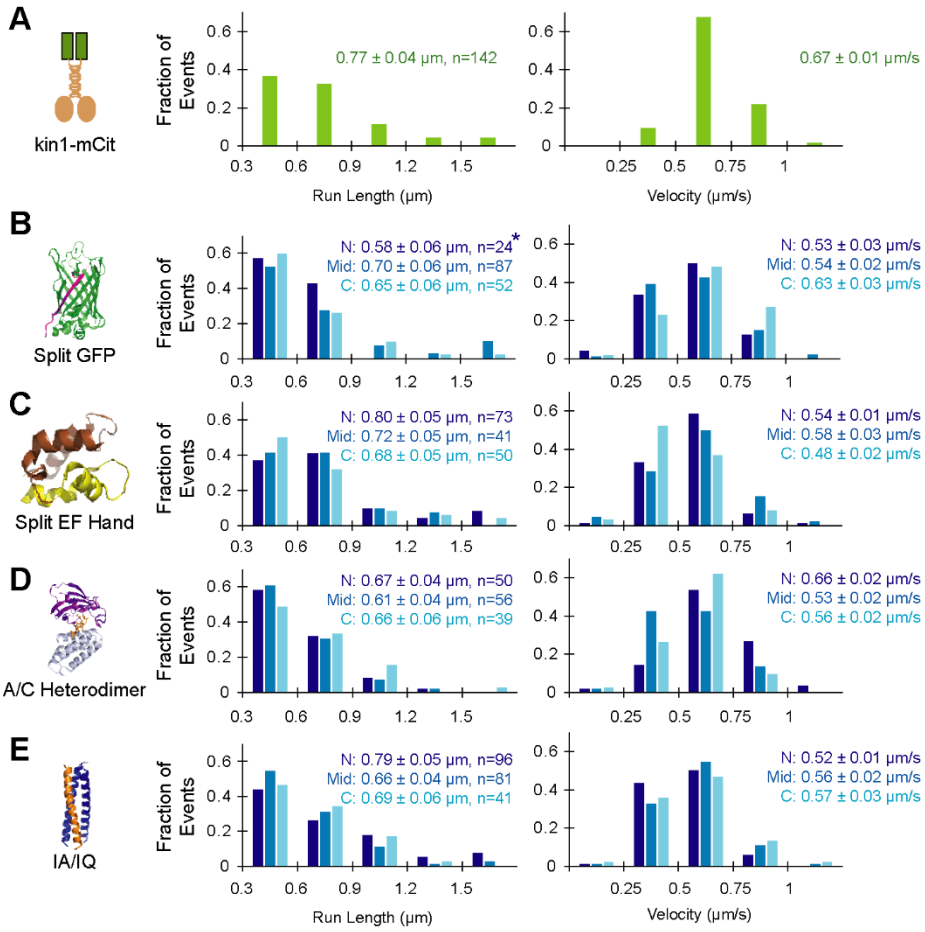

Figure 2.4. Characterization of linker components by single-molecule motility assays.

(A-E) Single molecule motility assays. The ability of each linker to connect a non-fluorescent kin1 motor to a GFP-labeled SAH scaffold was tested for linkers positioned at the N terminus (N), middle (Mid) or C terminus (C) of the scaffold (see Fig. 2.3A). Motor-linker and linker-scaffold-GFP components were co-expressed in COS7 cells and motility was analyzed in cell lysates. The run lengths (left panels) and velocities (right panels) of each population were plotted as histograms and the average ± S.E is indicated. **(A)** The motility of mCitrine (mCit)-labeled kin1 motors (n = 142 events) was recorded as a positive control. **(C)** For the split GFP linker, strands 1-10 of the GFP barrel [GFP(1-10)] were placed at N, Mid, and C locations (n = 24, 87, and 52 events, respectively) and strand 11 (GFP11) was fused to the C-terminus of kin1. * indicates poor expression of scaffold in COS7 cells, see Fig. 2.3B. **(D)** For the split EF Hand linker, the N-terminal half of the EF Hand was placed at the N (n = 73) or Mid (n = 41) locations and the C-terminal half of the EF Hand was placed at the C (n = 50) location. No self-assembly was observed for the N-terminal half of the EF Hand at the C location or for the C-terminal half of the EF Hand at the N location (data not shown). **(E)** For the A/C Heterodimer, DmrA (FKBP) was placed at the N, Mid, and C locations (n = 50, 56, and 39 events, respectively) whereas DmrC (FRB) was fused to kin1. **(F)** For the IA/IQ heterotrimeric coiled coil, the IQ sequence was placed at the N, Mid or C locations (n = 96, 81, and 41 events, respectively) and the IA sequence was fused to kin1.

Experiments in Figure 2.4 were conducted with Aslan Dizaji in the Verhey lab.

portion of the EF-Hand linker on the motor (data not shown). When we swapped the EF-Hand domains in this interaction, we were able to rescue interaction between the motor and scaffold (Fig. 2.3C, final lane, IP:kin1).

For single-molecule motility assays (Fig. 2.4), we placed a fluorescent protein (FP) on the scaffold component such that motility could only be observed when a non-fluorescent kin1 motor was linked to the fluorescent scaffold (see Fig. 2.3A for schematic). Motility was observed for motor-scaffold complexes formed by every linker arrangement (Fig. 2.4B-E) except when the N-terminal half of the split EF-hand linker was fused to the C-terminus of the scaffold, consistent with the co-IP data discussed above (data not shown). Quantification of the motility events demonstrated that each motor-linker-scaffold complex displayed run length and velocity distributions similar to those of kin1-FP alone (Fig. 2.4A). These results demonstrate that our scaffold and linker components have the potential to generate defined multi-protein complexes for analysis in cell lysates, and that the presence of linkers and scaffolds do not interfere with the enzymatic activity of the motor.

2.3.2 Verifying multiple protein assembly in live cells

We next verified that the linkers could be used for simultaneous recruitment of two proteins to the same scaffold in cells. To do this, we used Förster resonance energy transfer (FRET, see Appendix) to measure the relative proximity of two scaffold-associated proteins. To determine the detection limits of the mCherry-split GFP (split superfolder "sfGFP") FRET experiments, we

first analyzed a linked mCherry-sfGFP construct as a positive control (mCherry-12aa-sfGFP) to define maximal FRET efficiency (Fig. 2.5B, top row). As a negative control, mCherry and sfGFP were transfected separately to define minimal FRET efficiency (Fig. 2.5B, second row). To test our linker and scaffold constructs, a superfolder GFP FRET donor was attached to one end of the scaffold via the split GFP linker and a mCherry FRET acceptor was recruited to the other end of scaffold via the DmrA/DmrC linker system (Fig. 2.5A). In the absence of A/C heterodimerizer, little to no FRET was observed between scaffold-associated GFP and cytosolic mCherry (Fig. 2.5B,C). Addition of the A/C heterodimerizer caused recruitment of mCherry to the scaffold-GFP complex and a FRET signal that varied with separation distance. The highest FRET efficiencies were obtained for GFP and mCherry separated by a short peptide sequence (GSG), moderate FRET was observed for a 5 nm scaffold, and no FRET was observed for a 10 nm scaffold (Fig. 2.5B,C). To ensure that a one-hour A/C heterodimerizer treatment was sufficient for recruitment of mCherry to the scaffold, we next performed a timecourse experiment using the short peptide separation (GSG). Addition of A/C heterodimerizer resulted in maximal FRET efficiencies after ~45 minutes, whereas addition of ethanol resulted in no change in FRET efficiency (Fig. 2.6). Together, the results from these FRET experiments indicate that assembly of multi-protein complexes can be regulated both spatially (Fig. 2.5) and temporally (Fig. 2.6) in live COS7 cells.

We next wanted to test whether we could assemble these protein complexes at defined locations inside the cell. For example, controlled assembly at the plasma membrane could allow for studies of the endomembrane system including cellular import studies. To achieve this, we enriched the mCherry-DmrC component via a myrsitoylation-palmitoylation signal which anchors the N-terminus of this protein at the plasma membrane (Fig. 2.7A). Additionally, controlled

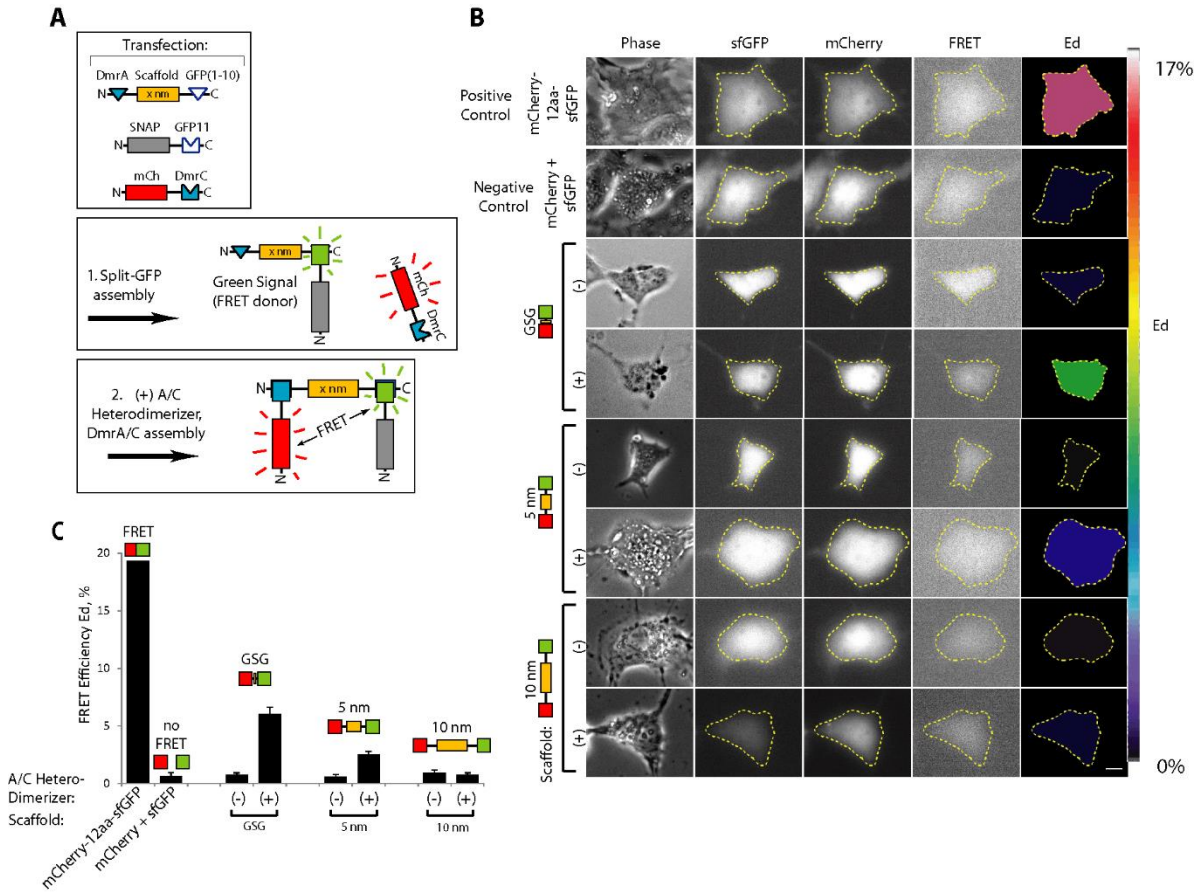

Figure 2.5. Assembly of two proteins on a scaffold in live cells.

(A) Schematic of multi-protein assembly. Plasmids encoding the indicated components were expressed in COS7 cells (Transfection). Self-assembly of the split GFP linker (step 1) recruits the SNAP-GFP11 component to the DmrA-scaffold-GFP(1-10), resulting in green fluorescence. Addition of A/C heterodimerizer (step 2) recruits the mCherry-DmrC component, resulting in FRET. **(B,C)** FRET donor (split GFP) and FRET acceptor (mCherry) components were recruited to scaffolds of 0 nm (GSG peptide), 5 nm SAH, or 10 nm SAH by addition of A/C heterodimerizer for 1 hr and FRET was determined in live cells. **(B)** Representative raw phase and fluorescence images and calculated FRET efficiency (Ed) images. Yellow dotted line indicates the outline of each cell. Scale bar = 10 µm. For a positive FRET control, a linked mCherry-sfGFP construct was used (mCherry-12aa-sfGFP). For a negative FRET control, mCherry and sfGFP were coexpressed. All other panels indicate mCherry and split GFP separated by the indicated scaffold (GSG peptide, 5 nm SAH, or 10 nm SAH). Scale bar = 10 µm. **(C)** Calculated FRET efficiencies (Ed). N ≥ 31 cells in three independent experiments for each condition. ***$p < 0.0001$; n.s., not significant as compared to the (-) A/C Heterodimerizer condition. Data are presented as the average ± S.E.M.

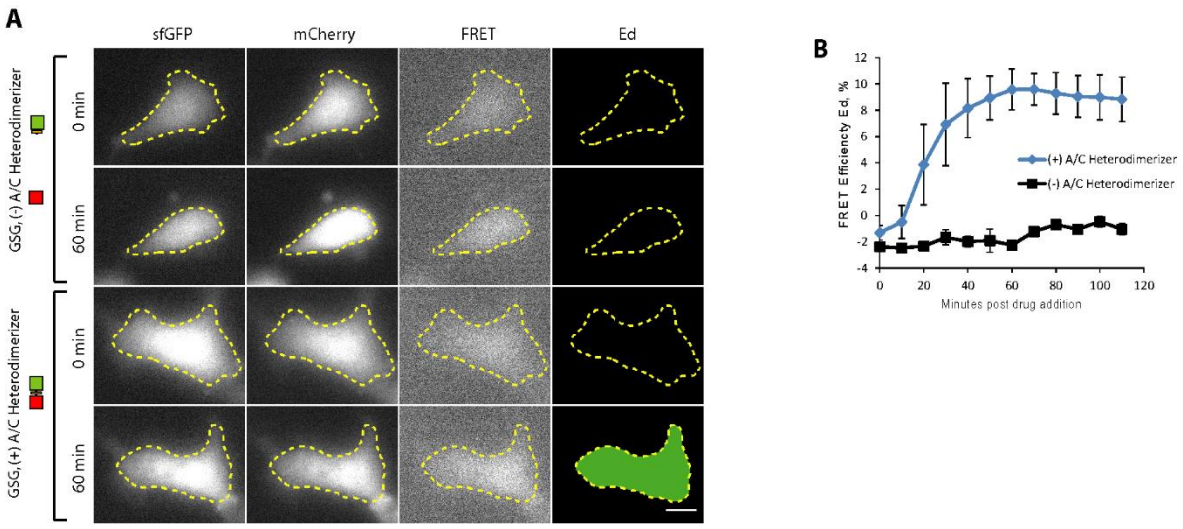

Figure 2.6. Time course of FRET upon addition of A/C heterodimerizer.

(A) Representative raw fluorescence images and calculated FRET efficiency (Ed) images for mCherry and split GFP FRET pairs separated by a GSG peptide at 0 or 60 min after the addition of ethanol or A/C heterodimerizer. Scale bar = 10 µm**. (B)** Quantification of FRET efficiency over time. Images were acquired every 10 min and Ed was calculated from n= 2 (ethanol) or 3 (heterodimerizer) cells. Data are presented as average ± SD.

assembly at defined cellular organelles would allow studies of specific cellular processes in great detail. To verify the possibility of such assembly, we enriched the mCherry-DmrC component at the lysosomal surface via fusion to the lysosomal membrane protein Lamp1 (Fig. 2.8A). For both cases, in the absence of A/C heterodimerizer, DmrA-scaffold-split GFP complexes remained cytosolic (Fig. 2.7B, Fig. 2.8B, lower panels) but addition of A/C heterodimerizer resulted in recruitment to the plasma membrane (Fig. 2.7B, upper panels) or lysosome (Fig. 2.8B, upper panels). These subcellular recruitment results indicate that our scaffold and linker components can be used to generate defined multi-protein complexes in a location-specific manner inside cells. Together with the FRET results, we have now shown that we can assemble complexes of proteins in COS7 cells that are regulated by a) separation distance b) time and c) location in the cell.

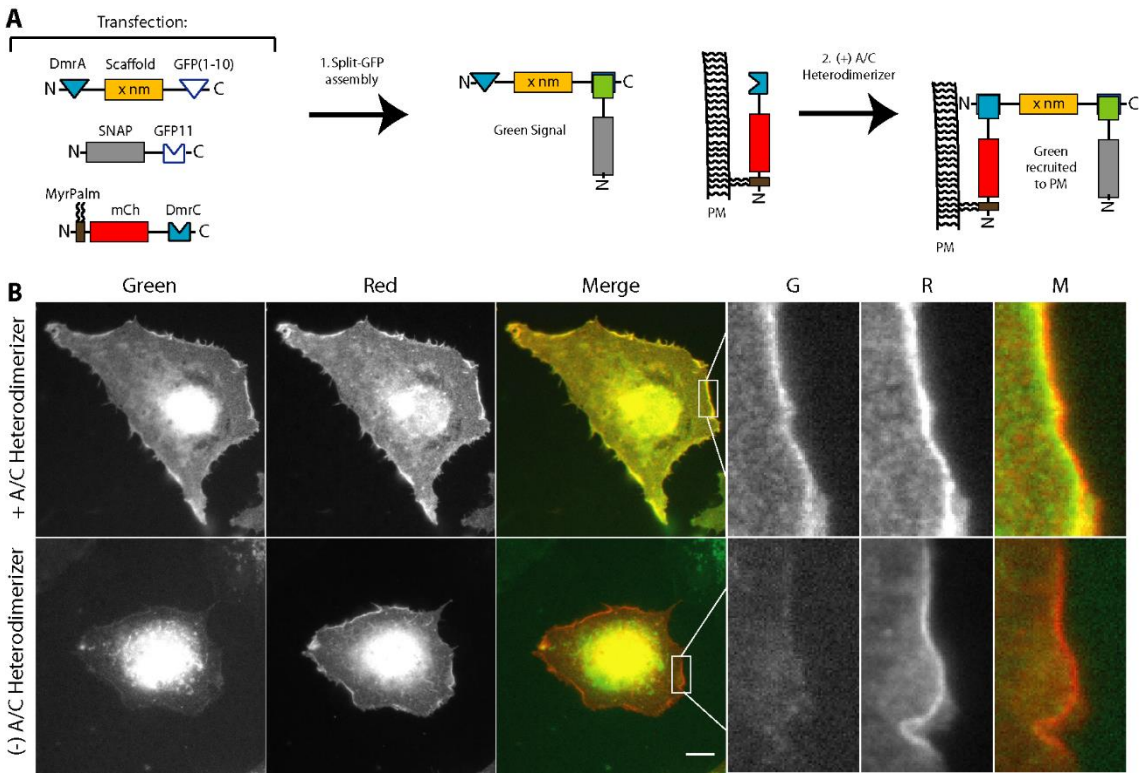

Figure 2.7. Assembly of multi-protein complexes at the plasma membrane.

(A,B) Step-wise assembly of a multi-protein complex at the plasma membrane in live cells. **(A)** Schematic of experimental setup. COS7 cells were transfected with plasmids for expression of the indicated components. The split GFP self-assembles (step 1) and is recruited to the MyrPalm-mCherry component on the plasma membrane by addition of A/C heterodimerizer (step 2). **(B)** Representative images of cells incubated in the absence or presence of A/C heterodimerizer for 1 hr. The three panels on the far right display magnified views of the white boxed region in the Merge channel. Scale bar = 10 µm.

Experiments in Figure 2.7 were performed by Kristin Schimert in the Verhey lab.

2.3.4 Attaching toolbox protein components to beads via biotin linkage

Although most of the work presented in this dissertation focuses on single-molecule approaches, we wanted to create a system that would be easily adaptable to *in vitro* applications that are commonly used in the field. Specifically, the attachment of these protein complexes to

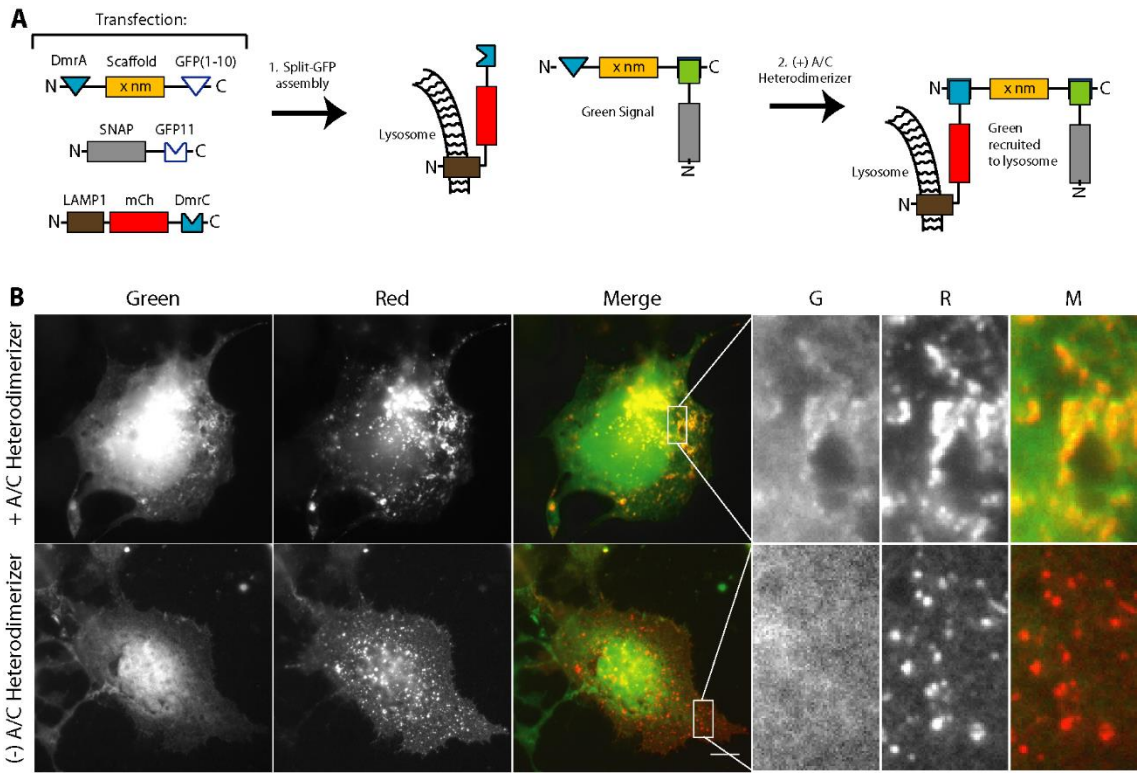

Figure 2.8. Assembly of multi-protein complexes at lysosomes.

(A,B) Step-wise assembly of a multi-protein complex on the lysosome in live cells. **(A)** Schematic of experimental setup. COS7 cells were transfected with plasmids for expression of the indicated components. The split GFP self-assembles (step 1) and is recruited to the LAMP1-mCherry component on the lysosome by addition of A/C heterodimerizer (step 2). **(B)** Images of cells incubated in the absence or presence of A/C heterodimerizer for 1 hr. The three panels on the far right display magnified views of the white boxed region in the Merge channel. Scale bar = 10 μm.

Experiments in Figure 2.7 were performed by Kristin Schimert in the Verhey lab.

---

relatively large (~1-2 μm) polystyrene or latex beads would allow both optical trapping studies (Svoboda and Block, 1994) and experiments in a defined viscoelastic environment (Gagliano, 2010). These experiments would allow the force response to be studied in great detail (Fig. 2.9A,B), in contrast to the multiple motor assays performed in Chapter 4 that take place in the absence of any external load. We thus set out to attach our motor complexes to beads in a way

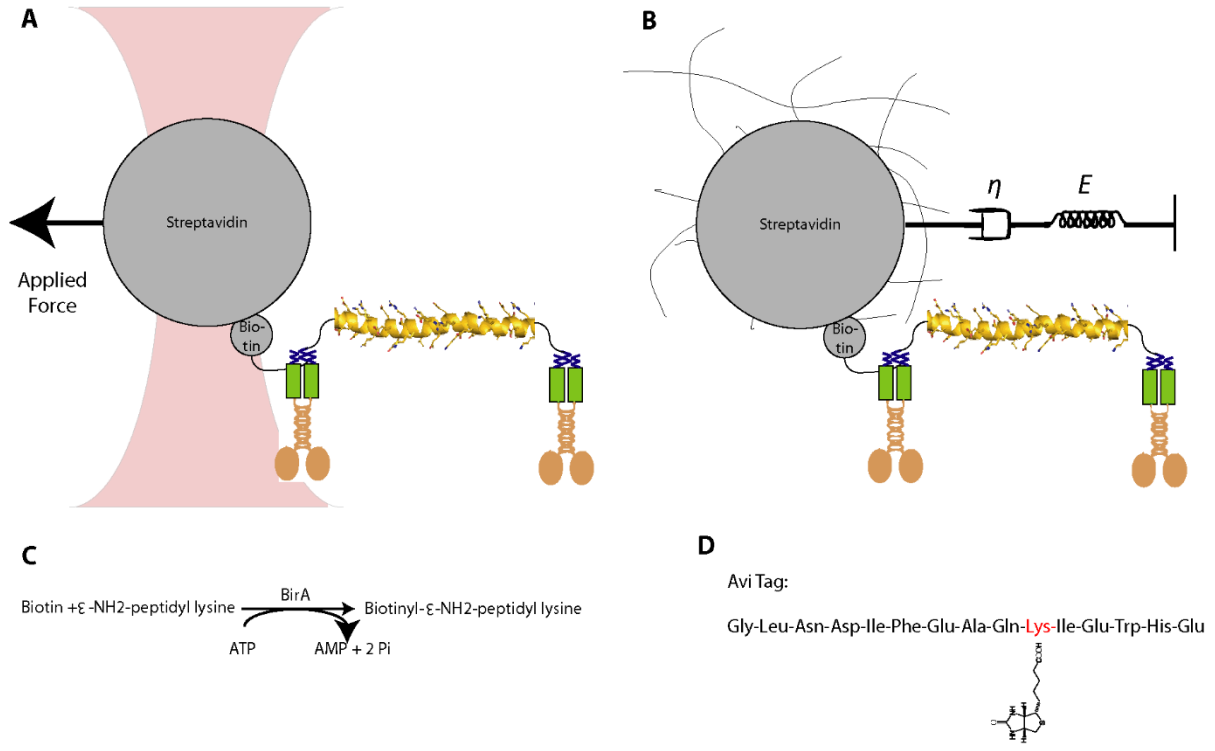

Figure 2.9. Biotin-streptavidin linkages for force-based experiments.

(A,B) To study the effect of force on multiple motor complexes, a force can be applied externally via an optical trap if the complex is conjugated to a large (1-2 μm) bead **(A)**. Alternatively, the velocity of beads moving through a viscoelastic environment is expected to depend on the number of engaged motors **(B)**. **(C)** A bacterial biotin ligase conjugates a small biotin molecule to the lysine residue of a 15-aa AviTag **(D)** in an ATP-dependent manner.

---

that did not require purification of protein components. To achieve this, we used a high-affinity biotin-streptavidin interaction (Broyer et al., 2011) for protein-bead conjugation.

To biotinylate proteins in cells, we used the 15 amino acid AviTag (Tirat et al., 2006), which was developed by the company Avidity (Fig 2.9C-D). This tag mimics the minimal biotin acceptor domain recognized by the enzyme biotin ligase, which attaches biotin to a carrier domain of cellular carboxylases and decarboxylases. When a fusion protein containing the AviTag is expressed alongside the bacterial biotin ligase BirA, the BirA enzyme attaches endogenous biotin

to a lysine residue on the tag via a peptidyl bond (Fig. 2.9C-D). This method thus allows specific conjugation of these biotinylated proteins to streptavidin- or neutravidin-coated beads *in vitro*, even when other proteins are present such as in a cell lysate.

To test the efficiency of this tag, we first tested whether we could directly biotinylate kin1 motors in COS7 cells by co-expressing kin1-AviTag with BirA (Fig. 2.10A. Upon co-expression, a biotin signal was detected via western blot at the appropriate molecular weight of the motor whereas no signal was detected in the absence of BirA or kin1-Avi (Fig. 2.10B., left lanes). To simplify transfections in future experiments, we used a retroviral method to generate a COS7 cell line stably expressing HA-BirA (Fig. 2.10B, right lanes, Fig. 2.10C). This cell line showed sufficient biotinylation of kin1-Avi upon motor expression only (Fig. 2.10B, lane 6), suggesting that expression of Avi-Tagged proteins in this stable HA-BirA cell line is sufficient for biotinylation.

Next, we wanted to study whether biotinylated motors from these cell lysates could be functionally conjugated to avidin-, streptavidin-, or neutravidin-coated beads. Of these, neutravidin is preferable because it contains the highest specificity for biotin and has a near-neutral isoelectric point (Marttila et al., 2000). We tested the efficiency of neutravidin-functionalized 1-μm fluorescent beads by introducing them to flow chambers coated with BSA-biotin. We found many more beads stuck to the BSA-biotin surface than a BSA surface (Fig. 2.10D.), suggesting that the beads were coated with binding-competent neutravidin. To test whether we could functionally attach biotin-labeled motors to these beads, we incubated these neutravidin beads with cell lysates from the HA-BirA stable line overexpressing kin1-Avi. These beads showed frequent and processive motility along microtubules (Fig. 2.10E), suggesting that this method is valid for functionally conjugating motors from cell lysates onto large beads for *in vitro* motility or optical

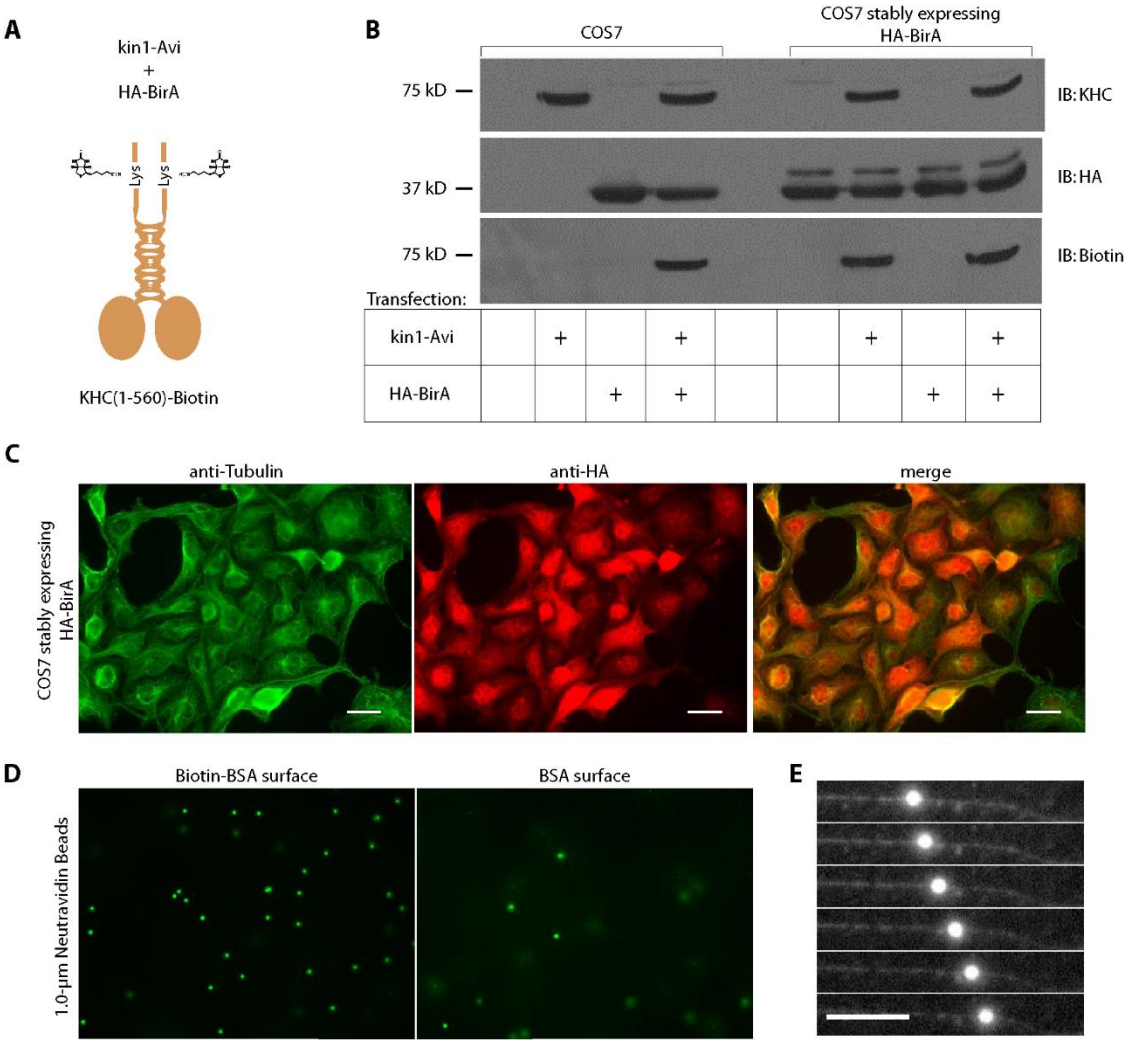

Figure 2.10. Verifying biotinylation of Avi-tagged motor.

(A) To verify the AviTag in our system, we transfected kin1 fused to the AviTag (kin1-Avi) alongside an HA-tagged bacterial biotin ligase (HA-BirA). **(B)** Verifying biotinylation by SDS-PAGE and western blot. The indicated constructs (denoted by +, bottom) were transfected in COS7 cells. Proteins in cell lysates run on SDS-PAGE and detected by immunoblotting (IB) with an antibody to kin1 (IB: KHC), an antibody to HA (IB: HA), or Avidin-HRP, which detects biotin (IB: Biotin). **(C)** COS7 cells stably expressing HA-BirA verified by immunostaining with an antibody to tubulin (left) or HA (middle), where HA was detected in nearly all cells (merge, right). **(D)** Neutravidin-coated beads were verified by imaging the beads immobilized on a Biotin-BSA coated surface (left) compared to a BSA-coated surface (right). **(E)** The motility of biotinylated kin1 conjugated to neutravidin beads was verified in motility assays and displayed as a kymograph (Scale bar, 5 µm, images separated by 2 s).

trapping assays. We were also able to use the same technique to attach biotinylated motors to streptavidin-labeled quantum dots for motility assays (data not shown).

To test if other protein components could be biotinylated with this technique, we fused the AviTag to the N-terminus of one of our scaffold constructs (AviTag-3xmCitrine-IQ-30 nm SAH–IQ, hereafter referred to as Avi-Scaffold). When this protein was expressed in HA-BirA-expressing COS7 cells, we observed no biotinylation whereas the kin1-Avi construct showed a strong biotin signal via western blot (Fig. 2.11A). As an alternative method, we replaced the AviTag with a related 23-aa tag (de Boer et al., 2003). This construct (db-Scaffold) also showed no biotinylation when co-expressed with HA-BirA (Fig. 2.11B, lane 3). Finally, we fused the AviTag to the C-terminus of our scaffold construct rather than the N-terminus (3xmCitrine-IQ-30 nm SAH-IQ-AviTag, "Scaffold-Avi"). This construct showed extremely strong biotinylation when co-expressed with HA-BirA, suggesting that the AviTag needs to be placed at the C-terminus in order for the biotin ligase enzyme to properly access the exposed lysine residue (Fig 2.11B, lane 4).

Based on these experiments, we conclude that 1) we can use the AviTag method to efficiently biotinylate our constructs, 2) this tag must be placed at the C-terminus for effective biotin labeling, and 3) cell lysates containing these constructs can be used to conjugate biotinylated proteins to neutravidin-labeled beads for functional *in vitro* assays.

2.3.5 Using two split-GFP linkers to create multi-motor assemblies

As a first attempt at assembling two-motor complexes, we transfected a green kin1 fused to the GFP11 portion of the split GFP linker along with a 30-nm scaffold containing two GFP(1-

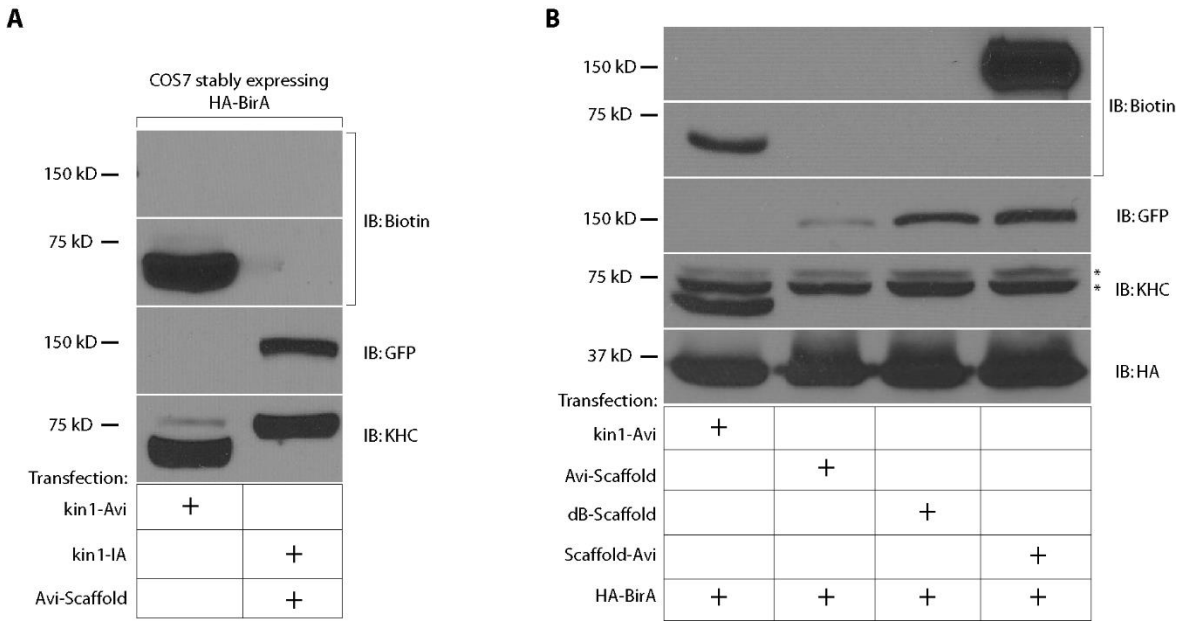

Figure 2.11. AviTag can only be biotinylated at the C-terminus.

(A) Testing for scaffold biotinylation by SDS-PAGE and western blot when AviTag is located at the N-terminus. The indicated constructs (denoted by +, bottom) were transfected in COS7 cells. Proteins in cell lysates run on SDS-PAGE and detected by immunoblotting (IB) with an antibody to kin1 (IB: KHC), an antibody to GFP, which detects mCit-labeled scaffold (IB: GFP), or Avidin-HRP, which detects biotin (IB: Biotin). **(B)** Testing for scaffold biotinylation under different conditions. The indicated constructs (denoted by +, bottom) were transfected in COS7 cells. Proteins in cell lysates run on SDS-PAGE and detected by immunoblotting (IB) with an antibody to kin1 (IB: KHC), an antibody to GFP, which detects mCit-labeled scaffold (IB: GFP), an andtibody to HA (IB: HA) or Avidin-HRP, which detects biotin (IB: Biotin). * denotes non-specific bands on western blot.

10) portions of the split GFP linker. When these constructs were coexpressed, we thus expected the two kin1 motors to assemble on the scaffold separated by 30 nm (Fig. 2.12A). When we performed single-molecule motility assays on cell lysates containing these constructs, we observed that the two-motor constructs displayed significantly longer run lengths (1.3 ± 0.3 μm) than single motors (0.6 ± 0.1 μm) (Fig. 2.12B-C).

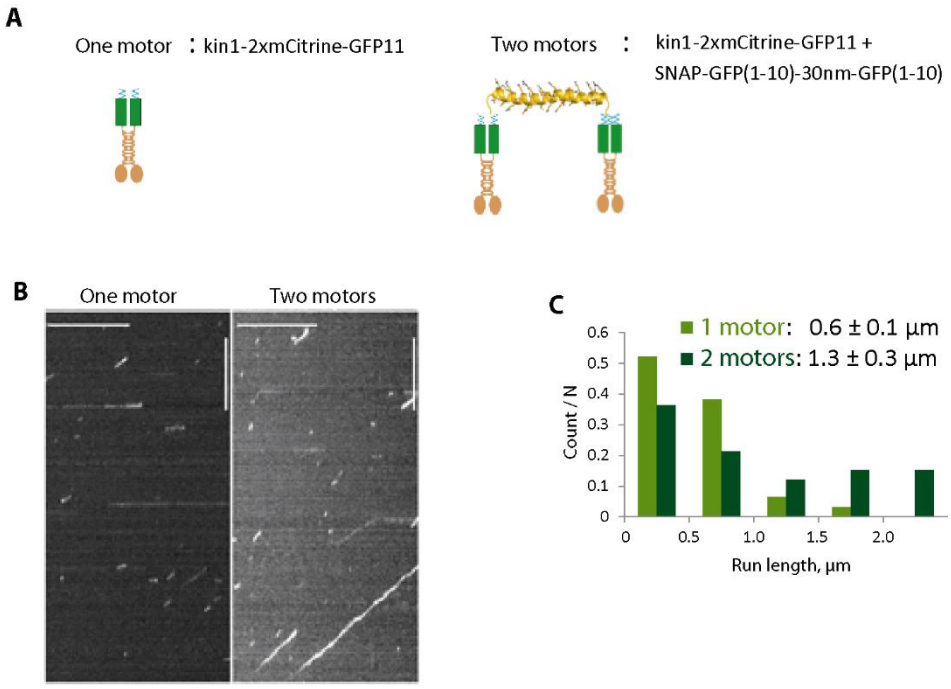

Figure 2.12. Investigating two-motor motility using two split GFP linkers for assembly.

(A) Schematic of experimental setup. COS7 cells were transfected with plasmids for assembly of two kin1-2xmCitrine motors on a 30 nm scaffold in cells. Two copies of the split GFP linker were used for assembly. **(B)** Representative kymographs. Time is on the x-axis (scale bar, 5 sec) and distance is on the y-axis (scale bar, 5 µm). **(C)** The run lengths were determined for all observed events in the single motor condition and the two-motor condition. The population data is plotted in histograms. The average ± S.E.M. is indicated on the graph.

Although this preliminary result was promising, a number of factors made these experiments difficult to interpret. First, and most importantly, the precise number of motors present in an observed motility event is extremely difficult to ascertain with this experimental setup, and thus many of the supposed "two-motor" events likely only contain one motor. Because both motors are labeled with the same fluorophore, we expect that two-motor events should have a higher intensity than single motors, and that these brighter events might display higher run lengths due to the presence of additional motors. To test this, we created a scatter plot of run length vs. the initial fluorescence intensity for all observed events (Fig. 2.13B-C). As expected,

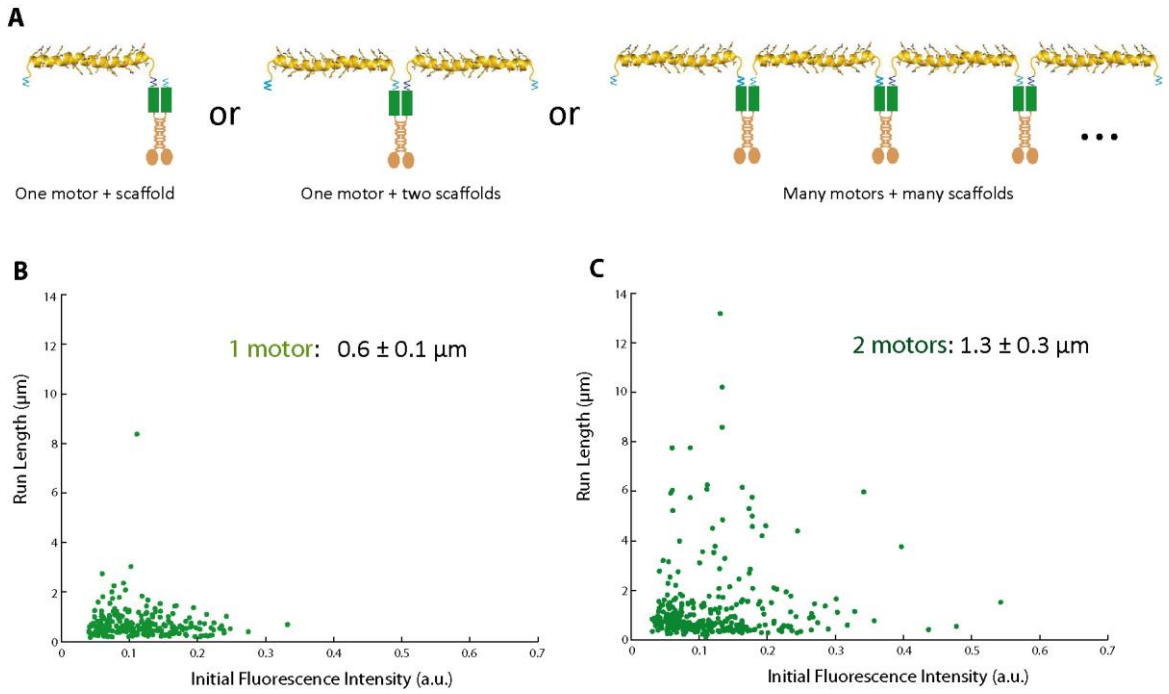

Figure 2.13. Possible multimer formation using two split GFP linkers.

(A) Schematic of potential multimer formation. COS7 cells were transfected with plasmids for assembly of two kin1-2xmCitrine motors on a 30 nm scaffold in cells. Two copies of the split GFP linker were used for assembly. **(B)** Run length vs. intensity scatter plots for single motors (kin1-2xmCitrine alone). x-axis represents the fluorescence intensity of a particle in its first frame of detection. The average run length ± S.E.M. is indicated on the graph. **(C)** Run length vs. intensity scatter plots for two kin1-2xmCitrine motors attached by a 30 nm scaffold. x-axis represents the fluorescence intensity of a particle in its first frame of detection. This distribution also likely includes a high proportion of single motors due to incomplete scaffold assembly. The average run length ± S.E.M. is indicated on the graph.

---

we did see a greater number of bright events for two-motor constructs, but we also observed a large number of events that appeared identical in intensity to single-motor events, which greatly complicated data interpretation. Second, the heterodimeric split-GFP linkage likely leads to the formation of chains containing multiple motors. Because each motor is a dimer containing two free GFP11 linker domains, it is possible for a single motor to link to two separate scaffolds and theoretically continue indefinitely (Fig. 2.13A). Importantly, these chains were not observed in

later experiments where two different linkers were used to attach motors to the scaffold (Chapter 4). We speculate that the relative irreversibility of the split-GFP linker could drive chain formation over time and thus artificially increase the run length of supposed "two-motor" constructs. Third, we later show (Chapter 3) that GFP molecules are susceptible to oligomerization in single-molecule assays. We speculate that using multiple copies of this split-GFP linker may also lead to this oligomerization and thus artificially increase run lengths. Overall, while this experiment provided valuable preliminary data and suggested that our approach was feasible, this type of experiment was eventually abandoned for two-color experiments that were far easier to interpret (Chapter 4).

2.4 Discussion

In this chapter, I describe a new method for assembling multi-protein complexes of defined composition and geometry in mammalian cells that is broadly applicable to studying cellular signaling, motility and organization. A major advantage to our protein-based assembly method is the ability to study molecular behavior within the cellular environment. As cell biologists continue to study the biochemical and biomechanical properties of single molecules, it is becoming increasingly important to understand how groups of these molecules work together to accomplish diverse tasks inside the cell. The technique outlined in this chapter provides one possible approach to investigate this emerging problem. This chapter also highlights an important message in protein synthetic biology: often, an empirical, experimental approach is more advantageous than a predictive, theoretical approach in studies such as this (see Chapter 5). In other words, in order to construct a protein with a desired function, multiple genes with various orientations and linkers must be tested, although all of these permutations should work in theory.

At this point in the development of this system, we have a) convincingly shown that multi-protein complexes can be assembled in cells and b) tentatively shown that multi-kinesin assemblies lead to enhanced run lengths *in vitro*. Unfortunately, these latter experiments were difficult to interpret due to the reasons outlined in the previous section. We thus set out to develop a two-color TIRF microscopy approach, where each motor in the two-motor assembly was labeled with a different fluorophore. Such an approach would convincingly show that two-motor assemblies are present and would allow for the direct comparison of two-motor assemblies to single motors. While testing fluorophores for this proposed experiment, we noticed that certain subset of fluorophores led to aberrantly long run lengths in single-molecule motility assays. This observation led us to characterize a number of fluorescent proteins in single-molecule motility assays, where we found that this subset of fluorophores was prone to oligomerization when fused to dimeric kinesin-1 motors. After determining the ideal fluorophores for a two-color TIRF study in Chapter 3, we return in Chapter 4 to a detailed study of two-kinesin assemblies using these approaches.

2.5 References

Baboolal, T.G., Sakamoto, T., Forgacs, E., White, H.D., Jackson, S.M., Takagi, Y., Farrow, R.E., Molloy, J.E., Knight, P.J., Sellers, J.R., *et al.* (2009). The SAH domain extends the functional length of the myosin lever. Proceedings of the National Academy of Sciences of the United States of America *106*, 22193-22198. doi: 10.1073/pnas.0909851106

Barlan, K., Rossow, M.J., and Gelfand, V.I. (2013). The journey of the organelle: teamwork and regulation in intracellular transport. Current opinion in cell biology *25*, 483-488. doi: 10.1016/j.ceb.2013.02.018

Broyer, R.M., Grover, G.N., and Maynard, H.D. (2011). Emerging synthetic approaches for protein-polymer conjugations. Chemical communications *47*, 2212-2226. doi: 10.1039/c0cc04062b

Burkhard, P., Ivaninskii, S., and Lustig, A. (2002). Improving coiled-coil stability by optimizing ionic interactions. Journal of molecular biology *318*, 901-910. doi: 10.1016/S0022-2836(02)00114-6

Cai, D., McEwen, D.P., Martens, J.R., Meyhofer, E., and Verhey, K.J. (2009). Single molecule imaging reveals differences in microtubule track selection between Kinesin motors. PLoS biology *7*, e1000216. doi: 10.1371/journal.pbio.1000216

Cai, D., Verhey, K.J., and Meyhofer, E. (2007). Tracking single Kinesin molecules in the cytoplasm of mammalian cells. Biophysical journal *92*, 4137-4144. doi: 10.1529/biophysj.106.100206

de Boer, E., Rodriguez, P., Bonte, E., Krijgsveld, J., Katsantoni, E., Heck, A., Grosveld, F., and Strouboulis, J. (2003). Efficient biotinylation and single-step purification of tagged transcription factors in mammalian cells and transgenic mice. Proceedings of the National Academy of Sciences of the United States of America *100*, 7480-7485. doi: 10.1073/pnas.1332608100

DeRose, R., Miyamoto, T., and Inoue, T. (2013). Manipulating signaling at will: chemically-inducible dimerization (CID) techniques resolve problems in cell biology. Pflugers Archiv : European journal of physiology *465*, 409-417. doi: 10.1007/s00424-012-1208-6

Derr, N.D., Goodman, B.S., Jungmann, R., Leschziner, A.E., Shih, W.M., and Reck-Peterson, S.L. (2012). Tug-of-war in motor protein ensembles revealed with a programmable DNA origami scaffold. Science *338*, 662-665. doi: 10.1126/science.1226734

Efremov, A.K., Radhakrishnan, A., Tsao, D.S., Bookwalter, C.S., Trybus, K.M., and Diehl, M.R. (2014). Delineating cooperative responses of processive motors in living cells. Proceedings of the National Academy of Sciences of the United States of America *111*, E334-343. doi: 10.1073/pnas.1313569111

Furuta, K., Furuta, A., Toyoshima, Y.Y., Amino, M., Oiwa, K., and Kojima, H. (2013). Measuring collective transport by defined numbers of processive and nonprocessive kinesin motors. Proceedings of the National Academy of Sciences of the United States of America *110*, 501-506. doi: 10.1073/pnas.1201390110

Gagliano, J., Walb, M., Blaker, B., Macosko, J.C., and Holzwarth, G. (2010). Kinesin velocity increases with the number of motors pulling against viscoelastic drag. European Biophysics Journal *39*

Hill, D.B., Plaza, M.J., Bonin, K., and Holzwarth, G. (2004). Fast vesicle transport in PC12 neurites: velocities and forces. European biophysics journal : EBJ *33*, 623-632. doi: 10.1007/s00249-004-0403-6

Holton, J., and Alber, T. (2004). Automated protein crystal structure determination using ELVES. Proceedings of the National Academy of Sciences of the United States of America *101*, 1537-1542. doi: 10.1073/pnas.0306241101

Hoppe, A., Christensen, K., and Swanson, J.A. (2002). Fluorescence resonance energy transfer-based stoichiometry in living cells. Biophysical journal *83*, 3652-3664. doi: 10.1016/S0006-3495(02)75365-4

Julius, M.A., Yan, Q., Zheng, Z., and Kitajewski, J. (2000). Q vectors, bicistronic retroviral vectors for gene transfer. BioTechniques *28*, 702-708

Kammerer, R.A., Kostrewa, D., Progias, P., Honnappa, S., Avila, D., Lustig, A., Winkler, F.K., Pieters, J., and Steinmetz, M.O. (2005). A conserved trimerization motif controls the topology of short coiled coils. Proceedings of the National Academy of Sciences of the United States of America *102*, 13891-13896. doi: 10.1073/pnas.0502390102

Khmelinskii, A., Keller, P.J., Bartosik, A., Meurer, M., Barry, J.D., Mardin, B.R., Kaufmann, A., Trautmann, S., Wachsmuth, M., Pereira, G., *et al.* (2012). Tandem fluorescent protein timers for in vivo analysis of protein dynamics. Nature biotechnology *30*, 708-714. doi: 10.1038/nbt.2281

Kiyokawa, T., Kanaori, K., Tajima, K., Kawaguchi, M., Mizuno, T., Oku, J., and Tanaka, T. (2004). Selective formation of AAB- and ABC-type heterotrimeric alpha-helical coiled coils. Chemistry *10*, 3548-3554. doi: 10.1002/chem.200305729

Knight, P.J., Thirumurugan, K., Xu, Y., Wang, F., Kalverda, A.P., Stafford, W.F., 3rd, Sellers, J.R., and Peckham, M. (2005). The predicted coiled-coil domain of myosin 10 forms a novel elongated domain that lengthens the head. The Journal of biological chemistry *280*, 34702-34708. doi: 10.1074/jbc.M504887200

Kural, C., Kim, H., Syed, S., Goshima, G., Gelfand, V.I., and Selvin, P.R. (2005). Kinesin and dynein move a peroxisome in vivo: a tug-of-war or coordinated movement? Science *308*, 1469-1472. doi: 10.1126/science.1108408

Levi, V., Serpinskaya, A.S., Gratton, E., and Gelfand, V. (2006). Organelle transport along microtubules in Xenopus melanophores: evidence for cooperation between multiple motors. Biophysical journal *90*, 318-327. doi: 10.1529/biophysj.105.067843

Lindman, S., Johansson, I., Thulin, E., and Linse, S. (2009). Green fluorescence induced by EF-hand assembly in a split GFP system. Protein science : a publication of the Protein Society *18*, 1221-1229. doi: 10.1002/pro.131

Litowski, J.R., and Hodges, R.S. (2002). Designing heterodimeric two-stranded alpha-helical coiled-coils. Effects of hydrophobicity and alpha-helical propensity on protein folding, stability, and specificity. The Journal of biological chemistry *277*, 37272-37279. doi: 10.1074/jbc.M204257200

Mallik, R., Petrov, D., Lex, S.A., King, S.J., and Gross, S.P. (2005). Building complexity: an in vitro study of cytoplasmic dynein with in vivo implications. Current biology : CB *15*, 2075-2085. doi: 10.1016/j.cub.2005.10.039

Marttila, A.T., Laitinen, O.H., Airenne, K.J., Kulik, T., Bayer, E.A., Wilchek, M., and Kulomaa, M.S. (2000). Recombinant NeutraLite avidin: a non-glycosylated, acidic mutant of chicken avidin that exhibits high affinity for biotin and low non-specific binding properties. FEBS letters *467*, 31-36

Pinaud, F., and Dahan, M. (2011). Targeting and imaging single biomolecules in living cells by complementation-activated light microscopy with split-fluorescent proteins. Proceedings of the National Academy of Sciences of the United States of America *108*, E201-210. doi: 10.1073/pnas.1101929108

Rogers, A.R., Driver, J.W., Constantinou, P.E., Kenneth Jamison, D., and Diehl, M.R. (2009). Negative interference dominates collective transport of kinesin motors in the absence of load. Physical chemistry chemical physics : PCCP *11*, 4882-4889. doi: 10.1039/b900964g

Sage, D., Neumann, F.R., Hediger, F., Gasser, S.M., and Unser, M. (2005). Automatic tracking of individual fluorescence particles: application to the study of chromosome dynamics.

IEEE transactions on image processing : a publication of the IEEE Signal Processing Society *14*, 1372-1383

Shubeita, G.T., Tran, S.L., Xu, J., Vershinin, M., Cermelli, S., Cotton, S.L., Welte, M.A., and Gross, S.P. (2008). Consequences of motor copy number on the intracellular transport of kinesin-1-driven lipid droplets. Cell *135*, 1098-1107. doi: 10.1016/j.cell.2008.10.021

Sivaramakrishnan, S., Spink, B.J., Sim, A.Y., Doniach, S., and Spudich, J.A. (2008). Dynamic charge interactions create surprising rigidity in the ER/K alpha-helical protein motif. Proceedings of the National Academy of Sciences of the United States of America *105*, 13356-13361. doi: 10.1073/pnas.0806256105

Sivaramakrishnan, S., Sung, J., Ali, M., Doniach, S., Flyvbjerg, H., and Spudich, J.A. (2009). Combining single-molecule optical trapping and small-angle x-ray scattering measurements to compute the persistence length of a protein ER/K alpha-helix. Biophysical journal *97*, 2993-2999. doi: 10.1016/j.bpj.2009.09.009

Soppina, V., Norris, S.R., Dizaji, A.S., Kortus, M., Veatch, S., Peckham, M., and Verhey, K.J. (2014). Dimerization of mammalian kinesin-3 motors results in superprocessive motion. Proceedings of the National Academy of Sciences of the United States of America *111*, 5562-5567. doi: 10.1073/pnas.1400759111

Svoboda, K., and Block, S.M. (1994). Biological applications of optical forces. Annual review of biophysics and biomolecular structure *23*, 247-285. doi: 10.1146/annurev.bb.23.060194.001335

Thorn, K.S., Ubersax, J.A., and Vale, R.D. (2000). Engineering the processive run length of the kinesin motor. The Journal of cell biology *151*, 1093-1100

Tirat, A., Freuler, F., Stettler, T., Mayr, L.M., and Leder, L. (2006). Evaluation of two novel tag-based labelling technologies for site-specific modification of proteins. International journal of biological macromolecules *39*, 66-76. doi: 10.1016/j.ijbiomac.2006.01.012

Vale, R.D., Schnapp, B.J., Reese, T.S., and Sheetz, M.P. (1985). Organelle, bead, and microtubule translocations promoted by soluble factors from the squid giant axon. Cell *40*, 559-569

Vershinin, M., Carter, B.C., Razafsky, D.S., King, S.J., and Gross, S.P. (2007). Multiple-motor based transport and its regulation by Tau. Proceedings of the National Academy of Sciences of the United States of America *104*, 87-92. doi: 10.1073/pnas.0607919104

Xu, J., Shu, Z., King, S.J., and Gross, S.P. (2012). Tuning multiple motor travel via single motor velocity. Traffic *13*, 1198-1205. doi: 10.1111/j.1600-0854.2012.01385.x

Chapter 3 A survey of fluorescent tags in kinesin-1 single molecule assays reveals aberrant run lengths due to tag-induced oligomerization

This chapter has been adapted from the following manuscript:

Norris, S.R., Núñez, M.F., and Verhey, K.J. (2014). Influence of fluorescent tag on the motility properties of kinesin-1 in single-molecule assays. Under Revision.

Author contributions:

S.R.N. and K.J.V. designed research. S.R.N. and M.F.N. performed research. S.R.N. analyzed data. S.R.N. and K.J.V. wrote the paper with input from all authors.

3.1 Introduction

In Chapter 2, I introduced and characterized a new method for creating multi-protein complexes in living cells. I then showed that complexes of two kinesin-1 motors, where both motors were attached by a split GFP linker, led to enhanced run lengths compared to single motors. These results were difficult to interpret, however, primarily because two-motor complexes could not be distinguished from single motors. To address this, a two-color TIRF assay was proposed where the first motor was labeled with a green fluorescent protein (FP) and the second motor was labeled with a red FP, thus enabling confirmation of two-motor assembly on a scaffold via colocalization. In order to proceed with this two-color TIRF assay, we first needed to validate

these green and red FPs such that they fit the following criteria: 1) they must be spectrally separated such that the red FP did contaminate the signal in our green channel and vice versa (i.e., crosstalk and bleedthrough of the fluorescence), and 2) these FPs must not impair motor function in any way and 3) these FPs must provide sufficient signal for single-molecule analysis. Determining the proper FP combination that fit all three criteria was a non-negligible task, as many of the spectrally convenient and bright FPs actually led to aberrant single-molecule motility properties when fused to kinesin-1. Chapter 3 presents this survey of FPs for use in single-molecule motility assays, which we believe will serve as a valuable reference for the field.

Historically, the development of TIRF microscopy allowed scientists to visualize the motility of single kinesin motors labeled by small organic fluorophores such as Cy3 or Cy5 (Vale et al., 1996). The identification and optimization of fluorescent proteins (FPs) (Chalfie et al., 1994; Dedecker et al., 2013) provided a powerful technique for genetically labeling proteins and allowed the single molecule properties of kinesin motors in cells to be directly compared to their properties *in vitro* (Cai et al., 2007). Thus, a growing demand has emerged for bright FPs of various output colors that are applicable for single-molecule studies both in cells and *in vitro*.

A large number of FPs are now available that are derived from a variety of different organisms and display variable spectral properties and biostability (Dedecker et al., 2013). Most FPs consist of either a GFP-fold (typically green emission) or DsRed-fold (typically red emission) structure consisting of an interior tripeptide chromophore that is protected by an exterior β-barrel, where the fluorescent properties are defined by the chromophore structure and local environment of the barrel interior (Dedecker et al., 2013). Although direct comparisons have been made of the spectral properties of various FPs, these properties can vary widely depending on excitation method (e.g. arc lamp vs. laser excitation) and experimental environment (Shaner et al., 2008).

Additionally, alternative methods for fluorescently labeling proteins have been developed such as SNAP (Juillerat et al., 2003) and HALO (Los et al., 2008) tags, which are engineered enzymes that link covalently to small fluorescent ligands. However, there are relatively few studies where FPs and enzyme-based fluorophores have been compared and tested under the same experimental conditions, especially for single-molecule applications.

Here we test ten different fluorescent tags for single-molecule imaging of a truncated dimeric form of kinesin-1. We first confirm fluorescence intensities and photostability in our single-molecule motility assays, and then compare the motility properties of each fusion protein as obtained by kymograph analysis. We find that the fluorescent tags do not affect the velocity of the motor but that several FPs (EGFP, mEGFP, tagRFPt, mApple) lead to aberrantly long run lengths. We determine that this effect is not salt-dependent, but rather reflects the tendency of these FPs to oligomerize. In addition, we find that the utility of the enzyme-based tags such as SNAP or HALO depends on the fluorescent ligand and these tags do not outperform the FPs. Overall, this study provides a valuable survey of fluorophores for single-molecule imaging using TIRF-based imaging.

3.2 Materials and methods

Plasmids. A truncated, constitutively active version of the kinesin-1 motor rat KIF5C (aa 1-560) [KHC(1-560), (Cai et al., 2009; Cai et al., 2007)] was used. Different fluorescent tags were genetically fused to the C-terminus via restriction digestion and ligation. Most constructs were generated using AgeI and BsrGI enzymes; KHC(1-560)-HALO was generated using AgeI and MfeI and KHC(1-560)-mNeGr was generated using Acc65I and BsrGI. Short linker sequences

situated between KHC(1-560) and the tag protein are from the multiple cloning site: LVPGGGGGGGGGPVAT for EGFP, mEGFP, 2xmCh, mApple, and tagRFPt tagged motors; LVPRARDPPVAT for SNAP, HALO, tdTom, and mCit tagged motors; and LVPRARDPLE for the mNeGr tagged motor. Plasmids encoding HALO tag, SNAP tag, and mNeonGreen were purchased from Promega (Madison, WI), New England Biolabs (Ipswich, MA), and Allele Biotechnology (San Diego, CA) respectively. mApple was obtained from Addgene (#54567, Cambridge, MA) where the plasmid was provided by the laboratory of M. Davidson (Florida State University) (Kremers et al., 2009). A tandem dimer of mCherry was synthesized by DNA 2.0 (Menlo Park, CA). Plasmids encoding tagRFPt and tdTomato were gifts from D. Cai (University of Michigan). A plasmid encoding EGFP was a gift from J. Swanson (University of Michigan). Monomeric GFP (A206K) was generated by QuikChange site-directed mutagenesis of EGFP (Stratagene, La Jolla, CA). All plasmids were verified by DNA sequencing.

Cell culture, transfection, lysis, and normalization of motor concentration. COS7 cells were cultured, transfected and lysed as described (Cai et al., 2007; Soppina et al., 2014). Briefly, COS7 cells were grown in DMEM + 10% (vol/vol) Fetal Clone III (Thermo Fisher, Waltham, MA) and 2 mM L-glutamine at 37°C with 5% (vol/vol) CO_2. Cells were transfected with 1 μg of plasmid DNA using Expressfect (Denville Scientific, Metuchen, NJ). After overnight expression (16 h), the cells were trypsinized and harvested by low-speed centrifugation at 1,500 x g at 4°C. The pellet was washed once in DMEM, resuspended in 25 μL lysis buffer (25 mM HEPES/KOH, 115 mM potassium acetate, 5 mM sodium acetate, 5 mM $MgCl_2$, 0.5 mM EGTA, and 1% Triton X-100, pH 7.4) freshly supplemented with 1 mM ATP, 1 mM PMSF and protease inhibitors (10 μg/mL leupeptin, 5 μg/mL chymostatin, 3 μg/mL elastatinal, and 1 mg/mL pepstatin). After clarifying the lysate by centrifugation at 16,000 x g at 4°C, aliquots were snap

frozen in liquid nitrogen and stored at -80°C. The amount of motor in the COS7 lysates was normalized across constructs by a dot-blot in which increasing volumes of COS7 lysates were spotted onto a nitrocellulose membrane which was air-dried and immunoblotted with a monoclonal antibody to kinesin-1 (MAb1614, Millipore, Billerica, MA). The spots within the linear regime were quantified to normalize the motor concentration across lysates.

SNAP and HALO ligand labeling. COS7 cells expressing KHC(1-560)-SNAP or KHC(1-560)-HALO were labeled with cell-permeable SNAP or HALO ligands prior to lysis. The indicated ligand (SNAP-Cell Oregon Green, NEB #S9104S; SNAP-Cell 505-STAR, NEB #S9103S; SNAP-Cell TMR-STAR, NEB #S9105S; HALOTag Oregon Green ligand, Promega #G2801; HALOTag diAcFAM ligand, Promega #G8272; HALOTag TMR ligand, Promega #G8251) was added to 1 mL of DMEM in a 6-well, 35-mm plate per manufacturer's suggestion: 5 μM for SNAP-Cell Oregon Green, 5 μM for SNAP-Cell 505-STAR, 3 μM for SNAP-Cell TMR-STAR, 1 μM for HALOTag Oregon Green, 1 μM for HALOTag diAcFAM ligand, and 5 μM for HALOTag TMR ligand. After 30 min incubation, cells were washed 3x in DMEM and incubated in DMEM for 30 min before lysis to remove unbound ligand.

Single-molecule motility assays. All assays were performed as described previously (Soppina et al., 2014) at room temperature in a narrow flow-cell (~10 μL volume) prepared by attaching a clean #1.5 cover slip to a glass slide with double-sided tape. HiLyte-647 labeled microtubules were polymerized from purified tubulin (Cytoskeleton, Denver, CO) in BRB80 buffer (80 mM PIPES/KOH, 1 mM EGTA, and 1 mM $MgCl_2$, pH 6.8) supplemented with 1 mM GTP at 37°C for 15 min. Polymerized microtubules were stored at room temperature after addition of five volumes of prewarmed BRB80 containing 20 μM taxol and additional 15 min incubation at 37°C. Polymerized microtubules were diluted in P12 buffer (12 mM PIPES/KOH, 1 mM

EGTA, and 2 mM $MgCl_2$, pH 6.8) containing 20 μM taxol and then infused into a flow-cell and incubated for 5 min at room temperature to adsorb onto the coverslip. Subsequently, 50 μL of blocking buffer (10 mg/mL BSA in P12 buffer with 10 μM taxol) was introduced and incubated for 10 min to prevent nonspecific binding of kinesin motors onto the coverslip surface. Finally, lysates containing equal amounts of motor proteins (typically 0.1 - 1.0 μL) were added to flow chambers in a motility mixture in either P12 buffer or physiological-salt buffer (25 mM HEPES/KOH, 115 mM potassium acetate, 5 mM sodium acetate, 5 mM $MgCl_2$, and 0.5 mM EGTA, pH 7.4). The ionic strength (I.S.) of each buffer was calculated based on the molar concentration of each ion and its counterion based on http://biomol.net. Each motility mixture also contained 2 mM ATP, 10 mg/mL BSA, 10 μM taxol, and oxygen-scavenging components to reduce photobleaching (1 mM DTT, 1 mM $MgCl_2$, 10 mM glucose, 0.1 mg/mL glucose oxidase, and 0.08 mg/mL catalase). The motility data for each construct were obtained from at least two independent protein preparations.

Image acquisition. Images for single-molecule motility assays were acquired using a Nikon TiE/B microscope with a 100X 1.49 NA oil immersion TIRF objective (Nikon, Melville, NY) equipped with three 20 mW diode lasers (488nm, 561nm, 640nm) combined into a single fiber and controlled via AOTF (Agilent, Santa Clara, CA). Images were collected via an EMCCD detector (iXon X3 DU897, 512x512, 16μm array, Andor, Belfast, UK). For imaging in green and/or red, the microscope used a dual-band laser polychroic mirror (ZT488/561rpc, Chroma Technology, Rockingham, VT), a dual-band sputtered emission filter (ZET488/561m, Chroma), and a dual-band sputtered clean-up filter (ZET488/561x, Chroma) where either the 488nm (2mW power, used for EGFP, mEGFP, mNeGr, mCit, SNAP-OreGr488, SNAP-505-STAR, HALO-OreGr488, HALO-diAcFAM) or 561nm (4mW power, used for tdTom, tagRFPt, mApple, 2xmCh,

SNAP-TMR, HALO-TMR) laser was used for TIR-based illumination. Images were acquired continuously with 100 ms exposures, and image acquisition was controlled by Nikon Elements software.

Kymograph analysis. In order to avoid complications arising from variation in signal to noise ratio or point spread function for different fluorescent tags, motility events were analyzed by kymograph analysis. Maximum intensity projections were generated to determine the location of microtubules and kymographs were generated (width = 5 pixels) along these tracks using Elements (Nikon). Only constant velocity events of at least five frames (500 ms) were considered, and stalled events were ignored. Kymographs were generated with distance on the y-axis and time on the x-axis. Run length was defined as the vertical component of the kymograph, which is the distance traveled along the microtubule, in μm. Dwell time was defined as the horizontal component of the kymograph, which is the time spent in a constant velocity segment, in s. Velocity was defined as the run length divided by dwell time, in μm/s.

Cumulative distribution functions (CDFs). CDFs of velocities and run lengths were generated via MATLAB and mean values were obtained as described (Thorn et al., 2000). CDFs were used for statistical analysis because they are continuous and do not introduce subjective binning. Using MATLAB, run length CDFs above a minimum t_0 = 0.5 μm were fit to the hypothetical CDF for an exponential distribution using a nonlinear least squares fit with the free parameter *t*:

$$CDF(x) = 1 - e^{(x_0 - x)/t}$$

The mean run length was then determined by adding the minimum run length t_0 to t. Errors were estimated by the bootstrap technique (Thorn et al., 2000). Each distribution was resampled 200 X

and fit to the appropriate equation. The standard deviation of the fitted parameter over the resampled data sets was taken as the error for each fitted quantity.

Velocity CDFs were fit to the hypothetical CDF for a normal distribution using a nonlinear least squares fit with free parameters μ (mean) and σ (standard deviation):

$$CDF(x) = \frac{1}{2}\left[1 + erf\left(\frac{x-\mu}{\sqrt{2\sigma^2}}\right)\right]$$

Photobleaching Assays. Quantitative photobleaching assays were performed as described (Soppina et al., 2014). Small volumes of COS7 lysates (~1:20 dilution from motility conditions) containing equal amounts of FP-tagged motors were diluted in blocking solution (15 mg/mL BSA in P12 buffer) and flowed into an empty chamber. The motors were allowed to incubate for 2 minutes to nonspecifically adsorb to the glass surface. 50 μL of blocking solution was then introduced to remove non-adsorbed motors. The surface-bound motors were imaged in TIRF with increased laser power (10mW for 488nm, 6 mW for 561nm). The fluorescence intensity profile of ~200 motors from two independent protein preparations for each construct was then plotted as a function of time, and the number of discrete photobleaching steps was counted and displayed as a histogram for the population.

Calculation of landing rates. The on rate (k_{on}) for each construct was determined from the single-molecule motility data. A relative landing rate was defined as [number of events / (unit time * unit microtubule length)] where time was defined as the recording time (in minutes) and microtubule length was determined by measuring the length of the HiLyte-647 labeled microtubule in the 640nm channel (in μm). The number of motility events was determined for least 4 different microtubules for each construct from two independent experiments.

Estimating fraction of run lengths above a certain threshold. The probability distribution function for a run length distribution is as follows, where the mean of the distribution is defined as λ^{-1} :

$$PDF(x) = \lambda e^{-\lambda x}$$

The probability of *x* falling between 3 μm and ∞ is the definite integral of this function where λ= 1 to reflect a mean run length of 1 μm:

$$\int_3^{\infty} e^{-x} dx = 0.0498, \text{ or } 4.98\%.$$

3.3 Results

3.3.1 Fluorescent tags can influence kinesin-1 run length in single-molecule motility assays

To determine whether different fluorescent tags can affect kinesin motility properties, we fused a variety of fluorescent tags to the C-terminus of a constitutively active version of the kinesin-1 motor KIF5C(1-560) (Fig. 3.1A). We tested ten fluorescent markers: four green FPs, four red FPs, and two enzyme-based tags that can be labeled with cell-permeable small organic fluorophores (Table 3.1). These fluorophores represent a wide range of potential tags in the green-red spectrum, were derived from different organisms, and are well-characterized in terms of oligomeric state (Kremers et al., 2011; Shaner et al., 2005).

To examine the motility properties of each fluorophore-tagged KHC(1-560), we transfected COS7 cells with the construct of interest, harvested cell lysates, and performed single-

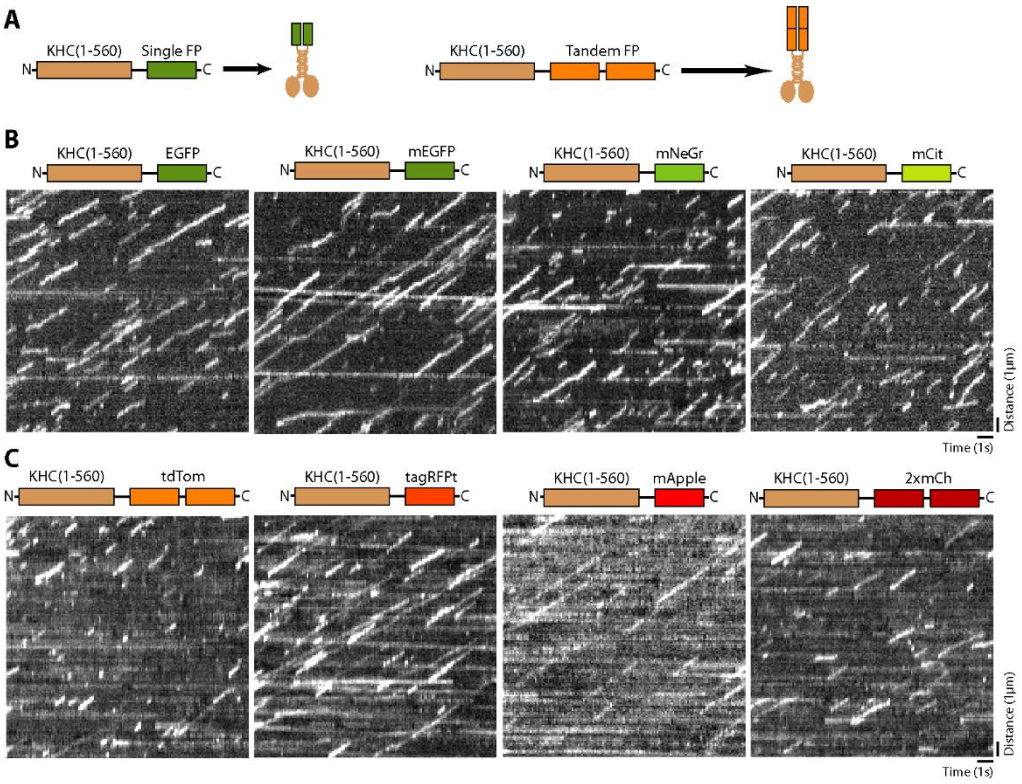

Figure 3.1. A survey of FPs for labeling kinesin-1 in single-molecule motility assays.

(A) Schematic. A dimeric, constitutively active kinesin-1 motor [KHC(1-560)] was tagged at the C-terminus with single or tandem FPs. **(B-C)** Lysates of COS7 cells expressing the indicated KHC(1-560)-FP motors were analyzed in single-molecule motility assays via TIRF microscopy. Representative kympographs were generated from the movies for **(B)** KHC(1-560) tagged with the indicated green FPs, or **(C)** KHC(1-560) tagged with the indicated red FPs. Time is on the x-axis (scale bar, 1 s) and distance is on the y-axis (scale bar, 1 μm).

molecule motility assays using total internal reflection fluorescence (TIRF) microscopy (Soppina et al., 2014). The motility of each construct can be analyzed in a kymograph where run distance is displayed vertically and time is displayed horizontally (Fig. 3.1B-C). An important parameter for imaging at the single-molecule level and determining motility properties via kymographs or automated tracking software is the brightness of the fluorophore. In our hands, mCitrine and tagRFPt provided relatively weak fluorescence signals and mApple was barely detectable above the background fluorescence (Fig. 3.1B-C). EGFP, mEGFP, mNeGr, tdTom, and 2xmCh provided

significantly brighter signals that were amenable to kymograph analysis (Fig. 3.1B-C). For all of the FP-tagged motors tested, the majority of the processive events terminated abruptly rather than being preceded by a loss in signal, indicating that the rate of photobleaching was significantly slower than the typical off-rate of a motile event (Fig. 3.1B-C).

For the enzyme-based tags, KHC(1-560) was labeled with either SNAP or HALO proteins and the indicated fluorescent ligand was added prior to cell lysis (Fig. 3.2A). For the SNAP tag, the TMR ligand provided the strongest signal, whereas the green fluorescent ligands (OreGr-488 and 505-STAR) were significantly weaker (Fig. 3.2B). For the HALO tag, the TMR ligand provided sufficient signal for tracking at the single-molecule level, whereas the OreGr488 signal was much weaker and no labeling was detected for the diAcFAM ligand (Fig. 3.2C). Similar to FP-tagged motors (Fig. 3.1B-C), SNAP-505-STAR, SNAP-TMR, and HALO-TMR showed little indication of photobleaching under our experimental conditions (Fig.3.2B-C).

For each fluorescently-tagged KHC(1-560) construct, the run lengths and velocities of individual motility events were determined from the kymographs and plotted as a histogram for the population (Fig. 3.3A-C). Mean run lengths and velocities were then determined by fitting each distribution to its corresponding cumulative distribution function (CDF). The mean velocities did not vary substantially across the different fluorescently-tagged KHC(1-560) constructs (Fig. 3.3E, Fig. 3.4, and Table 3.2), suggesting that none of the fluorescent tags interfere with the enzymatic activity of kinesin-1. In contrast, the mean run lengths showed wide variability between the different fluorescently-tagged constructs, ranging from 0.76 ± 0.02 μm for KHC(1-560)-tdTom to 1.81 ±0.09 μm for KHC(1-560)-mApple (Fig. 3.3D, Fig. 3.4, and Table 3.2). These variations in run length did not correlate with the photostability, published oligomeric state, or source

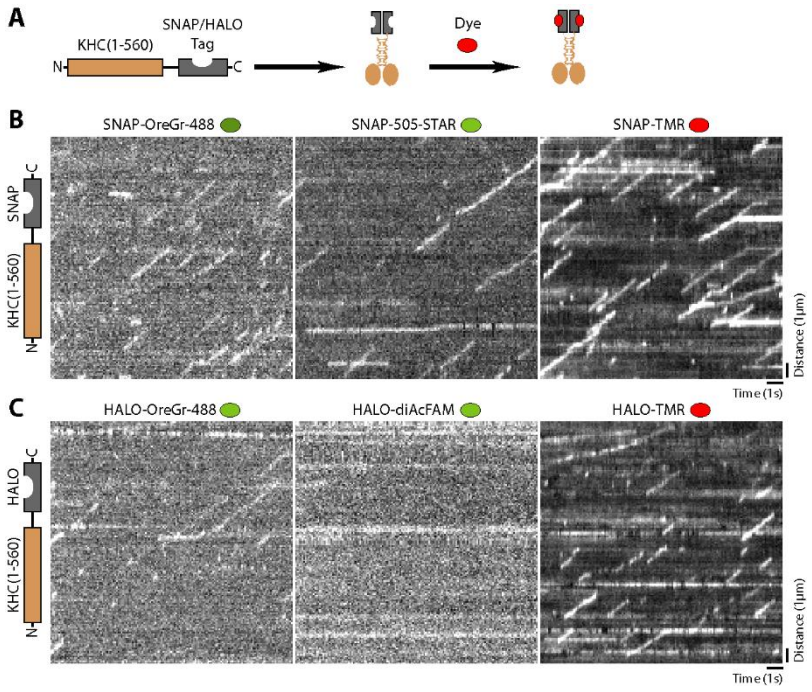

Figure 3.2. A survey of enzyme tags and fluorescent ligands for labeling kinesin-1 in single-molecule motility assays.

(A) Schematic. A dimeric, constitutively active kinesin-1 motor [KHC(1-560)] was tagged at the C-terminus with an enzyme (SNAP or HALO) tag that covalently links to a fluorescent dye. **(B-C)** Enzyme-tagged KHC(1-560) motors expressed in COS7 cells were labeled with the indicated dyes prior to cell lysis and analysis by TIRF microscopy. Representative kymographs were generated from the movies of **(B)** KHC(1-560)-SNAP and **(C)** KHC(1-560)-HALO motors in cell lysates. Time is on the x-axis (scale bar, 1 s) and distance is on the y-axis (scale bar, 1 μm).

organism of the fluorescent tag (Table 3.1), suggesting that these factors do not contribute to the observed FP-dependent run lengths.

3.3.2 FP-specific oligomerization influences kinesin-1 run length independent of electrostatics

Analysis of the run length histograms indicated that the kinesin-1 constructs with the longest mean run lengths displayed a significant fraction of events with a run length > 3 μm

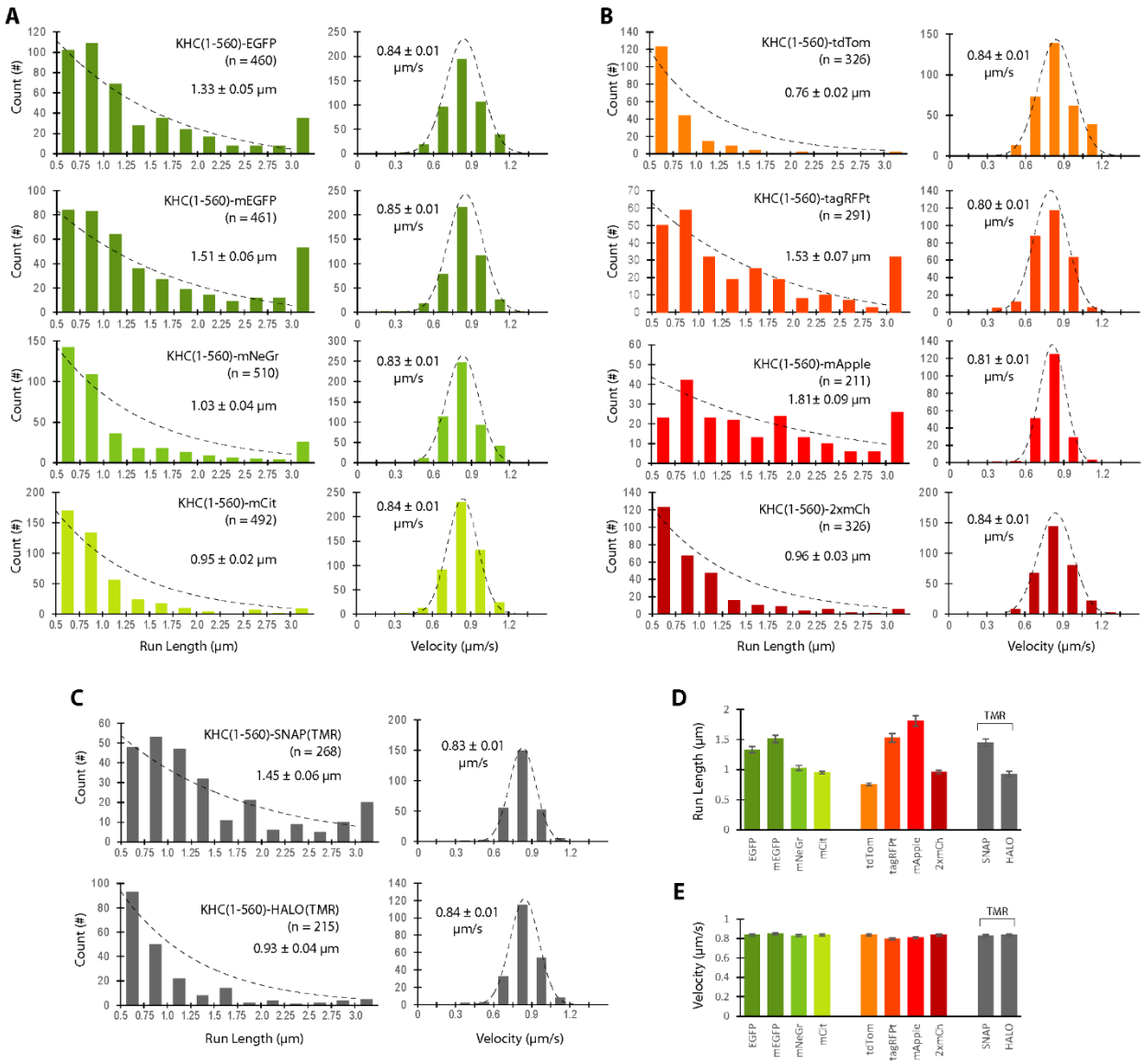

Figure 3.3. Motility properties of fluorescently-tagged KHC(1-560) motors in P12 motility buffer.

(A-C) The run lengths and velocities for individual KHC(1-560) motors tagged with (A) green FPs, (B) red FPS, or (C) enzyme tags were determined via kymograph analysis and then plotted as histograms for the population. The mean run length and velocity values (insets) were obtained by fit to the CDF, which was then overlaid as a probability distribution function (dotted line) on the histogram. Error is reported as the standard deviation from bootstrapping. **(D-E)** Comparison of the mean (D) run length and (E) velocity values for each motor as determined by CDF fit. Data are presented as the mean ± the standard deviation from bootstrapping.

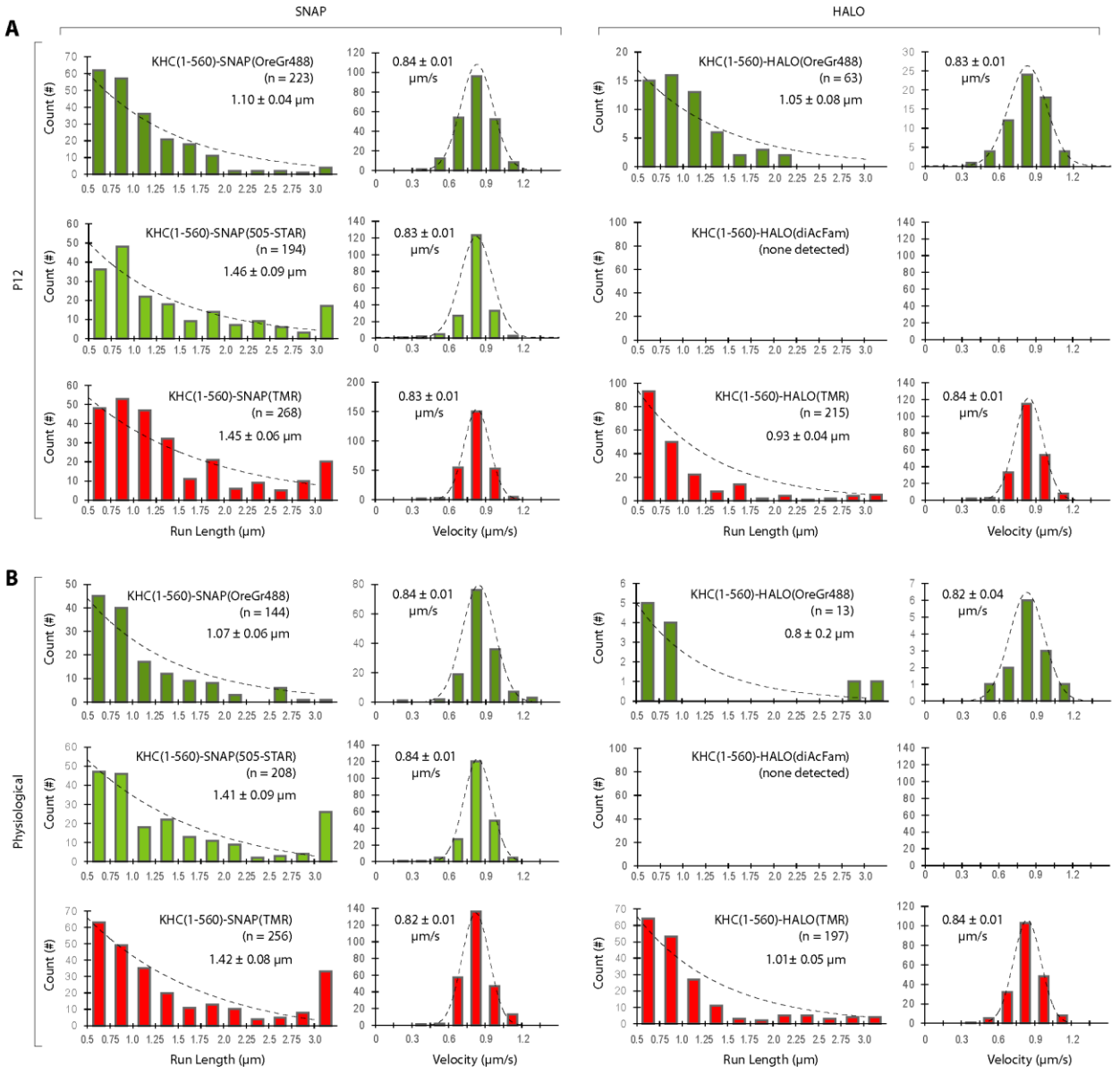

Figure 3.4. Characterization of different SNAP and HALO ligands.

(A-B) Motility properties for various SNAP (left) and HALO (right) ligands were compared in standard P12 motility buffer **(A)** and under physiological buffer conditions **(B)**. The mean run length and velocity values (insets) were obtained by CDF fit, which was then overlaid as a population distribution function (dotted line) on the histogram. Error is reported as the standard deviation from bootstrapping. SNAP- and HALO-Oregon Green ligands were barely detectable at 488 nm excitation, likely leading to shorter run lengths than other SNAP-ligands, and HALO-diAcFAM was not detectable at 488 nm. SNAP-505-STAR, SNAP-TMR, and HALO-TMR ligands were readily detectable at 488, 561, and 561 nm excitation, respectively.

(rightmost bins in Fig. 3.3A-C). For events characterized by an exponential run length distribution with a mean of 1 μm, the probability of a motile event with a run length greater than 3 μm is < 5% (see Materials and Methods). However, the percent of motile events greater than 3 μm was 7.6% for KHC(1-560)-EGFP, 11.5% for KHC(1-560)-mEGFP, 11.0% for KHC(1-560)-tagRFPt, 12.3% for KHC(1-560)-mApple, and 7.5% for KHC(1-560)-SNAP-TMR. Thus, the increased number of run lengths greater than 3 μm appears to be the defining feature that distinguishes fluorophores that influence kinesin-1 versus those that do not.

We speculated that differences in surface charge between FPs may influence the motor's run length due to interactions of the FP with the negatively-charged microtubule surface. To test this, we carried out single-molecule motility assays for each fluorescently-tagged KHC(1-560) motor under physiological ionic strength and pH conditions (ionic strength I.S. = 145 mM, pH 7.4, Fig. 3.5). Similar to the motility in standard P12 motility buffer (I.S. = 28 mM, pH 6.8, Fig. 3.3), the fluorescent tag had no effect on the mean velocity values (Fig. 3.5E), but we still observed mean run lengths that were fluorophore-dependent (Fig. 3.5D). Importantly, KHC(1-560) motors tagged with EGFP, mEGFP, tagRFPt, mApple and SNAP-TMR still displayed an increased number of run lengths greater than 3 μm (rightmost bins in run length histograms in Fig 3.5A-C). These results indicate that the influence of the fluorescent tag on the motor's run length is not due to charge interactions between the fluorescent marker and the microtubule.

We then speculated that oligomerization of the fluorescent tags might play a role in aberrant kinesin-1 run lengths. To examine this possibility, we compared the run length values for KHC(1-560) motors tagged with EGFP, which is susceptible to weak dimerization, to the run length values of motors tagged with mEGFP whose A206K mutation abolishes dimerization (Zacharias et al., 2002). Surprisingly, fusion of mEGFP actually led to longer runs for KHC(1-

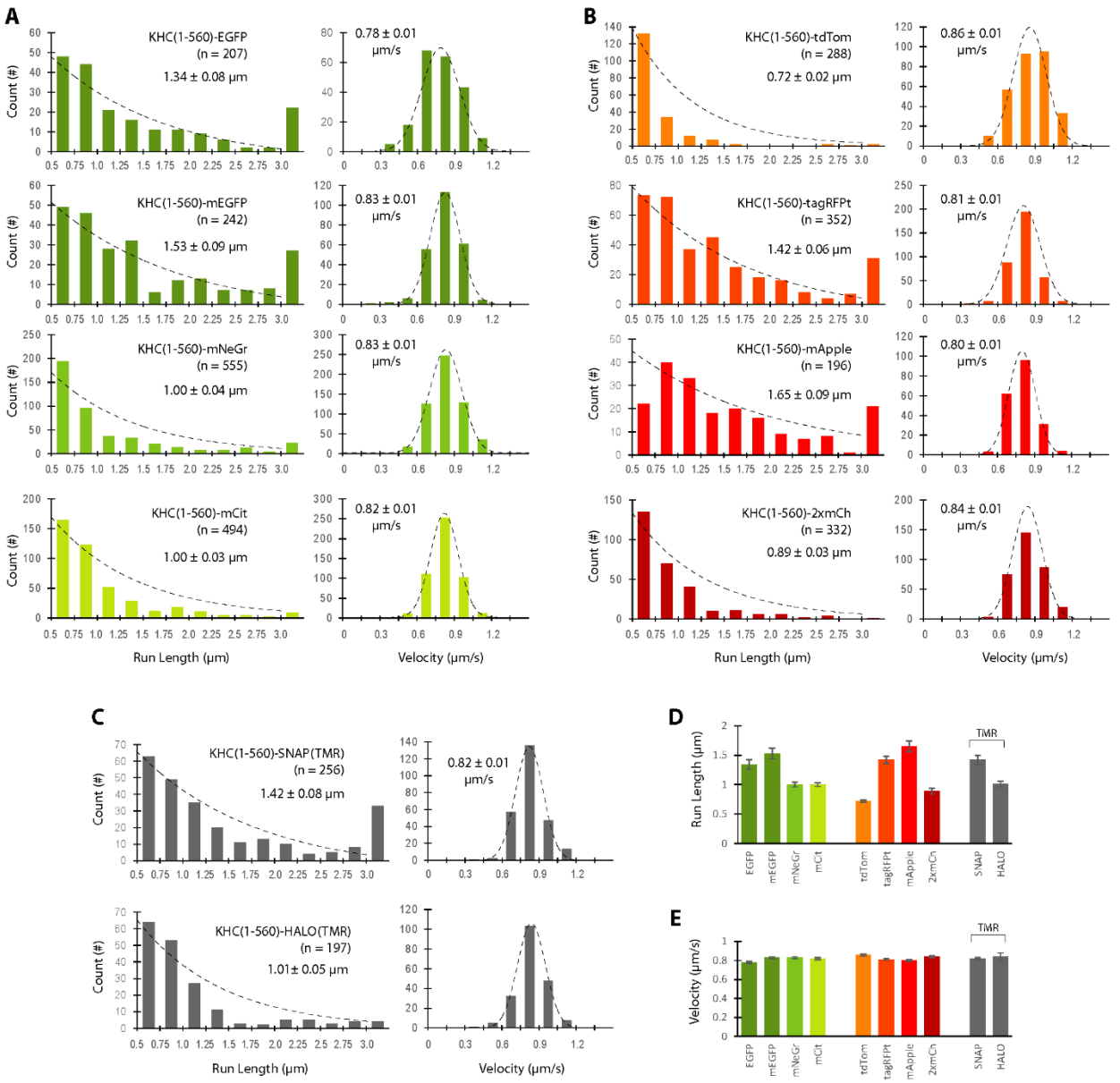

Figure 3.5. Motility properties of fluorescently-tagged KHC(1-560) motors at physiological salt conditions.

(A-C) The run lengths and velocities for individual KHC(1-560) motors tagged with (A) green FPs, (B) red FPS, or (C) enzyme tags were determined via kymograph analysis and then plotted as histograms for the population. The mean run length and velocity values (insets) were obtained by CDF fit, which was then overlaid as a probability distribution function (dotted line) on the histogram. Error is reported as the standard deviation from bootstrapping. **(D-E)** Comparison of the mean (D) run length and (E) velocity values for each motor as determined by CDF fit. Data are presented as the mean ± the standard deviation from bootstrapping.

560) (1.53 ± 0.09 μm versus 1.34 ± 0.08 μm, Fig. 3.3A,D, Table 3.2) due to an increase in the percent of motile events greater than 3 μm (11.0% versus 7.6%). Similar results were obtained under physiological buffer conditions (Fig. 3.5A,D, Table 3.2). These results suggest that simple dimerization of FPs is not the underlying cause of kinesin-1's increased run length. Since fusion of the FPs to dimeric proteins such as KHC(1-560) could cause proximity-induced interactions not observed in ensemble assays of FP dimerization (Olenych et al., 2007), we directly measured the oligomeric state of seven of the fluorescently-tagged motors using single-molecule photobleaching assays. We were unable to perform these assays on KHC(1-560)-mApple, as the signal was too weak, or on the SNAP- and HALO-tagged motors due to complications from incomplete labeling. Importantly, the KHC(1-560)-FP constructs which showed aberrantly long run lengths (EGFP, mEGFP, and tagRFPt, Figs. 3.3 and 3.5) also showed a significant portion of molecules with more photobleaching steps than the expected value for a dimeric kinesin motor (Figs. 3.6 and 3.7). This was particularly striking for KHC(1-560)-mEGFP and KHC(1-560)-tagRFPt, where three or four photobleaching steps were frequently observed (Figs. 3.6 and 3.7) although just two steps are expected for a dimeric motor, suggesting that this oligomerization was tag-dependent. Overall, the strong correlation between KHC(1-560)-FP oligomerization and run length suggests that a number of FPs can undergo unanticipated homo-interactions when brought into close proximity upon fusion to a dimeric protein.

3.3.3 FP tags can also influence the motor's landing rate

While analyzing the motility properties of KHC(1-560) motors tagged with different fluorophores, we noticed that the number of motility events also seemed to vary between

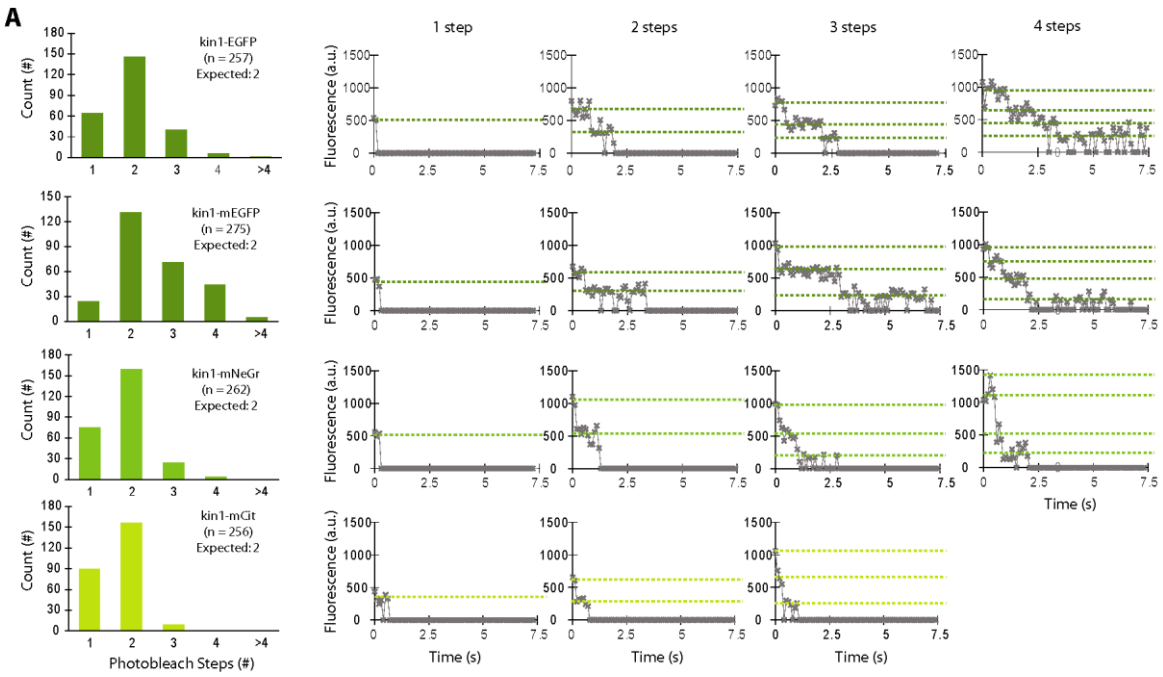

Figure 3.6. Photobleaching quantification and example intensity traces for KHC(1-560)-Green FPs.

(A) Green FPs fused to kin-1 were immobilized on a glass surface and imaged with high-intensity laser excitation, whereupon the intensity trace of each event was analyzed. Intensity traces from individual events were classified by the number of discrete steps (right) and the population data was plotted as a histogram (left). (Expected) denotes the predicted number of photobleaching steps for a completely dimeric motor.

constructs. To quantify this, we normalized the amount of each tagged KHC(1-560) motor across constructs and quantified the landing rate of each motor as the number of events per unit time per unit microtubule length. As reported previously (Vale et al., 1996), the landing rate depended only weakly on ionic strength, with most motors showing a slightly decreased affinity for the microtubule under physiological salt conditions (Fig. 3.8). For the green FPs, mNeGr appeared to positively influence the landing rate of kinesin-1 as more motility events were observed for KHC(1-560)-mNeGr than for other motors at the same concentration (Fig 3.8). This construct also appeared "stickier" in our experiments, typically decorating the imaging surface more than

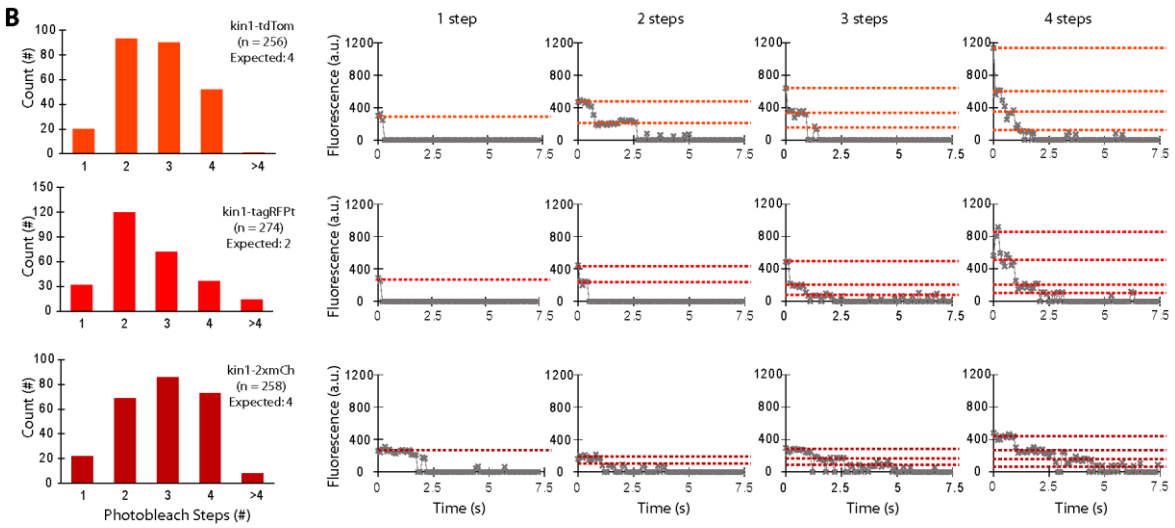

Figure 3.7. Photobleaching quantification and example intensity traces for KHC(1-560)-Red FPs.

(A) Green FPs fused to kin-1 were immobilized on a glass surface and imaged with high-intensity laser excitation, whereupon the intensity trace of each event was analyzed. Intensity traces from individual events were classified by the number of discrete steps (right) and the population data was plotted as a histogram (left). (Expected) denotes the predicted number of photobleaching steps for a completely dimeric motor.

other constructs (horizontal lines in Fig. 3.1B and data not shown). For the red FPs, little difference in landing rate was observed between the constructs (Fig. 3.8) with the exception that fusion to mApple caused a decrease in kinesin-1 motility events, perhaps due to detection issues due to weaker signal (Fig. 3.1C). Since equal amounts of SNAP- and HALO-tagged motors were added to the assay, the landing rate provides an estimate of the labeling efficiency of each ligand. For both SNAP and HALO tags, the TMR ligand was more efficient at labeling (we estimate up to 80% of motors were labeled with at least one TMR ligand) than any of the green dyes (Fig 3.8). Additionally, we found no correlation between landing rate and run length, effectively ruling out the idea that enhanced MT affinity led to enhanced processivity (Fig. 3.9).

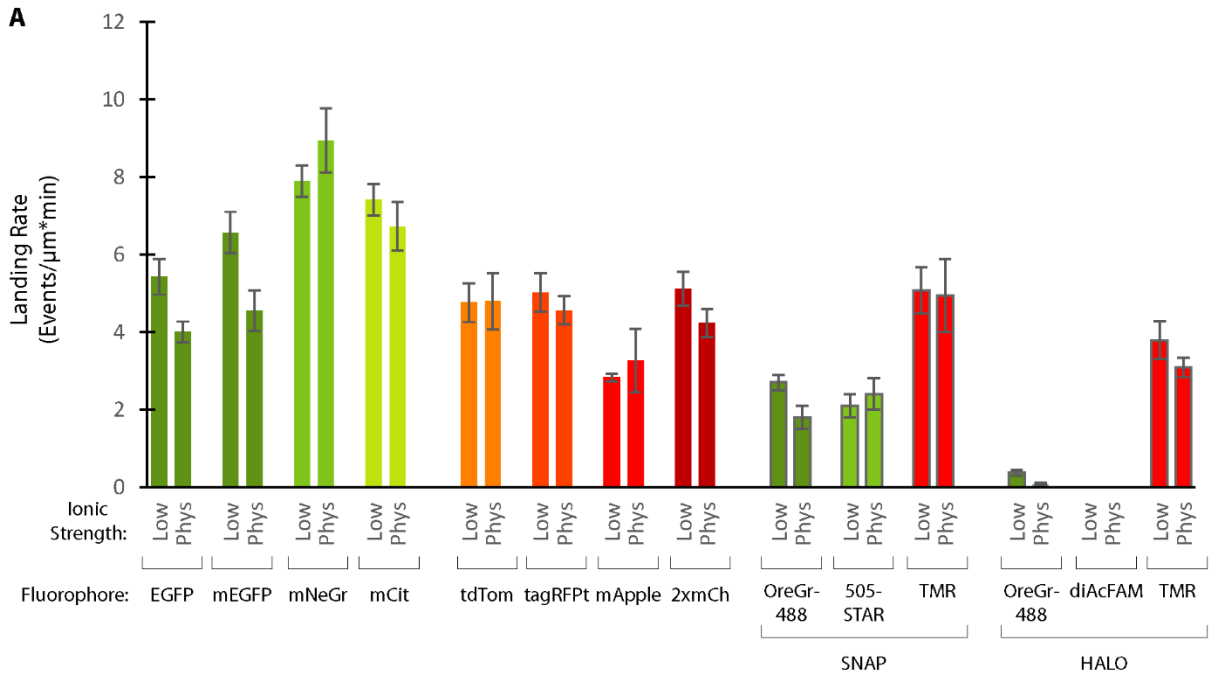

Figure 3.8. Landing rates of fluorescently-tagged KHC(1-560) motors.

(A) The amount of fluorescently-tagged KHC(1-560) motors in cell lysates was normalized by western blot. Equal amounts of motor were added to single-molecule motility assays and the landing rate was quantified as the # events per µm microtubule per min. Error is provided as S.E.M. At least four different microtubules from two different experiments were quantified for each construct.

3.4 Discussion

In this study, we compare the performance of ten different fluorescent tags (eight FPs, SNAP and HALO) in single-molecule motility assays when fused to dimeric kinesin-1. We find that mNeGr and mCit provide the best green FP tags for imaging of kinesin-1 motors, whereas GFP and mEGFP have a high tendency to oligomerize. Although mNeGr is preferable for its brightness with 488 nm excitation, this FP appears to be "stickier" in our single-molecule assays. We find that, based on its well-behaved motility properties and low oligomerization tendency, mCherry provides the best red FP tag for imaging, where its low fluorescence intensity is

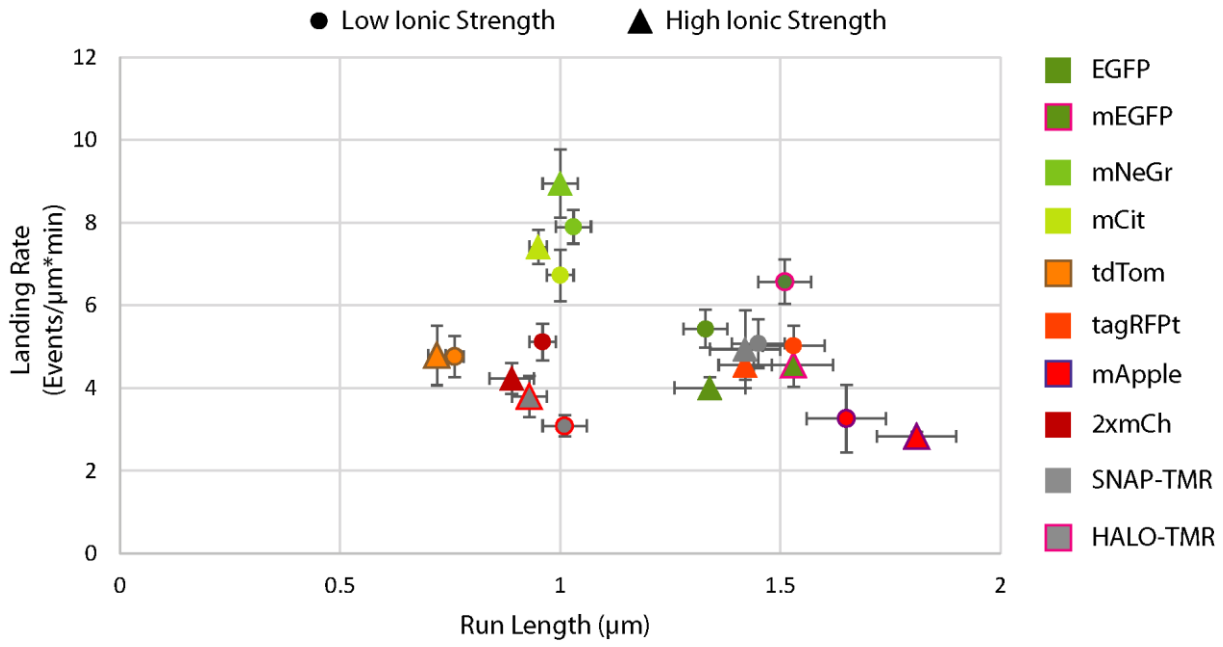

Figure 3.9. Correlating landing rate and run length.

Scatter plot of the calculated landing rate of each motor as determined by event frequency (y-axis, see Fig. 3.8) and the calculated run length as determined by CDF fit (x-axis, see Fig. 3.3 and Fig. 3.5). Error bars indicate standard error. No correlation was observed between the two parameters.

augmented by generating a tandem dimer. Importantly, we find that a subset of the fluorophores (EGFP, mEGFP, tagRFPt, mApple, SNAP) cause aberrant run lengths, presumably due to oligomerization. These results emphasize that FPs are not inert tags and can influence the behavior of the protein they are fused to. In most single-molecule studies of kinesin motors, the aberrant run lengths generated by the FP partner can be ignored by excluding the longest bin of motile events as this leads to only relatively small reductions in run length after mean analysis (Zhu and Dixit, 2011). Aberrant run lengths due to FP oligomerization is more likely to influence the interpretation of motor behavior when run length is used as a measure of motor output.

Essentially all FPs exist in nature as either tight dimers or tetramers caused by interactions between adjacent barrel exteriors, and thus most FP-fusion proteins have a tendency to oligomerize

(Shaner et al., 2005). These oligomeric tendencies can largely be alleviated by mutagenesis, at least when examined using biochemical techniques such as size-exclusion chromatography (Shaner et al., 2013) or analytical ultracentrifiguation (Zacharias et al., 2002). Although most of the FPs used in this study (mEGFP, mNeGr, mCit, tagRFPt, mApple) were found to be monomeric in solution, the proteins may be prone to oligomerization artifacts when a high local concentration is generated by fusion to oligomeric proteins (Olenych et al., 2007). For example, Constantini et al. found that tagRFP and EGFP were susceptible to oligomerization when fused to the cytoplasmic face of a resident endoplasmic reticulum membrane protein (Costantini et al., 2012). Additionally, Landgraf et al. showed that superfolder GFP, mCherry, and to a lesser extent tagRFPt, formed aberrant foci when expressed as fusion proteins to oligomeric Clp protease in *E. coli* (Landgraf et al., 2012). Additionally, many red FPs, including tagRFP, were recently found to cause artificial puncta formation when used to label secretory pathway components (Han et al., 2014). These results emphasize the need to independently confirm the oligomeric state of each fusion protein, especially as fluorescent proteins continue to evolve and advance (Dedecker et al., 2013).

It is interesting to note that this tendency to oligomerize when fused to a multimeric protein does not seem to be conserved among FPs derived from the same source protein. We find, for example, that EGFP and mEGFP seem prone to oligomerization but mCit does not, although only a handful of amino acids differ between these FPs. mCit differs from mEGFP by the amino acid changes L64F, T65G, V68L, Q69M, S72A, and T203Y, and all of these mutations are on the interior of the barrel. A previous study also showed that GFPmut3, which shares the T65G and S72A mutations with mCit, is substantially less likely to form oligomeric artifacts in *E. coli*, suggesting that these residues on the interior of the barrel can unexpectedly influence multimerization (Landgraf et al., 2012). Additionally, cysteine residues C48 and C70 of GFP

variants have been shown to cause oligomerization via formation of disulphide bonds, and mutations in adjacent residues such as Q69M could also be inhibiting this behavior (Griesbeck et al., 2001; Jain et al., 2001). Together, this suggests that small perturbations on either the surface or the interior of the protein can greatly influence these oligomeric tendencies and a predictive trend is difficult to identify.

In this study, we also reported the relative effectiveness of various cell-permeable SNAP and HALO ligands for single-molecule imaging of kinesin-1 motors. We found that for both SNAP and HALO tags, TMR consistently provides the brightest fluorescence signal in single-molecule motility assays (Fig. 3.2) and provides the highest efficiency of labeling when confirmed by motor landing rate (Fig. 3.8). The HALO tag and TMR ligand were recently used successfully to label dynein motors in single molecule assays via the dynactin subunit $p150^{Glued}$ (Ayloo et al., 2014). Importantly, even though the same fluorophore was used for visualization, SNAP-TMR and HALO-TMR showed different run lengths in single-molecule motility assays (Fig. 3.3), suggesting that this aberrant behavior is due to the specific coupling of this ligand-protein pair. Interestingly, two out of the three SNAP dyes (505-STAR and TMR) led to long run lengths, whereas OreGr488 led to characteristically short runs. We believe that oligomerization of SNAP tag itself leads to longer runs similar to FP constructs, but that longer runs are not detectable via the very dim OreGr488 dye (Fig. 3.2A). A comprehensive analysis of various cell-impermeable SNAP ligands in single-molecule studies was recently reported (Bosch et al., 2014), and these authors also found high variability in the effectiveness of the dyes for single-molecule imaging. These results emphasize that fluorescent dyes need to be tested under specific experimental conditions.

3.5 Conclusion

Here we present a survey of ten fluorescent tags to label kinesin-1 motors in single-molecule motility assays and find that a subset of these (EGFP, mEGFP, tagRFPt, mApple, SNAP-TMR) are susceptible to low-order oligomer formation which can introduce aberrant behavior of the kinesin-1 motor. These proteins should thus be avoided when they need to be fused to an oligomeric partner or in an integral membrane fusion where the local concentration is very high. Additionally, we provide comparisons in single-molecule imaging quality for each fluorescent tag. Of the green FPs studied, mNeonGreen provides the best imaging quality and has a relatively low susceptibility to oligomerize but appears to stick to other proteins and the glass surface. mCitrine appears to be the most well-behaved of the green FPs, but is not optimized for 488 nm excitation. Of the red FPs studied, tandem mCherry provides the best imaging quality without compromising native motor properties. SNAP and HALO tags provide great versatility for imaging in multiple colors but typically are not brighter or more photostable than FPs in single-molecule studies. Overall, this study should serve as a valuable reference in designing single-molecule experiments in multiple colors.

Table 3.1. Properties of fluorescent tags used in Chapter 3.

Fluorescent protein	Excitation [a] (nm)	Emission [b] (nm)	Brightness [c]	Photostability [d]	Oligomeric state	Source organism (original protein)	Reference
Enhanced GFP (EGFP)	488	507	34	174	Weak dimer	*A. Victoria* (GFP)	(Cormack et al., 1996; Heim et al., 1995)
Monomeric EGFP (mEGFP)	488	507	34	150	Monomer	*A. Victoria* (GFP)	(Zacharias et al., 2002)
Monomeric NeonGreen (mNeGr)	506	517	94	158	Monomer	*B. lanceolatum* (LanYFP)	(Shaner et al., 2013)
Monomeric Citrine (mCit)	516	529	59	49	Monomer	*A. Victoria* (GFP)	(Griesbeck et al., 2001; Zacharias et al., 2002)
Tandem Tomato (tdTom)	554	581	95	98	Tandem dimer	*Discosoma sp.*(DsRed)	(Shaner et al., 2004)
Tag RFP-t (tagRFPt)	555	584	33	337	Monomer (Shaner et al., 2008) or Weak dimer (Han et al., 2014)	*E. quadricolor* (eqFP578)	(Merzlyak et al., 2007; Shaner et al., 2008)
Monomeric Apple (mApple)	568	592	37	4.8 [f]	Monomer	*Discosoma sp.*(DsRed)	(Shaner et al., 2008)
Tandem monomeric Cherry (2xmCh)	587	610	32 [e]	Unknown	Tandem dimer	*Discosoma sp.*(DsRed)	(Shaner et al., 2004)
SNAP tag	Ligand-dependent				Monomer	*H. sapiens* (O^6-Alkylguanine-DNA Alkyltransferase)	(Juillerat et al., 2003)
HALO tag	Ligand-dependent				Monomer	*Rhodococcus sp.* (Haloalkane Dehalogenase)	(Los et al., 2008)

[a] Major excitation peak.

[b] Major emission peak.

[c] Product of extinction coefficient and quantum yield as reported in reference, in $(mM * cm)^{-1}$. Many brightness values originally summarized in (Shaner et al., 2005).

[c] Defined as the time for bleaching from an initial emission rate of 1,000 photons/s down to 500 photons/s under arc lamp illumination.

[e] Defined as twice the reported value of single mCherry in (Shaner et al., 2008).

[f] mApple shows much higher photostability under confocal illumination, see (Shaner et al., 2008).

Table 3.2. Compiled data for fluorescently-tagged KHC(1-560) motors in Chapter 3.

FP (dye)	Ionic Strength*	Velocity (µm/s) ± Bootstrap S.E.	RL (µm) ± Bootstrap S.E.	n (events)	Landing rate [events/(µm*s)] ± S.E.M.	Motor oligomeric state from photo-bleaching
EGFP	Low	0.84 ± 0.01	1.33 ± 0.05	460	5.4 ± 0.5	Mostly dimer
EGFP	Phys.	0.78 ± 0.01	1.34 ± 0.08	207	4.0 ± 0.3	
mEGFP	Low	0.85 ± 0.01	1.51 ± 0.06	461	6.6 ± 0.5	Dimer + Tetramer
mEGFP	Phys.	0.83 ± 0.01	1.53 ± 0.09	242	4.6 ± 0.5	
mNeGr	Low	0.83 ± 0.01	1.03 ± 0.04	510	7.9 ± 0.4	Dimer
mNeGr	Phys.	0.83 ± 0.01	1.00 ± 0.04	555	8.9 ± 0.8	
mCit	Low	0.84 ± 0.01	0.95 ± 0.02	492	7.4 ± 0.4	Dimer
mCit	Phys.	0.82 ± 0.01	1.00 ± 0.03	494	6.7 ± 0.6	
tdTom	Low	0.84 ± 0.01	0.76 ± 0.02	326	4.8 ± 0.5	Dimer
tdTom	Phys.	0.86 ± 0.01	0.72 ± 0.02	288	4.8 ± 0.7	
tagRFPt	Low	0.80 ± 0.01	1.53 ± 0.07	291	5.0 ± 0.5	Dimer + Tetramer
tagRFPt	Phys.	0.81 ± 0.01	1.42 ± 0.06	352	4.6 ± 0.4	
mApple	Low	0.81 ± 0.01	1.81 ± 0.09	211	2.8 ± 0.1	
mApple	Phys.	0.80 ± 0.01	1.65 ± 0.09	196	3.3 ± 0.8	
2xmCh	Low	0.84 ± 0.01	0.96 ± 0.03	326	5.1 ± 0.4	Dimer
2xmCh	Phys.	0.84 ± 0.01	0.89 ± 0.05	332	4.2 ± 0.4	
SNAP (OreGr488)	Low	0.82 ± 0.01	1.10 ± 0.04	223	2.7 ± 0.2	
SNAP (OreGr488)	Phys.	0.84 ± 0.01	1.07 ± 0.06	144	1.8 ± 0.3	
SNAP (505-STAR)	Low	0.83 ± 0.01	1.46 ± 0.09	194	2.1 ± 0.3	
SNAP (505-STAR)	Phys.	0.84 ± 0.01	1.41 ± 0.09	208	2.4 ± 0.4	
SNAP (TMR)	Low	0.83 ± 0.01	1.45 ± 0.06	268	5.1 ± 0.6	
SNAP (TMR)	Phys.	0.82 ± 0.01	1.42 ± 0.08	256	4.9 ± 0.9	
HALO (OreGr488)	Low	0.83 ± 0.01	1.05 ± 0.08	63	0.37 ± 0.07	
HALO (OreGr488)	Phys.	0.82 ± 0.04	0.8 ± 0.2	13	0.08 ± 0.03	
HALO (TMR)	Low	0.84 ± 0.01	0.93 ± 0.04	215	3.8 ± 0.5	
HALO (TMR)	Phys.	0.84 ± 0.01	1.01 ± 0.05	197	3.1 ± 0.3	

*Low ionic strength (I.S.) buffer: 12 mM PIPES/KOH, 1 mM EGTA, and 2 mM $MgCl_2$, pH 6.8, I.S. = 28 mM. Physiological (Phys.) ionic strength buffer: 25 mM HEPES/KOH, 115 mM potassium acetate, 5 mM sodium acetate, 5 mM $MgCl_2$, and 0.5 mM EGTA, pH 7.4, I.S. = 145 mM.

3.6 References

Ayloo, S., Lazarus, J.E., Dodda, A., Tokito, M., Ostap, E.M., and Holzbaur, E.L. (2014). Dynactin functions as both a dynamic tether and brake during dynein-driven motility. Nature communications *5*, 4807. doi: 10.1038/ncomms5807

Block, S.M., Goldstein, L.S., and Schnapp, B.J. (1990). Bead movement by single kinesin molecules studied with optical tweezers. Nature *348*, 348-352. doi: 10.1038/348348a0

Bosch, P.J., Correa, I.R., Jr., Sonntag, M.H., Ibach, J., Brunsveld, L., Kanger, J.S., and Subramaniam, V. (2014). Evaluation of Fluorophores to Label SNAP-Tag Fused Proteins for Multicolor Single-Molecule Tracking Microscopy in Live Cells. Biophysical journal *107*, 803-814. doi: 10.1016/j.bpj.2014.06.040

Brady, S.T. (1985). A novel brain ATPase with properties expected for the fast axonal transport motor. Nature *317*, 73-75

Cai, D., McEwen, D.P., Martens, J.R., Meyhofer, E., and Verhey, K.J. (2009). Single molecule imaging reveals differences in microtubule track selection between Kinesin motors. PLoS biology *7*, e1000216. doi: 10.1371/journal.pbio.1000216

Cai, D., Verhey, K.J., and Meyhofer, E. (2007). Tracking single Kinesin molecules in the cytoplasm of mammalian cells. Biophysical journal *92*, 4137-4144. doi: 10.1529/biophysj.106.100206

Chalfie, M., Tu, Y., Euskirchen, G., Ward, W.W., and Prasher, D.C. (1994). Green fluorescent protein as a marker for gene expression. Science *263*, 802-805

Cormack, B.P., Valdivia, R.H., and Falkow, S. (1996). FACS-optimized mutants of the green fluorescent protein (GFP). Gene *173*, 33-38

Costantini, L.M., Fossati, M., Francolini, M., and Snapp, E.L. (2012). Assessing the tendency of fluorescent proteins to oligomerize under physiologic conditions. Traffic *13*, 643-649. doi: 10.1111/j.1600-0854.2012.01336.x

Dedecker, P., De Schryver, F.C., and Hofkens, J. (2013). Fluorescent proteins: shine on, you crazy diamond. Journal of the American Chemical Society *135*, 2387-2402. doi: 10.1021/ja309768d

Griesbeck, O., Baird, G.S., Campbell, R.E., Zacharias, D.A., and Tsien, R.Y. (2001). Reducing the environmental sensitivity of yellow fluorescent protein. Mechanism and applications. The Journal of biological chemistry *276*, 29188-29194. doi: 10.1074/jbc.M102815200

Han, L., Zhao, Y., Zhang, X., Peng, J., Xu, P., Huan, S., and Zhang, M. (2014). RFP tags for labeling secretory pathway proteins. Biochemical and biophysical research communications *447*, 508-512. doi: 10.1016/j.bbrc.2014.04.013

Heim, R., Cubitt, A.B., and Tsien, R.Y. (1995). Improved green fluorescence. Nature *373*, 663-664. doi: 10.1038/373663b0

Jain, R.K., Joyce, P.B., Molinete, M., Halban, P.A., and Gorr, S.U. (2001). Oligomerization of green fluorescent protein in the secretory pathway of endocrine cells. The Biochemical journal *360*, 645-649

Juillerat, A., Gronemeyer, T., Keppler, A., Gendreizig, S., Pick, H., Vogel, H., and Johnsson, K. (2003). Directed evolution of O6-alkylguanine-DNA alkyltransferase for efficient labeling of fusion proteins with small molecules in vivo. Chemistry & biology *10*, 313-317

Kremers, G.J., Gilbert, S.G., Cranfill, P.J., Davidson, M.W., and Piston, D.W. (2011). Fluorescent proteins at a glance. Journal of cell science *124*, 157-160. doi: 10.1242/jcs.072744

Kremers, G.J., Hazelwood, K.L., Murphy, C.S., Davidson, M.W., and Piston, D.W. (2009). Photoconversion in orange and red fluorescent proteins. Nature methods *6*, 355-358. doi: 10.1038/nmeth.1319

Landgraf, D., Okumus, B., Chien, P., Baker, T.A., and Paulsson, J. (2012). Segregation of molecules at cell division reveals native protein localization. Nature methods *9*, 480-482. doi: 10.1038/nmeth.1955

Los, G.V., Encell, L.P., McDougall, M.G., Hartzell, D.D., Karassina, N., Zimprich, C., Wood, M.G., Learish, R., Ohana, R.F., Urh, M., *et al.* (2008). HaloTag: a novel protein labeling technology for cell imaging and protein analysis. ACS chemical biology *3*, 373-382. doi: 10.1021/cb800025k

Merzlyak, E.M., Goedhart, J., Shcherbo, D., Bulina, M.E., Shcheglov, A.S., Fradkov, A.F., Gaintzeva, A., Lukyanov, K.A., Lukyanov, S., Gadella, T.W., *et al.* (2007). Bright

monomeric red fluorescent protein with an extended fluorescence lifetime. Nature methods *4*, 555-557. doi: 10.1038/nmeth1062

Olenych, S.G., Claxton, N.S., Ottenberg, G.K., and Davidson, M.W. (2007). The fluorescent protein color palette. Current protocols in cell biology / editorial board, Juan S Bonifacino [et al] *Chapter 21*, Unit 21 25. doi: 10.1002/0471143030.cb2105s36

Shaner, N.C., Campbell, R.E., Steinbach, P.A., Giepmans, B.N., Palmer, A.E., and Tsien, R.Y. (2004). Improved monomeric red, orange and yellow fluorescent proteins derived from Discosoma sp. red fluorescent protein. Nature biotechnology *22*, 1567-1572. doi: 10.1038/nbt1037

Shaner, N.C., Lambert, G.G., Chammas, A., Ni, Y., Cranfill, P.J., Baird, M.A., Sell, B.R., Allen, J.R., Day, R.N., Israelsson, M., *et al.* (2013). A bright monomeric green fluorescent protein derived from Branchiostoma lanceolatum. Nature methods *10*, 407-409. doi: 10.1038/nmeth.2413

Shaner, N.C., Lin, M.Z., McKeown, M.R., Steinbach, P.A., Hazelwood, K.L., Davidson, M.W., and Tsien, R.Y. (2008). Improving the photostability of bright monomeric orange and red fluorescent proteins. Nature methods *5*, 545-551. doi: 10.1038/nmeth.1209

Shaner, N.C., Steinbach, P.A., and Tsien, R.Y. (2005). A guide to choosing fluorescent proteins. Nature methods *2*, 905-909. doi: 10.1038/nmeth819

Soppina, V., Norris, S.R., Dizaji, A.S., Kortus, M., Veatch, S., Peckham, M., and Verhey, K.J. (2014). Dimerization of mammalian kinesin-3 motors results in superprocessive motion. Proceedings of the National Academy of Sciences of the United States of America *111*, 5562-5567. doi: 10.1073/pnas.1400759111

Thorn, K.S., Ubersax, J.A., and Vale, R.D. (2000). Engineering the processive run length of the kinesin motor. The Journal of cell biology *151*, 1093-1100

Vale, R.D. (2003). The molecular motor toolbox for intracellular transport. Cell *112*, 467-480

Vale, R.D., Funatsu, T., Pierce, D.W., Romberg, L., Harada, Y., and Yanagida, T. (1996). Direct observation of single kinesin molecules moving along microtubules. Nature *380*, 451-453. doi: 10.1038/380451a0

Vale, R.D., Reese, T.S., and Sheetz, M.P. (1985). Identification of a novel force-generating protein, kinesin, involved in microtubule-based motility. Cell *42*, 39-50

Yildiz, A., Tomishige, M., Vale, R.D., and Selvin, P.R. (2004). Kinesin walks hand-over-hand. Science *303*, 676-678. doi: 10.1126/science.1093753

Zacharias, D.A., Violin, J.D., Newton, A.C., and Tsien, R.Y. (2002). Partitioning of lipid-modified monomeric GFPs into membrane microdomains of live cells. Science *296*, 913-916. doi: 10.1126/science.1068539

Zhu, C., and Dixit, R. (2011). Single molecule analysis of the Arabidopsis FRA1 kinesin shows that it is a functional motor protein with unusually high processivity. Molecular plant *4*, 879-885. doi: 10.1093/mp/ssr077

Chapter 4 Two kinesin motors walk independently *in vitro* and in COS7 cells

Portions of this chapter have been adapted from the following publication:

Norris, S.R., Soppina, V., Dizaji, A.S., Schimert, K.I., Sept, D., Cai, D., Sivaramakrishnan, S., and Verhey, K.J. (2014). A method for multi-protein assembly in cells reveals independent action of kinesins in complex. *Journal of Cell Biology*, Accepted.

Author contributions:

S.R.N., V.S., D.C., and K.J.V. designed research. S.R.N., V.S., A.S.D., and K.S. performed research. A.S.D., D.S., and S.S. contributed new reagents or analytic tools. S.R.N. and A.S.D. analyzed data. S.R.N. and K.J.V. wrote the paper with input from all authors.

4.1 Introduction

In Chapter 2, I introduced a system of protein toolbox components for assembling multi-protein complexes in live cells. I began by characterizing the individual components of the system and performed proof-of-principle experiments to show complex assembly in cells. At the end of Chapter 2, I introduced preliminary data showing that assemblies of two kinesin-1 motors displayed enhanced run lengths relative to kinesin-1, but these experiments were difficult to interpret. I thus motivated the need to develop a two-color TIRF microscopy assay to investigate two-motor behavior with greater clarity. In Chapter 3, I discussed the various fluorescent tags that

could be used in such a two-color study. In the current chapter (Chapter 4), I use these insights to study two-motor behavior both *in vitro* and in live cells.

Processive molecular motors such as kinesin and dynein hydrolyze ATP to walk on polarized microtubule (MT) tracks in eukaryotic cells. These motors are largely responsible for the trafficking and organization of subcellular cargoes including organelles, vesicles, mRNA particles, and even viruses (Vale, 2003). Defects in intracellular transport have been linked to a range of diseases including neurodegeneration and cancer (Hirokawa et al., 2010; Yu and Feng, 2010). Although the biophysical and biochemical properties of individual motor proteins are well-characterized, the collective behavior of motors is less clear despite evidence that multiple motors are present on a given cellular cargo [e.g. (Ashkin et al., 1990; Hendricks et al., 2012; Hendricks et al., 2010; Laib et al., 2009; Miller and Lasek, 1985; Shubeita et al., 2008; Snow et al., 2004; Soppina et al., 2009)]. Detailed investigation of this collective behavior is crucial and necessary for understanding transport processes in the cell.

Intuitively, multiple motors are expected to cooperate to generate longer transport distances and sufficient force to pull a bulky cargo through the crowded cytoplasm at efficient speeds. Previous work reconstituting motor/cargo interactions *in vitro* supported these ideas, showing enhanced run lengths and higher forces for multiple kinesin-1 motors on plastic beads or quantum dots (Beeg et al., 2008; Block et al., 1990; Conway et al., 2012; Vershinin et al., 2007). Theoretical studies using mean-field and Monte Carlo approaches represent ideal motor efficiency and generally agree with these *in vitro* studies (Klumpp and Lipowsky, 2005; Kunwar et al., 2008). In contrast, recent *in vitro* studies using precisely defined DNA-based motor assemblies show that the run length enhancements caused by multiple kinesin-1 motors are much smaller than what is predicted by theory, and assemblies of exactly two motors show only a modest run length increase

(Derr et al., 2012; Furuta et al., 2013; Rogers et al., 2009). This result has been interpreted as negative interference between kinesin motors (Rogers et al., 2009) that can result in a decrease in motor velocity at very high motor concentrations (Bieling et al., 2008; Conway et al., 2012; Furuta et al., 2013). A load-dependent study of DNA-based motor assemblies showed that although two kinesin-1 motors are capable of generating additional force, they typically only utilized the action of one motor (Jamison et al., 2010). Thus, any cooperation between kinesin motors remains poorly understood.

Consistent with these recent observations of poor kinesin cooperativity *in vitro*, the transport of cellular cargoes is largely unaffected by a change in kinesin-1 number (Efremov et al., 2014; Shubeita et al., 2008). However, information regarding multiple motor behavior in live cells has been difficult to ascertain due to a lack of precise motor number control and the presence of endogenous competing motors (Barlan et al., 2013). Indeed, methods that directly correlate multi-motor behavior *in vitro* with that in cells are lacking. To address these issues, we developed a system for linking protein components with defined spacing and composition in cells (Chapter 2). This system is widely applicable to the study of multi-protein assemblies in cells and enables the study of multi-motor transport in a manner that a) more closely mimics the physiological state of motor-cargo linkages and b) reveals the influence of cellular architecture on motility events. In this chapter, we use a two-color TIRF microscopy approach to first confirm previous studies with complexes of two kinesin-1 motors, and then use the system to study the cooperative behaviors that arise when a slow kinesin-1 motor and a fast kinesin-3 motor are linked *in vitro* and in live cells. We find that two motors in complex largely function as individual motors that alternate their activities.

4.2 Materials and Methods

Plasmids. Constitutively active versions of the kinesin-1 motor rat KIF5C (aa 1-560) and the kinesin-3 motor rat KIF1A (aa 1-393 with the leucine zipper dimerizing segment of GCN4) have been described (Cai et al., 2009; Cai et al., 2007; Soppina et al., 2014). DNA fragments encoding SAH domains of various lengths were generated by PCR cloning of the relevant sequences: 5 nm helix from *H. sapiens* translation initiation factor IF-2; 10 nm helix from *S. scrofa* Myosin VI medial tail; 20 nm helix from *S. cerevisiae* mannosyltransferase MNN4; and 30 nm helix from *T. vaginalis* Kelch-motif family protein (Sivaramakrishnan et al., 2008; Sivaramakrishnan et al., 2009). The 60 nm helix is a tandem repeat of 30 nm helices separated by four tandem Gly-Ser-Gly (GSG) sequences. Multiple GSG repeats were also included between all scaffold and linker components to ensure flexibility and rotational freedom of each component. IA/IQ fusions were generated by insertion of oligonucleotides encoding the peptides. Plasmids encoding FKBP and FRB were obtained from Ariad Pharmaceuticals (Cambridge, MA) and are now available from Clontech (Mountain View, CA) as DmrA and DmrC, respectively. Plasmids encoding mNeonGreen were obtained from Allele Biotechnology (San Diego, CA). EF Hand and tandem mCherry sequences were synthesized (DNA 2.0, Menlo Park, CA). Plasmids encoding split superfolder GFP components were a gift from F. Pinaud (University of Southern California). The above components were subcloned behind the cytomegalovirus promoter in the EGFP-N1 vector (Clontech, Mountain View, CA); this vector also contains a SV40 origin for replication in mammalian cells and a kanamycin resistance cassette for amplification in *E. coli*. All plasmids were verified by DNA sequencing.

Cell culture. COS cells were cultured, transfected and lysed as described (Chapter 2) (Cai et al., 2007; Soppina et al., 2014).

***In vitro* single molecule motility assays**. Motor proteins in lysates containing 20 μM ATP (low ATP condition) or 2 mM ATP (saturating ATP condition) were added to flow chambers in P12 buffer (12 mM PIPES/KOH, 1 mM EGTA, and 2 mM $MgCl_2$, pH 6.8). To drive *in vitro* complex formation via split EF-Hand linkages, 5 μL of each lysate was incubated for 10 min on ice in the presence of 1 mM $CaCl_2$ and 1-5 μL of this mixed lysate was used for subsequent imaging. In all other motility assays, 0.5-5 μL of lysate was added directly to flow chambers containing HiLyte-647 labeled, taxol-stabilized MTs (Cytoskeleton, Denver, CO) and 45 μL of oxygen scavenger buffer (1 mM DTT, 1 mM MgCl2, 20 μM or 2 mM ATP, 10 mM glucose, 0.1 mg/mL glucose oxidase, 0.08 mg/mL catalase, 10 mg/mL BSA, and 10 μM taxol in P12). Motility assays were carried out at room temperature using a Nikon Ti-E/B microscope with a 100X 1.49 NA oil immersion TIRF objective with 1.5X tube lens (Nikon) equipped with three 20 mW diode lasers (488nm, 561nm, 640nm) combined into a single fiber and rapidly controlled via AOTF (Agilent, Santa Clara, CA). Images were collected via an EMCCD detector (iXon X3 DU897, 512x512, 16μM array, Andor). For near simultaneous, two-color imaging, the microscope was modified to include a dual-band laser polychroic mirror (ZT488/561rpc, Chroma), a dual-band sputtered emission filter (ZET488/561m, Chroma), and a dual-band sputtered clean-up filter (ZET488/561x, Chroma) and the AOTF was used to rapidly switch between 488 nm (2mW power) and 561 nm (4mW power) laser excitation with 50 ms exposures in each channel. Images were acquired continuously in saturating ATP and at 1 Hz for limiting ATP. Two-color colocalized events were defined as events that were separated by less than one pixel in both x and y for at least 20% of event lifetime. To avoid possible tracking differences arising from different fluorescence properties, only the run length and velocity values from the 488nm channel are reported.

Analysis of complexes containing two kinesin-1 motors *in vitro*. For analysis of kinesin-1 motility events, movies were converted to .tif stacks using ImageJ (National Institutes of Health, Bethesda, MD) and a standard deviation projection map (Image > Stack > Z Project) was created to generate a map of the MT tracks. MATLAB tracking software (Jaqaman et al. 2008) was used to automatically generate single-particle trajectories. This method uses a global optimization algorithm to generate complete trajectories of single particles even if particle signal is temporarily lost due to high background or signal loss. Default software parameters were used, except a rolling window time-average of three frames and a Gaussian mixed-model fit (10 iterations, $\alpha = 0.05$) were used to determine the subpixel location of particles. For particle tracking, the maximum gap to be closed was one frame, the minimum length of each connected trajectory was two frames, and parameters for directed motion with no diffusion were used. Only trajectories lasting at least five frames were considered. Non-processive trajectories were eliminated by classifying each event as linear or random based on the asymmetry in the scatter of particle positions along each trajectory, and keeping only linear events (Huet et al., 2006; Jaqaman et al., 2008). For two-color experiments, each channel (488nm, 561nm) was analyzed separately and the final trajectories were compared.

In the absence of scaffold, only 4.2% of kin1-mNeGr and kin1-2xmCh events were found to colocalize in the green and red channels, whereas more colocalized events were observed in the presence of scaffold. Complete multi-protein assembly is apparently limited by the dilute conditions of our assays. All four linkers were able to assemble kinesin motors on SAH scaffolds and resulted in similar motility properties for two-kin-1 complexes. Two-motor complexes assembled using the split GFP and the split EF Hand linkers showed a higher percentage of two motors in complex (colocalized kin1-mNeGr and kin1-2xmCh) than for complexes assembled via

the IQ/IA or DmrA/C linkers, presumably due to their higher affinities and the irreversible nature of the split GFP association. Thus, the split GFP and split EF Hand linkers were used for all two-motor assemblies reported in this study. The percentage of two-color events was also higher for shorter scaffolds (5, 10, or 20 nm), likely due to their higher expression levels.

To analyze the contribution of one- versus two-motor motility events to the population (Fig. 4.4), we assume that each motor independently has an identical mean velocity μ and standard deviation σ, with an associated probability distribution function (PDF):

$$PDF_{1motor}(x) = \frac{1}{\sigma_1\sqrt{2\pi}} e^{-\frac{(x-\mu_1)^2}{2\sigma_1^2}}$$

If two kinesin-1 motors are simultaneously bound to the MT, then the observed velocity distribution of the two-motor complex will be described by a PDF (blue line in Fig. 4.4) that is a combination of the two independent normal distributions with a standard deviation smaller than that of a single kinesin-1 motor by a factor of $\sqrt{2}$, as predicted by the central limit theorem.

$$PDF_{2motor}(x) = \frac{1}{\sigma_2\sqrt{2\pi}} e^{-\frac{(x-\mu_2)^2}{2\sigma_2^2}}$$

$$\text{Where } \mu_2 = (\mu_1 + \mu_1)/2 = \mu_1; \quad \text{and} \quad \sigma_2 = \frac{\sqrt{\sigma_1^2 + \sigma_1^2}}{2} = \frac{\sigma_1}{\sqrt{2}}$$

If only one motor engages the microtubule at a time, then the PDF should resemble that of a single motor (green line in Fig. 4.4). The experimentally-derived probability distribution for two kinesin-1 motors in complex (yellow dotted line in Fig. 4.4) falls in between these values. To determine the proportion of events driven by an individual motor in the complex, the observed two-motor standard deviation σ_2 was fit by:

$$\sigma_{observed} = \alpha * \sigma_1 + \left((1+\alpha) * \sigma_2\right)$$

Where α, a value that falls between 0 and 1, is the proportion of the single-motor contribution. The limits of α are defined by the fact that at α=0, two-motor events are driven by both motors (blue line in Fig. 4.4) and when α=1, two-motor events are driven by only one of the motors (green line in Fig. 4.4). We find that α=0.35 best describes the experimental data (yellow line in Fig. 4.4). Experimental data in Fig. 4.4 excludes data using the 30nm SAH which showed a significant decrease in mean velocity.

Analysis of complexes containing a kinesin-1 and a kinesin-3 motor *in vitro*. For analysis of kin1 + kin3 motility events, the high velocity of kin3 and the relatively weak signal of mCherry prevented analysis using the automated tracking routine. Instead, kymograph analysis was used. Maximum intensity projections were generated to determine the location of MTs and kymographs were generated (width = 5 pixels) along these tracks using Elements (Nikon, Melville, NY) for measuring run lengths and velocities. Only events of at least five frames (500 ms) were considered. For two-color, two-motor events, the reported velocity and run length values are only for segments where red and green trajectories overlap. Slow events were defined as two-motor events with a velocity slower than the mean + one standard deviation of kin1 alone. Fast events were defined as two-motor events with a velocity faster than the mean - one standard deviation of kin3 alone. Intermediate events were defined as two-motor events with a velocity between these thresholds. Speed-changing events were defined as two-color events with at least two discrete velocity segments (> 5 frames for each velocity).

Cumulative distribution functions (CDFs). CDFs of velocities and run lengths were generated via MATLAB and mean values were obtained as described (Thorn et al., 2000). CDFs

were used for statistical analysis because they are continuous and do not introduce any subjective binning. To obtain mean run length values, run length distributions were first reorganized into a CDF with the built-in MATLAB function ecdf, then the lsqcurvefit function was used to generate a least squares fit of the experimental CDF to the hypothetical distribution from x_0 to infinity, where x_0 is the minimum run length 0.3 μm (run length values less than 0.3 μm were deleted from the run length CDF):

$$CDF(x) = 1 - e^{(x_0 - x)/t},$$

where the decay constant *t* is the only fitted parameter. The mean run length for the distribution is then defined by adding the minimum run length x_0 to the decay constant. Errors were estimated by the bootstrap technique (Thorn et al., 2000) by using the MATLAB function bootfunc for resampling. Each distribution was resampled 200x and refit to the above CDF equation. The standard deviation of the bootstrap distribution for the resampled data sets was taken as the error for each fitted quantity.

Mean velocity values were obtained in an identical way only no minimum velocity was defined. Velocity CDFs were fit to the hypothetical CDF for a normal distribution using a nonlinear least squares fit with free parameters μ (mean) and σ (standard deviation):

$$CDF(x) = \frac{1}{2}\left[1 + erf\left(\frac{x - \mu}{\sqrt{2\sigma^2}}\right)\right]$$

Two-peaked Gaussian fits in Fig. 4.8 and 4.10 were obtained by fitting velocity CDFs to the hypothetical CDF for the sum of two normal distributions using a nonlinear least squares fit with free parameters μ_1 (mean of peak 1), σ_1 (standard deviation of peak 1), μ_2 (mean of peak 2) σ_2 (standard deviation of peak 2), and φ (relative contribution of peak 1, value between 0 and 1):

$$CDF(x) = \frac{\phi}{2}\left[1 + erf\left(\frac{x-\mu_1}{\sqrt{2\sigma_1^{\,2}}}\right)\right] + \frac{1-\phi}{2}\left[1 + erf\left(\frac{x-\mu_2}{\sqrt{2\sigma_2^{\,2}}}\right)\right]$$

Dotted lines in Fig. 4.8 and 4.10 were obtained by plotting the probability distribution function (PDF) of the sum of two Gaussians with the parameters obtained from the CDF fit above, and comparing to the binned data histogram:

$$PDF(x) = \frac{\phi}{\sigma_1\sqrt{2\pi}} Exp\left[\frac{-(x-\mu_1)^2}{2\sigma_1^{\,2}}\right] + \frac{1-\phi}{\sigma_2\sqrt{2\pi}} Exp\left[\frac{-(x-\mu_2)^2}{2\sigma_2^{\,2}}\right]$$

Live cell two-color single molecule assays and kymograph analysis. Live cell TIRF assays were performed as described (Cai et al., 2009). COS7 cells on a glass-bottomed dish (MatTek, Ashland, MA) were imaged at 37°C by TIRF microscopy (see above) at 25 ms exposures for each channel. Although 4-8 hrs after transfection was optimal for detecting single kinesin motors in the crowded cellular environment (Cai et al., 2007) , we found that very few two-motor complexes formed in this time period. Thus, cycloheximide (100 µg/mL # 94271, Amresco, Solon, OH) was added to and maintained in the cell culture media starting at 4 hrs after transfection to retain low protein expression but allow complex formation. For imaging, cells were treated with nocodazole, washed 3x in DMEM, and images were collected at 37˚C in Leibowitz L-15 without phenol red (Life Technologies #21083-027). Standard deviation maps were generated using ImageJ to show the location of motility events in cells. To decrease autofluorescence background and quantify motility events, the minimum intensity projection was subtracted from each pixel and then maximum intensity projection maps and kymographs were generated (max width = 5 pixels) along these tracks (Elements, Nikon). Two-color events were defined as processive, unidirectional events that colocalized within 1 pixel for at least three consecutive frames. Only continuous,

stationary tracks were considered in subsequent analysis. Kymograph analysis was carried out as described for kinesin-1 + kinesin-3 motors *in vitro*. Slow, fast, and intermediate events were defined as for analysis of *in vitro* events. Speed-changing events were two-color events with at least two easily discrete velocity segments (> 3 frames).

Wormlike chain modeling. To determine how much force is felt by each motor as both motors are engaged with the microtubule, we modeled the scaffold as a wormlike chain approximation where the contour length L_0 (end-to-end distance at full extension) and persistence length P (related to stiffness) are defined (Marko and Siggia, 1995):

$$F(x) = \frac{k_B T}{P} * \frac{1}{4}\left(1 - \frac{x}{L_0}\right)^{-2} - \frac{1}{4} + \frac{x}{L_0}$$

Because most experiments were performed with a 20 nm scaffold, we used contour length L_0 = 20 nm. Based on previous studies of the SAH (Sivaramakrishnan et al., 2009), we used a persistence length P = 15 nm. Using this model, we predict the motors will feel an internal force of 2.4 pN when the end-to-end separation of the helix is 16 nm, with the internal force rapidly increasing as a function of end-to-end separation.

4.3 Results

4.3.1 Two kinesin-1 motors show minimal cooperation *in vitro*

In the current chapter, we first use this system to investigate the cooperative behavior of two kinesin-1 motors attached to the same scaffold. Although previous studies have rigorously characterized the behavior of complexes of two kinesin-1 motors (see introduction), we wanted to confirm these results in our system to ensure that our components were not adversely affecting the system. To test this, we labeled a truncated, constitutively active version of the kinesin-1 motor, KIF5C(1-560) (hereafter referred to as kin1) with either monomeric Neon Green (mNeGr) or tandem mCherry (2xmCh) FPs, as this pair of FPs was determined to be optimal for two-color single molecule imaging (Chapter 3). A kin1-mNeGr motor was recruited to one end of a 20 nm scaffold in cells via the split GFP linker system (providing tandem green FPs), and a kin1-2xmCh motor was recruited to the other end of the scaffold in cell lysates via the split EF Hand linker system (Fig. 4.1A). Similar results were obtained using other linker systems (e.g. IA/IQ, see Materials and Methods). Motility events were observed by two-color TIRF microscopy and analyzed using an automated subpixel-resolution tracking routine (Jaqaman et al., 2008) where two-motor events were considered to be trajectories that overlapped by less than one pixel in the green and red channels. The split GFP was used to link the green kin1 motor because a false-positive, two-color signal would result if the red kin1 motor was used alongside the fluorescent split GFP.

Single kin1-mNeGr and kin1-2xmCh motors displayed characteristic kinesin-1 motility properties with velocities of 0.74 ± 0.01 μm/s and run lengths of 0.84 ± 0.03 μm (Fig. 4.2, Table 4.1). In the presence of scaffold, complexes containing two kinesin-1 motors on a 20-nm scaffold (co-localized kin1-mNeGr and kin1-2xmCh events) displayed no change in mean velocity but an increase in run length to 1.08 ± 0.04 μm/s (Fig. 4.3A-C, Table 4.1). The ~1.3-fold increase in run

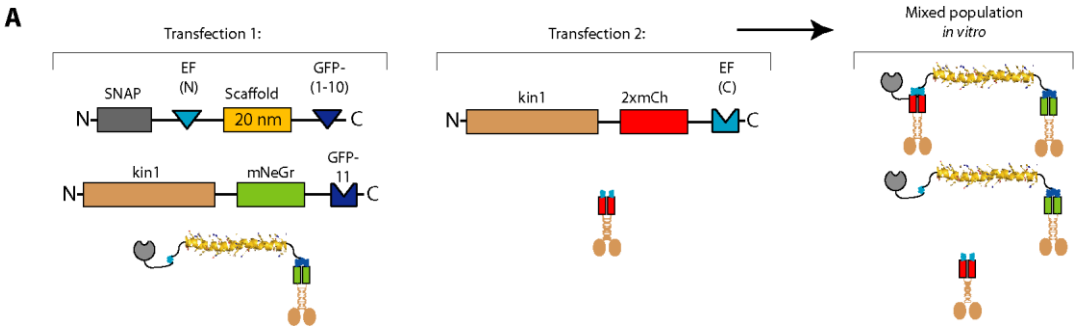

Figure 4.1. Investigating assemblies of two kinesin-1 motors in vitro.

(A) Schematic of experimental setup. COS7 cells were transfected with plasmids for self-assembly of kin1-mNeGr on the scaffold by the split GFP linker (Transfection 1) or for expression of kin1-2xmCh (Transfection 2). The cell lysates were mixed and the kin1-2xmCh component was recruited to the kin1-splitGFP-scaffold via the split EF Hand linker.

---

length is statistically significant ($p<0.001$, two-sample KS test), and consistent with previous work using DNA-based assemblies (Rogers et al., 2009), but is less than what is predicted from theoretical models (Klumpp and Lipowsky, 2005).

One possible explanation for why two kinesin-1 motors in complex display minimal cooperativity is that geometric constraints limit the MT access of the second motor. Alternatively, as suggested by (Driver et al., 2010), both motors may have access to the MT but only one motor is able to effectively engage for motility. In this case, the motility of the assembly is driven by a mixture of one-motor and two-motor states. To verify the engagement state of the second motor, we took two approaches: 1) a detailed analysis of the velocity distributions of these two-kin1 complexes under saturating ATP conditions and 2) a study of the same complexes under limiting ATP conditions to increase the pause time of each motor on the MT surface.

First, we examined the velocity distributions of the two-motor complexes compared to the single motor state (Fig. 4.4). As stated above, the mean velocity was identical within standard

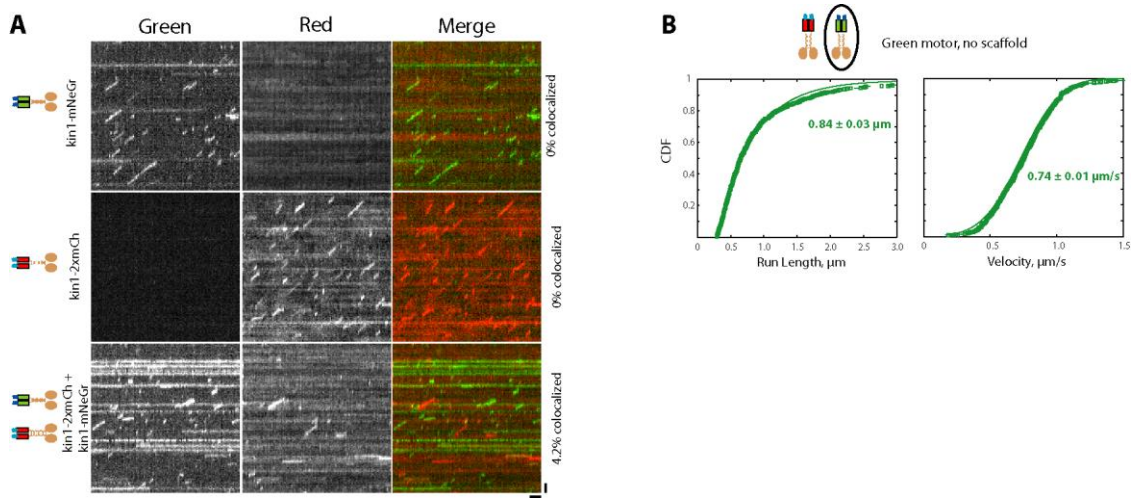

Figure 4.2. Single kin1 motors display characteristic motility properties in vitro.

(A,B) Motility data for single kin1 motors. **(A)** Representative kymographs of kin1-mNeGr expressed alone (top row), kin3-2xmCh expressed alone (middle row), or kin1-mNeGr and kin3-2xmCh in absence of scaffold (bottom row). Scale bars = 1 µm vertical, 1 s horizontal. % colocalized indicates the percentage of two-motor events (the percentage of green events that colocalize with red events via automated tracking analysis). **(B)** CDFs of the run length (left) and velocity (right) for the kin1-mNeGr events when kin1-mNeGr and kin3-2xmCh were expressed in absence of scaffold. n = 622 events.

---

error for single motors and two-motor complexes (Fig. 4.3). However, the two-motor events display a tighter distribution of velocities than single motors (Fig. 4.4). This is expected due to the central limit theorem, which predicts that the standard deviation for a two-motor body (assuming each motor has an identical velocity distribution) would be smaller by a factor of $\frac{1}{\sqrt{2}}$.

This prediction assumes that both motors are fully engaged and contributing equally to the net motion, such that the observed velocity is actually a mean of two identical motor observations. Interestingly, although the observed two-motor velocity distribution (yellow points, Fig. 4.4) is smaller than the velocity distribution of a single motor (green points, Fig. 4.4), it is not as small as this predicted value which assumes complete engagement of both motors (blue line, Fig. 4.4).

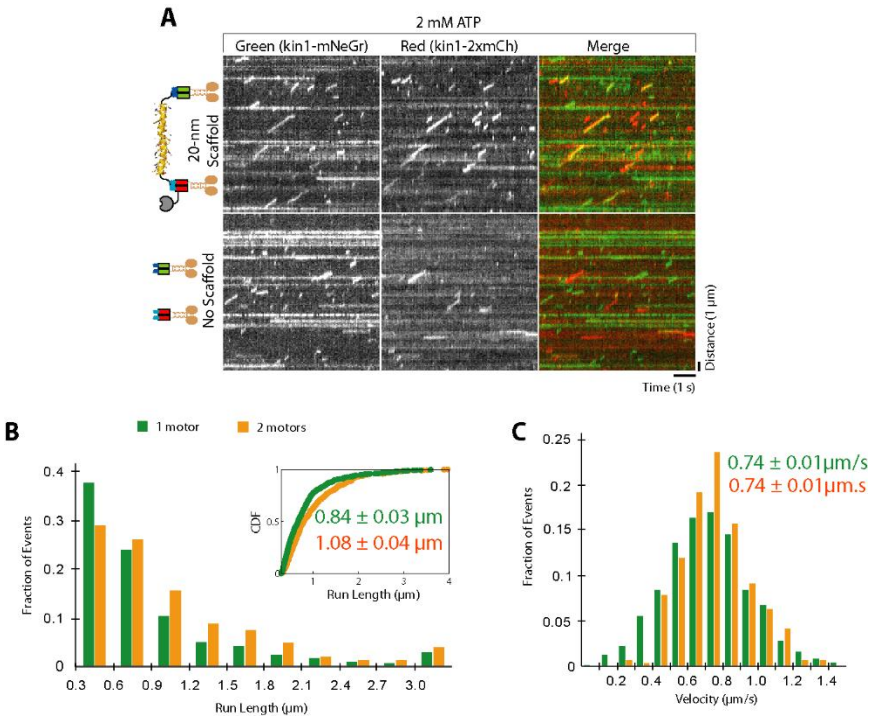

Figure 4.3. Two kinesin-1 motors show minimal cooperation in saturating ATP conditions.

(A-C) Motors in lysates were imaged by single molecule microscopy at saturating ATP (2 mM). **(A)** Representative kymographs. In the absence of scaffold, only individual red or green events are observed. In the presence of scaffold, the co-localizing red and green events (yellow) represent assembled two-motor complexes. Time is on the x-axis (scale bar, 1 sec) and distance is on the y-axis (scale bar, 1 µm). **(B,C)** The (B) run lengths and (C) velocities were determined for single kin1-mNeGr motors in the absence of scaffold (green bars, n=622 events) and for two-color two-motor events in the presence of scaffold (yellow bars, n=318 events). The population data from two independent experiments were plotted in histograms. The inset in the run length graph shows the same data fit to a CDF.

Thus, this indicates a mixture of states where either one or two motors are engaged (yellow line, Fig. 4.4, see Materials and Methods).

Although the velocity distribution analysis suggests that both motors are typically not engaging the MT simultaneously, we needed to verify that both motors are geometrically able to simultaneously engage the MT in our experimental system. To test this, we examined two-motor motility under limiting ATP conditions (20 µM) in order to increase the pause time of each motor

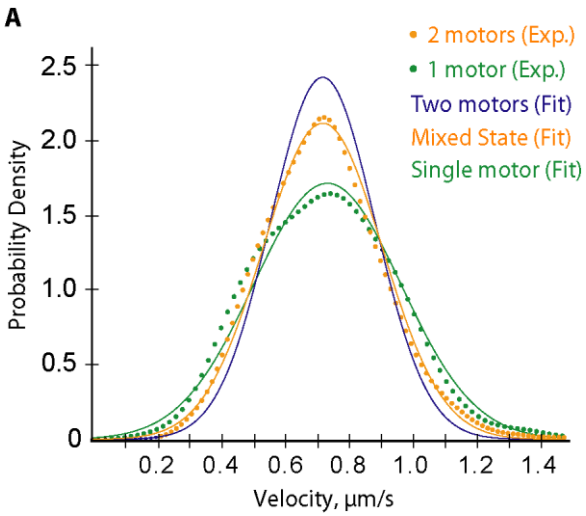

Figure 4.4. Velocity distribution analysis of assemblies with two kinesin-1 motors.

(A) Probability densities for the experimentally-obtained velocities of one motor (kin1-mNeGr, green dotted line, n=622 events) and two-motor (kin1-mNeGr + kin1-mCh, yellow dotted line, n = 1454) events. Solid lines show fits to theoretically-derived distribution functions for two-motor motility events driven by only one motor (green line), both motors (blue line) or a mixed state where either one or two motors can contribute (yellow line).

David Sept (Biomedical Engineering, University of Michigan) proposed and performed analysis for Fig. 4.4.

---

on the MT surface (Xu et al., 2012). We found that two-motor complexes show a substantial increase in run length at limiting ATP (2.6 ± 0.2 µm) relative to single motors (1.10 ± 0.04 µm, Fig. 4.5A-C, Table 4.1). Together, these data suggest that while two-motor kinesin-1 complexes are capable of coordinating to produce longer runs, the two-motor complexes mostly behave as a single motor under saturating ATP conditions.

The SAH-based scaffolds also allowed us to investigate the influence of separation distance on motor cooperativity (Fig. 4.6). Interestingly, two motors were better able to cooperate for an increased run length when separated by shorter scaffolds (5, 10, or 20 nm) than when separated by longer scaffolds (30 or 60 nm) (Fig. 4.6B,D, Table 4.1). At the longer separations, no significant increase in run length was observed ($p>0.01$, two-sample KS test). Because the shorter scaffolds

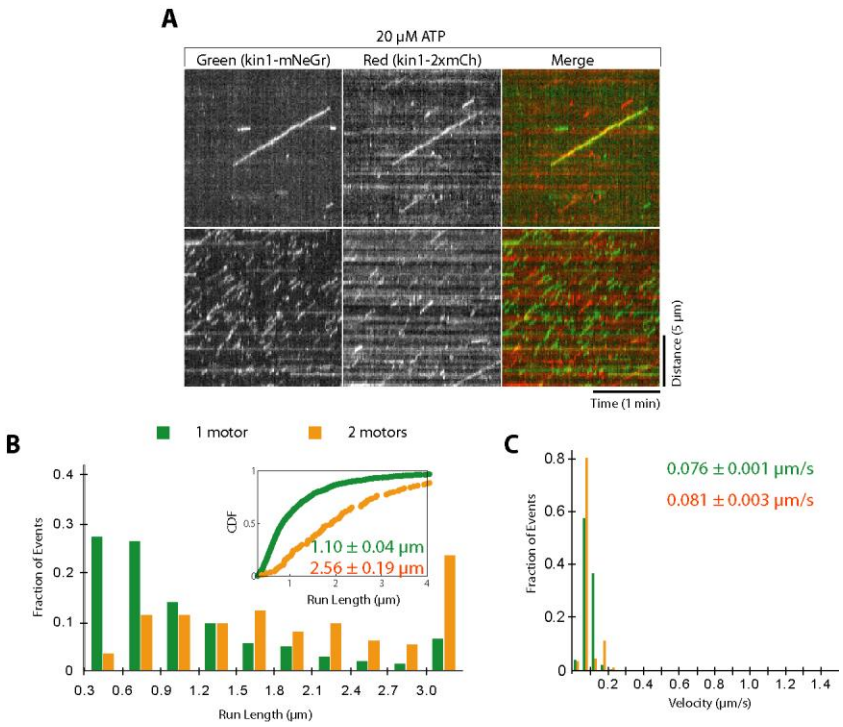

Figure 4.5. Two kinesin-1 motors show enhanced cooperation in limiting ATP conditions.

(A-C) Motors in lysates were imaged by single molecule microscopy at limiting ATP (20 µM). **(A)** Representative kymographs. Time is on the x-axis (scale bar, 1 min) and distance is on the y-axis (scale bar, 5 µm). **(B,C)** The (B) run lengths and (C) velocities were determined for single kin1-mNeGr motors in the absence of scaffold (green bars, n=840 events) and for two-color two-motor events in the presence of scaffold (yellow bars, n=116 events). The population data from two independent experiments were plotted in histograms. The inset in the run length graph shows the same data fit to a CDF.

---

are more rigid (Sivaramakrishnan et al., 2009), this result indicates that motor cooperativity is enhanced by a rigid connection (see Discussion). Overall, our results for complexes of two kinesin-1 motors suggest that these motors typically work independently when in complex and neither help nor hinder the partner motor.

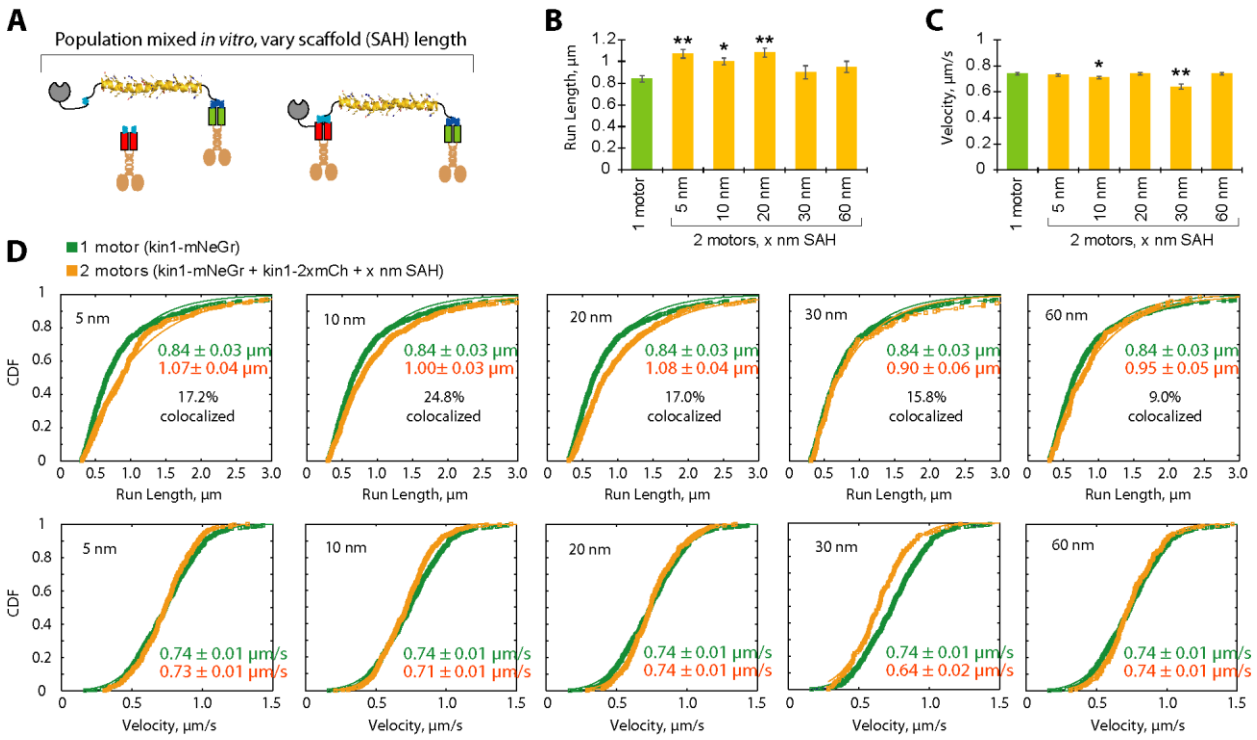

Figure 4.6. Cooperativity between kinesin-1 motors is influenced by separation distance.

(A) Schematic of experimental setup. COS7 cell lysates were mixed as in Fig. 4.1 with different SAH domains providing variable separation distances between motors and motility was recorded by TIRF microscopy. **(B)** CDFs of run lengths (top panels) and velocities (bottom panels) for two kin1 motors separated by the indicated SAH helix length (yellow). The motility of single kin1-mNeGr motors (green) is included as a reference for each data set. The average ± S.E is indicated on each graph. % colocalized indicates the percentage of two-motor events (the percentage of green events that colocalize with red events via automated tracking analysis) in each population. **(C,D)** Graphs of mean **(C)** run lengths and **(D)** velocities for single kin1-mNeGr motors (green; n = 622 events) or for two kin1 motors separated by the indicated SAH helix length (yellow; n = 311 for 5nm, n = 626 for 10nm, n = 318 for 20nm, n = 124 for 30nm, n = 199 for 60nm). **p < 0.001; *p < 0.01 as compared to the single kin1 motor (two-sample KS-test). Data are presented as the average ± S.E.

4.3.2 A slow and a fast kinesin motor in complex do not cooperate *in vitro*

We next used our protein-based biosynthetic system to determine the emergent behaviors that arise when two different types of kinesin motors are attached to the same cargo. For this, we paired kinesin-1 with KIF1A, an extremely fast and superprocessive member of the kinesin-3

family (Soppina et al., 2014). Kinesin-1 and kinesin-3 are both essential for neuronal trafficking and are known to cooperate during hyphal growth in *Ustilago maydis* (Barkus et al., 2008; Schuchardt et al., 2005).

A slow kinesin-1 motor labeled with mNeGr (kin1-mNeGr) was attached to one end of a scaffold using the split GFP linker and a fast kinesin-3 motor labeled with 2xmCherry (kin3-2xmCh) was attached to the other end using the split EF-Hand linker (Fig. 4.7A). In the absence of scaffold, green kin1 and red kin3 motors walked independently on the same track with characteristic motility properties (Fig. 4.7B, Table 4.1). Kin1 motors displayed an average velocity of 0.80 ± 0.02 μm/s and average run length of 0.74 ± 0.02 μm whereas kin3 displayed significantly higher average velocity (1.76 ± 0.03 μm/s) and run length (7.9 ± 0.2 μm) (Fig. 4.7D, Table 4.1). In the presence of scaffold, the two-motor events exhibited an average velocity of 1.01 ± 0.03 μm/s (Fig. 4.7D, Table 4.1), suggesting that the motors coordinate their motilities to generate intermediate speeds. However, careful dissection of the individual motility events revealed diverse behaviors not compatible with motor coordination (Fig. 4.7C). 51% of the two-motor events were classified as slow as their velocities matched those of single kin1 motors whereas 11% of the two-motor events were classified as fast as their velocities matched those of single kin3 motors (Fig. 4.7C, Table SI). Only 8% of the two-motor events displayed intermediate velocities. The remaining 30% of the two-motor events exhibited alternating periods of slow and fast movement (Fig. 4.7C), suggesting a possible alternating action mechanism between kin1 and kin3. Interestingly, although kinesin-3 motors have a higher affinity for MTs than kinesin-1 motors (Soppina and Verhey, 2014; Woehlke et al., 1997), kin1 appears to dominate two-motor motility *in vitro*, suggesting that it can act as a brake to slow down overall velocity. These results

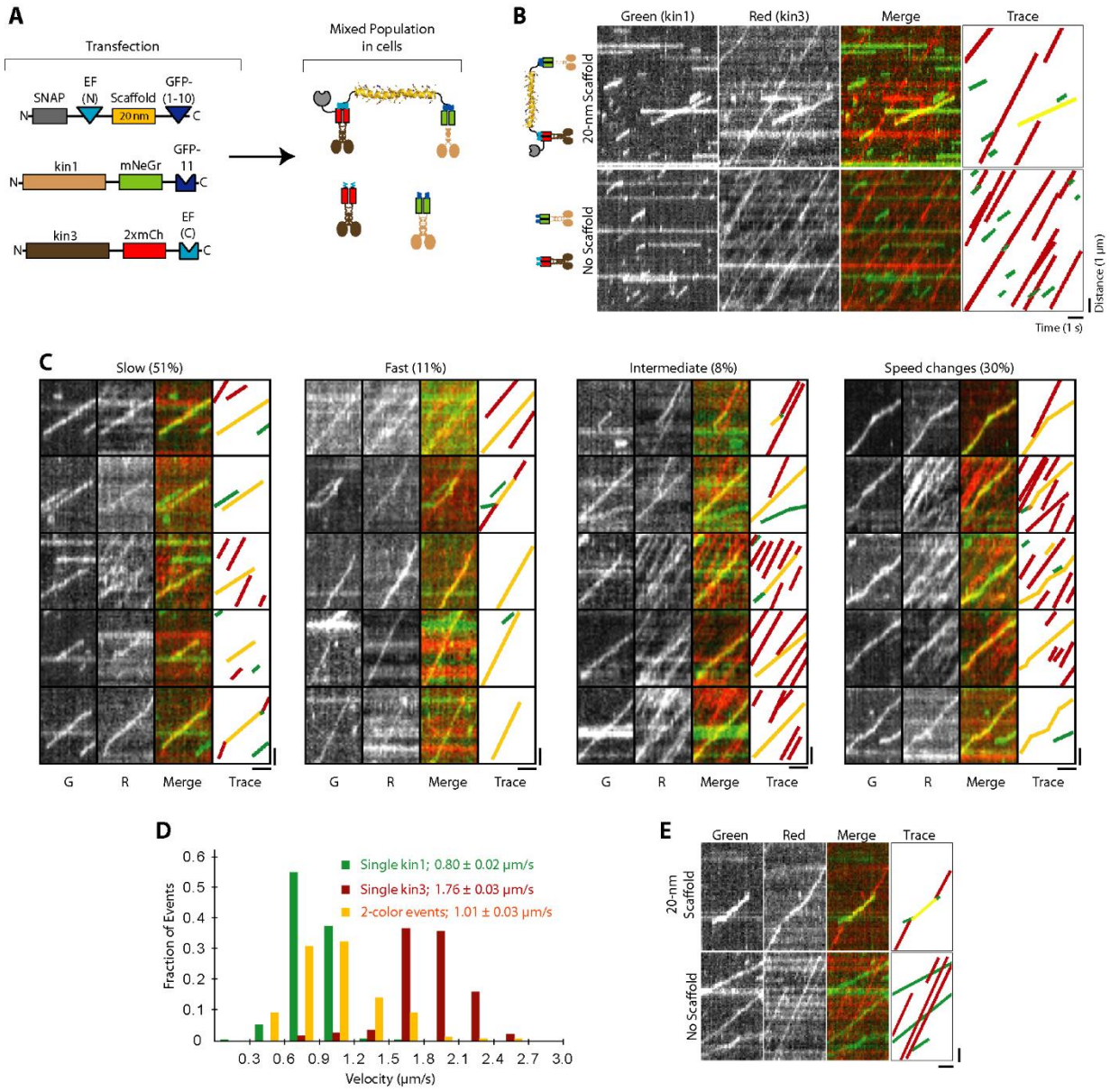

Figure 4.7. Slow kinesin-1 and fast kinesin-3 motors in complex do not coordinate but alternate their activities in vitro.

(A) Schematic of experimental setup. COS7 cells were transfected with plasmids for self-assembly of a slow kin1-mNeGr motor and a fast kin3-2xmCh motor on a 20 nm scaffold in cells. **(B-E)** Analysis of kin1+kin3 motility *in vitro*. **(B)** Representative kymographs. In the presence of scaffold, a subset of the motility events show colocalized green and red trajectories (yellow in merge). In the absence of scaffold, kin1-mNeGr (green) and kin3-2xmCh (red) walk independently with characteristic speeds and processivities. Time is on the x-axis (scale bar, 1 sec) and distance is on the y-axis (scale bar, 1 µm). **(C)** Representative kymographs of the four types of behavior observed for complexes of kin1-mNeGr + kin3-2xmCh assembled on a 20 nm scaffold and analyzed *in vitro*. Slow, n = 103 events; Fast, n = 23 events; Intermediate, n = 17 events; Speed change, n = 60 events; Total two-color events, n = 203 events.

Scale bars = 1 μm vertical, 1 s horizontal. **(D)** The velocities were determined for single kin1-mNeGr motors (green bars, n=207 events) and single kin3-2xmCh motors in the absence of scaffold (red bars, n=211 events), and for two-color two-motor events in the presence of scaffold (yellow bars, n=203 events) in three independent experiments. The average ± S.E is indicated**. (E)** Representative kymographs of merging and splitting behaviors observed for kin1+kin3 complexes. In the presence of scaffold, kin1-mNeGr (green) and kin3-2xmCh (red) traces were observed to merge together (11% of all two-color events) and to split apart (21% of all two-color events). Scale bars = 1 μm vertical, 1 s horizontal.

support the conclusion that kinesin motors in complex work independently and additionally show that the motors can "take turns" or alternate their activities.

Two-motor complexes containing a slow kin1 motor and a fast kin3 motor also engaged in interesting merging and splitting behaviors. In 11% of all two-motor events, kin1 and kin3 motors were observed to move independently before merging and moving together on the MT (Fig. 4.7E). In 21% of all two-motor events, the complexed kin1 and kin3 motors split apart and continued as individual motors (Fig. 4.7E). Merging and splitting behaviors were not observed for two kinesin-1 motors present on the same scaffold (Fig. 4.3), suggesting that these behaviors are due to slow and fast motors influencing each other's motility. The majority of the splitting events (74%) were preceded by a period of slow velocity. We speculate that as the slow kin1 motor moves processively, the fast kin3 motor is attempting to engage with the track and when it does, it exerts a force that results in dissociation of the motor-scaffold linkage.

4.3.3 Two-motor complexes behave in a track-dependent manner in COS7 cells

A major advantage to our protein-based approach is the potential to assemble two-motor complexes and track their behavior in live cells. After overnight expression, kin3-2xmCh motors

accumulated at the plus ends of MTs in the cell periphery, presumably due to their superprocessivity (Soppina et al., 2014), whereas the moderately processive kin1-mNeGr motors were more diffusely distributed (Fig. 4.8A, no scaffold). In the presence of scaffold, kin1 was redistributed to the cell periphery due to the activity of the associated kin3 motor (Fig. 4.8A), providing validation of two-motor assembly at high expression.

To resolve individual motility events in live cells, we limited protein expression to 4 hours before TIRF imaging (Cai et al., 2009). Even at low expression levels, kin3 motors and linked kin1+kin3 motors accumulated at the plus ends of MTs in the cell periphery, making it difficult to track motility events along cytoplasmic MTs. We thus released individual kin3 and linked kin1+kin3 motors into the cytoplasm by treating cells with the MT-depolymerizing agent nocodazole (NZ) for 5 minutes prior to imaging (Fig. 4.9). To analyze motility events, we generated standard deviation (SD) maps (Cai et al., 2009) to locate MTs (Fig. 4.8B) and then generated kymographs along each track (Fig. 4.8C). Two-motor complexes moved at a mean velocity of 3.2 ± 0.1 μm/s, which falls roughly between the individual motor velocities of 1.55 ± 0.02 μm/s for kin1 and 4.29 ± 0.05 μm/s for kin3 at 37°C in live cells (Fig. 4.8D, Table 4.1). Analysis of individual two-motor motility events revealed that the mean intermediate velocity was due to the linked kin1 and kin3 motors acting independently. Similar to *in vitro*, we observed four types of two-motor behavior in live cells: slow (31%), fast (42%), intermediate (14%), and changes (13%) in velocity (Fig. 4.8G). That the majority of two-motor events in cells display fast kin3-like velocities (Fig. 4.8G) was surprising given the dominance of slow kin1-like events *in vitro* (Fig. 4.7D). The dramatic shift in kin3 engagement can be seen in the velocity distributions for two-motor complexes in live cells, which now appear bimodal and are best fit by a two-peaked Gaussian distribution (Fig. 4.8E). These findings show that slow kin1 and fast kin3 motors in a

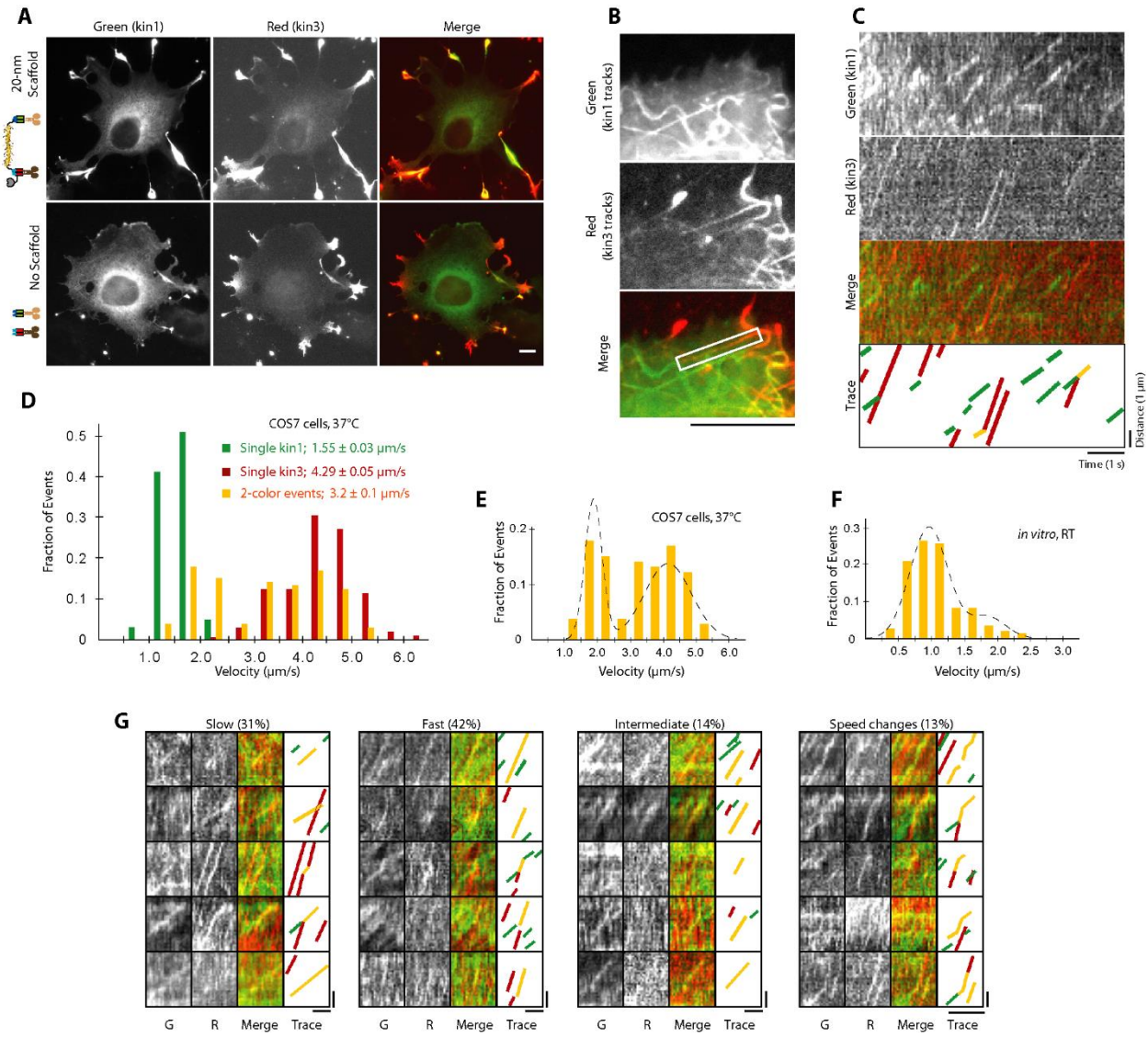

Figure 4.8. Slow kinesin-1 and fast kinesin-3 motors in complex alternate their activities in COS7 cells.

(A) Representative images of fixed COS7 cells expressing kin1-mNeGr (green) and kin3-2xmCh (red) in presence or absence of scaffold. Scale bar = 10 µm. **(B-G)** COS7 cells expressing kin1-mNeGr, kin3-2xmCh, and a 20 nm scaffold were briefly treated with NZ (see Fig. 4.9A) and imaged live by TIRF microscopy. From the movie, a standard deviation map was generated **(B)** to visualize the motility tracks. Scale bar = 10 µm. The MT track in the white boxed region in (B) was used to generate **(C)** kymographs in each channel. Scale bars = 1 µm vertical, 1 s horizontal. **(D)** The velocities of kin1-mNeGr in the absence of scaffold (green bars, n = 102 events), kin3-2xmCh in the absence of scaffold (red, n = 210 events), and two-motor complexes (yellow, n = 106 events) were determined and are plotted as a histogram for each population. **(E-F)** The velocity distributions of kin1+kin3 complexes in COS7 cells at 37°C (E) compared to kin1+kin3 complexes *in vitro* at room temperature (RT) (F). The velocities show a clear bimodal distribution in COS7 cells whereas the slow kin1 motor dominates *in vitro*. n = 106 events in COS7 cells, n

= 203 events *in vitro*, three independent experiments each. **(G)** Representative kymographs of the four types of behavior observed for kin1+kin3 complexes in live cells: slow, fast, intermediate, and speed change events.

two-motor complex behave as individual motors in cells and that kin1 is unable to dominate the motility behavior.

We hypothesized that the relative ability of either kin1 or kin3 to dominate two-motor motility events is influenced by the MT itself. Our previous work demonstrated that kinesin-1 motors are selective in cells and prefer to move along the stable MTs marked by post-translational modifications whereas kinesin-3 motors are non-selective and use all MTs for motility (Cai et al., 2009). We thus predicted that the motors would equally engage with the stable MTs whereas kin3 motors would be better able to engage on dynamic MTs. To test this, we treated cells with NZ at times and concentrations that selectively enrich specific subsets of MTs (Piperno et al., 1987). Treatment of cells with low levels of NZ results in enrichment of stable, modified MTs (Fig. 4.10A, middle panel). In this case, the behavior of the two-motor complexes was not changed in terms of mean velocity (3.1 ± 0.2 μm/s, Fig. 4.10B, middle panel, Table 4.1) or the proportion of slow kin1-like (31%) and fast kin3-like (43%) events observed (Fig. 4.10C). Individual kin1 and kin3 motor behavior was unchanged under any MT condition (Fig. 4.11). Thus, both kin1 and kin3 motors are able to effectively engage and drive motility of the complex on stable, modified MTs.

Treatment of cells with high levels of NZ depolymerizes nearly all MTs and NZ washout enables the examination of motility events on newly-grown (nascent) MTs (Fig. 4.10A, bottom panel). Under these conditions, the velocity distribution of the two-motor events was again fit by a two-peaked Gaussian but with an increase in the average velocity of two-motor complexes (3.4 ± 0.2 μm/s, Fig. 4.10B, bottom panel, Table 4.1). Importantly, a dramatic decrease in the number

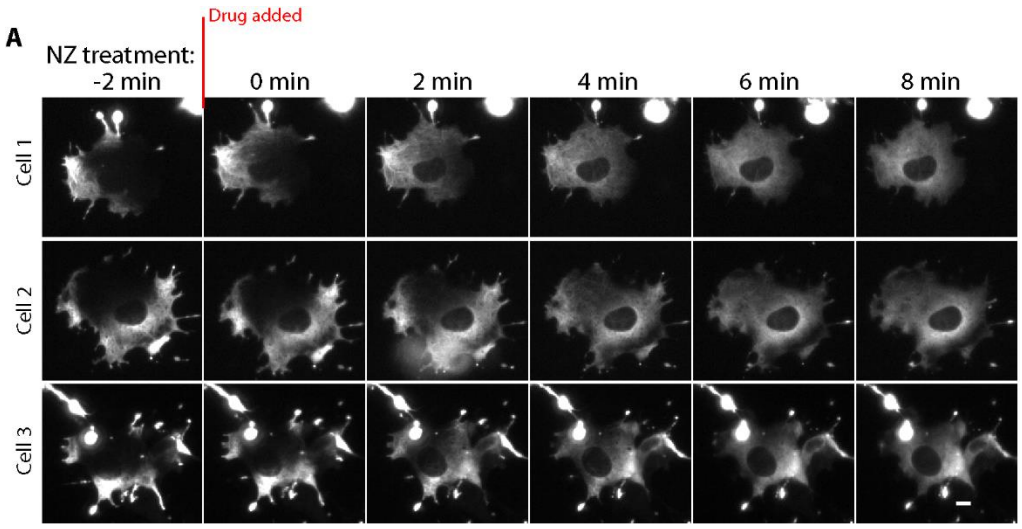

Figure 4.9. Nocodazole treatment to reset kinesin-3 into COS7 cytosol.

(A) Live COS7 cells expressing kin3-2xmCh were imaged during NZ treatment (33 µM). Images of three representative cells before (-2 min) and after addition (0-8 min) of NZ are shown. Superprocessive kin3-2xmCh motors accumulate at the plus ends of MTs at the cell periphery but are released into the cytosol upon NZ treatment. Scale bar = 10 µm.

---

of slow kin1-like motility events was observed under these conditions (from 31% to 14%, Fig. 4.10C). These results suggest that kin3 can dominate motility events under conditions where kin1 displays a decreased affinity for the MT track. We conclude that the slower kin1 motor typically dominates two-motor motility events. This is observed both *in vitro* on homogeneous MTs and in cells on stable MTs. The fast kin3 motors are only able to dominate motility events in cells on the dynamic population of MTs which kin1 does not prefer.

4.4 Discussion

In Chapter 2, I described a new method for assembling multi-protein complexes of defined composition and geometry in mammalian cells that is broadly applicable to studying cellular

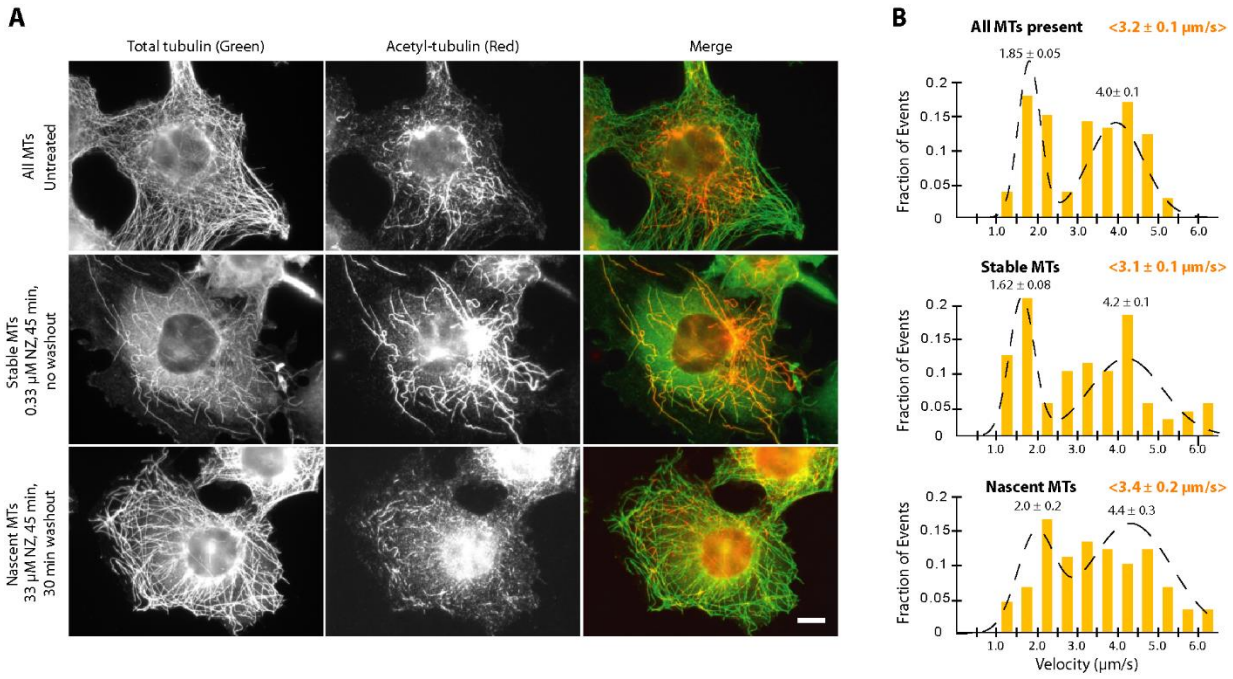

C

Microtubule state	NZ treatment	n (events)	% slow	% fast	% intermediate	% speed change
in vitro (unknown PTMs, taxol - stabilized	n/a	203	51	11	8	30
All, Heterogeneous	33 µM, 5 min, washout	106	31	42	14	13
Stable, modified	0.33 µM, 45 min, no washout	84	31	43	5	21
Nascent, unmodified	33 µM, 45 min, washout	90	14	44	16	26

Figure 4.10. The contribution of kinesin-1 versus kinesin-3 to motility of the complex is influenced by the MT state.

(A) Characterization of the MT populations in COS7 cells under various nocodazole (NZ) treatments. COS7 cells were treated with NZ for the indicated times and then fixed and stained with antibodies to total tubulin (green) and K40-acetyled α-tubulin (red) which marks stable MTs. Scale bar = 10 µm. **(B)** Velocity distributions for kin1+kin3 complexes (two-color events) in (top) untreated COS7 cells containing heterogeneous MT tracks (n = 106 events), (middle) NZ-treated cells containing stable MTs (n = 84 events), and (bottom) cells containing nascent MTs upon NZ washout (n = 90 events). The average velocity ± SE of the kin1+kin3 complexes under each condition is indicated by yellow text in brackets at the top of each graph. The average velocities ± SE of each peak in the distribution is indicated by black text above the peak. See Fig. 4.11 for histograms of the single kin1 and kin3 motors under the different conditions.

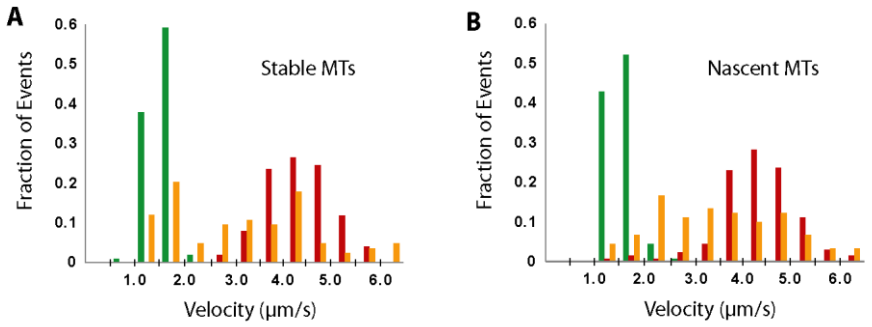

Figure 4.11. Additional velocity distribution data from COS7 MT conditions.

(A-B) Velocities on stable versus nascent MTs in live COS7 cells. **(A)** The velocities of kin1-mNeGr (green, n=103 events), kin3-2xmCh (red, n=102 events), and two-motor complexes (yellow, n=84 events) on stable MTs (NZ treatment) were determined and are plotted as a histogram for the populations. **(B)** The velocities of kin1-mNeGr (green, n=138 events), kin3-2xmCh (red, n=135 events), and two-motor complexes (yellow, n=90 events) on nascent MTs (NZ washout) were determined and are plotted as a histogram for the populations.

signaling, motility and organization. In the current chapter, we applied this assembly method to compare, for the first time, the cooperative behavior of two-kinesin complexes *in vitro* to that in live cells. We find that two kinesin motors in complex act independently (do not help or hinder each other) and that they can alternate their activities. For complexes containing a fast and a slow kinesin motor, the outcome in cells is a bimodal distribution of fast and slow velocities that is influenced by the state of the MT track where the motility event takes place. In cells and *in vitro*, we find that the protein-protein attachments between motor and scaffold are dynamic and that the force exerted by one motor can result in dissociation of the complex.

Our finding that assemblies of two kinesin-1 motors display a small but significant 1.3-fold increase in run length relative to single motors generally agrees with previous *in vitro* studies that showed a 1.3- to 2.7-fold increase in run length for two kinesin-1 motors assembled on a DNA scaffold or attached to antibodies (Derr et al., 2012; Furuta et al., 2013; Rogers et al., 2009; Xu et al., 2012). The fact that these experimentally-derived increases in run length fall short of the

predicted theoretical values (Klumpp and Lipowsky, 2005) suggests that multi-motor complexes are influenced by a factor not replicated in the modeling. One component likely to influence the ability of kinesin motors to coordinate their motion is the stiffness of the linkage. A more rigid connecting element could be beneficial to multiple motor coordination by allowing motors to effectively communicate via force transduction through a stiff mechanical component. Indeed, the largest increases in run length for two kinesin-1 assemblies have been found for rigid DNA assemblies (Derr et al., 2012; Furuta et al., 2013) whereas more flexible assemblies have resulted in less cooperativity (this study and Rogers et al., 2009). In addition, we found that increasing the length of our scaffold, which effectively decreases the rigidity of the connecting element, dampens the cooperative effect on run length (Fig. 4.6). A fluid linkage between motors, such as the lipid bilayer of a vesicular cargo, would then be expected to result in no cooperativity; indeed, recent work in cells demonstrated that motor number does not impact the run length of cargoes such as lipid droplets or peroxisomes (Efremov et al., 2014; Shubeita et al., 2008).

Our work provides the first analysis of the emergent behaviors that arise when plus-end directed kinesin motors with different motility properties are attached to the same cargo, in this case a SAH scaffold. We find that two-motor assemblies comprised of a slow kinesin-1 motor and a fast kinesin-3 motor rarely move with intermediate velocities, in contrast to previous work where mixtures of slow and fast motors displayed intermediate velocities in MT gliding assays (Bieling et al., 2010; Pan et al., 2006). These findings highlight the importance of investigating population behaviors at the single molecule level. Analysis of individual events *in vitro* demonstrated that, of all two-motor events, most (62%) displayed either kin1-like (51%) or kin3-like (11%) motility properties rather than an intermediate velocity (8%). In addition, 30% of the two-motor events were observed to change speed while in motion, alternating between slow kin1-driven motility and

fast kin3-driven motility. These results suggest an alternating action mechanism in which only one motor is active at a time.

A major advantage to our protein-based assembly method is the ability to study molecular behavior within the cellular environment. Indeed, we directly compared the motility of kin1+kin3 complexes *in vitro* to that in live cells. We found that the slow kin1 motor dominates the motility events *in vitro* on homogeneous microtubules whereas the fast kin3 motor can dominate the motility events in cells where the heterogeneous microtubule network provides MT tracks that are not utilized by kin1. These findings emphasize that studying intracellular trafficking events in cells reveals emergent properties that cannot be ascertained from *in vitro* assays.

Single molecule analysis also revealed dynamic merging and splitting behaviors for fast and slow motors in complex. Such merging and splitting behaviors were not observed for complexes containing two kinesin-1 motors, suggesting that this is a novel behavior that arises when motors with different velocities are present on the same scaffold. The majority of the splitting behaviors (74%) occurred after periods of slow transport. We interpret this to mean that if the fast kin3 motor engages with the MT during a motility event driven by the slow kin1 motor, then kin3 generates an internal force on the two-motor complex that results in dissociation of the motor-scaffold complex. Our observation of such dynamic behaviors is likely due to our use of more physiological protein-protein linkages between the motors and the scaffold. By modeling the 20-nm SAH scaffold as a wormlike chain (WLC) using the published SAH persistence length (Sivaramakrishnan et al., 2009), we predict that the SAH exerts a restoring force of 2-4 pN as it approaches its maximum extension (see Materials and Methods). The magnitude of this force is less than the stall force of either motor (Svoboda and Block, 1994; Tomishige et al., 2002) and is comparable to the rupture force of non-covalent protein-protein interactions (Weisel et al., 2003).

We believe the most likely scenario underlying the splitting of slow and fast motor complexes is the dissociation of the split EF Hand linker since the split GFP linkage is essentially irreversible (Pinaud and Dahan, 2011). Unless motor-cargo attachments in cells are strengthened by additional mechanisms, it seems likely that similar forces could cause motors to dissociate from their cargoes during motility events.

Taken together, our results indicate that kinesin motors present on the same scaffold or cargo typically do not coordinate their activities but rather act independently and can alternate their activities. What then is the functional output of attaching several motors to a cellular cargo? We can envision two outputs of multi-motor cooperativity that are critical for motor-driven transport in cells. First, multiple kinesins can work together to increase force generation under applied loads. Indeed, multiple kinesin-1 motors cooperate to maintain motor velocity when pulling against a viscous drag (Gagliano, 2010; Jamison et al., 2012) and are required to generate sufficient force for tube formation (Campas et al., 2008; Leduc et al., 2004). Second, the presence of multiple motors may enable the cargo to avoid traffic jams or navigate around obstacles on the microtubule track (Ross et al., 2008; Schroeder et al., 2010).

The protein-based assembly system we developed can be used to generate higher order motor complexes, for example, teams of three or more kinesin motors in a variety of geometric arrangements. The system will also be useful to probe the functional output of kinesin stalk and tail domains by utilizing full-length motors as well as light chains and other associated proteins, especially in combination with RNAi inhibition or mutagenesis approaches. Furthermore, this assembly system can be used to study not just multiple kinesin motors, but the interplay of kinesins with dynein and myosin motors. Recent studies indicate that kinesin and dynein motors in complex engage in a tug-of-war or co-dependence when present on cellular organelles (Hancock,

2014) and that teams of processive myosin motors can cooperate both *in vitro* and in live cells (Efremov et al., 2014; Hariadi et al., 2014; Lu et al., 2012). The methods we have developed will be useful to understand how the mechanical properties of each motor allow it to influence and be influenced by other motors in complex. Additionally, the tools developed here will be useful for studying other cellular processes that require the assembly of defined macromolecular structures such as signaling pathways and intracellular transport events.

Table 4.1. Summary of single molecule motility events observed in Chapter 4.*

Motors	Scaffold	Location	Temp.	MTs	ATP	Tracking	Velocity ± SE (μm/s)	Run Length ± SE (μm)	n
kin1-mNeGr		*In vitro*	RT	Bovine brain	2 mM	Automated	0.74 ± 0.01	0.84 ± 0.01	622
kin1-mNeGr + kin1-2xmCh	5 nm	*In vitro*	RT	Bovine brain	2 mM	Automated	0.73 ± 0.01	1.07 ± 0.04	311
kin1-mNeGr + kin1-2xmCh	10 nm	*In vitro*	RT	Bovine brain	2 mM	Automated	0.71 ± 0.01	1.00 ± 0.03	626
kin1-mNeGr + kin1-2xmCh	20 nm	*In vitro*	RT	Bovine brain	2 mM	Automated	0.74 ± 0.01	1.08 ± 0.04	318
kin1-mNeGr + kin1-2xmCh	30 nm	*In vitro*	RT	Bovine brain	2 mM	Automated	0.64 ± 0.02	0.90 ± 0.06	124
kin1-mNeGr + kin1-2xmCh	60 nm	*In vitro*	RT	Bovine brain	2 mM	Automated	0.74 ± 0.01	0.95 ± 0.05	199
kin1-mNeGr		*In vitro*	RT	Bovine brain	20 μM	Automated	0.076 ± 0.001	1.10 ± 0.04	840
kin1-mNeGr + kin1-2xmCh	20 nm	*In vitro*	RT	Bovine brain	20 μM	Automated	0.081 ± 0.003	2.56 ± 0.19	116
kin1-mNeGr		*In vitro*	RT	Bovine brain	2 mM	Kymograph	0.80 ± 0.02	0.74 ± 0.02	207
kin3-2xmCh		*In vitro*	RT	Bovine brain	2 mM	Kymograph	1.76 ± 0.03	7.9 ± 0.2	211
kin1-mNeGr + kin3-2xmCh	20 nm	*In vitro*	RT	Bovine brain	2 mM	Kymograph	1.01 ± 0.03	3.1 ± 0.2	203
kin1-mNeGr + kin3-2xmCh "Slow"	20 nm	*In vitro*	RT	Bovine brain	2 mM	Kymograph	0.82 ± 0.03	2.5 ± 0.3	103
kin1-mNeGr + kin3-2xmCh "Fast"	20 nm	*In vitro*	RT	Bovine brain	2 mM	Kymograph	1.71 ± 0.07	3.6 ± 0.8	23
kin1-mNeGr + kin3-2xmCh "Intermediate"	20 nm	*In vitro*	RT	Bovine brain	2 mM	Kymograph	1.09 ± 0.03	3.0 ± 0.4	17
kin1-mNeGr + kin3-2xmCh "Speed-Change"	20 nm	*In vitro*	RT	Bovine brain	2 mM	Kymograph	1.02 ± 0.04	3.8 ± 0.3	60
kin1-mNeGr		COS7	37°C	All		Kymograph	1.55 ± 0.03		102
kin3-2xmCh		COS7	37°C	All		Kymograph	4.29 ± 0.05		210
kin1-mNeGr + kin3-2xmCh	20 nm	COS7	37°C	All		Kymograph	3.2 ± 0.1		106
kin1-mNeGr		COS7	37°C	Modified		Kymograph	1.55 ± 0.03		103
kin3-2xmCh		COS7	37°C	Modified		Kymograph	4.29 ± 0.07		102
kin1-mNeGr + kin3-2xmCh	20 nm	COS7	37°C	Modified		Kymograph	3.1 ± 0.2		84
kin1-mNeGr		COS7	37°C	Nascent		Kymograph	1.55 ± 0.02		138
kin3-2xmCh		COS7	37°C	Nascent		Kymograph	4.29 ± 0.07		135
kin1-mNeGr + kin3-2xmCh	20 nm	COS7	37°C	Nascent		Kymograph	3.4 ± 0.2		90

* *In vitro* experiments (Fig. 4.1-4.7) were performed at room temperature whereas COS7 experiments (Fig. 4.8-4.11) were performed at 37°C. Automated tracking was used for Fig. 4.1-4.6 and kymograph analysis was used for Figure 4.7-4.11. Average velocities and run lengths are from fits to CDF, when possible. Standard error is defined as the standard deviation from bootstrapping.

4.5 References

Ashkin, A., Schutze, K., Dziedzic, J.M., Euteneuer, U., and Schliwa, M. (1990). Force generation of organelle transport measured in vivo by an infrared laser trap. Nature *348*, 346-348. doi: 10.1038/348346a0

Barkus, R.V., Klyachko, O., Horiuchi, D., Dickson, B.J., and Saxton, W.M. (2008). Identification of an axonal kinesin-3 motor for fast anterograde vesicle transport that facilitates retrograde transport of neuropeptides. Molecular biology of the cell *19*, 274-283. doi: 10.1091/mbc.E07-03-0261

Barlan, K., Rossow, M.J., and Gelfand, V.I. (2013). The journey of the organelle: teamwork and regulation in intracellular transport. Current opinion in cell biology *25*, 483-488. doi: 10.1016/j.ceb.2013.02.018

Beeg, J., Klumpp, S., Dimova, R., Gracia, R.S., Unger, E., and Lipowsky, R. (2008). Transport of beads by several kinesin motors. Biophysical journal *94*, 532-541. doi: 10.1529/biophysj.106.097881

Bieling, P., Kronja, I., and Surrey, T. (2010). Microtubule motility on reconstituted meiotic chromatin. Current biology : CB *20*, 763-769. doi: 10.1016/j.cub.2010.02.067

Bieling, P., Telley, I.A., Piehler, J., and Surrey, T. (2008). Processive kinesins require loose mechanical coupling for efficient collective motility. EMBO reports *9*, 1121-1127. doi: 10.1038/embor.2008.169

Block, S.M., Goldstein, L.S., and Schnapp, B.J. (1990). Bead movement by single kinesin molecules studied with optical tweezers. Nature *348*, 348-352. doi: 10.1038/348348a0

Cai, D., McEwen, D.P., Martens, J.R., Meyhofer, E., and Verhey, K.J. (2009). Single molecule imaging reveals differences in microtubule track selection between Kinesin motors. PLoS biology *7*, e1000216. doi: 10.1371/journal.pbio.1000216

Cai, D., Verhey, K.J., and Meyhofer, E. (2007). Tracking single Kinesin molecules in the cytoplasm of mammalian cells. Biophysical journal *92*, 4137-4144. doi: 10.1529/biophysj.106.100206

Campas, O., Leduc, C., Bassereau, P., Casademunt, J., Joanny, J.F., and Prost, J. (2008). Coordination of Kinesin motors pulling on fluid membranes. Biophysical journal *94*, 5009-5017. doi: 10.1529/biophysj.107.118554

Conway, L., Wood, D., Tuzel, E., and Ross, J.L. (2012). Motor transport of self-assembled cargos in crowded environments. Proceedings of the National Academy of Sciences of the United States of America *109*, 20814-20819. doi: 10.1073/pnas.1209304109

Derr, N.D., Goodman, B.S., Jungmann, R., Leschziner, A.E., Shih, W.M., and Reck-Peterson, S.L. (2012). Tug-of-war in motor protein ensembles revealed with a programmable DNA origami scaffold. Science *338*, 662-665. doi: 10.1126/science.1226734

Driver, J.W., Rogers, A.R., Jamison, D.K., Das, R.K., Kolomeisky, A.B., and Diehl, M.R. (2010). Coupling between motor proteins determines dynamic behaviors of motor protein assemblies. Physical chemistry chemical physics : PCCP *12*, 10398-10405. doi: 10.1039/c0cp00117a

Efremov, A.K., Radhakrishnan, A., Tsao, D.S., Bookwalter, C.S., Trybus, K.M., and Diehl, M.R. (2014). Delineating cooperative responses of processive motors in living cells. Proceedings of the National Academy of Sciences of the United States of America *111*, E334-343. doi: 10.1073/pnas.1313569111

Furuta, K., Furuta, A., Toyoshima, Y.Y., Amino, M., Oiwa, K., and Kojima, H. (2013). Measuring collective transport by defined numbers of processive and nonprocessive kinesin motors. Proceedings of the National Academy of Sciences of the United States of America *110*, 501-506. doi: 10.1073/pnas.1201390110

Gagliano, J., Walb, M., Blaker, B., Macosko, J.C., and Holzwarth, G. (2010). Kinesin velocity increases with the number of motors pulling against viscoelastic drag. European Biophysics Journal *39*

Hancock, W.O. (2014). Bidirectional cargo transport: moving beyond tug of war. Nature reviews Molecular cell biology *15*, 615-628. doi: 10.1038/nrm3853

Hariadi, R.F., Cale, M., and Sivaramakrishnan, S. (2014). Myosin lever arm directs collective motion on cellular actin network. Proceedings of the National Academy of Sciences of the United States of America. doi: 10.1073/pnas.1315923111

Hendricks, A.G., Holzbaur, E.L., and Goldman, Y.E. (2012). Force measurements on cargoes in living cells reveal collective dynamics of microtubule motors. Proceedings of the National Academy of Sciences of the United States of America *109*, 18447-18452. doi: 10.1073/pnas.1215462109

Hendricks, A.G., Perlson, E., Ross, J.L., Schroeder, H.W., 3rd, Tokito, M., and Holzbaur, E.L. (2010). Motor coordination via a tug-of-war mechanism drives bidirectional vesicle transport. Current biology : CB *20*, 697-702. doi: 10.1016/j.cub.2010.02.058

Hirokawa, N., Niwa, S., and Tanaka, Y. (2010). Molecular motors in neurons: transport mechanisms and roles in brain function, development, and disease. Neuron *68*, 610-638. doi: 10.1016/j.neuron.2010.09.039

Huet, S., Karatekin, E., Tran, V.S., Fanget, I., Cribier, S., and Henry, J.P. (2006). Analysis of transient behavior in complex trajectories: application to secretory vesicle dynamics. Biophysical journal *91*, 3542-3559. doi: 10.1529/biophysj.105.080622

Jamison, D.K., Driver, J.W., and Diehl, M.R. (2012). Cooperative responses of multiple kinesins to variable and constant loads. The Journal of biological chemistry *287*, 3357-3365. doi: 10.1074/jbc.M111.296582

Jamison, D.K., Driver, J.W., Rogers, A.R., Constantinou, P.E., and Diehl, M.R. (2010). Two kinesins transport cargo primarily via the action of one motor: implications for intracellular transport. Biophysical journal *99*, 2967-2977. doi: 10.1016/j.bpj.2010.08.025

Jaqaman, K., Loerke, D., Mettlen, M., Kuwata, H., Grinstein, S., Schmid, S.L., and Danuser, G. (2008). Robust single-particle tracking in live-cell time-lapse sequences. Nature methods *5*, 695-702. doi: 10.1038/nmeth.1237

Klumpp, S., and Lipowsky, R. (2005). Cooperative cargo transport by several molecular motors. Proceedings of the National Academy of Sciences of the United States of America *102*, 17284-17289. doi: 10.1073/pnas.0507363102

Kunwar, A., Vershinin, M., Xu, J., and Gross, S.P. (2008). Stepping, strain gating, and an unexpected force-velocity curve for multiple-motor-based transport. Current biology : CB *18*, 1173-1183. doi: 10.1016/j.cub.2008.07.027

Laib, J.A., Marin, J.A., Bloodgood, R.A., and Guilford, W.H. (2009). The reciprocal coordination and mechanics of molecular motors in living cells. Proceedings of the National Academy of Sciences of the United States of America *106*, 3190-3195. doi: 10.1073/pnas.0809849106

Leduc, C., Campas, O., Zeldovich, K.B., Roux, A., Jolimaitre, P., Bourel-Bonnet, L., Goud, B., Joanny, J.F., Bassereau, P., and Prost, J. (2004). Cooperative extraction of membrane nanotubes by molecular motors. Proceedings of the National Academy of Sciences of the United States of America *101*, 17096-17101. doi: 10.1073/pnas.0406598101

Lu, H., Efremov, A.K., Bookwalter, C.S., Krementsova, E.B., Driver, J.W., Trybus, K.M., and Diehl, M.R. (2012). Collective dynamics of elastically coupled myosin V motors. The Journal of biological chemistry *287*, 27753-27761. doi: 10.1074/jbc.M112.371393

Marko, J.F., and Siggia, E.D. (1995). Stretching DNA. Macromolecules *28*, 8759-8770. doi: Doi 10.1021/Ma00130a008

Miller, R.H., and Lasek, R.J. (1985). Cross-bridges mediate anterograde and retrograde vesicle transport along microtubules in squid axoplasm. The Journal of cell biology *101*, 2181-2193

Pan, X., Ou, G., Civelekoglu-Scholey, G., Blacque, O.E., Endres, N.F., Tao, L., Mogilner, A., Leroux, M.R., Vale, R.D., and Scholey, J.M. (2006). Mechanism of transport of IFT particles in C. elegans cilia by the concerted action of kinesin-II and OSM-3 motors. The Journal of cell biology *174*, 1035-1045. doi: 10.1083/jcb.200606003

Pinaud, F., and Dahan, M. (2011). Targeting and imaging single biomolecules in living cells by complementation-activated light microscopy with split-fluorescent proteins. Proceedings of the National Academy of Sciences of the United States of America *108*, E201-210. doi: 10.1073/pnas.1101929108

Piperno, G., LeDizet, M., and Chang, X.J. (1987). Microtubules containing acetylated alpha-tubulin in mammalian cells in culture. The Journal of cell biology *104*, 289-302

Rogers, A.R., Driver, J.W., Constantinou, P.E., Kenneth Jamison, D., and Diehl, M.R. (2009). Negative interference dominates collective transport of kinesin motors in the absence of load. Physical chemistry chemical physics : PCCP *11*, 4882-4889. doi: 10.1039/b900964g

Ross, J.L., Shuman, H., Holzbaur, E.L., and Goldman, Y.E. (2008). Kinesin and dynein-dynactin at intersecting microtubules: motor density affects dynein function. Biophysical journal *94*, 3115-3125. doi: 10.1529/biophysj.107.120014

Schroeder, H.W., 3rd, Mitchell, C., Shuman, H., Holzbaur, E.L., and Goldman, Y.E. (2010). Motor number controls cargo switching at actin-microtubule intersections in vitro. Current biology : CB *20*, 687-696. doi: 10.1016/j.cub.2010.03.024

Schuchardt, I., Assmann, D., Thines, E., Schuberth, C., and Steinberg, G. (2005). Myosin-V, Kinesin-1, and Kinesin-3 cooperate in hyphal growth of the fungus Ustilago maydis. Molecular biology of the cell *16*, 5191-5201. doi: 10.1091/mbc.E05-04-0272

Shubeita, G.T., Tran, S.L., Xu, J., Vershinin, M., Cermelli, S., Cotton, S.L., Welte, M.A., and Gross, S.P. (2008). Consequences of motor copy number on the intracellular transport of kinesin-1-driven lipid droplets. Cell *135*, 1098-1107. doi: 10.1016/j.cell.2008.10.021

Sivaramakrishnan, S., Spink, B.J., Sim, A.Y., Doniach, S., and Spudich, J.A. (2008). Dynamic charge interactions create surprising rigidity in the ER/K alpha-helical protein motif. Proceedings of the National Academy of Sciences of the United States of America *105*, 13356-13361. doi: 10.1073/pnas.0806256105

Sivaramakrishnan, S., Sung, J., Ali, M., Doniach, S., Flyvbjerg, H., and Spudich, J.A. (2009). Combining single-molecule optical trapping and small-angle x-ray scattering measurements to compute the persistence length of a protein ER/K alpha-helix. Biophysical journal *97*, 2993-2999. doi: 10.1016/j.bpj.2009.09.009

Snow, J.J., Ou, G., Gunnarson, A.L., Walker, M.R., Zhou, H.M., Brust-Mascher, I., and Scholey, J.M. (2004). Two anterograde intraflagellar transport motors cooperate to build sensory cilia on C. elegans neurons. Nature cell biology *6*, 1109-1113. doi: 10.1038/ncb1186

Soppina, V., Norris, S.R., Dizaji, A.S., Kortus, M., Veatch, S., Peckham, M., and Verhey, K.J. (2014). Dimerization of mammalian kinesin-3 motors results in superprocessive motion. Proceedings of the National Academy of Sciences of the United States of America *111*, 5562-5567. doi: 10.1073/pnas.1400759111

Soppina, V., Rai, A.K., Ramaiya, A.J., Barak, P., and Mallik, R. (2009). Tug-of-war between dissimilar teams of microtubule motors regulates transport and fission of endosomes. Proceedings of the National Academy of Sciences of the United States of America *106*, 19381-19386. doi: 10.1073/pnas.0906524106

Soppina, V., and Verhey, K.J. (2014). The family-specific K-loop influences the microtubule on-rate but not the superprocessivity of kinesin-3 motors. Molecular biology of the cell *25*, 2161-2170. doi: 10.1091/mbc.E14-01-0696

Svoboda, K., and Block, S.M. (1994). Force and velocity measured for single kinesin molecules. Cell *77*, 773-784

Thorn, K.S., Ubersax, J.A., and Vale, R.D. (2000). Engineering the processive run length of the kinesin motor. The Journal of cell biology *151*, 1093-1100

Tomishige, M., Klopfenstein, D.R., and Vale, R.D. (2002). Conversion of Unc104/KIF1A kinesin into a processive motor after dimerization. Science *297*, 2263-2267. doi: 10.1126/science.1073386

Vale, R.D. (2003). The molecular motor toolbox for intracellular transport. Cell *112*, 467-480

Vershinin, M., Carter, B.C., Razafsky, D.S., King, S.J., and Gross, S.P. (2007). Multiple-motor based transport and its regulation by Tau. Proceedings of the National Academy of Sciences of the United States of America *104*, 87-92. doi: 10.1073/pnas.0607919104

Weisel, J.W., Shuman, H., and Litvinov, R.I. (2003). Protein-protein unbinding induced by force: single-molecule studies. Current opinion in structural biology *13*, 227-235

Woehlke, G., Ruby, A.K., Hart, C.L., Ly, B., Hom-Booher, N., and Vale, R.D. (1997). Microtubule interaction site of the kinesin motor. Cell *90*, 207-216

Xu, J., Shu, Z., King, S.J., and Gross, S.P. (2012). Tuning multiple motor travel via single motor velocity. Traffic *13*, 1198-1205. doi: 10.1111/j.1600-0854.2012.01385.x

Yu, Y., and Feng, Y.M. (2010). The role of kinesin family proteins in tumorigenesis and progression: potential biomarkers and molecular targets for cancer therapy. Cancer *116*, 5150-5160. doi: 10.1002/cncr.25461

Chapter 5 Discussion and conclusions

In this dissertation, I first introduced a novel system for assembling defined complexes of multiple proteins inside living cells (Chapter 2). Based on observations made while characterizing this system, I then presented a survey of the efficiency of various fluorescent tags for use in single molecule motility assays (Chapter 3). Finally, I used this system to study cooperative behavior between kinesin motors, showing that motors walk independently *in vitro* and behave in a track-dependent manner in live cells (Chapter 4). This technique provides a powerful tool for studying biological processes of groups of proteins in their native environment, and will hopefully be valuable both for the molecular motors field and cell biology in general. In this chapter, I first discuss the role of works such as this in the greater scheme of scientific research, then I discuss general lessons and principles that we have learned through the development of this technique. Following this, I discuss future directions for this project in detail and share preliminary data where necessary. Finally, I conclude with an assessment of where our work fits in the greater field and how investigators may use our techniques to advance their own research.

5.1 More is different: considering the impact of scale in cell biology

In 1972, P.W. Anderson published the now highly-cited article *More is different – broken symmetry and nature of hierarchical structure of science* (Anderson, 1972). In this article, Anderson begins by acknowledging the reductionist hypothesis, which he presumes most scientists accept without question. A given system, this hypothesis argues, is governed by a set of

fundamental laws. These laws, in turn, are determined by simplifying a system into its most constituent, "reduced," parts. If all of these fundamental, reduced laws are completely understood, one could then apply this knowledge to create a predictive model for the system. Often, this approach works quite well. Newtonian physics, for instance, is often described as a reductionist system. We can very accurately describe the emergent behavior of a car by breaking it down into its reduced parts: the engine (one part) generates a force that spins the wheels (another part) through a series of gears and axels (more parts), and so on. Each part can be described perfectly through Newtonian physics, and the assembled system (the car) works because the reductionist hypothesis holds.

Perhaps unsurprisingly, this approach is not infallible. Consider all-atom molecular dynamics (MD) simulations, for instance (MacKerell et al., 1998). Using only the known atomic makeup of the system and so-called "force-fields" which describe the physical interactions between these atoms, these amazing simulations can predict, with reasonable accuracy, the folding structure and dynamics of proteins on the millisecond level (Shaw et al., 2009). What, then (besides unconscionable memory and processing requirements), is preventing us from applying these simulations to a higher order system? Why can't we run an all-atom MD simulation on an entire cell? For that matter, why not the entire universe?

The problem, Anderson argues, is one of scale and complexity. He convincingly shows, through a number of beautiful examples, that the fundamental laws of a system on one scale should not be used to describe its behavior on another. Indeed, the best way to describe a system on one scale is often in terms of the emergent behaviors of the smaller scale. Engineers designing trains powered by superconductors, for instance, are aware of the quantum phenomena leading to superconductivity but only design the trains in terms of their more macroscopic behavior.

Consider the following: elementary particle physics can describe chemistry, which can describe molecular biology, which can cell biology, which (continuing down the line) can eventually describe psychology, which can describe the social sciences. Obviously, one does not describe sociology in terms of quarks. An important philosophical question, then, becomes apparent. At what point does one define a scale in terms of another smaller scale's emergent behaviors? And how much information do we lose to this process?

The overall theme of this dissertation's work is to reconcile two such scales. Bridging the knowledge gap between the single molecule level and the cellular level and beyond is a daunting task. Ultimately, "top-down" cell-based approaches such as siRNA inhibition, immunostaining, or genetics must somehow meet "bottom-up" approaches such as single molecule biophysics or structural biology. One crucial component of the union at this intermediate, or "meso," scale is the study of collections of multiple proteins in the cell. Proteins can assemble to create incredible nanomachines such as the kinetochore (Cheeseman and Desai, 2008), communicate with each other via signal transduction pathways (Stock et al., 2000), or define organelles and subdomains within the cell (Voeltz et al., 2002).

This dissertation studies how groups of multiple molecular motor proteins work together for efficient intracellular cargo transport. Single-molecule approaches give us an incredible wealth of information about molecular motors on one scale. Defects in these motors on the single-molecule scale often lead to unhealthy cells (the next scale up), which can often lead to unhealthy humans (another scale entirely). In order for a rigorous and novel mesoscale protein study, two criteria must be met: 1) complexes of multiple proteins must be rigorously defined in both number and separation, and 2) these pheonomena must be studied in the native cellular environment. The approach introduced in this dissertation is the first such study to satisfy both criteria.

5.2 Protein engineering: the case for empiricism over prediction

The work in this dissertation represents an alternative approach to constructing multi-protein assemblies using protein components. *In vitro* engineered nanostructures such as DNA origami (Rothemund, 2006) and carbon nanotubes (De Volder et al., 2013) are invaluable tools for studying biological processes on the nano-scale, and these techniques have enjoyed a great popularity in recent decades. Engineers are able to create these structures with great precision in part because of the simplicity of their core components – allotropes of atomic carbon in the case of nanotubes, or just four nucleotide bases in the case of DNA origami. Successful protein engineering, on the other hand, has consistently proven to be a much more daunting task (Arpino et al., 2013; Brannigan and Wilkinson, 2002). This is, in large part, due to the complexity of the core components: twenty diverse amino acids with variable hydrophobicity, charge, and size. This "base-twenty" system leads to incredibly complex structures whose folding properties are still hotly debated over fifty years after the question was originally posed (Dill and MacCallum, 2012).

Although great strides have been made in recent years, the predictive (or *de novo*) design of physiologically sized proteins is notoriously difficult due to the complexity of protein folding (Schneider, 2014). The design of individual *de novo* small peptide components, on the other hand, such as coiled-coils (Kiyokawa et al., 2004) or very short inhibitory peptides (less than ~20 amino acids) (Javadpour et al., 1996) have typically been much more successful than larger assemblies. The complexity of these *de novo* proteins has continued to grow in recent years, as shown by the successful design of various β sheet-based hydrogel systems and α helix-based nanoparticles (Boyle and Woolfson, 2011). Just last year, a landmark study was published where investigators created tetrahedral or pyramidal structures from a single *de novo* polypeptide, thus greatly enhancing nanoscale precision of protein designs in three dimensions (Gradisar et al., 2013). As

computing power and predictive methods continue to advance, the still-nascent *de novo* protein field is poised to explode in future years.

Currently, successful protein engineering currently requires a far more empirical, experimental approach (see this study) versus the more predictive, design-based approach used in DNA origami-based techniques (Derr et al., 2012; Hariadi et al., 2014). Often, individual protein components that have been previously characterized, such as chemically-induced dimeric proteins (DeRose et al., 2013), the single alpha helix (SAH) domain (Knight et al., 2005; Sivaramakrishnan et al., 2008), or naturally occurring coiled-coil pentamers (Efimov et al., 1994; Malashkevich et al., 1996) are used as tools to assemble the system of interest (Grunberg and Serrano, 2010). This again emphasizes the role of scale: instead of explaining each component in terms of its atomic detail (i.e., the balanced and opposing positive and negative side chains of the SAH domain), we instead describe the SAH in terms of its emergent behavior (i.e., a 30 nm rigid spacer component). The details of each component are always considered in the initial experimental design, of course, but occasionally unanticipated issues arise during characterization.

Chapter 2 of this dissertation illustrates numerous examples of the necessity for this experimental approach to protein design. For instance, we attempted to use a number of previously characterized coiled-coil peptides to link motors to scaffolds (Burkhard et al., 2002; Holton and Alber, 2004; Kammerer et al., 2005; Kiyokawa et al., 2004; Litowski and Hodges, 2002). While some of these potential linkers were ultimately successful at driving motor-scaffold association, a number of them resulted in either no linkage (Burkhard et al., 2002) or extremely inefficient linkages (Holton and Alber, 2004; Litowski and Hodges, 2002). Similarly, the split EF Hand linker (Lindman et al., 2009) was shown to only drive assembly in certain orientations. Other unforeseeable issues also became apparent over the course of this study, such as the unstable nature

of constructs containing a split GFP tag at the N-terminus (Chapter 2), or aberrant kinesin-1 run lengths due to the presence of some fluorescent proteins (Chapter 3). Although we can speculate as to the cause of these behaviors -- the linkers are likely inefficient due to limited molecular accessibility, and the aberrant run lengths are likely due to tag-driven oligomerization -- simply cloning and testing the constructs has proven to be the only reliable and efficient method to test for these properties. Overall, future protein engineers must be aware that even well-conceived experiments are not guaranteed to work, and an empiricist's "shotgun" approach to cloning and testing, utilizing numerous redundant constructs, is often the most efficient method for design.

5.3 Future steps

5.3.1 Two-motor transport: what are the crucial parameters?

In Chapter 4, we performed a series of experiments where a truncated kinesin-1 motor (rat KIF5C, aa 1-560, hereafter referred to as kin1) and a truncated, dimeric kinesin-3 motor (rat KIF1A, aa 1-393 with the leucine zipper dimerizing segment of GCN4, hereafter referred to as kin3) were attached to a 20 nm SAH scaffold. We found that, *in vitro*, the two motors often walked independently where the net velocity of the complex alternated between the fast kin3 velocity and the slow kin1 velocity. Overall, the slow kin1 motor seemed to dominate *in vitro* such that the net velocity of the complex seemed limited by the slowest member of the team. When we performed the same experiment in COS7 cells, we found that, while the complexes still alternated between the two characteristic velocities, kin1 no longer dominated and the net velocities seemed to be distributed in a bimodal fashion. We then performed a series of followup experiment where we used nocodazole (NZ) treatments to alter the state of the microtubule tracks in the cell, presumably

altering the affinity between the slow kin1 motor and the track. We found that this changed the distribution of velocity events, suggesting a key role for motor-track binding affinity in determining emergent multiple motor transport behavior.

To thoroughly examine the role of on-rate and similar parameters in multiple motor transport, we require a more quantitative model. Recently, the laboratory of Erkan Tuzel at Worchester Polytechnic Institute developed a Monte Carlo method describing the action of mixed populations of kinesin motors (i.e., fast and slow) (Arpag et al., *in press*). In this study, the Tuzel group collaborated with the laboratory of William Hancock at Penn State University and to successfully implement their model and recapitulate experimental data from microtubule gliding assays. Although this initial study focused on the collective behavior of many motors in an inverted gliding orientation, the model can theoretically be applied to smaller numbers of motors attached to a cargo. We propose to perform a series of kin1 + kin3 experiments in collaboration with the Tuzel group where we alter key parameters and compare to predictions from the Monte Carlo model. These experiments will allow us to determine the crucial parameters for multi-kinesin behavior and will allow us to apply these universally to groups of multiple molecular motors.

The basics of the Monte Carlo model are as follows (Fig. 5.1A). At each time step, each bound motor has a finite probability of stepping forward on the microtubule, described by the following:

$$p_{step} = 1 - e^{-v\tau/\delta};$$

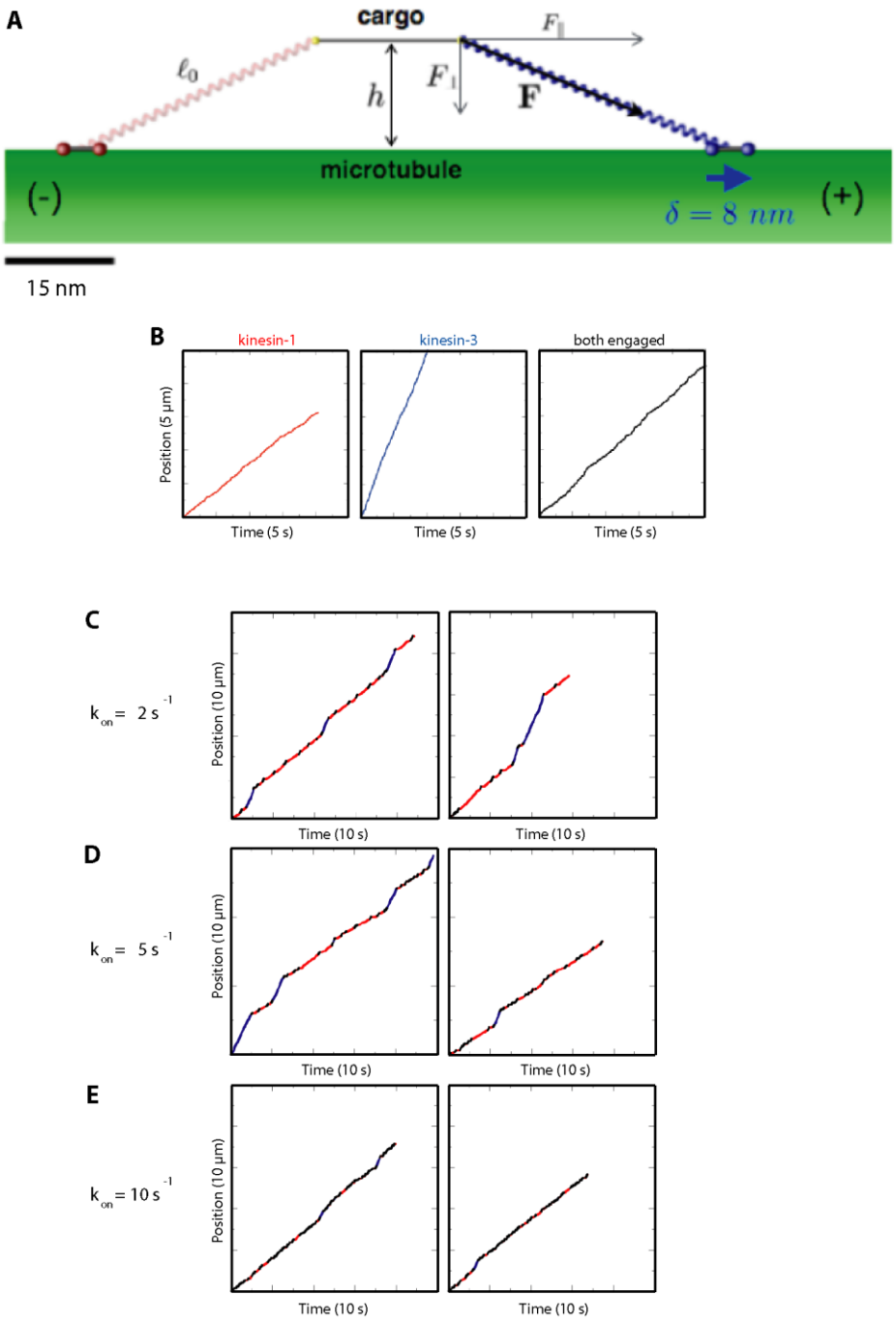

Figure 5.1. Monte Carlo modeling of two motors attached to a cargo.

(A) Two motors (kin1 and kin3 in this example) are attached to a relatively rigid cargo. At each time interval, each bound motor has a finite probability of stepping forward (depends on the velocity of the motor) or detaching from the microtubule (depends on the force the motor feels as transduced through the cargo). Each unbound motor has a finite probability of attaching to the microtubule (depends on k_{on}). This model also considers contributions from Brownian motion. **(B)** Representative kymographs generated by simulation for kin1 alone (left, red), kin3 alone (middle, blue)

and both motors engaged with the microtubule (black, right). **(C-E)** Representative kymographs generated by simulation for two motors on a cargo where k_{on} for each motor is 2 s^{-1} **(C)**, 5 s^{-1} **(D)**, and 10 s^{-1} **(E)**.

Goker Arpag in the Tuzel lab (Physics, Worcester Polytechnic Institute) performed simulations and created Fig. 5.1.

Where δ is the step size (8 nm), τ is the time step of the simulation, and v is the motor velocity, which in turn depends on the applied force felt by motor:

$$v = v_u\left(1-\frac{F(l)}{F_S}\right);$$

Where v_u is the characteristic unloaded velocity of kin1 or kin3, $F(l)$ is the force currently sensed by the motor in a direction parallel to the axis of the track, which depends on its extension l, and F_S is the characteristic stall force of each motor. The motor force is assumed to be linear, where force is only applied when the motor is extended beyond its rest length:

$$|F| = \kappa_s(l-l_0)\Theta(l-l_0);$$

$$\Theta(l-l_0)=\begin{cases}1 & if\ l>l_0\\ 0 & if\ l\le l_0\end{cases};$$

Where l is the extension of the motor stalk, l_0 is the rest length of the motor stalk, and κ_s is the estimated spring constant of the motor stalk.

At each time step, the bound motor also has a finite probability of detaching from the microtubule:

$$p_{unbind} = \tau \cdot k_{off}(F);$$

Where $k_{off}(F)$ is the force-dependent off-rate (see Arpag et al., 2014 for derivation):

Kinesin	$k_{off}^{hind}(F)\ [s^{-1}]$	$k_{off}^{asst}(F)\ [s^{-1}]$
1	$0.79\,e^{-F/6.1}$	$0.79 + 1.56\,F$
3	$1.433\,e^{\lvert F\rvert/0.5}$	

At each time step, each *unbound* motor has a finite probability of attaching to the microtubule:

$$p_{unbind} = \tau \cdot k_{on};$$

Where the on rate is likely to be roughly inversely proportional to the length of the scaffold connecting the motors (as the scaffold increases in length, the unbound motor is more likely to diffuse away from the microtubule). The model also considers a viscosity-dependent Brownian contribution to the overall net motion of the cargo. Overall, the model is quite well-developed, but two contributions need to be fine-tuned to accurately describe the motion of our system, spefically: (1) the contribution of the SAH scaffold to force transduction, and (2) various contributions to the on-rate of the motor such as the K-loop in the case of kin3 (see below) or the scaffold length in the case of an unbound motor relying on diffusion to re-engage with the track.

Early simulations describing our experimental setup have revealed the importance of the motor on-rate in determining overall motion. When the simulation is used to generate kymographs analogous to our experimental data, individual kin1 and kin3 motors move with a relatively constant characteristic velocity (Fig. 5.1B, left, middle). When kin1 + kin3 motors are forced to remain bound to the microtubule (Fig. 5.1B, right), they move with a velocity most similar to kin1, suggesting that the overall motion of the complex is limited by the slowest motor under this condition. This suggests that a number of "slow" events we observed in our experiments in

Chapter 3 were not driven by kin1 alone but actually by complexes where both kin1 and kin3 are engaged with the track, as we speculated. When both motors are allowed to unbind and rebind (Fig. 5.1C-E), a number of interesting behaviors are observed. First, the overall motion seems to alternate between three states: only-kin1-engaged (red segments), only-kin3-engaged (blue segments) and both motors engaged (black segments). This behavior largely matches our experimental observations (Chapter 4). Second, the proportion of time the complex spends in each state seems to depend crucially on the on-rate of each motor. At low motor on-rates (Fig. 5.1C), the complex often alternates between fast and slow behavior and spends relatively little time in the two-motor-bound state. As motor on-rates continue to increase (Fig. 5.1D-E), the complex spends more time in the two-motor-bound state and the overall velocity of the complex decreases. Interestingly, the kin1 and kin3 motors have identical on-rates for each simulation, and the observed velocity still shows a significant change. If one were to alter the individual on-rates of each motor, one would predict different velocity profiles corresponding to which motor has a higher on-rate. Thus, preliminary modeling data shows that the affinity of individual motor-microtubule interactions is a crucial parameter in determining the emergent behavior of multi-motor intracellular transport.

Motor on-rates are a highly tunable process inside the cell, where the motor can have different affinities for the track based simply on inherent motor domain properties (Soppina and Verhey, 2014) or post-translational modifications of the microtubule track (Cai et al., 2009). Based on previous work (Soppina and Verhey, 2014), we have access to a number of motor domain mutations that directly affect the on-rate of each motor. Wild-type KIF1A contains a sequence of positively-charged amino acids (the "K-loop") that interacts with a sequence of negatively-charge amino acids on the microtubule (the "E-hook"), which leads to an increased on-rate for these

motors. By deleting the K-loop in kin3 for our experiments, we can decrease kin3's on-rate roughly ten-fold. Similarly, by introducing a K-loop in kin1, we can increase kin1's on-rate roughly four-fold. By performing the two-motor experiment with all permutations (WTkin1 + WTkin3, high affinity kin1 + WTkin3, WTkin1 + low affinity kin3, high affinity kin1 + low affinity kin3) and directly comparing these on-rates to the simulation results, we can theoretically describe the contribution of the motor on-rate in great detail. Based on other unpublished results, we also have access to motors with increased off-rates and decreased velocities, which would be helpful in further verification of the model. Overall, this study would allow us to describe, in great detail, how individual motor properties contribute to multi-kinesin transport.

5.3.2 Increasing motor copy number with our scaffold-based system

An obvious next step for this system would be to increase the number of motors present on a given scaffold. This would more accurately represent the number of motors on an endogenous cellular cargo, which varies widely but is typically estimated to be between 1 and 7 for microtubule-based motors (see Chapter 1). In theory, our system allows us to increase the number of motors indefinitely by including additional linker domains on the scaffold (see Fig. 5.2C), where we are limited only by the lower expression levels of these larger scaffold proteins. Additionally, because we have four well-characterized linkers, we can theoretically attach up to four *unique* motors to the scaffold, where we would be limited only by technical issues of simultaneously expressing a large number of proteins.

In vitro DNA-based approaches allow an increase in motor copy number with relative ease, where the number of motors can be verified directly via gel-shift assays or electron microscopy of

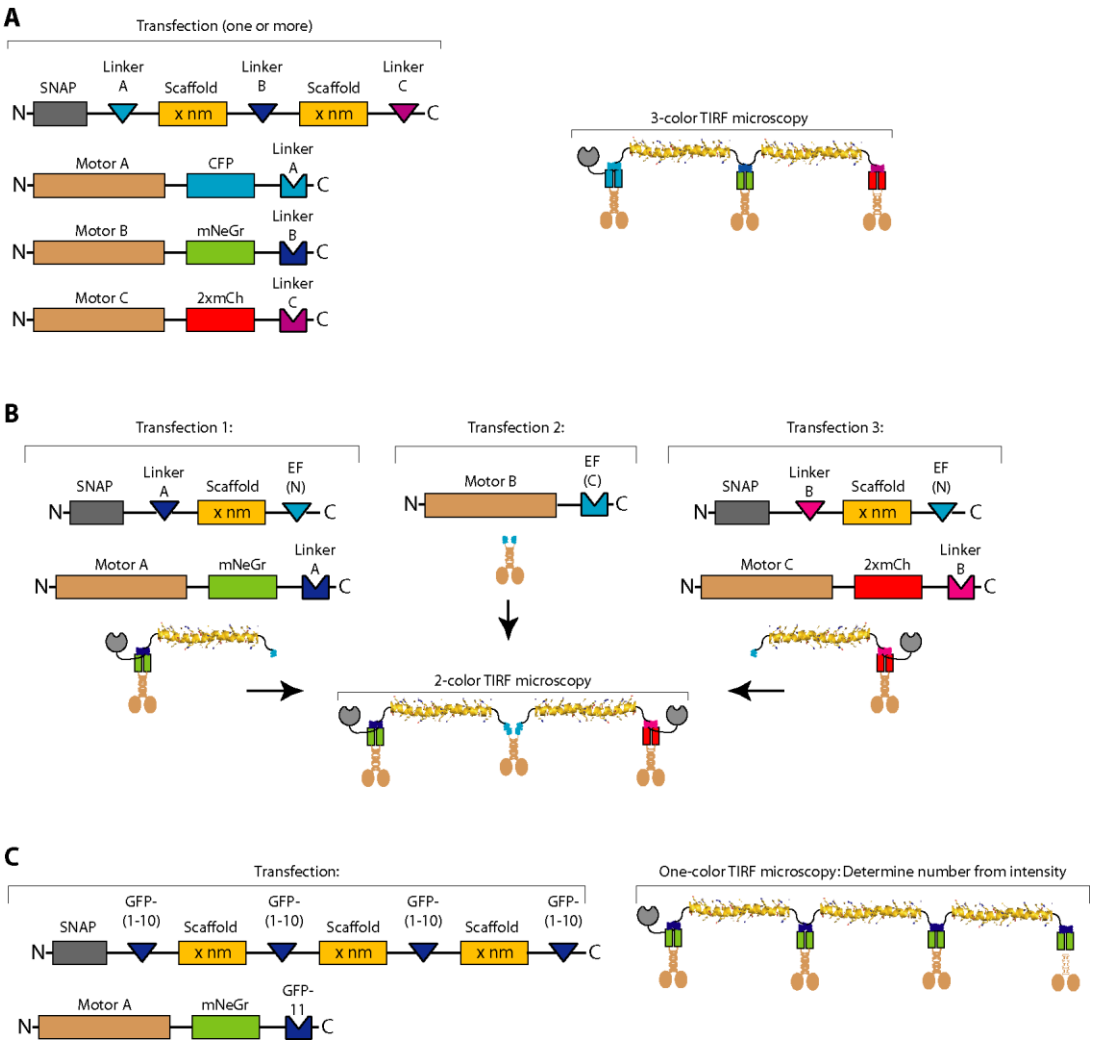

Figure 5.2. Methods for assembling additional motors on a SAH-based scaffold.

(A) The use of three unique motor-linker combinations would allow verification of three-motor assembly by three-color TIRF microscopy. **(B)** The use of an intermediate "bridge" motor would allow verification of three-motor assembly by two-color TIRF microscopy. **(C)** The use of redundant linker domains on a single scaffold would allow the recruitment of multiple copies of the same motor. This technique would require assembly verification by another method such as analysis of fluorescence intensity.

---

purified components (Derr et al., 2012; Furuta et al., 2013). Our approach, on the other hand, requires no protein purification and thus we must use an alternate approach to verify complete motor assembly. We found that two-color TIRF microscopy provides the simplest verification,

where one motor is labeled with a green fluorescent protein and the other motor is labeled with a red fluorescent protein (Chapter 4). Because this technique requires direct visualization of each motor, extending this approach to more motors becomes technically challenging.

The most conceptually straightforward method for extending the number of motors is simply to perform three-color single molecule TIRF microscopy (Fig. 5.2A). This technique would be a technical feat as two-color TIRF is already challenging, but is theoretically possible with the addition of a cyan (or far-red, although far-red FPs tend to be very ineffective) fluorescent protein and a triple-bandpass filter set. Such an experiment would provide a wealth of information – if three motors (motor A, B, and C) were attached to a scaffold, all permutations could be examined in the same field of view (motor A alone, motor A + B, motor A + B + C, etc.). This would allow direct comparisons of motor separation (A + C would be spaced farther than A + B, for instance) with the added benefit of internal controls from individual motors in the same chamber. The main disadvantage to this technique, as mentioned, is the technical difficulty of three-color TIRF imaging.

An alternate approach (Fig. 5.2B) would allow three-motor assembly that could be verified by two-color TIRF microscopy. This approach would utilize the high affinity of the heterodimeric split EF-hand linker to assemble three-motor complexes *in vitro*. In this approach, motor B would act as a "bridge" to attach both existing motor-scaffold assemblies via the split EF hand, where the required C-terminal end of the linker is present only on motor B. In this orientation, a two-color TIRF signal should only be possible in the presence of motor B. The biggest disadvantage to this technique would likely be the inefficiency of linker assembly.

A third approach (Fig. 5.2C) would use redundant linker domains to recruit an indefinite number of identical motors to the same scaffold. This approach has the added benefit of using

multiple split GFP linkers, which shows the highest efficiency of the linkers we tested. Preliminary experiments with these constructs have shown some promise (Chapter 2), and extending this technique to additional motors is conceptually straightforward. These preliminary experiments have revealed two significant complications, however. First, the verification of multiple-motor assembly is not as straightforward as probing for two-color colocalization, as in Chapter 4. This proposed technique would require an estimation of motor number based on fluorescence intensity, which is difficult in single-molecule TIRF experiments. In bulk assays, fluorescence intensity depends linearly on fluorophore concentration, which is the basis of many fluorescence spectroscopy experiments. In practice, for single-molecule assays, this intensity correlates with fluorophore number but can deviate from a purely linear relationship due to the low signal-to-noise ratio (see, for example, the initial fluorescence of photobleaching traces in Chapter 3). In addition, not all fluorophores mature to a competent fluorescent state, thus further complicating interpretation due to the presence of "dark" fluorophores. Another complicating factor for this technique is the heterodimeric nature of the split GFP linker. Because multiple copies of this linker are present and the assembly is irreversible on these time scales, this permits the assembly of long strings of multiple motors where one motor potentially connects to two scaffolds and thus creates indefinite strings of N motors (see Chapter 2). Importantly, this phenomenon was decidedly not observed in experiments with two different linkers (Chapter 4) but could be expected to contribute substantially here due to the nature of the split GFP linkage.

Overall, our SAH-based scaffold approach could (and should) be extended to additional motors to more accurately recreate intracellular cargo transport. Multiple strategies are theoretically possible, but each introduces significant drawbacks and would require additional

characterization. Ultimately, each approach should be attempted before determining which is the most technically feasible.

5.3.3 Studying the cooperative transport of mutant kinesin with disease phenotypes

Defective microtubule-based transport in cells leads to a number of disease phenotypes, including neurodegeneration (Salinas et al., 2008), polycystic kidney disease (Gerdes et al., 2009), and cancer (Yu and Feng, 2010). Neurodegeneration provides an insightful model system for studying the disease impact of defective motor transport. Neurons contain extremely long projections and possess a high degree of asymmetry, and thus directed intracellular transport is absolutely critical for proper neuronal function and health. As a result, genetic defects in transport such as kinesin motor mutations are often manifest as neurodegenerative phenotypes. Specific mutations in kinesin motors have been shown to cause Charcot-Marie-Tooth disease (Zhao et al., 2001), hereditary spastic paraplegia (Reid et al., 2002), and congenital fibrosis of the extraocular muscles (Yamada et al., 2003). A number of studies have directly correlated defects in axonal transport to defects in single molecule motility for specific motor mutations (Salinas et al., 2008). However, more subtle motor defects may lead to inhibited *cooperative* motor transport where the single molecule motility appears unaffected. Such a scenario would require more careful dissection of multiple motor transport using a system such as the one introduced in this dissertation. Here, I introduce one such scenario where we have performed preliminary experiments to investigate this behavior.

Previous work in *Drosophila* has shown that Khc mutants inhibit neuronal sodium channel activity, action potentials, and neurotransmitter secretion, which can cause progressive distal

paralysis in larvae (Hurd and Saxton, 1996). Most of these defects are a direct result of inhibited axonal transport, which is crucial for neuronal health and signaling. By screening for missense mutations that disrupt axonal transport, Brendza et al. identified a particular mutation in the motor domain of Khc, E164A, located near the microtubule binding site (Brendza et al., 1999). This mutation was lethal in Drosophila third instar larvae (Brendza et al., 1999) and was thought to play a key role in the mechanochemical coordination between motor heads, perhaps via formation of a salt bridge intermediate. This mutation was previously independently identified to be in loop 8 of the motor domain of human kinesin (Woehlke et al., 1997). Follow-up studies then showed that E164A, as well as the more severe E164K mutation, led to a defective motor where only one of the motor heads could bind and hydrolyze ATP and thus appeared to "stall" on the microtubule (Klumpp et al., 2004a; Klumpp et al., 2003; Klumpp et al., 2004b). These studies, and other genetic follow-up studies, suggested a structural linkage between loop 8 and the nucleotide binding site, perhaps via α5-loop 12-α4-loop 11 (Djagaeva et al., 2012).

Later observations by the laboratory of Jennifer Ross at the University of Massachusetts Amherst revealed intriguing behavior for the human E157A and E157K mutations (unpublished data). In microtubule gliding assays, the Ross group found that microtubule velocities were reduced for E157A/K mutants relative to wild-type. However, single molecule studies with the same mutants did not show reduced velocities relative to wild-type. Based on these observations they speculated that there must be a defect in cooperative motor transport for this mutation rather than single motor transport. In order to fully understand this defect, it would be ideal to perform experiments on defined numbers of mutant vs. wild-type motors.

To test this mutation in our system, we used site-directed mutagenesis on a kinesin-1 motor [rat KHC(1-560)-2xmCit-GFP11] to generate the same motor with an E158K mutation. We then

coexpressed this motor with a scaffold containing two GFP(1-10) linker domains to recruit two copies of the motor to the scaffold (Fig. 5.3A-B). Preliminary experiments revealed a number of interesting behaviors. First, we observed that this mutation indeed leads to a processive motor, in contrast to previous published work described above which reported that this motor is bound to the microtubule and unable to walk (Fig. 5.3C). Second, we noticed no significant difference in motility behavior between one copy of the E158K motor and two copies of the E158K motor, whereas there was a significant difference in run length between one and two copies of the wild-type kinesin-1 motor (Fig. 5.3C). Because this particular experiment used two copies of the same linker, these results must be treated with some amount of skepticism as outlined in Chapter 2 and the previous section (i.e., two-motor assembly is not guaranteed and N-motor assemblies due to chain formation are possible). We also found that the E158K mutation displays decreased affinity for microtubules relative to the wild-type motor, regardless of nucleotide state (Fig. 5.3D), as determined by landing rate (see Chapter 3). These preliminary experiments suggest that this mutation displays interesting behavior relative to wild-type and indeed may be implicated in defective cooperative transport by multiple motors.

In order for a careful examination of this mutant's behavior, a two-color TIRF approach (similar to Chapter 4) should be pursued, where the wild-type motor is labeled in one color and E158K in another. Only this method ensures complete two-motor assembly and comparison to the single-motor state. Importantly, the contribution of the mutant can be studied in a number of different configurations (Fig. 5.3E-G). For example, a mutant motor can be assembled in complex with a wild-type (Fig. 5.3E), two mutant motors can be assembled in complex (Fig. 5.3F), or heterodimeric motors can be assembled where one motor head is wild-type and one motor head contains the mutation (Fig. 5.3G), thus perhaps simulating a heterozygous mutation. This latter

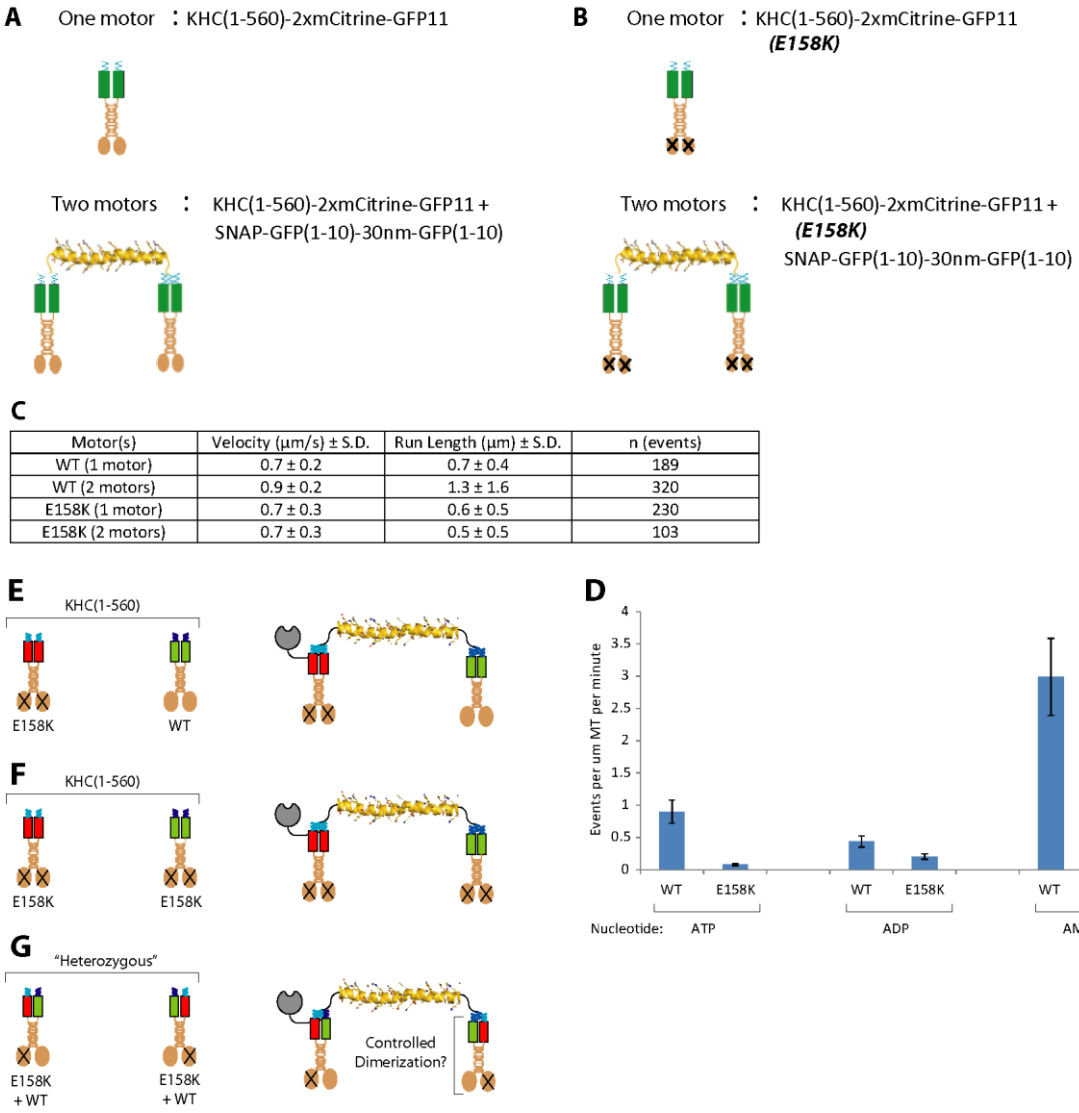

Figure 5.3. Studying the cooperative transport of disease phenotype motors.

(A-B) Schematic of preliminary experiments. 2xmCit-tagged kinesin-1 with a split GFP linker (top, "one motor") was coexpressed with a 30 nm SAH scaffold with two copies of the complementary split GFP linker to assemble two-motor complexes (bottom, "two motors"). This was done for either wild-type kinesin-1 **(A)** or E158K kinesin-1 **(B)**. **(C)** Preliminary results for two-motor E158K assemblies. **(D)** Quantifying landing rate for WT vs. E158K motors in various nucleotide states. Nucleotide concentration was 2 mM. Equal amounts of proteins were determined by western blot and flowed for each experiment. **(E-G)** Schematics for future two-color TIRF experiments on mutant motors. **(E)** Mutant and wild-type (WT) motors in complex. **(F)** Two mutant motors in complex, similar to **(A)**. **(G)** Simulating heterozygous mutations with one WT motor head and one mutant motor head. This approach would require controlled dimerization to prevent unwanted homo-dimers as in **(E)** and **(F)**.

method would likely require a different technique to control dimerization, whereas cross-dimerization can be avoided in the former two methods by mixing lysates via the split EF hand linker (Chapter 4). Ultimately, such a technique could be used to thoroughly investigate the role of kinesin mutations in multiple-motor transport.

5.3.4 Using this technique to study other cytoskeletal motors

It should be noted that, although only dimeric kinesin motors were studied in this dissertation, this approach is certainly compatible with other cytoskeletal motors such as dynein or myosin. In order for this approach to generally work, each motor must be (1) labeled with a fluorescent protein tag and (2) specifically recruited to the scaffold. Although additional characterization must be performed in the context of these other motors, previous studies have shown that this is theoretically possible.

Because of their complicated assembly, dynein motors can be labeled in a number of locations, and no field consensus has yet been reached for single molecule assays. For example, either the motor domain can be labeled directly (Reck-Peterson et al., 2006), or subunits of the dynactin complex, which binds the dynein intermediate chain (Schroer, 2004), can be labeled, such as dynamitin (Ross et al., 2006) or $p150^{Glued}$ (Ayloo et al., 2014). It is important to note that the overexpression of one subunit of dynein does not lead to an overall increase in the number of active dynein motors inside the cell; in order for proper dynein motor function, these subunits must be assembled in the proper stoichiometry. Additionally, overexpression of particular subunits could act as a dominant negative to inhibit overall retrograde transport inside the cell. Processive myosin motors, on the other hand, can easily be labeled directly via fusion of a fluorescent protein to one

end of the motor domain, a technique that has been used to directly observe single-molecule motility of processive myosin motors (Purcell et al., 2002; Rock et al., 2001).

To determine a strategy for recruiting dynein or myosin motors to our SAH-based scaffold constructs, we can refer to established assays for recruiting these motors to cargoes in live COS7 cells (Efremov et al., 2014; Kapitein et al., 2010; Kapitein et al., 2013). These studies exclusively use the DmrA/C system to recruit motors to larger cargoes such as peroxisomes, such that the number of recruited motors likely far exceeds the endogenous motor number. By replacing the DmrA/C tags in these published constructs with the linker of our choice, and replacing the peroxisome-targeting domain with the scaffold sequence, we should have a number of viable approaches for recruiting these motors. Myosin V or VI recruitment is conceptually straightforward and analogous to kinesin, where the linker domain can simply be placed at the far C-terminus of the fluorescent protein. Myosin can also be recruited through adaptors such as melanophilin (Kapitein et al., 2010). In this study, the authors also successfully recruited dynein to cellular cargoes both via direct recruitment of dynein heavy chain and through recruitment of the dynein adaptor Bicaudal D, both of which could conceivably be valid approaches for our scaffold system.

In summary, a number of techniques have been established to both label and recruit myosin and dynein motors to specific cargoes in living cells. By using these established techniques as a road map, we should be able to extend our multiple motor motility assays to additional motor types with relative ease.

5.4 Overall conclusions

The work presented in this dissertation has resulted in a number of conclusions that the field will hopefully appreciate. First, we offer a valuable conclusion for the kinesin field specifically: we demonstrate, with direct visual evidence, that two kinesin motors walk independently rather than cooperatively. This has long been inferred from other experiments such as optical trapping experiments (Jamison et al., 2010) and other mounting experimental evidence that multiple kinesin motors do not greatly benefit from an increase in copy number (Barlan et al., 2013). Second, and perhaps more importantly: we conclusively show that multiple proteins can be assembled and studied in defined groups, and that this assembly can take place in living cells. This has potentially large implications in the field of cell biology. The signaling field, for instance, has attempted to create protein-based scaffolding systems to study pathway dynamics (Bashor et al., 2008), and this field could certainly benefit from a system with increased spatial control such as ours. Our system could theoretically be used to study any intracellular system based on groups of multiple interacting proteins. Third, and finally, this work emphasizes that it is absolutely critical to adapt an empirical approach to protein engineering projects. Such projects are certainly possible, but these must be approached with an open mind, where unanticipated setbacks are the norm and many parallel strategies are used simultaneously.

5.5 References

Anderson, P.W. (1972). More Is Different - Broken Symmetry and Nature of Hierarchical Structure of Science. Science *177*, 393-&. doi: DOI 10.1126/science.177.4047.393

Arpino, J.A., Hancock, E.J., Anderson, J., Barahona, M., Stan, G.B., Papachristodoulou, A., and Polizzi, K. (2013). Tuning the dials of Synthetic Biology. Microbiology *159*, 1236-1253. doi: 10.1099/mic.0.067975-0

Ayloo, S., Lazarus, J.E., Dodda, A., Tokito, M., Ostap, E.M., and Holzbaur, E.L. (2014). Dynactin functions as both a dynamic tether and brake during dynein-driven motility. Nature communications *5*, 4807. doi: 10.1038/ncomms5807

Barlan, K., Rossow, M.J., and Gelfand, V.I. (2013). The journey of the organelle: teamwork and regulation in intracellular transport. Current opinion in cell biology *25*, 483-488. doi: 10.1016/j.ceb.2013.02.018

Bashor, C.J., Helman, N.C., Yan, S., and Lim, W.A. (2008). Using engineered scaffold interactions to reshape MAP kinase pathway signaling dynamics. Science *319*, 1539-1543. doi: 10.1126/science.1151153

Boyle, A.L., and Woolfson, D.N. (2011). De novo designed peptides for biological applications. Chemical Society reviews *40*, 4295-4306. doi: 10.1039/c0cs00152j

Brannigan, J.A., and Wilkinson, A.J. (2002). Protein engineering 20 years on. Nature reviews Molecular cell biology *3*, 964-970. doi: 10.1038/nrm975

Brendza, K.M., Rose, D.J., Gilbert, S.P., and Saxton, W.M. (1999). Lethal kinesin mutations reveal amino acids important for ATPase activation and structural coupling. The Journal of biological chemistry *274*, 31506-31514

Burkhard, P., Ivaninskii, S., and Lustig, A. (2002). Improving coiled-coil stability by optimizing ionic interactions. Journal of molecular biology *318*, 901-910. doi: 10.1016/S0022-2836(02)00114-6

Cai, D., McEwen, D.P., Martens, J.R., Meyhofer, E., and Verhey, K.J. (2009). Single molecule imaging reveals differences in microtubule track selection between Kinesin motors. PLoS biology *7*, e1000216. doi: 10.1371/journal.pbio.1000216

Cheeseman, I.M., and Desai, A. (2008). Molecular architecture of the kinetochore-microtubule interface. Nature reviews Molecular cell biology *9*, 33-46. doi: 10.1038/nrm2310

De Volder, M.F., Tawfick, S.H., Baughman, R.H., and Hart, A.J. (2013). Carbon nanotubes: present and future commercial applications. Science *339*, 535-539. doi: 10.1126/science.1222453

DeRose, R., Miyamoto, T., and Inoue, T. (2013). Manipulating signaling at will: chemically-inducible dimerization (CID) techniques resolve problems in cell biology. Pflugers Archiv : European journal of physiology *465*, 409-417. doi: 10.1007/s00424-012-1208-6

Derr, N.D., Goodman, B.S., Jungmann, R., Leschziner, A.E., Shih, W.M., and Reck-Peterson, S.L. (2012). Tug-of-war in motor protein ensembles revealed with a programmable DNA origami scaffold. Science *338*, 662-665. doi: 10.1126/science.1226734

Dill, K.A., and MacCallum, J.L. (2012). The protein-folding problem, 50 years on. Science *338*, 1042-1046. doi: 10.1126/science.1219021

Djagaeva, I., Rose, D.J., Lim, A., Venter, C.E., Brendza, K.M., Moua, P., and Saxton, W.M. (2012). Three routes to suppression of the neurodegenerative phenotypes caused by kinesin heavy chain mutations. Genetics *192*, 173-183. doi: 10.1534/genetics.112.140798

Efimov, V.P., Lustig, A., and Engel, J. (1994). The thrombospondin-like chains of cartilage oligomeric matrix protein are assembled by a five-stranded alpha-helical bundle between residues 20 and 83. FEBS letters *341*, 54-58

Efremov, A.K., Radhakrishnan, A., Tsao, D.S., Bookwalter, C.S., Trybus, K.M., and Diehl, M.R. (2014). Delineating cooperative responses of processive motors in living cells. Proceedings of the National Academy of Sciences of the United States of America *111*, E334-343. doi: 10.1073/pnas.1313569111

Furuta, K., Furuta, A., Toyoshima, Y.Y., Amino, M., Oiwa, K., and Kojima, H. (2013). Measuring collective transport by defined numbers of processive and nonprocessive kinesin motors. Proceedings of the National Academy of Sciences of the United States of America *110*, 501-506. doi: 10.1073/pnas.1201390110

Gerdes, J.M., Davis, E.E., and Katsanis, N. (2009). The vertebrate primary cilium in development, homeostasis, and disease. Cell *137*, 32-45. doi: 10.1016/j.cell.2009.03.023

Gradisar, H., Bozic, S., Doles, T., Vengust, D., Hafner-Bratkovic, I., Mertelj, A., Webb, B., Sali, A., Klavzar, S., and Jerala, R. (2013). Design of a single-chain polypeptide tetrahedron assembled from coiled-coil segments. Nature chemical biology *9*, 362-366. doi: 10.1038/nchembio.1248

Grunberg, R., and Serrano, L. (2010). Strategies for protein synthetic biology. Nucleic acids research *38*, 2663-2675. doi: 10.1093/nar/gkq139

Hariadi, R.F., Cale, M., and Sivaramakrishnan, S. (2014). Myosin lever arm directs collective motion on cellular actin network. Proceedings of the National Academy of Sciences of the United States of America. doi: 10.1073/pnas.1315923111

Holton, J., and Alber, T. (2004). Automated protein crystal structure determination using ELVES. Proceedings of the National Academy of Sciences of the United States of America *101*, 1537-1542. doi: 10.1073/pnas.0306241101

Hurd, D.D., and Saxton, W.M. (1996). Kinesin mutations cause motor neuron disease phenotypes by disrupting fast axonal transport in Drosophila. Genetics *144*, 1075-1085

Jamison, D.K., Driver, J.W., Rogers, A.R., Constantinou, P.E., and Diehl, M.R. (2010). Two kinesins transport cargo primarily via the action of one motor: implications for intracellular transport. Biophysical journal *99*, 2967-2977. doi: 10.1016/j.bpj.2010.08.025

Javadpour, M.M., Juban, M.M., Lo, W.C., Bishop, S.M., Alberty, J.B., Cowell, S.M., Becker, C.L., and McLaughlin, M.L. (1996). De novo antimicrobial peptides with low mammalian cell toxicity. Journal of medicinal chemistry *39*, 3107-3113. doi: 10.1021/jm9509410

Kammerer, R.A., Kostrewa, D., Progias, P., Honnappa, S., Avila, D., Lustig, A., Winkler, F.K., Pieters, J., and Steinmetz, M.O. (2005). A conserved trimerization motif controls the topology of short coiled coils. Proceedings of the National Academy of Sciences of the United States of America *102*, 13891-13896. doi: 10.1073/pnas.0502390102

Kapitein, L.C., Schlager, M.A., van der Zwan, W.A., Wulf, P.S., Keijzer, N., and Hoogenraad, C.C. (2010). Probing intracellular motor protein activity using an inducible cargo trafficking assay. Biophysical journal *99*, 2143-2152. doi: 10.1016/j.bpj.2010.07.055

Kapitein, L.C., van Bergeijk, P., Lipka, J., Keijzer, N., Wulf, P.S., Katrukha, E.A., Akhmanova, A., and Hoogenraad, C.C. (2013). Myosin-V opposes microtubule-based cargo transport and drives directional motility on cortical actin. Current biology : CB *23*, 828-834. doi: 10.1016/j.cub.2013.03.068

Kiyokawa, T., Kanaori, K., Tajima, K., Kawaguchi, M., Mizuno, T., Oku, J., and Tanaka, T. (2004). Selective formation of AAB- and ABC-type heterotrimeric alpha-helical coiled coils. Chemistry *10*, 3548-3554. doi: 10.1002/chem.200305729

Klumpp, L.M., Brendza, K.M., Gatial, J.E., 3rd, Hoenger, A., Saxton, W.M., and Gilbert, S.P. (2004a). Microtubule-kinesin interface mutants reveal a site critical for communication. Biochemistry *43*, 2792-2803. doi: 10.1021/bi035830e

Klumpp, L.M., Brendza, K.M., Rosenberg, J.M., Hoenger, A., and Gilbert, S.P. (2003). Motor domain mutation traps kinesin as a microtubule rigor complex. Biochemistry *42*, 2595-2606. doi: 10.1021/bi026715r

Klumpp, L.M., Hoenger, A., and Gilbert, S.P. (2004b). Kinesin's second step. Proceedings of the National Academy of Sciences of the United States of America *101*, 3444-3449. doi: 10.1073/pnas.0307691101

Knight, P.J., Thirumurugan, K., Xu, Y., Wang, F., Kalverda, A.P., Stafford, W.F., 3rd, Sellers, J.R., and Peckham, M. (2005). The predicted coiled-coil domain of myosin 10 forms a novel elongated domain that lengthens the head. The Journal of biological chemistry *280*, 34702-34708. doi: 10.1074/jbc.M504887200

Lindman, S., Johansson, I., Thulin, E., and Linse, S. (2009). Green fluorescence induced by EF-hand assembly in a split GFP system. Protein science : a publication of the Protein Society *18*, 1221-1229. doi: 10.1002/pro.131

Litowski, J.R., and Hodges, R.S. (2002). Designing heterodimeric two-stranded alpha-helical coiled-coils. Effects of hydrophobicity and alpha-helical propensity on protein folding, stability, and specificity. The Journal of biological chemistry *277*, 37272-37279. doi: 10.1074/jbc.M204257200

MacKerell, A.D., Bashford, D., Bellott, M., Dunbrack, R.L., Evanseck, J.D., Field, M.J., Fischer, S., Gao, J., Guo, H., Ha, S., *et al.* (1998). All-atom empirical potential for molecular modeling and dynamics studies of proteins. The journal of physical chemistry B *102*, 3586-3616. doi: 10.1021/jp973084f

Malashkevich, V.N., Kammerer, R.A., Efimov, V.P., Schulthess, T., and Engel, J. (1996). The crystal structure of a five-stranded coiled coil in COMP: a prototype ion channel? Science *274*, 761-765

Purcell, T.J., Morris, C., Spudich, J.A., and Sweeney, H.L. (2002). Role of the lever arm in the processive stepping of myosin V. Proceedings of the National Academy of Sciences of the United States of America *99*, 14159-14164. doi: 10.1073/pnas.182539599

Reck-Peterson, S.L., Yildiz, A., Carter, A.P., Gennerich, A., Zhang, N., and Vale, R.D. (2006). Single-molecule analysis of dynein processivity and stepping behavior. Cell *126*, 335-348. doi: 10.1016/j.cell.2006.05.046

Reid, E., Kloos, M., Ashley-Koch, A., Hughes, L., Bevan, S., Svenson, I.K., Graham, F.L., Gaskell, P.C., Dearlove, A., Pericak-Vance, M.A., *et al.* (2002). A kinesin heavy chain (KIF5A) mutation in hereditary spastic paraplegia (SPG10). American journal of human genetics *71*, 1189-1194. doi: 10.1086/344210

Rock, R.S., Rice, S.E., Wells, A.L., Purcell, T.J., Spudich, J.A., and Sweeney, H.L. (2001). Myosin VI is a processive motor with a large step size. Proceedings of the National Academy of Sciences of the United States of America *98*, 13655-13659. doi: 10.1073/pnas.191512398

Ross, J.L., Wallace, K., Shuman, H., Goldman, Y.E., and Holzbaur, E.L. (2006). Processive bidirectional motion of dynein-dynactin complexes in vitro. Nature cell biology *8*, 562-570. doi: 10.1038/ncb1421

Rothemund, P.W. (2006). Folding DNA to create nanoscale shapes and patterns. Nature *440*, 297-302. doi: 10.1038/nature04586

Salinas, S., Bilsland, L.G., and Schiavo, G. (2008). Molecular landmarks along the axonal route: axonal transport in health and disease. Current opinion in cell biology *20*, 445-453. doi: 10.1016/j.ceb.2008.04.002

Schneider, G. (2014). De novo Molecular Design (Zurich, SUI: Wiley-VCH).

Schroer, T.A. (2004). Dynactin. Annual review of cell and developmental biology *20*, 759-779. doi: 10.1146/annurev.cellbio.20.012103.094623

Shaw, D.E., Dror, R.O., Salmon, J.K., Grossman, J.P., Mackenzie, K.M., Bank, J.A., Young, C., Deneroff, M.M., Batson, B., Bowers, K.J., *et al.* (2009). Millisecond-Scale Molecular Dynamics Simulations on Anton. Proceedings of the Conference on High Performance Computing Networking, Storage and Analysis

Sivaramakrishnan, S., Spink, B.J., Sim, A.Y., Doniach, S., and Spudich, J.A. (2008). Dynamic charge interactions create surprising rigidity in the ER/K alpha-helical protein motif. Proceedings of the National Academy of Sciences of the United States of America *105*, 13356-13361. doi: 10.1073/pnas.0806256105

Soppina, V., and Verhey, K.J. (2014). The family-specific K-loop influences the microtubule on-rate but not the superprocessivity of kinesin-3 motors. Molecular biology of the cell *25*, 2161-2170. doi: 10.1091/mbc.E14-01-0696

Stock, A.M., Robinson, V.L., and Goudreau, P.N. (2000). Two-component signal transduction. Annual review of biochemistry *69*, 183-215. doi: 10.1146/annurev.biochem.69.1.183

Voeltz, G.K., Rolls, M.M., and Rapoport, T.A. (2002). Structural organization of the endoplasmic reticulum. EMBO reports *3*, 944-950. doi: 10.1093/embo-reports/kvf202

Woehlke, G., Ruby, A.K., Hart, C.L., Ly, B., Hom-Booher, N., and Vale, R.D. (1997). Microtubule interaction site of the kinesin motor. Cell *90*, 207-216

Yamada, K., Andrews, C., Chan, W.M., McKeown, C.A., Magli, A., de Berardinis, T., Loewenstein, A., Lazar, M., O'Keefe, M., Letson, R., *et al.* (2003). Heterozygous mutations of the kinesin KIF21A in congenital fibrosis of the extraocular muscles type 1 (CFEOM1). Nature genetics *35*, 318-321. doi: 10.1038/ng1261

Yu, Y., and Feng, Y.M. (2010). The role of kinesin family proteins in tumorigenesis and progression: potential biomarkers and molecular targets for cancer therapy. Cancer *116*, 5150-5160. doi: 10.1002/cncr.25461

Zhao, C., Takita, J., Tanaka, Y., Setou, M., Nakagawa, T., Takeda, S., Yang, H.W., Terada, S., Nakata, T., Takei, Y., *et al.* (2001). Charcot-Marie-Tooth disease type 2A caused by mutation in a microtubule motor KIF1Bbeta. Cell *105*, 587-597

Appendix Studying cargo-induced dimerization via FRET

Portions of this chapter have been adapted from the following publication:

Soppina, V., Norris, S.R., Dizaji, A.S., Kortus, M., Veatch, S., Peckham, M., and Verhey, K.J. (2014). Dimerization of mammalian kinesin-3 motors results in superprocessive motion. Proceedings of the National Academy of Sciences of the United States of America *111*, 5562-5567.

Author contributions:

V.S. and K.J.V. designed research. V.S., S.R.N., and M.K. performed research. A.S.D., S.V., and M.P. contributed new reagents/analytic tools. M.P. generated helical net plots. V.S., S.R.N., A.S.D., S.V., and K.J.V. analyzed data. V.S. and K.J.V. wrote the paper.

A.1 Introduction

In order for molecular motors to function efficiently, they must exist in the proper oligomeric state (Vale, 2003). Conventional wisdom dictates that most processive motors have two-headed structures and thus exist as a dimer, where the motor steps in a hand-over-hand fashion. This is thought to be advantageous because, as one motor head unbinds the microtubule track and swings forward, the dimeric motor remains bound to the track via the second motor head. This two-headed mechanism has been observed directly via superresolution microscopy for kinesin and myosin motors (Yildiz et al., 2004a; Yildiz et al., 2004b) and is thought to be crucial for efficient transport. Indeed, the vast majority of processive motors exist as dimers and walk in

a hand-over-hand fashion (Schliwa, 2003). For instance, processive myosin V (Mehta et al., 1999) and myosin VI (Wells et al., 1999) motors walk as processive dimers whereas nonprocessive conventional muscle myosin works as teams of monomers to contract muscle fibers (Huxley, 1969). Processive cytoplasmic dynein also utilizes a dimerization domain to drive two-headed motion (Reck-Peterson et al., 2006; Shima et al., 2006), although the detailed mechanism of two-headed dynein stepping is far more complex than that of myosin or kinesin (Vallee et al., 2004). Similar to myosin and dynein, most processive kinesin motors also exist as dimers, where dimerization is mediated by an alpha-helical coiled coil segment located in the motor stalk domain known as the neck coil (Hirokawa et al., 2009b; Verhey et al., 2011). Importantly, not all kinesins exist as dimers. The wide genetic variety in the kinesin superfamily also gives rise to nonconventional motors such as MT depolymerases such as MCAK where the minimal depolymerization domain is a monomer (Maney et al., 2001), or tetrameric motors such as kinesin-5 family members that crosslink and slide microtubules (Cross and McAinsh, 2014).

A.1.2 KIF1A: monomer or dimer?

Significant debate in the field centers on the oligomeric state of the processive motor *Mm*KIF1A/*Ce*UNC104, a member of the extensive kinesin-3 family (Hirokawa et al., 2009a) (Fig. A.1). Early studies of this motor showed that mutations in the gene encoding *Ce*UNC104 led to severe defects in synaptic vesicle transport, a phenotype typically associated with mutations in processive motors (Okada et al., 1995). Interestingly, biophysical characterizations of this motor in the same study indicated that it behaved as a monomer *in vitro*. This led to a number of followup studies investigating how a monomeric motor could lead to processive motion along MTs (Hirokawa et al., 2009a). One popular theory proposed that monomeric KIF1A's processivity

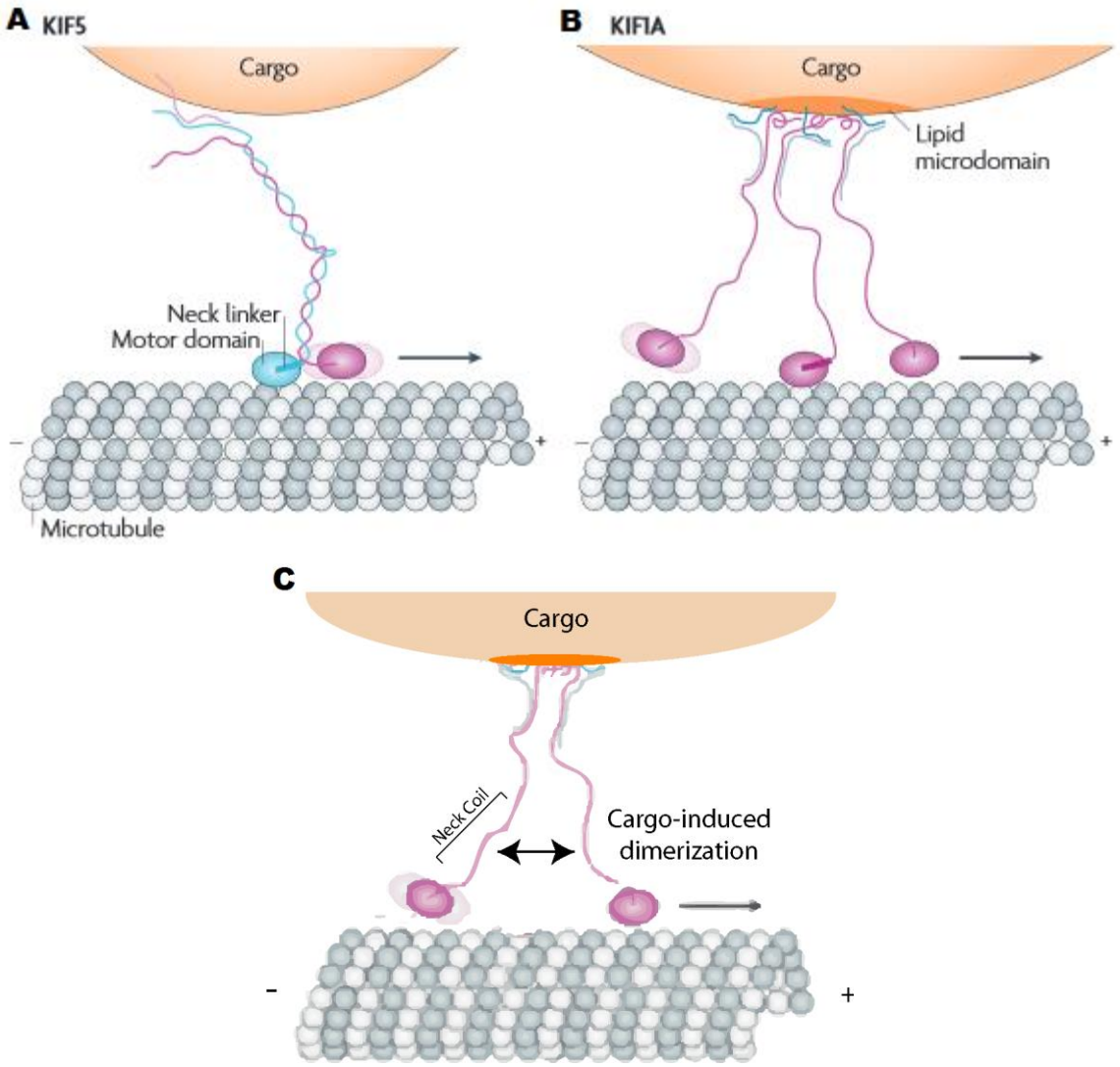

Figure A.1. A proposed motility model for kinesin-1 and KIF1A

(A) Cargo transport by kinesin-1 (KIF5) towards the microtubule plus end. KIF5 monomers form a parallel dimer with the motor domains on one end and the cargo binding domains on the other. **(B)** A proposed motility model for cargo transport by KIF1A towards the microtubule plus end. KIF1A monomers were thought to form a cluster on the lipid microdomain of cargo vesicles, resulting in motility. **(C)** An alternate motility model for cargo transport by KIF1A. As local concentration on the cargo surface increases, KIF1A undergoes cargo-induced dimerization via its neck coil (NC) domain.

Figure used, with permission, from Hirokawa, N., Nitta, R., and Okada, Y. (2009). The mechanisms of kinesin motor motility: lessons from the monomeric motor KIF1A. Nature reviews Molecular cell biology 10, 877-884.

arose from a charge-driven biased diffusion along the MT surface (Okada et al., 2003), but the speeds observed for monomeric KIF1A in these assays were significantly slower than the speeds observed in gliding assays (Okada et al., 1995; Pierce et al., 1999) or *in vivo* (Lee et al., 2003; Zhou et al., 2001). Another study showed that forced dimerization of KIF1A led to much higher velocity and processivity than its monomeric form (Tomishige et al., 2002), further suggesting that the monomeric form of KIF1A is not sufficient for processive motility. KIF1A has also been shown to be capable of homodimerization in COS7 cells (Hammond et al., 2009), perhaps in a concentration-dependent manner. Another study showed that mutation of the supposed dimerization domain of KIF1A eliminated motility on liposomes (Klopfenstein et al., 2002), suggesting that this dimerization is necessary as a trigger to activate processive motility. The currently favored model for this motor is a cargo-induced dimerization model where local clustering of the motor induces dimerization via its neck coil domain (NC) and thus activates processive transport (Fig. A.1C), a phenomenon which has been previously observed for myosin VI (Phichith et al., 2009; Yu et al., 2009), myosin X (Umeki et al., 2011), and myosin VIIA (Sakai et al., 2011).

KIF1A's oligomerization behavior suggests that other kinesin-3 motors may function by a similar mechanism. The kinesin-3 family is one of the largest among the kinesin superfamily and consists of five subfamilies in mammals (KIF1, KIF13, KIF14, KIF16, and KIF28) (Klopfenstein et al., 2002). Interestingly, sequence analysis showed that the kinesin-3 family has a much shorter alpha-helical dimerization segment (neck coil) than other kinesin motors such as kinesin-1, suggesting that they have a lower tendency to dimerize in solution (Verhey et al., 2011). Thus, we set out to study whether other members of the kinesin-3 family also undergo monomer-to-dimer transitions that are mediated by cargo binding.

A.1.3 Measuring the oligomeric state of proteins

The oligomeric state of a protein can be measured *in vitro* in a number of ways: classic size-exclusion chromatography (Folta-Stogniew, 2006), *in vitro* fluorescence correlation spectroscopy (Chakraborty et al., 2012), analytical ultracentrifugation (De Marco et al., 2003), NMR relaxation measurements (Lee et al., 2006), static light scattering (Nettleship et al., 2008), and single-molecule sequential photobleaching, which our lab commonly uses in the case of motors (Cai et al., 2007b; Hammond et al., 2009). Probing the oligomeric state of proteins in living cells or *in vivo* tends to be more complicated due to experimental complications, but a number of tools are now available to test this: fluorescence fluctuation spectroscopy (Chen et al., 2003), fluorescence correlation spectroscopy (Gaglia et al., 2013), laser scanning microscopy (Digman et al., 2008), and other creative non-invasive fluorescence techniques (Webber et al., 2009). One extremely powerful technique to examine protein oligomerization in cells is FRET, or Förster Resonance Energy Transfer (Bader and Beck-Sickinger, 2004). This method has previously been used in our lab to study the oligomeric state of motors (Hammond et al., 2009) and provides a valuable tool which we utilized in this study to measure kinesin-3 dimerization.

A.1.4 Förster Resonance Energy Transfer – background and introduction

Since the theoretical introduction of FRET in the 1940's (Förster, 1946), scientists have harnessed the power of this phenomenon in combination with modern microscopy to develop an indispensable technique for cell biologists and biophysicists (Sun et al., 2011). FRET involves dipole-dipole energy transfer between two fluorophores, a phenomenon which only occurs when the two fluorophores are in close proximity (< 10 nm) and are oriented correctly. As a general

technique, FRET is a versatile tool in the motors field. It has been used to confirm the oligomeric state of motors (Hammond et al., 2009), study motor-cargo interactions (Danquah et al., 2012; Jeshtadi et al., 2010) and study intramotor conformational changes (Cai et al., 2007a; Espenel et al., 2013), all inside living cells (see Fig. A.2 for schematics of inter-molecular and intra-molecular FRET). Importantly, FRET has also been used *in vitro* to study the motor's biomechanical cycle in great detail (Mori et al., 2007; Verbrugge et al., 2009).

Although the basic phenomenon leading to FRET is well-established, a number of different FRET-based techniques have been developed for specific applications (Lakowicz, 2006). Generally speaking, when FRET donor molecules such as CFP or GFP (i.e., blue-shifted relative to acceptor) are excited by the appropriate wavelength, energy is transferred via dipole-dipole interaction to FRET acceptors such as YFP or RFP (i.e., red-shifted relative to donor). This transfer efficiency is proportional to $\frac{1}{r^6}$, where r is the distance between FRET partners. This rapid spatial decay in transfer efficiency allows FRET to act as an extremely sensitive molecular ruler on the nanometer scale, where FRET only occurs at molecular separations less than ~10 nm. In addition to the distance between FRET molecules, transfer efficiency also depends on a number of other factors, including the quantum yields of both partner fluorophores, extinction coefficients of both fluorophores, and relative orientation of the pair.

A.1.5 How to measure FRET

This FRET-based energy transfer can be observed, measured and quantified in three ways: sensitized emission of the acceptor, dampened photobleaching of the donor, and decreased

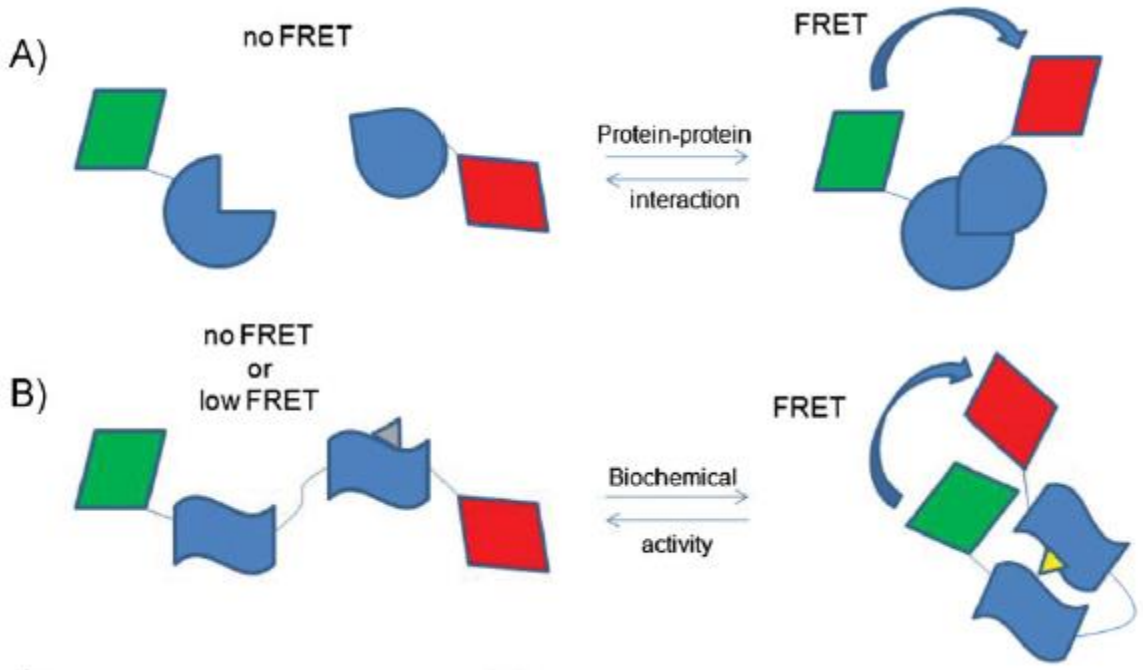

Figure A.2. Inter-molecular and intra-molecular energy transfer.

(A) The cartoon describes two proteins diffusing independently, one tagged with a green FP (donor) and the other tagged with a red FP (acceptor). When interaction occurs, the distance and orientation of the tagged proteins allow FRET to occur. **(B)** A protein with two subunits is tagged with a green FP (donor) and a red FP (acceptor). When a conformational change occurs, both donor and acceptor are close enough for FRET to occur.

Figure used, with permission, from Padilla-Parra, S., and Tramier, M. (2012). FRET microscopy in the living cell: different approaches, strengths and weaknesses. BioEssays : news and reviews in molecular, cellular and developmental biology *34*, 369-376.

---

lifetimes of the donor. Sensitized emission provides the most conceptually straightforward method of measuring FRET. When the donor transfers energy to the acceptor, the acceptor's electrons are moved to an excited state (see Fig. A.3 for summary of energy transfer pathways) (Jares-Erijman and Jovin, 2006). Radiative (i.e., fluorescence) relaxation from the acceptor's excited state results in fluorescence emission with properties specific to the acceptor. Measurement of this enhanced acceptor fluorescence (i.e., imaging using donor excitation wavelengths and acceptor emission

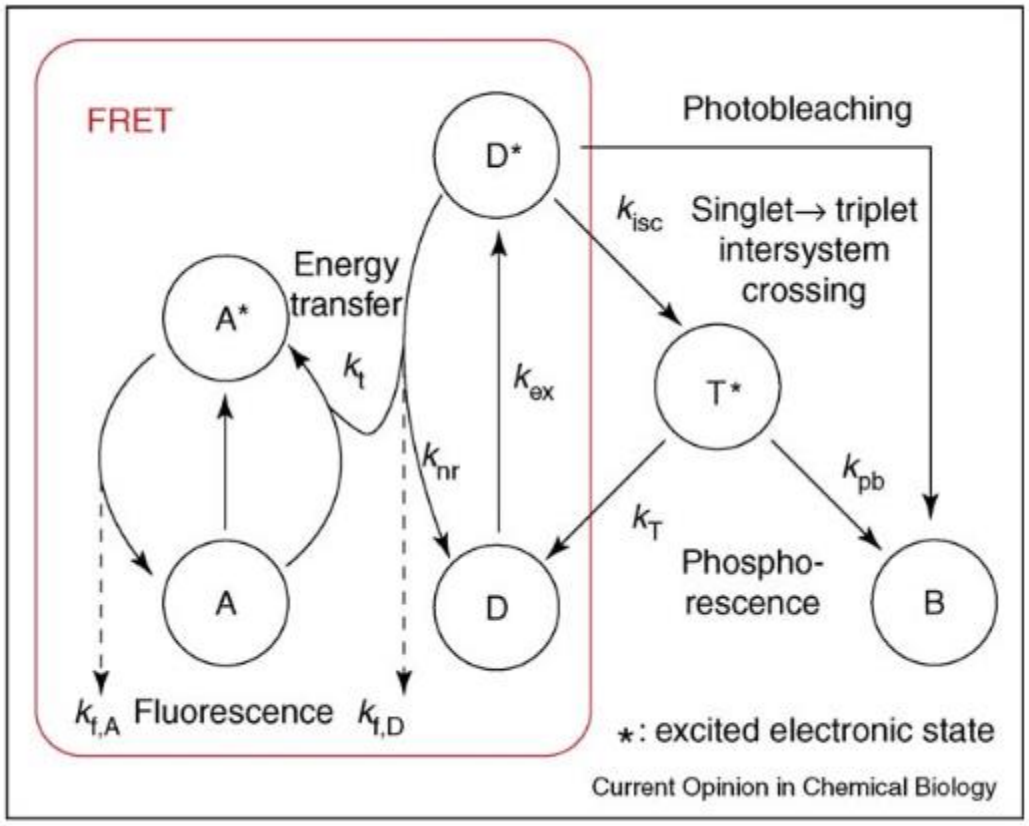

Figure A.3. Energy transfer pathways.

A donor D (middle, bottom) is excited by absorption of light (k_{ex}) to its excited state (D^*), where it can deactivate via a number of pathways: fluorescence emission ($k_{f,D}$), non-radiative relaxation (k_{nr}), intersystem crossing to the triplet state (k_{iSC}) whereupon it can undergo photobleaching (k_{pb}), and resonance energy transfer (k_t) to a nearby acceptor (A). The latter, in turn, undergoes deactivation, including the possibility of a fluorescent emission ($k_{f,a}$).

Figure used, with permission, from Jares-Erijman, E.A., and Jovin, T.M. (2006). Imaging molecular interactions in living cells by FRET microscopy. Current opinion in chemical biology 10, 409-416.

---

wavelengths) in the presence of FRET is known as sensitized emission. Single-molecule FRET allows direct observation of this phenomenon for individual FRET pairs via *in vitro* TIRF microscopy (Roy et al., 2008).

Photobleaching and lifetime measurements also allow observations of FRET, where the fluorescence properties of the donor are measured rather than those of the acceptor. In general, photobleaching occurs after a fluorophore electron's relatively rare transition from an excited singlet state to the excited triplet state, after which the fluorophore undergoes covalent modifications to abolish its fluorescence (Ghauharali and Brakenhoff, 2000). The presence of a nearby acceptor molecule provides an alternative energy transition pathway via FRET, thus lowering the likelihood of the singlet to triplet transition implicated in photobleaching. By measuring the rate of photobleaching in the donor channel, scientists can thus monitor the levels of FRET, where dampened photobleaching indicates more FRET.

Fluorescence lifetime imaging (FLIM) provides an additional technique for measuring FRET (Wallrabe and Periasamy, 2005), where lifetime is defined as the amount of time the fluorophore spends in the excited state. The presence of a nearby FRET acceptor allows an additional nonradiative (i.e., non-fluorescent) transfer of energy for the FRET donor, which effectively decreases the amount of time the FRET donor spends in the excited state. By studying fluorescence lifetime distributions of the donor, which can be described by an exponential function, scientists can monitor the level of FRET where shorter donor lifetimes indicate more FRET. This can be performed either a) in the time domain, by briefly pulsing a sample with donor excitation and measuring the fluorescence decay, or b) in the frequency domain, where a sample is repeatedly excited in a sinusoidal fashion and emission phase shifts are measured to detect FRET (Lakowicz, 2006).

A.1.5.1 Using the FRET stoichiometry method to calculate FRET contribution

Early methods for measuring FRET were unable to determine whether a low FRET signal was truly due to the absence of a complex or if this was a false negative due to local excesses of free donor or acceptor molecules. This distinction is particularly important in live cells where overexpression conditions may lead to variable acceptor and donor concentrations, especially where concentrations can vary locally based on the localization of the particular fusion protein under study. This concern was circumvented by the development of so-called 3-cube FRET techniques, which use a series of three images (donor excitation + emission, acceptor excitation + emission, donor excitation + acceptor emission, see Fig. A.4) to systematically separate the true FRET contribution from fluorescence bleedthrough (Padilla-Parra and Tramier, 2012; Piston and Kremers, 2007). One of these so-called 3-cube FRET techniques, FRET stoichiometry, also allows quantification of the molar ratio of acceptor to donor via algebraic image processing (Hoppe et al., 2002). This technique has been used to study a variety of cellular processes including G-protein activation (Hoppe and Swanson, 2004), intramolecular activation of motor proteins (Cai et al., 2007a), and the oligomeric state of motor proteins (Hammond et al., 2009). This technique was recently expanded to N-way FRET, which allows FRET-based characterization of groups of multiple proteins (Hoppe et al., 2013). Other techniques, such as FLIM-based FRET (see above), allow similar measurements with supposedly increased sensitivity (Espenel et al., 2013), but FLIM requires specialized equipment to excite fluorophores and detect lifetimes on nanosecond time scales, whereas the FRET stoichiometry approach can be used with any fluorescence-based microscope equipped with the correct filter sets.

The basics behind FRET stoichiometry are as follows. For extended experimental details and FRET equations, see (Hoppe et al., 2002) or the materials and methods section of Chapter 2. All images in the process (calibration and experimental) are corrected for bias (pixel-to-pixel

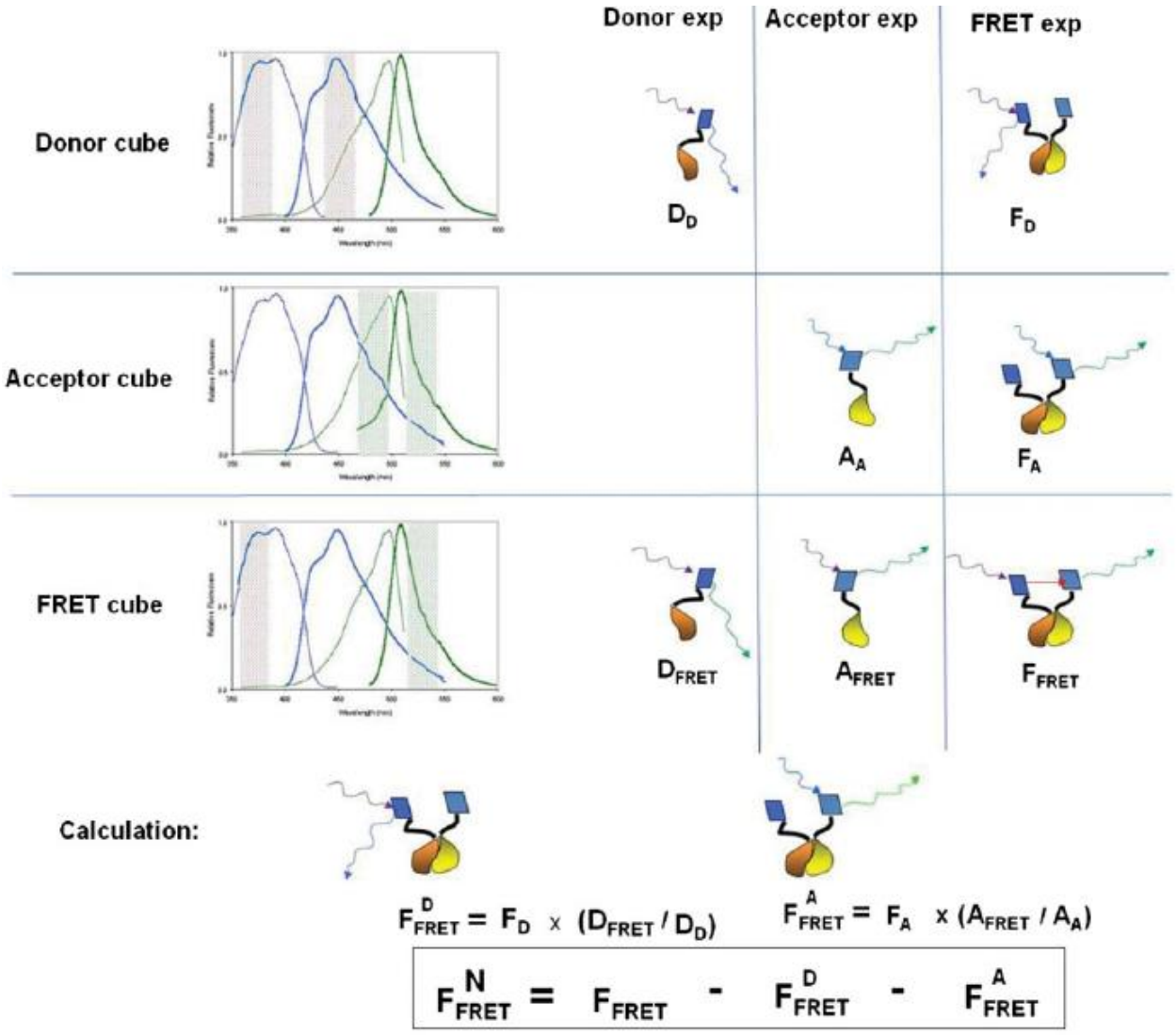

Figure A.4. 3-cube FRET.

This technique is used to measure the FRET signal corrected from the donor spectral bleed-through into the acceptor channel and the direct acceptor excitation. The technique measures the fluorescence images from three spectral configurations: the donor cube (donor excitation and donor emission, D in subscript), the acceptor cube (acceptor excitation and acceptor emission, A in subscript) and the FRET cube (donor excitation and acceptor emission, FRET in subscript). The measurements pertaining to the three cubes are carried out for the FRET experiment (F) and two controls having donor only (D) and acceptor only (A). The donor spectral bleedthrough into acceptor channel during the FRET experiment (F_{FRET}^{D}) is determined by calculating the product of the intensity of FRET experiment in the D-cube (F_D) by the correction ratio of the intensity of the same donor image in the FRET-cube (D_{FRET}) and in the D-cube (D_D). The acceptor direct excitation using FRET-cube during FRET experiment (F_{FRET}^{A}) is determined by calculating the product of the intensity of FRET experiment in the A-cube (F_A) by the correction ratio of the intensity of the same acceptor image in the FRET-cube (A_{FRET}) and in the A-cube (A_A). These two bleed-through corrections are then

subtracted from the measured intensity in the FRET-cube during FRET experiment (F_{FRET}) to recover the real FRET intensity of the experiment (F_{FRET}^{N}). This value corresponds to the corrected signal coming from the FRET process received in the acceptor channel after direct excitation of the donor. Its quantity depends directly on the concentration of the donor and/or acceptor and is usually normalized by the donor intensity for the FRET experiment (F_D) or the acceptor intensity of the FRET experiment (F_A).

Figure used, with permission, from Padilla-Parra, S., and Tramier, M. (2012). FRET microscopy in the living cell: different approaches, strengths and weaknesses. BioEssays : news and reviews in molecular, cellular and developmental biology *34*, 369-376.

---

variation of the detector), shade (uneven illumination), and background (nonzero intensity contributions from non-sample imaging regions). After these corrections, a series of calibration images is taken to calculate a series of constants which describe the bleedthrough contribution of each fluorophore and the characteristic FRET of the experimental system. α describes the spectral contamination of acceptor emission due to donor excitation, and is determined by 3-cube imaging of the acceptor alone. β describes the spectral contamination due to donor emission in the acceptor channel, and is determined by 3-cube imaging of the donor alone. γ and ξ describe the characteristic energy transfer of the particular FRET pair under study, and are determined by 3-cube imaging of a covalently-linked FRET pair which serves as a positive control. Together, these calibration constants describe both the imaging parameters of the microscope and of the particular FRET pair used throughout the study.

Once each of these contributions is quantified via calibration, normalized sensitized emission values can be calculated [see (Hoppe et al., 2002) for derivations]. These include sensitized emission, sensitized emission normalized by donor concentration (E_D), and sensitized emission normalized by acceptor concentration (E_A), which allow for the calculation of the molar ratio of acceptor to donor (R). E_{AVE}, which is the mean of E_D and E_A, is typically the reported

"FRET" value when the acceptor and donor are expressed in roughly equal proportion (e.g., this Appendix). E_D is reported when the acceptor is expressed at a higher level than the donor and thus FRET pairs typically have a high fraction of donor in complex (see Chapter 2 where donor splitGFP formation is rate-limiting).

To determine the dynamic range of FRET values, a negative and positive control must first be imaged. When cytosolic acceptor and donor molecules are co-expressed (e.g., co-expression of CFP and YFP), the fluorophores do not interact and thus a low value of E_{Av} is obtained after 3-cube imaging and FRET calculations. This value theoretically approaches zero assuming proper calibration and low noise. When a covalently-linked acceptor and donor molecule (e.g., expression of CFP-12aa-YFP where 12aa is a short peptide linker) is expressed and imaged via the 3-cube method, these fluorophores are constrained in close proximity and thus lead to the highest possible value of E_{AVE} for the system. This value theoretically approaches the independently-obtained FRET efficiency value as determined by fluorescence lifetime measurements, where more efficient FRET pairs such as CFP-YFP lead to higher maximal E_{AVE} values than inefficient FRET pairs such as GFP-mCherry. These two measurements thus define the dynamic range of the subsequent experiment. Overall, while FRET stoichiometry experiments require a significant amount of calibration and imaging of control constructs, the method provides an established technique for probing the oligomeric state of kinesin-3 motors.

A.2 Results

To examine the effect of cargo-binding on the oligomeric state of kinesin-3 motors, we studied the kinesin-3 family member KIF16B. Full-length KIF16B contains a C-terminal PX

domain which binds endosomes directly via PI(3)P and renders the motor entirely cargo-bound, a unique feature in the motor field (Hoepfner et al., 2005). A double point-mutation to residues neighboring the PX domain (L1248A and F1249A) has been shown to abolish KIF16B's cargo-binding (Blatner et al., 2007), presumably by disrupting hydrophobic interactions between motor tail and its endosomal cargo. Expression of full length KIF16B and this associated LF/AA mutant thus allows a positive and negative control for cargo-binding in cells, respectively.

To verify the cargo-binding behavior of this mutant, we first expressed full-length KIF16B in differentiated CAD cells, a mouse cell line that displays neuronal morphology (Fig. A.5). We found that wild-type KIF16B localizes to puncta throughout the cell (presumably early endosomes), where a number of these puncta are localized to cellular processes, a phenotype that is typically indicative of active transport. The LF/AA mutant, on the other hand, mislocalizes KIF16B to the cytosol and no puncta are observed.

To study the oligomeric state of KIF16B in the presence or absence of cargo, we used the FRET stoichiometry method described above to compare FRET levels between wild-type (cargo-bound) and LF/AA (cytosolic) KIF16B (Fig. A.6). The motors were tagged with monomeric versions of the FRET donor cyan fluorescent protein (mCFP) or the FRET acceptor Citrine (mCit) either at the N-terminus to measure the proximity of the motor domains (motor-to-motor FRET) or at the C-terminus to measure the proximity of the tail domains (tail-to-tail FRET) (Fig. A.6). We chose to measure both motor-to-motor FRET and tail-to-tail FRET to rule out possible artifacts arising from placement of the fluorescent tags, such as a false-positive FRET signal arising from molecular crowding on the surface of the endosome in the case of tail-to-tail FRET. Note that co-expression of mCit-tagged and mCFP-tagged motors does not ensure heterodimerization; two

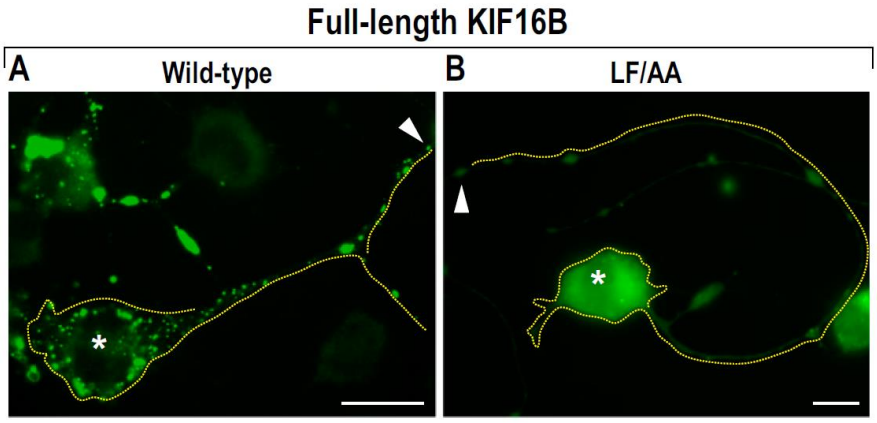

Figure A.5. Expression of full-length KIF16B in CAD cells.

KIF16B is tightly associated with its early endosomal cargo through its PX domain. **(A-B)** Representative images of differentiated CAD cells expressing C-terminal mCit-tagged **(A)** wild-type KIF16B or **(B)** the mutant KIF16B(LF/AA), which cannot bind to its endosomal cargo. Dotted yellow lines indicate the outline of transfected cells; white arrowheads indicate neurite tips; white asterisks indicate nucleu. (Scale bars, 20 μm.)

Virupakshi Soppina in the Verhey lab conducted experiments in Figure A.5, which was published in (Soppina et al., 2014).

KIF16B-mCit monomers may dimerize, for instance, which would result in a sub-optimal FRET signal.

Before testing the FRET efficiencies of each motor, we first needed to confirm the expression of each motor in the study and verify that the observed puncta were indeed early endosomes. To do this, we expressed each motor in COS7 cells and stained for the early endosomal marker EEA1 (Fig. A.7). We found that all constructs possessing the PX domain colocalized completely with early endosomes, whereas constructs containing the LF/AA mutant appeared cytosolic and showed no coexpression with EEA1 (Fig A.7B,E). We also noticed differences in localization for the wild-type motor; C-terminally tagged KIF16B dispersed early endosomes to the periphery of the cell (Fig. A.7A) where N-terminally tagged KIF16B did not

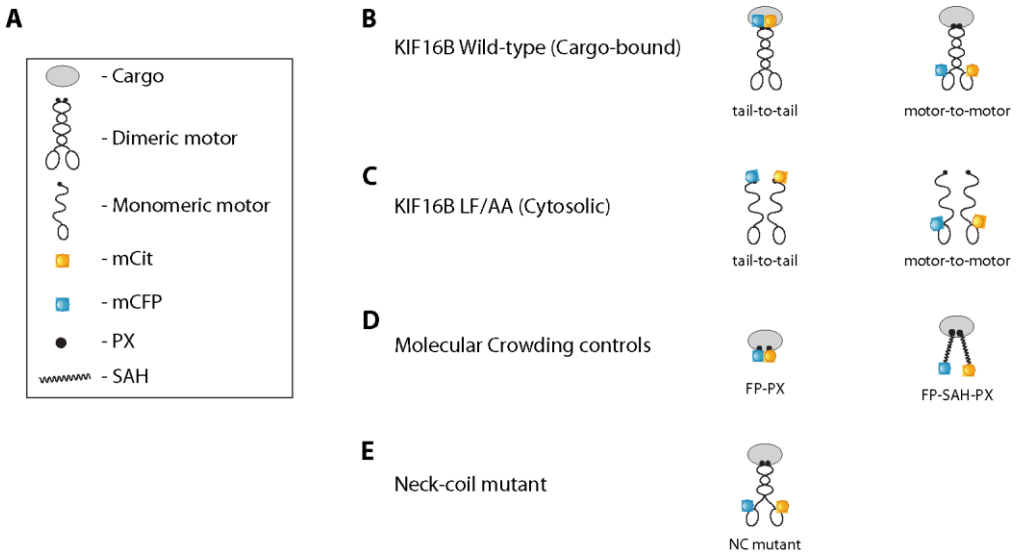

Figure A.6. Schematic of KIF16B FRET constructs.

(A) Legend. COS7 cells were coexpressed with **(B)** wild-type KIF16B tagged with FRET donor (mCFP) and acceptor (mCit) fluorescent proteins, **(C)** the cargo-binding mutant LF/AA tagged with mCFP and mCit, **(D)** donor and acceptor proteins targeted to the surface via the monomeric KIF16B PX domain (left) or donor and acceptor FPs extended 30 nm from the cargo surface by a SAH between the FP and PX domains, **(E)** the N-terminally tagged KIF16B NC mutant.

Virupakshi Soppina in the Verhey lab created Figure A.6, which was published in (Soppina et al., 2014).

(Fig A.7D). We speculate that the N-terminal location of the fluorescent protein interferes with motor activity thus preventing dispersion, an observation we have made previously for some N-terminally tagged kinesin-1 constructs (unpublished data). Overall, this localization behavior is consistent with previous studies (Blatner et al., 2007; Hoepfner et al., 2005) and overexpression in CAD cells (Fig. A.5), and thus we proceeded with the FRET study.

mCFP-mCit provides an efficient FRET pair which has been used previously in our lab to study the intramolecular conformation of kinesin-1 motors (Cai et al., 2007a). After extensive calibration to characterize the behavior of the mCFP-mCit FRET pair on the microscope (see

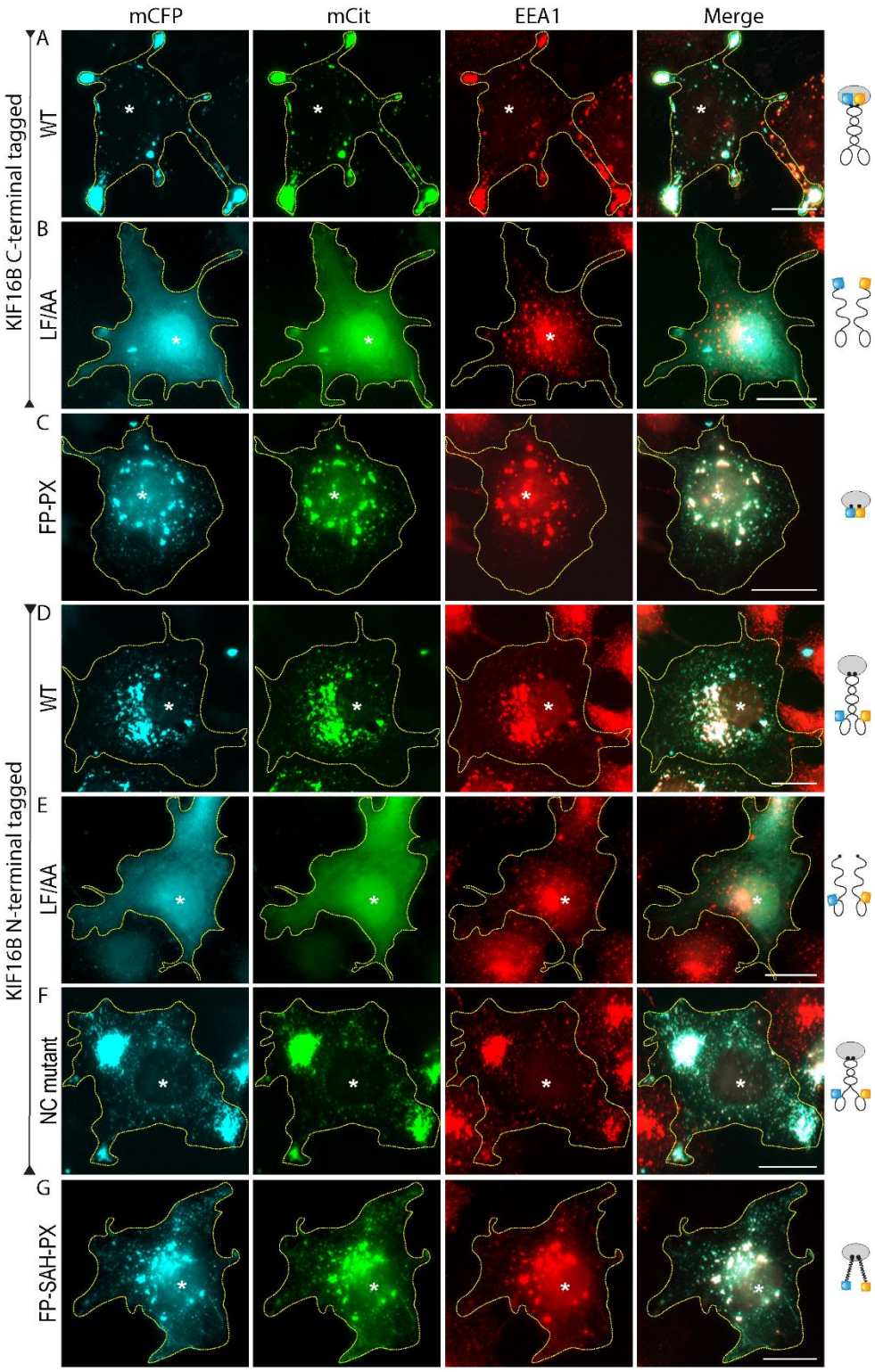

Figure A.7. Cellular distribution of KIF16B and control FRET constructs.

(A-G) Representative images of COS7 cells coexpressing mCFP (donor)- and mCit (acceptor)-tagged versions of wild-type KIF16B, mutant KIF16B, or control FRET constructs were fixed and immunostained for the cargo protein early endosome antigen (EEA1, red). Dotted yellow lines indicate the outline of transfected cells; white asterisks indicate nuclei (Scale bars, 10 μm.)

Virupakshi Soppina in the Verhey lab conducted experiments in Figure A.7, which was published in (Soppina et al., 2014).

---

above), we determined the dynamic range of the experiment by measuring the FRET efficiency of a negative control (co-expressed mCFP + mCit) and a positive control (linked mCFP-16aa-mCit). We found that the negative control exhibited very low FRET (E_{AVE} = 2.2 ± 0.9%), whereas the positive control exhibited very high FRET signal (E_{AVE} = 44.4 ± 1.8%), thus defining the experimental limits of our system (Fig A.8A,I)

For the cytosolic KIF16B(LF/AA) motors, very low levels of FRET were detected (E_{AVE} = 3.0 ± 1.8% for tail-to-tail, 3.3 ± 1.2% for motor-to-motor) that were similar to the negative control, suggesting that non-cargo-bound motors exist in a monomeric state (Fig. A.8C,F, all FRET measurements summarized in Fig. A.9). In contrast, wild-type KIF16B motors recruited to endosomes displayed significantly higher levels of FRET (E_{AVE} = 27.8 ± 6.2% for tail-to-tail, E_{AVE} = 12.1 ± 2.1% for motor-to-motor, $p < 0.0001$ for both), suggesting that cargo-bound motors exist in a dimeric state (Fig. A.8B,E, Fig. A.9). To ensure that this signal was due to neck-coil (NC) dependent dimerization, we generated a NC mutant where the hydrophobic residues in the "a" and "d" positions of the neck coil were changed to charged residues (Fig. A.6E), as described for *Ce*UNC-104 (Klopfenstein et al., 2002). The wild-type KIF16B motor showed significantly ($p < 0.0001$) higher motor-to-motor FRET than the NC mutant KIF16B (E_{AVE} = 8.2 ± 1.1% for NC mutant), suggesting that motor-to-motor FRET is dependent on motor dimerization via the NC

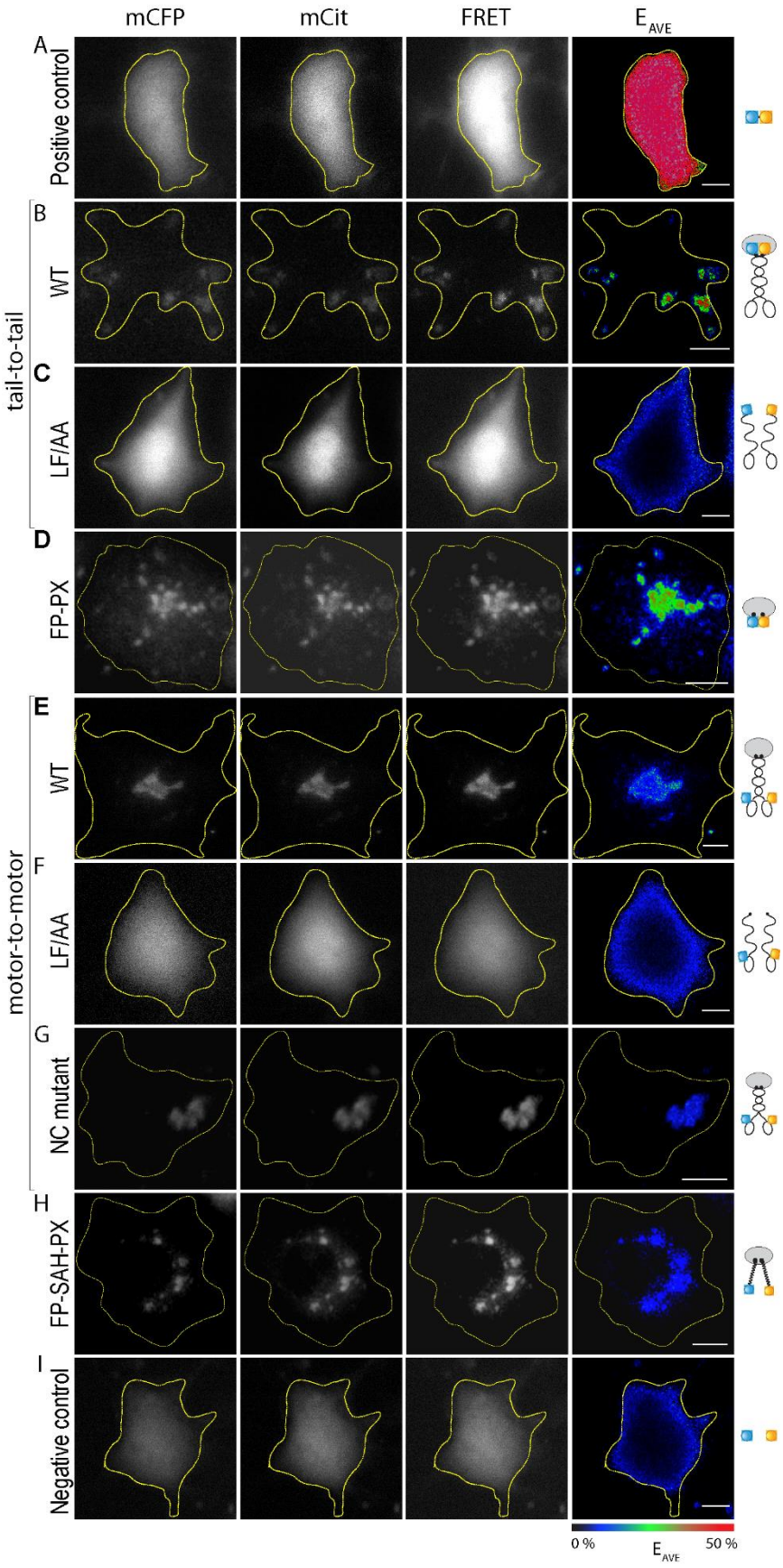
mCFP
mCit
FRET
E AVE
A
Positive control
tail-to-tail
B
WT
C
LF/AA
D
FP-PX
motor-to-motor
E
WT
F
LF/AA
G
NC mutant
H
FP-SAH-PX
I
Negative control
0 %
E AVE
50 %

Figure A.8. FRET microscopy in live COS7 cells.

Shown are representative images taken under mCFP imaging (first column), mCit imaging (second column), or FRET imaging (third column) conditions. From these images, the average FRET efficiency (E_{AVE}) (fourth column) was calculated. **(A)** As a positive FRET control, a mCFP-mCit fusion protein (linked by 16aa) was expressed. **(B and E)** Wild-type or **(C and F)** LF/AA mutant KIF16B motors were tagged with mCFP or mCit at **(B and C)** their C termini to measure FRET between the tail domains of individual KIF16B motors or at **(E and F)** their N termini to measure FRET between the motor domains of individual KIF16B motors. **(D)** FP-PX, the monomeric KIF16B-PX domain, was fused with mCFP or mCit. **(B and E)** Coexpression of mCFP- and mCit-tagged wild-type motors reveals a high FRET signal on the endosomal cargo, indicating that cargo-bound motors are dimeric. **(C and F)** coexpression of mCFP- and mCit-tagged LF/AA motors reveals little to no FRET signal, indicating that non-cargo-bound motors are monomeric. **(G)** NC mutant, where the hydrophobic residues in the "a" and "d" positions of the KIF16B neck coil were changed to glutamate and lysine residues, respectively. **(H)** FP-SAH-PX, where a 30 nm single α-helix (SAH) was inserted between the FP and PX domain in **(D)**. **(I)** As a negative FRET control, the FRET donor mCFP and FRET acceptor mCit proteins were coexpressed. (Scale bars, 10 μm.)

Experiments in Figure A.8 were conducted with Virupakshi Soppina in the Verhey lab. This figure was published in (Soppina et al., 2014).

(Fig. A.8G, Fig. A.9). We thus conclude that KIF16B undergoes cargo-induced, NC-based dimerization, where this process is likely driven by a higher local monomeric motor concentration on the membrane.

Interestingly, wild-type motors displayed a higher level of FRET for tail-to-tail measurements (Fig. A.8B) than for motor-to-motor measurements (Fig. A.8E), suggesting that the fluorophores were spaced more closely in the tail-to-tail configuration. To address the potential contribution of molecular crowding to our FRET signal, we tested two additional control constructs where mCFP and mCit were targeted to early endosomes in the absence of the KIF16B motor (Fig. A.6D). In the case of molecular crowding, we would expect to see a FRET signal when mCFP-PX and mCit-PX were co-expressed (Fig. A.6D, left), whereas this signal should be abolished upon addition of a 30-nm single alpha helix (SAH) (Sivaramakrishnan et al., 2008)

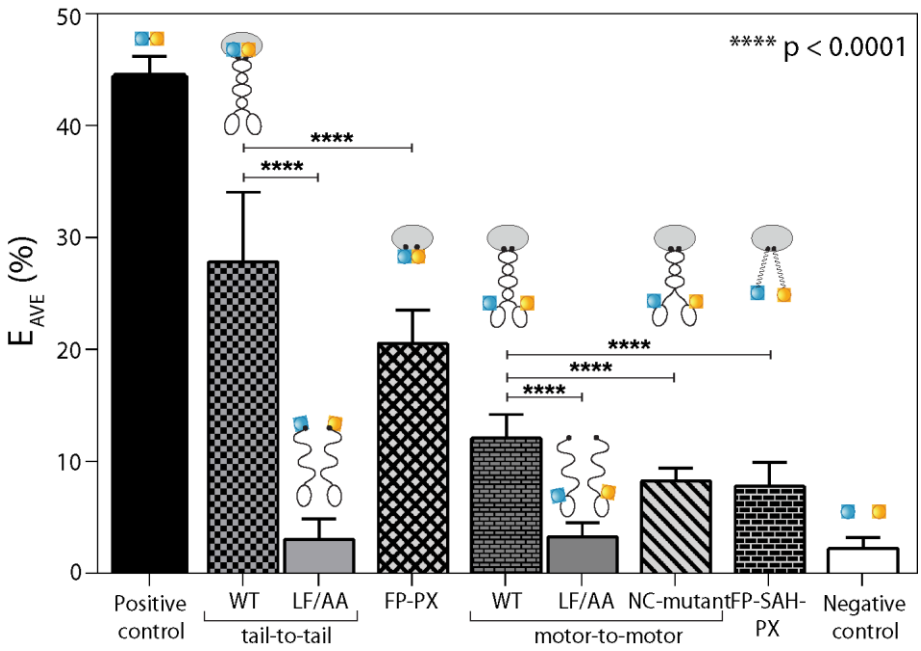

Figure A.9. Quantification of FRET efficiencies in live COS7 cells.

For a detailed description of constructs used in this experiment, see Fig. A.6. n = 25-40 cells each over three independent experiments. The data are presented as mean ± SD. P values were calculated using the two-tailed t test.

Experiments in Figure A.9 were conducted with Virupakshi Soppina in the Verhey lab. This figure was published in (Soppina et al., 2014).

---

between the fluorophore and the PX-domain (Fig. A.6D, right). We found that, while the FP-PX constructs do exhibit relatively high FRET (E_{AVE} = 20.5 ± 3.0%), these constructs display significantly less FRET than the tail-to-tail KIF16B constructs (E_{AVE} = 27.8 ± 6.2%, $p < 0.0001$). Unsurprisingly, when a 30 nm SAH is introduced to space the FRET pair 30 nm from the cargo, the FRET signal decreases drastically (E_{AVE} = 7.8 ± 2.1%). In the case of molecular crowding, we would also expect to see an increased FRET signal in the case of higher protein concentration, whereas a FRET signal purely from dimerization should be concentration independent. To test this, we created a scatter plot of FRET signal vs. protein concentration, as measured by

fluorescence intensity (Fig. A.10). Importantly, we found no correlation between FRET signal and fluorescence intensity for wild-type KIF16B tail-to-tail FRET, whereas the FP-PX FRET signal showed a clear correlation with fluorescence intensity (Fig A.10A). Similarly, we found no such correlation for wild-type KIF16B motor-to-motor FRET whereas the FP-SAH-PX constructs showed a weak linear relationship (Fig. A.10B). Additionally, at identical fluorescence intensities, the KIF16B motors always display a much higher FRET signal. This suggests that dimeric motors lead to a higher FRET signal than monomeric fluorescent proteins clustered on the same cargo. Taken together, these results indicate that, while molecular crowding does significantly contribute to the FRET signal in the case of the FP-PX construct, tail-to-tail FRET of KIF16B shows a significantly higher FRET signal presumably due to motor dimerization.

We next verified that cytosolic wild-type KIF16B was monomeric in solution via single-molecule photobleaching assays of cell lysates. To do this, the full-length motor was tagged with three tandem copies of mCit. In our previous work, we used this assay to determine the oligomeric state of KIF1A (Hammond et al., 2009). We thus used KIF1A as a control and also investigated the oligomeric state of additional kinesin-3 family members KIF13A and KIF13B, and KIF16B, whose molecular mechanisms of motor regulation and cargo transport are unknown. In photobleaching assays, the majority of molecules bleached in two or three steps (Fig. A.11A), indicating that all of the full-length kinesin-3 motors studied exist primarily in a momomeric state although some dimers are present in the population. This differs significantly from a truncated, dimeric kinesin-1 control [KHC(1-560)-3xmCit] (Fig. A.11B), thus confirming that kinesin-3 motors are largely monomeric in solution.

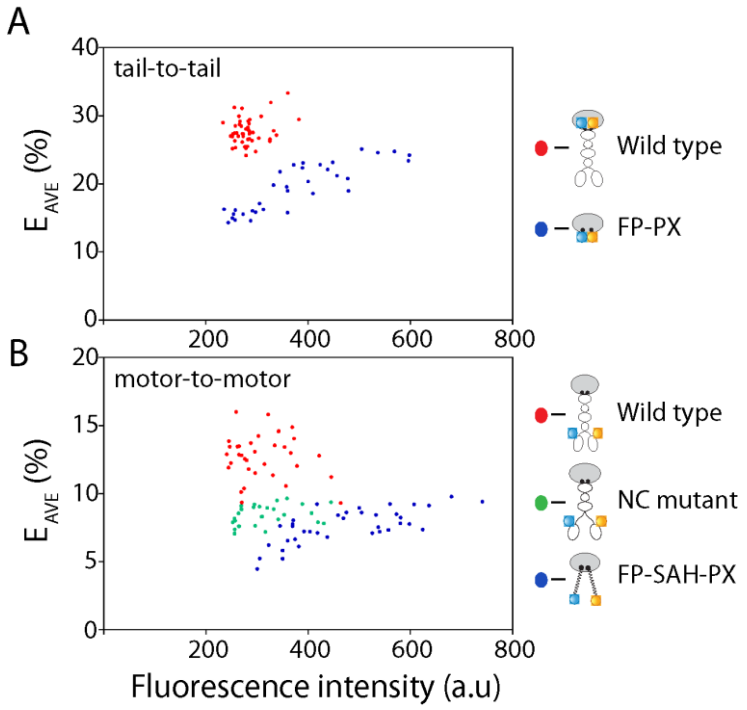

Figure A.10. Comparing FRET to fluorophore concentration.

The FRET value of each cell for the indicated tail-to-tail FRET construct construct **(A)** or motor-to-motor FRET construct **(B)** is displayed as a scatter plot where the y-axis indicates E_{AVE} and the x-axis indicates protein concentration (measured as fluorescence intensity).

Experiments in Figure A.8 were conducted with Virupakshi Soppina in the Verhey lab. This figure was published in (Soppina et al., 2014).

A.3 Discussion

To our knowledge, this is the first report to directly demonstrate cargo-mediated dimerization for full-length kinesin-3 motors on a cellular cargo. Subsequent experiments performed in (Soppina et al., 2014) demonstrated that forced dimeric versions of these kinesin-3 motors resulted in superprocessive motion, with characteristic velocities roughly twice as fast as

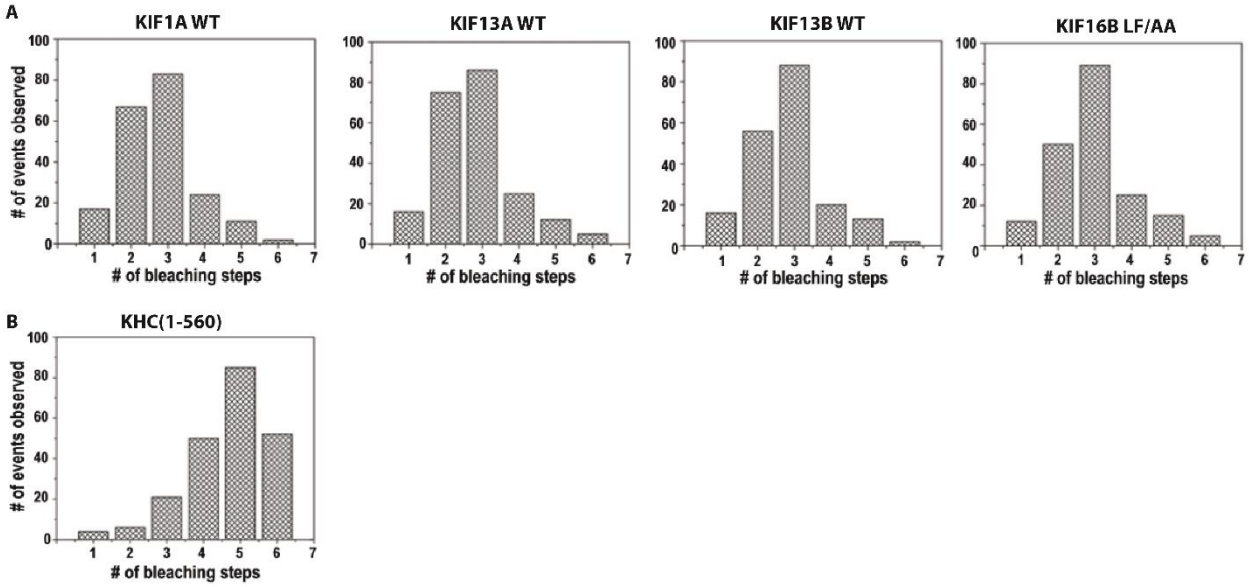

Figure A.11. Full-length kinesin-3 photobleaching experiments.

The oligomeric state of full-length kinesin-3 motors **(A)** KIF1A, KIF16B(LF/AA), KIF13A, and KIF13B were compared with that of an active dimeric kinesin-1 [KHC(1-560)] motor **(B)**. The fluorescence intensity over time was measured by TIRF microscopy for individual 3xmCit-tagged motors in COS7 cell lysates directly adsorbed onto the coverslip. The number of bleaching events per molecule was plotted in a histogram for the population. The majority of full-length kinesin-3 motors bleached in one to three steps, indicating that most of the molecules in the population are in a monomeric state. The majority of KHC(1-560) motors bleached in four to six steps, indicative of dimeric motors.

Virupakshi Soppina in the Verhey lab conducted experiments in Figure A.11, which was published in (Soppina et al., 2014).

---

kinesin-1 and run lengths of roughly 10 μm. Thus the transition from monomer-to-dimer appears to be essential for activating kinesin-3 motor activity on the cargo surface. Although this mechanism of regulation is so far unique among the kinesin superfamily, it is interesting to note that several members of the myosin superfamily have been demonstrated to undergo dimerization and activation upon cargo binding (Phichith et al., 2009; Sakai et al., 2011; Umeki et al., 2011; Yu et al., 2009). Thus, this work extends the parallels between the kinesin and myosin superfamilies.

Furthermore, these findings support two general principles of kinesin motor biochemistry. First, the NC segment is the minimal unit for dimerization of kinesin motors, and second, dimerization is a fundamental requirement for processive motion (see further experiments in Soppina et al., 2014). However, our results indicate that kinesin-3 motors use a unique mechanism of regulation in which the dimerization potential of the NC is regulated to ensure that cargo binding and processive motility are tightly linked.

Importantly, this technique for measuring FRET in live cells measures the steady state of oligomerization rather than dynamic transitions between monomer and dimer. Because of the time required to take images with the 3-cube technique (exposure time plus filter wheel movements) and because photons are collected from the entire cell, these measurements represent population averages over many seconds for the entire cell. Indeed, the temporal and spatial resolution of these experiments could be improved in a number of ways. Because frequency-domain FLIM-based FRET experiments sinusoidally probe the sample at many hundreds of MHz (Espenel et al., 2013), a FLIM-FRET approach could improve the temporal resolution of these experiments substantially to nanosecond resolution. Time-domain measurements (Elangovan et al., 2002) also allow incredible temporal resolution which have been pushed to picosecond resolution (Zhong et al., 2007). The FLIM-FRET method is also independent of change in probe concentration, photobleaching, and other factors that limit intensity-based steady-state measurements (Lakowicz, 2006), although these contributions can be limited via careful calibration as described above. Because FLIM-FRET leads to less experimental variability and because of its ability to measure interaction dynamics on the nanosecond scale endogenous to many protein-protein interactions, FLIM-FRET will likely soon be the field standard for protein interaction measurements, especially

as the technology continues to mature. The KIF16B experiments described here would likely benefit from such an experimental treatment.

Another criticism of our FRET-based dimerization assay is that these motors are likely overexpressed such that each cargo in these cells contains far more motors than endogenous cargoes. It would be advantageous, then, to reconstitute these experiments *in vitro* under controlled concentrations of motors and cargoes to study this behavior on the level of individual motors and cargoes. One potential approach could be reconstitute cargo transport on PI(3)P-containing liposomes and purified full length KIF16B. If KIF16B is labeled in two colors, one could observe single-molecule FRET and correlate this signal to liposomal motion. Alternatively, FIONA-based supper-resolution microscopy could be used in this setup to either to probe the proximity of two labeled KIF16B tail domains or observe hand-over-hand motion of two labeled motor domains (Yildiz et al., 2004b). Although experimentally time-consuming and difficult, such experiments could lead to amazing insight based on this enhanced spatial resolution.

As an interesting experimental note, the extent to which non-specific interactions contribute to FRET experiments (see Fig. A.10) is actively being studied. High concentrations of the FRET pair can lead to an anomalous signal between non-interacting molecules simply arising through proximity, although this contribution is relatively small in the cytosol where the fluorophores have more space to diffuse (Takanishi et al., 2006). This introduces an interesting double-edged sword: as fluorescence intensity increases, so does the signal to noise ratio, but this also potentially introduces unwanted contributions from non-specific FRET. In the case of membrane surfaces, this effect is enhanced because the fluorophores are constrained to a higher local concentration and are only allowed to diffuse in two dimensions rather than three. Earlier this year, King et al. gave this problem thoughtful theoretical and experimental consideration,

successfully calculating and verifying this contribution for a number of conditions (King et al., 2014). As part of this study, King et al. plotted FRET efficiencies as a function of the concentration of membrane-bound monomeric protein. Their plots qualitatively match our FRET-concentration curves for FP-PX, suggesting that this effect is what led to our observations.

A.4 Conclusion

Overall, these experiments reveal a mechanism of motor regulation that is unique to the kinesin field. Kinesin-3 motors are uniquely adapted to drive long-distance intracellular and axonal transport, and seem to be the marathon runners of the cellular world. This incredible processivity must be harnessed inside the cell, however, as motor activity in excess can lead to mislocalization of cargo or depletion of cellular ATP. Thus, this additional level of regulation via cargo-induced dimerization is necessary to activate this superprocessive transport only when needed by the cell.

A.5 References

Bader, J.E., and Beck-Sickinger, A.G. (2004). Fluorescence resonance energy transfer to study receptor dimerization in living cells. Methods in molecular biology *259*, 335-352. doi: 10.1385/1-59259-754-8:335

Blatner, N.R., Wilson, M.I., Lei, C., Hong, W., Murray, D., Williams, R.L., and Cho, W. (2007). The structural basis of novel endosome anchoring activity of KIF16B kinesin. The EMBO journal *26*, 3709-3719. doi: 10.1038/sj.emboj.7601800

Cai, D., Hoppe, A.D., Swanson, J.A., and Verhey, K.J. (2007a). Kinesin-1 structural organization and conformational changes revealed by FRET stoichiometry in live cells. The Journal of cell biology *176*, 51-63. doi: 10.1083/jcb.200605097

Cai, D., Verhey, K.J., and Meyhofer, E. (2007b). Tracking single Kinesin molecules in the cytoplasm of mammalian cells. Biophysical journal *92*, 4137-4144. doi: 10.1529/biophysj.106.100206

Chakraborty, M., Kuriata, A.M., Nathan Henderson, J., Salvucci, M.E., Wachter, R.M., and Levitus, M. (2012). Protein oligomerization monitored by fluorescence fluctuation spectroscopy: self-assembly of rubisco activase. Biophysical journal *103*, 949-958. doi: 10.1016/j.bpj.2012.07.034

Chen, Y., Wei, L.N., and Muller, J.D. (2003). Probing protein oligomerization in living cells with fluorescence fluctuation spectroscopy. Proceedings of the National Academy of Sciences of the United States of America *100*, 15492-15497. doi: 10.1073/pnas.2533045100

Cross, R.A., and McAinsh, A. (2014). Prime movers: the mechanochemistry of mitotic kinesins. Nature reviews Molecular cell biology *15*, 257-271. doi: 10.1038/nrm3768

Danquah, J.O., Botchway, S., Jeshtadi, A., and King, L.A. (2012). Direct interaction of baculovirus capsid proteins VP39 and EXON0 with kinesin-1 in insect cells determined by fluorescence resonance energy transfer-fluorescence lifetime imaging microscopy. Journal of virology *86*, 844-853. doi: 10.1128/JVI.06109-11

De Marco, V., De Marco, A., Goldie, K.N., Correia, J.J., and Hoenger, A. (2003). Dimerization properties of a Xenopus laevis kinesin-II carboxy-terminal stalk fragment. EMBO reports *4*, 717-722. doi: 10.1038/sj.embor.embor884

Digman, M.A., Dalal, R., Horwitz, A.F., and Gratton, E. (2008). Mapping the number of molecules and brightness in the laser scanning microscope. Biophysical journal *94*, 2320-2332. doi: 10.1529/biophysj.107.114645

Elangovan, M., Day, R.N., and Periasamy, A. (2002). Nanosecond fluorescence resonance energy transfer-fluorescence lifetime imaging microscopy to localize the protein interactions in a single living cell. Journal of microscopy *205*, 3-14

Espenel, C., Acharya, B.R., and Kreitzer, G. (2013). A biosensor of local kinesin activity reveals roles of PKC and EB1 in KIF17 activation. The Journal of cell biology *203*, 445-455. doi: 10.1083/jcb.201305023

Folta-Stogniew, E. (2006). Oligomeric states of proteins determined by size-exclusion chromatography coupled with light scattering, absorbance, and refractive index detectors. Methods in molecular biology *328*, 97-112. doi: 10.1385/1-59745-026-X:97

Förster, T. (1946). Naturwissenschafien. *6*, 166–175

Gaglia, G., Guan, Y., Shah, J.V., and Lahav, G. (2013). Activation and control of p53 tetramerization in individual living cells. Proceedings of the National Academy of Sciences of the United States of America *110*, 15497-15501. doi: 10.1073/pnas.1311126110

Ghauharali, R.I., and Brakenhoff, G.J. (2000). Fluorescence photobleaching-based image standardization for fluorescence microscopy. Journal of microscopy *198 (Pt 2)*, 88-100

Hammond, J.W., Cai, D., Blasius, T.L., Li, Z., Jiang, Y., Jih, G.T., Meyhofer, E., and Verhey, K.J. (2009). Mammalian Kinesin-3 motors are dimeric in vivo and move by processive motility upon release of autoinhibition. PLoS biology *7*, e72. doi: 10.1371/journal.pbio.1000072

Hirokawa, N., Nitta, R., and Okada, Y. (2009a). The mechanisms of kinesin motor motility: lessons from the monomeric motor KIF1A. Nature reviews Molecular cell biology *10*, 877-884. doi: 10.1038/nrm2807

Hirokawa, N., Noda, Y., Tanaka, Y., and Niwa, S. (2009b). Kinesin superfamily motor proteins and intracellular transport. Nature reviews Molecular cell biology *10*, 682-696. doi: 10.1038/nrm2774

Hoepfner, S., Severin, F., Cabezas, A., Habermann, B., Runge, A., Gillooly, D., Stenmark, H., and Zerial, M. (2005). Modulation of receptor recycling and degradation by the endosomal kinesin KIF16B. Cell *121*, 437-450. doi: 10.1016/j.cell.2005.02.017

Hoppe, A., Christensen, K., and Swanson, J.A. (2002). Fluorescence resonance energy transfer-based stoichiometry in living cells. Biophysical journal *83*, 3652-3664. doi: 10.1016/S0006-3495(02)75365-4

Hoppe, A.D., Scott, B.L., Welliver, T.P., Straight, S.W., and Swanson, J.A. (2013). N-way FRET microscopy of multiple protein-protein interactions in live cells. PloS one *8*, e64760. doi: 10.1371/journal.pone.0064760

Hoppe, A.D., and Swanson, J.A. (2004). Cdc42, Rac1, and Rac2 display distinct patterns of activation during phagocytosis. Molecular biology of the cell *15*, 3509-3519. doi: 10.1091/mbc.E03-11-0847

Huxley, H.E. (1969). The mechanism of muscular contraction. Science *164*, 1356-1365

Jares-Erijman, E.A., and Jovin, T.M. (2006). Imaging molecular interactions in living cells by FRET microscopy. Current opinion in chemical biology *10*, 409-416. doi: 10.1016/j.cbpa.2006.08.021

Jeshtadi, A., Burgos, P., Stubbs, C.D., Parker, A.W., King, L.A., Skinner, M.A., and Botchway, S.W. (2010). Interaction of poxvirus intracellular mature virion proteins with the TPR domain of kinesin light chain in live infected cells revealed by two-photon-induced fluorescence resonance energy transfer fluorescence lifetime imaging microscopy. Journal of virology *84*, 12886-12894. doi: 10.1128/JVI.01395-10

King, C., Sarabipour, S., Byrne, P., Leahy, D.J., and Hristova, K. (2014). The FRET signatures of noninteracting proteins in membranes: simulations and experiments. Biophysical journal *106*, 1309-1317. doi: 10.1016/j.bpj.2014.01.039

Klopfenstein, D.R., Tomishige, M., Stuurman, N., and Vale, R.D. (2002). Role of phosphatidylinositol(4,5)bisphosphate organization in membrane transport by the Unc104 kinesin motor. Cell *109*, 347-358

Lakowicz, J.R. (2006). Principles of Fluorescence Spectroscopy, Third Edition, Vol 13 (New York: Springer).

Lee, D., Hilty, C., Wider, G., and Wuthrich, K. (2006). Effective rotational correlation times of proteins from NMR relaxation interference. Journal of magnetic resonance *178*, 72-76. doi: 10.1016/j.jmr.2005.08.014

Lee, J.R., Shin, H., Ko, J., Choi, J., Lee, H., and Kim, E. (2003). Characterization of the movement of the kinesin motor KIF1A in living cultured neurons. The Journal of biological chemistry *278*, 2624-2629. doi: 10.1074/jbc.M211152200

Maney, T., Wagenbach, M., and Wordeman, L. (2001). Molecular dissection of the microtubule depolymerizing activity of mitotic centromere-associated kinesin. The Journal of biological chemistry *276*, 34753-34758. doi: 10.1074/jbc.M106626200

Mehta, A.D., Rock, R.S., Rief, M., Spudich, J.A., Mooseker, M.S., and Cheney, R.E. (1999). Myosin-V is a processive actin-based motor. Nature *400*, 590-593. doi: 10.1038/23072

Mori, T., Vale, R.D., and Tomishige, M. (2007). How kinesin waits between steps. Nature *450*, 750-754. doi: 10.1038/nature06346

Nettleship, J.E., Brown, J., Groves, M.R., and Geerlof, A. (2008). Methods for protein characterization by mass spectrometry, thermal shift (ThermoFluor) assay, and multiangle or static light scattering. Methods in molecular biology *426*, 299-318. doi: 10.1007/978-1-60327-058-8_19

Okada, Y., Higuchi, H., and Hirokawa, N. (2003). Processivity of the single-headed kinesin KIF1A through biased binding to tubulin. Nature *424*, 574-577. doi: 10.1038/nature01804

Okada, Y., Yamazaki, H., Sekine-Aizawa, Y., and Hirokawa, N. (1995). The neuron-specific kinesin superfamily protein KIF1A is a unique monomeric motor for anterograde axonal transport of synaptic vesicle precursors. Cell *81*, 769-780

Padilla-Parra, S., and Tramier, M. (2012). FRET microscopy in the living cell: different approaches, strengths and weaknesses. BioEssays : news and reviews in molecular, cellular and developmental biology *34*, 369-376. doi: 10.1002/bies.201100086

Phichith, D., Travaglia, M., Yang, Z., Liu, X., Zong, A.B., Safer, D., and Sweeney, H.L. (2009). Cargo binding induces dimerization of myosin VI. Proceedings of the National Academy of Sciences of the United States of America *106*, 17320-17324. doi: 10.1073/pnas.0909748106

Pierce, D.W., Hom-Booher, N., Otsuka, A.J., and Vale, R.D. (1999). Single-molecule behavior of monomeric and heteromeric kinesins. Biochemistry *38*, 5412-5421. doi: 10.1021/bi9830009

Piston, D.W., and Kremers, G.J. (2007). Fluorescent protein FRET: the good, the bad and the ugly. Trends in biochemical sciences *32*, 407-414. doi: 10.1016/j.tibs.2007.08.003

Reck-Peterson, S.L., Yildiz, A., Carter, A.P., Gennerich, A., Zhang, N., and Vale, R.D. (2006). Single-molecule analysis of dynein processivity and stepping behavior. Cell *126*, 335-348. doi: 10.1016/j.cell.2006.05.046

Roy, R., Hohng, S., and Ha, T. (2008). A practical guide to single-molecule FRET. Nature methods *5*, 507-516. doi: 10.1038/nmeth.1208

Sakai, T., Umeki, N., Ikebe, R., and Ikebe, M. (2011). Cargo binding activates myosin VIIA motor function in cells. Proceedings of the National Academy of Sciences of the United States of America *108*, 7028-7033. doi: 10.1073/pnas.1009188108

Schliwa, M. (2003). Molecular Motors (Weinheim, Germany: Wiley-VCH Verlag GmbH & Co.).

Shima, T., Imamula, K., Kon, T., Ohkura, R., and Sutoh, K. (2006). Head-head coordination is required for the processive motion of cytoplasmic dynein, an AAA+ molecular motor. Journal of structural biology *156*, 182-189. doi: 10.1016/j.jsb.2006.03.014

Sivaramakrishnan, S., Spink, B.J., Sim, A.Y., Doniach, S., and Spudich, J.A. (2008). Dynamic charge interactions create surprising rigidity in the ER/K alpha-helical protein motif. Proceedings of the National Academy of Sciences of the United States of America *105*, 13356-13361. doi: 10.1073/pnas.0806256105

Soppina, V., Norris, S.R., Dizaji, A.S., Kortus, M., Veatch, S., Peckham, M., and Verhey, K.J. (2014). Dimerization of mammalian kinesin-3 motors results in superprocessive motion. Proceedings of the National Academy of Sciences of the United States of America *111*, 5562-5567. doi: 10.1073/pnas.1400759111

Sun, Y., Wallrabe, H., Seo, S.A., and Periasamy, A. (2011). FRET microscopy in 2010: the legacy of Theodor Forster on the 100th anniversary of his birth. Chemphyschem : a European journal of chemical physics and physical chemistry *12*, 462-474. doi: 10.1002/cphc.201000664

Takanishi, C.L., Bykova, E.A., Cheng, W., and Zheng, J. (2006). GFP-based FRET analysis in live cells. Brain research *1091*, 132-139. doi: 10.1016/j.brainres.2006.01.119

Tomishige, M., Klopfenstein, D.R., and Vale, R.D. (2002). Conversion of Unc104/KIF1A kinesin into a processive motor after dimerization. Science *297*, 2263-2267. doi: 10.1126/science.1073386

Umeki, N., Jung, H.S., Sakai, T., Sato, O., Ikebe, R., and Ikebe, M. (2011). Phospholipid-dependent regulation of the motor activity of myosin X. Nature structural & molecular biology *18*, 783-788. doi: 10.1038/nsmb.2065

Vale, R.D. (2003). The molecular motor toolbox for intracellular transport. Cell *112*, 467-480

Vallee, R.B., Williams, J.C., Varma, D., and Barnhart, L.E. (2004). Dynein: An ancient motor protein involved in multiple modes of transport. Journal of neurobiology *58*, 189-200. doi: 10.1002/neu.10314

Verbrugge, S., Lansky, Z., and Peterman, E.J. (2009). Kinesin's step dissected with single-motor FRET. Proceedings of the National Academy of Sciences of the United States of America *106*, 17741-17746. doi: 10.1073/pnas.0905177106

Verhey, K.J., Kaul, N., and Soppina, V. (2011). Kinesin assembly and movement in cells. Annual review of biophysics *40*, 267-288. doi: 10.1146/annurev-biophys-042910-155310

Wallrabe, H., and Periasamy, A. (2005). Imaging protein molecules using FRET and FLIM microscopy. Current opinion in biotechnology *16*, 19-27. doi: 10.1016/j.copbio.2004.12.002

Webber, T.M., Allen, A.C., Ma, W.K., Molloy, R.G., Kettelkamp, C.N., Dow, C.A., and Gage, M.J. (2009). Conformational detection of p53's oligomeric state by FlAsH Fluorescence. Biochemical and biophysical research communications *384*, 66-70. doi: 10.1016/j.bbrc.2009.04.073

Wells, A.L., Lin, A.W., Chen, L.Q., Safer, D., Cain, S.M., Hasson, T., Carragher, B.O., Milligan, R.A., and Sweeney, H.L. (1999). Myosin VI is an actin-based motor that moves backwards. Nature *401*, 505-508. doi: 10.1038/46835

Yildiz, A., Park, H., Safer, D., Yang, Z., Chen, L.Q., Selvin, P.R., and Sweeney, H.L. (2004a). Myosin VI steps via a hand-over-hand mechanism with its lever arm undergoing fluctuations when attached to actin. The Journal of biological chemistry *279*, 37223-37226. doi: 10.1074/jbc.C400252200

Yildiz, A., Tomishige, M., Vale, R.D., and Selvin, P.R. (2004b). Kinesin walks hand-over-hand. Science *303*, 676-678. doi: 10.1126/science.1093753

Yu, C., Feng, W., Wei, Z., Miyanoiri, Y., Wen, W., Zhao, Y., and Zhang, M. (2009). Myosin VI undergoes cargo-mediated dimerization. Cell *138*, 537-548. doi: 10.1016/j.cell.2009.05.030

Zhong, W., Wu, M., Chang, C.W., Merrick, K.A., Merajver, S.D., and Mycek, M.A. (2007). Picosecond-resolution fluorescence lifetime imaging microscopy: a useful tool for sensing molecular interactions in vivo via FRET. Optics express *15*, 18220-18235

Zhou, H.M., Brust-Mascher, I., and Scholey, J.M. (2001). Direct visualization of the movement of the monomeric axonal transport motor UNC-104 along neuronal processes in living Caenorhabditis elegans. The Journal of neuroscience : the official journal of the Society for Neuroscience *21*, 3749-3755